

MIMO Over-The-Air Research, Development, and Testing

Guest Editors: Moray Rumney, Ryan Pirkl,
Markus Herrmann Landmann, and David A. Sanchez-Hernandez





MIMO Over-The-Air Research, Development, and Testing

International Journal of Antennas and Propagation

MIMO Over-The-Air Research, Development, and Testing

Guest Editors: Moray Rumney, Ryan Pirkl,
Markus Herrmann Landmann, and David A. Sanchez-Hernandez



Copyright © 2012 Hindawi Publishing Corporation. All rights reserved.

This is a special issue published in "International Journal of Antennas and Propagation." All articles are open access articles distributed under the Creative Commons Attribution License, which permits unrestricted use, distribution, and reproduction in any medium, provided the original work is properly cited.

Editorial Board

M. Ali, USA
Charles Bunting, USA
Felipe Catedra, Spain
Dau-Chyrh Chang, Taiwan
Deb Chatterjee, USA
Z. N. Chen, Singapore
Michael Yan Wah Chia, Singapore
Christos Christodoulou, USA
Shyh-Jong Chung, Taiwan
Lorenzo Crocco, Italy
Tayeb A. Denidni, Canada
Antonije R. Djordjevic, Serbia
Karu P. Esselle, Australia
Francisco Falcone, Spain
Miguel Ferrando, Spain
Vincenzo Galdi, Italy
Wei Hong, China
Hon Tat Hui, Singapore
Tamer S. Ibrahim, USA
Shyh-Kang Jeng, Taiwan
Mandeep Jit Singh, Malaysia

Nemai Karmakar, Australia
Se-Yun Kim, Republic of Korea
Ahmed A. Kishk, Canada
Tribikram Kundu, USA
Byungje Lee, Republic of Korea
Ju-Hong Lee, Taiwan
L. Li, Singapore
Yilong Lu, Singapore
Atsushi Mase, Japan
Andrea Massa, Italy
Giuseppe Mazzarella, Italy
Derek McNamara, Canada
C. F. Mecklenbräuker, Austria
Michele Midrio, Italy
Mark Mirotznik, USA
Ananda S. Mohan, Australia
P. Mohanan, India
Pavel Nikitin, USA
A. D. Panagopoulos, Greece
Matteo Pastorino, Italy
Massimiliano Pieraccini, Italy

Sadasiva M. Rao, USA
Sembiam R. Rengarajan, USA
Ahmad Safaai-Jazi, USA
Safieddin Safavi Naeini, Canada
Magdalena Salazar-Palma, Spain
Stefano Selleri, Italy
Krishnasamy T. Selvan, India
Zhongxiang Q. Shen, Singapore
John J. Shynk, USA
Seong-Youp Suh, USA
Parveen Wahid, USA
Yuanxun Ethan Wang, USA
Daniel S. Weile, USA
Quan Xue, Hong Kong
Tat Soon Yeo, Singapore
Jong Won Yu, Republic of Korea
Wenhua Yu, USA
Anping Zhao, China
Lei Zhu, Singapore

Contents

MIMO Over-The-Air Research, Development, and Testing, Moray Rumney, Ryan Pirkl, Markus Herrmann Landmann, and David A. Sanchez-Hernandez
Volume 2012, Article ID 467695, 8 pages

MIMO Channel Model with Propagation Mechanism and the Properties of Correlation and Eigenvalue in Mobile Environments, Yuuki Kanemiyo, Youhei Tsukamoto, Hiroaki Nakabayashi, and Shigeru Kozono
Volume 2012, Article ID 569864, 12 pages

Two-Stage Over-the-Air (OTA) Test Method for LTE MIMO Device Performance Evaluation, Ya Jing, Xu Zhao, Hongwei Kong, Steve Duffy, and Moray Rumney
Volume 2012, Article ID 572419, 6 pages

Metrics and Methods for Evaluation of Over-The-Air Performance of MIMO User Equipment, Yifei Feng, Werner L. Schroeder, Christoph von Gagern, Adam Tankielun, and Thomas Kaiser
Volume 2012, Article ID 598620, 15 pages

On the Performance of the Time Reversal SM-MIMO-UWB System on Correlated Channels, Hieu Nguyen, Van Duc Nguyen, Trung Kien Nguyen, Kiattisak Maichalernnukul, Feng Zheng, and Thomas Kaiser
Volume 2012, Article ID 929018, 8 pages

Correlation and Capacity Calculations with Reference Antennas in an Isotropic Environment, Thorkild B. Hansen
Volume 2012, Article ID 540649, 14 pages

Channel Modelling for Multiprobe Over-the-Air MIMO Testing, Pekka Kyösti, Tommi Jämsä, and Jukka-Pekka Nuutinen
Volume 2012, Article ID 615954, 11 pages

Dependence of Error Level on the Number of Probes in Over-the-Air Multiprobe Test Systems, Afroza Khatun, Tommi Laitinen, Veli-Matti Kolmonen, and Pertti Vainikainen
Volume 2012, Article ID 624174, 6 pages

MIMO Channel Capacity in 2D and 3D Isotropic Environments, Ryan J. Pirkl and Kate A. Remley
Volume 2012, Article ID 676405, 11 pages

3GPP Channel Model Emulation with Analysis of MIMO-LTE Performances in Reverberation Chamber, Nabil Arsalane, Moctar Mouhamadou, Cyril Decroze, David Carsenat, Miguel Angel Garcia-Fernandez, and Thierry Monédière
Volume 2012, Article ID 239420, 8 pages

MIMO Throughput Effectiveness for Basic MIMO OTA Compliance Testing, Adoración Marín-Soler, Guillermo Ypiña-García, Álvaro Belda-Sanchiz, and Antonio M. Martínez-González
Volume 2012, Article ID 495329, 10 pages

Mode-Stirred Chamber Sample Selection Technique Applied to Antenna Correlation Coefficient, Paul Hallbjörner, Juan D. Sánchez-Heredia, and Antonio M. Martínez-González
Volume 2012, Article ID 986514, 5 pages

On the Relationship between Field Amplitude Distribution, Its Maxima Distribution, and Field Uniformity inside a Mode-Stirred Reverberation Chamber, M. A. García-Fernández, C. Decroze, D. Carsenat, N. Arsalane, and G. Andrieu
Volume 2012, Article ID 483287, 7 pages

Editorial

MIMO Over-The-Air Research, Development, and Testing

**Moray Rumney,¹ Ryan Pirkl,² Markus Herrmann Landmann,³
and David A. Sanchez-Hernandez⁴**

¹Agilent Technologies, Edinburgh EH12 9DJ, UK

²National Institute of Standards and Technology, Boulder, CO 80305-3337, USA

³Fraunhofer Institute for Integrated Circuits (IIS), 91058 Erlangen, Germany

⁴Universidad Politécnica de Cartagena, GIMRE, Antiguo Cuartel de Antigones, 30202 Cartagena, Spain

Correspondence should be addressed to David A. Sanchez-Hernandez, david.sanchez@upct.es

Received 9 May 2012; Accepted 9 May 2012

Copyright © 2012 Moray Rumney et al. This is an open access article distributed under the Creative Commons Attribution License, which permits unrestricted use, distribution, and reproduction in any medium, provided the original work is properly cited.

1. Introduction to the Special Issue

Multiple-input multiple-output (MIMO) over-the-air (OTA) measurements and simulations for network and terminal performance evaluation and prediction have become very important research topics in recent years. Research into MIMO OTA for standardisation purposes has been ongoing in The Wireless Association (CTIA), the Third Generation Partnership Project (3GPP), and the European Cooperation in Science and Technology (COST) for three years. This is motivated by the urgent need to develop accurate, realistic, and cost-effective test standards for UMTS and LTE systems. Although many MIMO-capable networks are already deployed, there is pressure to finish the test standards by the end of 2012. While the first MIMO devices appeared some years ago and were commercially deployed two years ago, there are not yet any standards for testing MIMO performance OTA. The development of MIMO OTA test standards has proven to be particularly complex compared to single-input single-output (SISO) OTA, and developing a test standard is taking considerable time. Unlike SISO OTA, which was relatively straightforward and purely a function of the device, MIMO OTA is highly dependent on the interaction between the propagation characteristics of the radio channel and the receive antennas of the UE. Consequently, the existing SISO measurement techniques are unable to test the UE's MIMO properties. Many different MIMO test methods have been proposed, which vary widely in their propagation channel characteristics, size, and cost. Many challenges remain in the areas of identifying the optimal channel models and test method(s), and it is possible that the outcome could be

that more than one test methodology will be standardized. Current standards activities are concentrated on showing if the proposed test methodologies provide the same results, with the ultimate goal being to clearly differentiate good from bad MIMO devices. The aim of this special issue, guest edited by a balanced representation from across academia and industry is to provide a valuable source of information for the state of this important research area.

Section 2 of this introductory paper provides an introduction to MIMO OTA standardization activities, and Section 3 describes the different test methodologies under consideration by 3GPP/CTIA. A comparison between test methodologies is made in Section 4. A summary of the papers accepted for publication in this special issue is presented in Section 5. These articles discuss important aspects of MIMO OTA testing and the latest advances of all test methodologies. The research represents the latest thinking of well-known experts in industry and academia and will undoubtedly influence future decisions on testing standardization. Some conclusions and future work are provided in Section 6.

2. MIMO OTA Standardization Activities

The work to standardize MIMO OTA measurement methods and performance requirements has evolved from the SISO OTA standards developed by CTIA in 2001 and later by 3GPP. Significant research in support of these standards was provided by COST actions 259 [1] and 273 [2]. Two figures of merit were chosen for SISO OTA: Total Radiated Power

(TRP) and Total Reference Sensitivity (TRS), also known within CTIA as Total Isotropic Sensitivity (TIS). The TRP metric is calculated by computing the average of the radiated power over a sphere centred on the device under test (DUT). The TRS metric is the average over the same sphere of the minimum received power to achieve a particular bit error rate. This DUT receiver measurement is made while the DUT is transmitting at maximum power so that any radiated effects that might cause self-blocking or desensitization of the DUT receiver are fully captured.

The first CTIA SISO OTA specification [3] defined the TRP and TRS measurement methods to be made in an anechoic chamber using a reference antenna in two orthogonal polarizations. This method was also adopted by 3GPP in [4], which additionally specified device performance requirements. An alternative test method using a reverberation chamber was also specified in [4]. This was possible since it was shown empirically that the results obtained by averaging many individual measurements using a point source within an anechoic chamber were very similar to results achieved by averaging in a mode-stirred reverberation chamber, which over a suitable period of time will generate an isotropic field.

With the introduction of MIMO technology, and in particular spatial multiplexing, the methods developed for SISO OTA could not be directly used to measure the performance of MIMO devices. This led in late 2007 to the formation of a reverberation chamber subgroup within CTIA to study the feasibility of extending reverberation chambers for MIMO device testing. In April 2009, CTIA added an anechoic chamber subgroup to study the development of MIMO measurements in anechoic chambers. In 2009, the study of MIMO OTA was added to COST action 2100 and in March 2009, 3GPP approved the study item “Measurement of radiated performance for MIMO and multi-antenna reception for HSPA and LTE terminals” in [5]. In March 2011, the two CTIA groups were merged to create the MIMO OTA subgroup (MOSG), and finally, in February 2012, 3GPP approved the work item “Verification of radiated multi-antenna reception performance of UEs in LTE/UMTS” [6] to create a formal test specification for MIMO OTA.

The fundamental difference between SISO and MIMO performance is the radio propagation channel. For SISO, the DUT performance is independent of the channel, which is defined as isotropic and with no channel fading. The isotropy is achieved in the anechoic chamber by averaging many measurements made from a single angle of arrival/departure and in the reverberation chamber by the time domain averaging of the random angles of arrival/departure caused by the mode stirring.

An isotropic environment is necessary to evaluate TRP and TIS but is totally unsuited for evaluating the spatial multiplexing performance of MIMO devices. In order for spatial multiplexing to show any gain over SISO, operation requires that the signals received by each DUT antenna be sufficiently different that the DUT receiver can decode the individual data streams. In an isotropic environment, the signals received by each antenna will be the same and no spatial multiplexing gain will be possible. Thus to evaluate spatial multiplexing performance, it is necessary to subject

the DUT to a nonuniform field through a combination of varying the angular spread of the signal or its polarization or a combination of both. When this nonuniform field is received by a DUT, which has nonidentical antennas then the possibility of spatial multiplexing gain becomes non zero.

Consequently, the two main challenges in evaluating MIMO devices are first to define the channel conditions (including any noise or interference), in which the performance is to be evaluated and then to physically create that environment and test the device. The latter step represents a new challenge to the test industry because until now, the emulation of channel propagation conditions has been done electrically using a channel emulator with a cabled (galvanic) connection to the DUT. This is the traditional method for measuring receiver performance but clearly bypasses the DUT’s antennas and has no relevance to OTA testing. Thus, for MIMO OTA testing, the challenge of channel emulation has moved from the conducted domain to the radiated domain. This is a nontrivial problem that has been the subject of most of the industry research.

3. 3GPP Candidate Test Methodologies

As a result of the 3GPP study item, seven different test methods have been proposed to 3GPP in Technical Report 37.976 [7] for creating the necessary environment to test MIMO performance. The test methods fall into two main groups: five based on anechoic chambers and two based on reverberation chambers.

Anechoic chamber candidate methods are as follows:

- (A1) multiprobe method (arbitrary number and position),
- (A2) ring of probes method (symmetrical),
- (A3) two-stage method,
- (A4) two channel method,
- (A5) spatial fading emulator method.

Reverberation chamber candidate methods are as follows:

- (R1) basic or cascaded reverberation chamber,
- (R2) reverberation chamber with channel emulator.

The anechoic and reverberation methods take fundamentally different approaches towards achieving the same end goal—the creation of a spatially diverse radio channel. In the case of the anechoic chamber, multiple probes are used to launch signals at the DUT in order to create known angles of arrival, which map onto the required channel spatial model. This is a powerful approach although in order to achieve arbitrary channel model flexibility, large numbers of probes are required, which is costly and challenging to calibrate due to issues like backscatter. In the reverberation chamber method, the spatial richness is provided in 3D by relying on the natural reflections within the chamber, which are further randomized by use of mode stirrers that oscillate to provide a spatial field, which over long periods of time approaches an isotropic field. However, the instantaneous spatial field is not

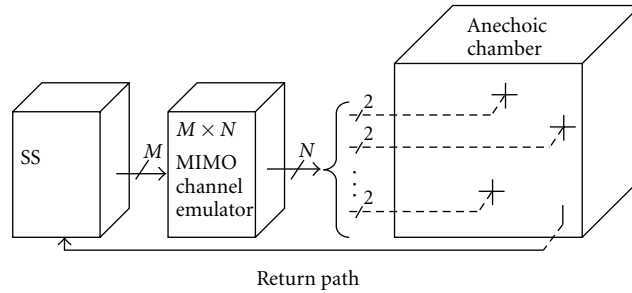


FIGURE 1: Multiprobe configuration (TR 37.976 [7] Figure 6.3.1.1-2).

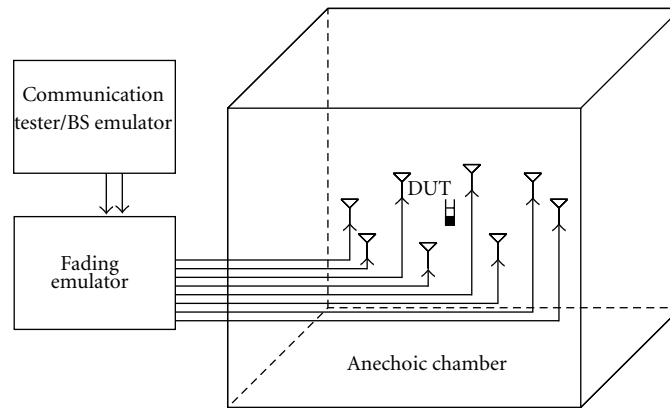


FIGURE 2: Example of MIMO/Multiantenna OTA test setup (TR 37.976 [7] Figure 6.3.1.2-1).

isotropic, which means that the reverberation chamber can be used to measure spatial multiplexing gain in decorrelated antennas. Each method will now be briefly introduced. For further details, refer to TR 37.976 [7].

3.1. A1 Multiprobe Method. The principle behind this method shown in Figure 1 is to create the desired channel model by positioning an arbitrary number of probe antennas in arbitrary positions within the anechoic chamber equidistant from the DUT, each antenna being faded by a channel emulator to provide the desired temporal component. By careful choice of the number and position of the probe antennas, it is possible to construct an arbitrarily complex radio propagation environment. The method is the most conceptually simple since there is a direct relationship between the required angular spread of the channel and the physical location of the probes.

A simple single cluster channel model with a narrow angular spread can be emulated using four antennas in a relatively small anechoic chamber with the DUT at one end and the probes at the other. More complex multicluster conditions can be generated with an increased number of probes and the transition to a larger anechoic chamber with the DUT placed in the centre and the probes on the perimeter of the chamber. The simplest configurations would locate the probes in the same azimuth plane to create a 2D environment. More complex 3D fields can be created by locating antennas on a different plane. The direct relationship between the probe antenna positions and the

emulated channel model mean that in order to test the DUT from all angles, the DUT must be mounted on a rotating and tilting platform.

3.2. A2 Ring of Probes Method. The ring of probes method is based on a symmetric ring of probe antennas equidistant around the DUT, which is placed at the centre of the anechoic chamber as shown in Figure 2. As with the multiprobe method, each probe is fed by a channel emulator to generate the temporal characteristics of the desired channel model. Where the symmetrical ring of probes method differs however is that there is no longer a fixed relationship between the probe antenna positions and the angle of departure. Instead, the spatial components of the channel model are mapped onto the equally spaced probe antennas in such a way that an arbitrary number of clusters with associated angular spreads can be generated. This more flexible approach enables any 2D spatial channel model without having to reposition (and recalibrate) the probe antennas.

The number of antennas in the ring affects the accuracy with which the spatial dimension of the channel model can be implemented. A typical configuration is a 22.5 degree raster with vertical and horizontal polarization at each location giving a total of 32 probes each independently driven by a channel emulator.

3.3. A3 Two-Stage Method. The two-stage method takes a fundamentally different approach to creating the necessary

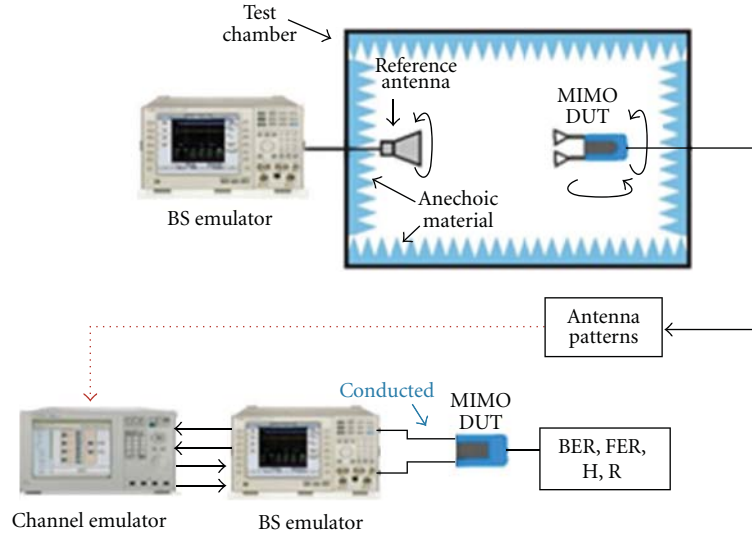


FIGURE 3: Proposed two-stage test methodology for MIMO OTA test (TR 37.976 [7] Figure 6.3.1.3.1-2).

conditions to test MIMO performance. It is illustrated in Figure 3. The first stage involves the measurement of the 3D antenna pattern of the DUT using an anechoic chamber of the size and type used for existing SISO tests. In order to measure the antenna pattern nonintrusively (i.e., without modification of the device or the attachment of cables), a special test function is required, which reports the received power per antenna and relative phase between antennas for a given received signal. The second stage takes the measured antenna pattern and convolves it with the desired channel model using a channel emulator. The output of the channel emulator then represents the faded downlink signal modified by the spatial properties of the DUT's antenna. This signal is then connected to the DUT's temporary antenna connectors as used for traditional conducted testing. The second stage does not require the use of an anechoic chamber.

The absolute accuracy of the DUT power measurement function is not critical since it is calibrated out as part of the second stage. The power linearity is more important but it too can also be linearized. The relative phase accuracy is important but this is an easier measurement for the DUT to make.

Since the 3D antenna pattern can easily be measured, the two-stage method can emulate any arbitrary 3D channel propagation condition. The rotation of the DUT relative to the channel model is accomplished by synthesis within the channel emulator. In its basic form where the antenna pattern is measured at a power well above reference sensitivity, a characteristic of the two-stage method is that the impact of self-interference is not captured.

Since spatial multiplexing requires relatively good SINR in order to provide gain, the spatial multiplexing performance at low signal levels is unlikely to be of significance. Standards exist for measuring SISO self-interference, and a study is underway to extend these simpler test systems for SIMO operation. However, since self-interference is included in the other MIMO candidate methodologies, work

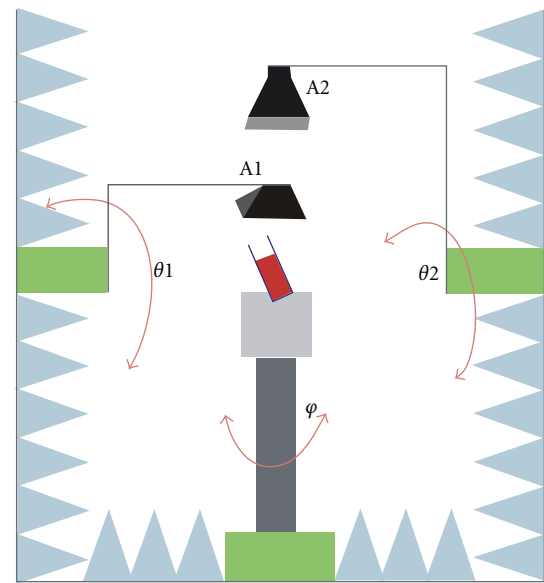


FIGURE 4: Two-Channel Method, antenna arrangement in anechoic chamber (TR 37.976 [7] Figure 6.3.1.4.1-1).

is underway to extend the two-stage method to include the evaluation of self-interference.

3.4. A4 Two-Channel Method. The two-channel method shown in Figure 4 is a special case of the multiprobe method and uses just two probes with no channel emulator. The angle of departure of the two downlink test signals can be configured for any azimuth, elevation, or polarization. The principle of the method is to evaluate the impact of the direction and angular separation of the two signals on the DUT performance. By carrying out a large number of tests using different combinations of angles, statistical analysis can be used to derive figures of merit for the DUT. Direct

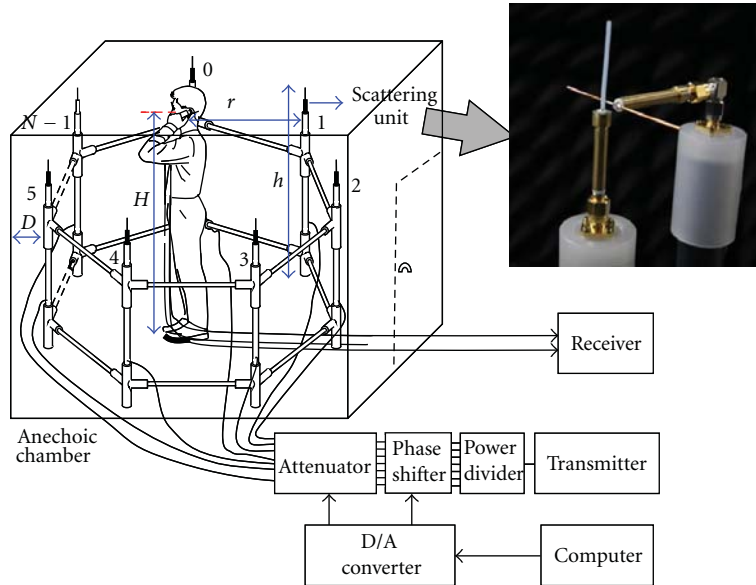


FIGURE 5: Experimental setup of the spatial fading emulator (TR 37.976 [7] Figure 6.3.1.5.1-1).

comparison with results achieved using more complex spatial signals with temporal variations is not possible, but results show this method to provide similar DUT ranking.

3.5. A5 Spatial Channel Emulation Method. The last of the anechoic chamber methods is a variation of the ring of probes method, where the channel emulation function is provided by a much simpler programmable attenuator and phase shifter per antenna. This is shown in Figure 5.

By controlling the amplitude and phase in real time, a Rayleigh distribution or other relevant multipath distribution can be obtained. This method generates an equal angular distribution for all propagation delays.

3.6. R1 Reverberation Chamber Method. The first of the reverberation-based methods uses the intrinsic reflective properties of the mode-stirred reverberation chamber to transform the downlink test signal into a rich 3D multipath signal. This is shown in Figure 6. The spatial characteristics of the signal are random and over time can be shown to be isotropic, but when observed over the time period of a demodulated data symbol, they are known to be highly directional. This nonuniformity provides the DUT with diverse signals on each antenna thus enabling spatial multiplexing gain.

The natural time domain response of the chamber can be modified by use of small amounts of RF absorptive material. The basic reverberation chamber is limited to a single power delay profile, and a relatively slow Doppler spectrum determined by the speed of the mode stirrer. Further control of the power delay profile and spatial aspects can be obtained by cascading two or more reverberation chambers as shown in Figure 7, and there has also been research by NIST and EMITE using nested chambers and coupled chambers.

In addition to the conventional Rayleigh 3D isotropic fading scenario emulated by single-cavity reverberation

chambers, multicavity multisource mode-stirred reverberation chambers employ deembedding algorithms for enhanced repeatability and have added capabilities to emulate different K-factors for Rician fading, different nonisotropic scenarios including single and multiple-cluster with partial door opening, and standardized or arbitrary amplitude power delay profiles (e.g., 802.11n, Nakagami-m, on-body and user-defined) using sample selection techniques.

3.7. R2 Reverberation Chamber and Channel Emulator Method. The final method shown in Figure 8 addresses the limitation of the basic or cascaded reverberation chamber by adding a channel emulator to the downlink prior to launching the signals into the chamber. This allows the temporal aspects of the desired channel model to be fully controlled, although the underlying natural and very short decay time of the chamber will slightly spread the power delay profile.

With the use of a channel emulator capable of negative time delay (inverse injection), multiple cavity mode-stirred reverberation chambers can accurately emulate the power delay profiles of 3GPP SCME channel models.

4. Comparison of Methods

All seven methods have unique attributes, some of which are desirable and others less so. Section 9.1 of TR 37.976 provides an extensive list of these attributes. A simplified summary of the key points is given in Table 1. This includes an assessment of the key technical areas still under study.

5. Summary of Papers Accepted for Publication

An unprecedented compilation of the latest research results for all methods can be found in this special issue. Twelve papers have been accepted for publication with an acceptance ratio below 32%.

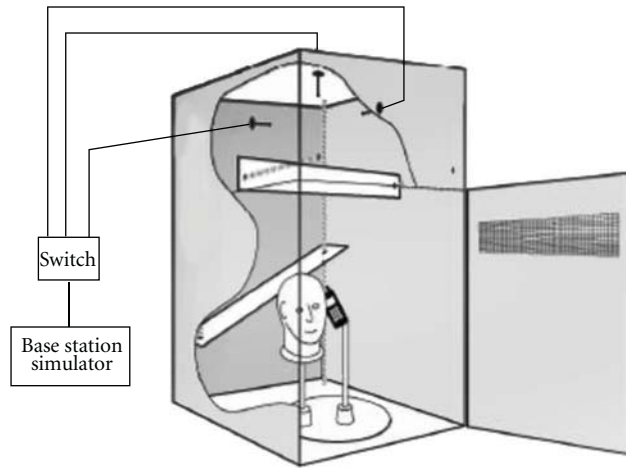


FIGURE 6: Reverberation chamber setup for devices testing with single cavity (TR 37.976 [7] Figure 6.3.2.1-1).

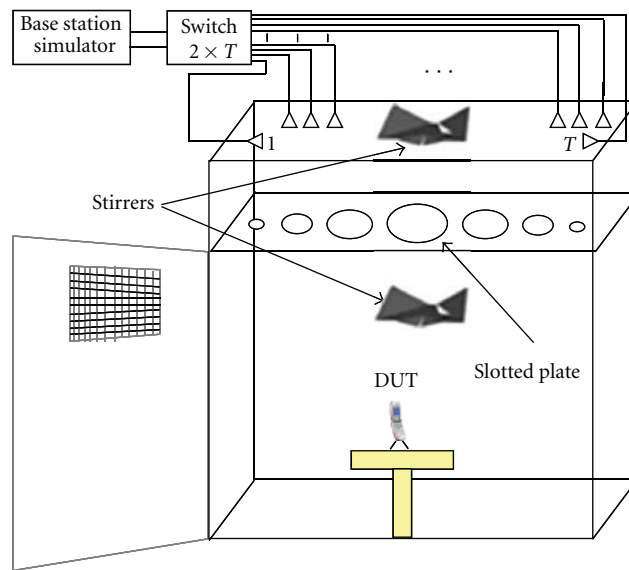


FIGURE 7: Reverberation chambers with multiple cavities (TR 37.976 [7] Figure 6.3.2.1-2).

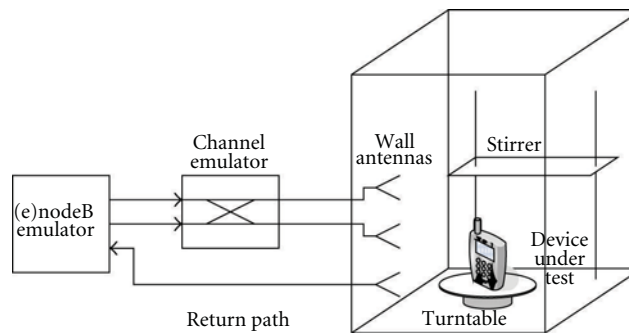


FIGURE 8: Test bench configuration for test using channel emulator and reverberation chamber for a 2×2 MIMO configuration TR 37.976 [7] Figure 6.3.2.2.1-1).

TABLE 1: Comparison of candidate methodologies.

Method	Pros	Cons	Future work
A1 Multiprobe	Conceptually simple	Limited flexibility Cost per probe	Calibration and validation
A2 Ring of probes	Arbitrarily flexible	Cost 3D very costly	Calibration and validation
A3 Two-stage	Low cost including 3D	Requires DUT test mode	Self-interference solution
A4 Two-channel	Very low cost	No temporal and limited spatial control	Correlation with other methods
A5 Spatial emulator	Low cost	Limitations in channel models	Calibration and correlation with other methods
R1 Reverb	Very low cost	Limited temporal and no spatial control	Calibration and evaluation of spatial aspects
R2 Reverb plus fader	Low cost	No spatial control	Calibration and evaluation of spatial aspects

Among the methodology-agnostic contributions, the work by Kanemiyo et al. in [8] highlights the still-existing differences between realistic fading channels and simplified channel models. A new channel model based on correlation with a given fixed theoretical correlation between antenna elements at the mobile is provided. This MIMO channel model can be used for studying the relationship between the correlation and eigenvalues for various propagation environments. These differences are also dealt with in the work by Nguyen et al. [9], wherein a specific channel model is derived using the promising time-reversal technique. By using Time-Reversal (TR), several data streams can be simultaneously transmitted by using only one antenna while outperforming a true MIMO-UWB (Ultra WideBand) system with multiple transmit antennas. The channel measurements are performed in a short-range indoor environment, using both line-of-sight and non-line-of-sight to verify the adopted correlated channel model. The interesting work by Pirkl and Remley [10] investigates the possibility of obtaining comparable throughput results between different test methodologies. In their work, it is demonstrated that, provided (1) the DUT is rotated to different orientations in the 2D statistically isotropic anechoic environment and (2) the dimensions of the DUT are on the order of a wavelength or less such that the element directivities will be low, we can expect that throughput statistics for a DUT in 2D and 3D statistically isotropic environments will be within 10% of each other. This suggests that test procedures for MIMO OTA wireless terminals in anechoic chamber (AC) and reverberation chamber (RC) methods should be comparable for the conditions studied.

Several papers provide interesting results for the RC methods. In [11], the joint research effort of SP in Sweden and UPCT in Spain show that it is possible for a multicavity RC to emulate different channel models with diverse levels of correlation using a novel sample-selection technique. The use of simple NIST channel models in a RC to emulate more complex channel models is an interesting method for standardisation. The 3GPP MIMO OTA Work Item in progress highlighted [12] a recent contribution by EMITE in which “*New figures of merit were presented which seem to be a very useful tool in order to analyze the large amount of information that will be available once a certain or set of methods are found to provide meaningful and comparable results.*” The new figures of merit, which are a statistical analysis of measured throughput, are presented in this issue by Marin-Soler et al.

[13]. These figures can indeed be very useful for determining the final goal of distinguishing between good and bad MIMO devices with a large set of measured throughput data obtained for a specific device following the 3GPP/CTIA test plans. The differences between test methods observed during measurement campaigns can be mitigated for RCs by the novel calibration method presented by García-Fernández et al. [14]. The new calibration method can provide a prediction of the field uniformity mean value from just one field amplitude measurement, taking advantage from the statistical laws that describe electromagnetic field distribution behavior, thus saving more than 95% of the calibration time and reducing realization costs. The ability of RCs to emulate the time domain aspects of 3GPP SCME channel models is demonstrated by Arsalane et al. [15]. In their work, a multicluster channel with the same delay spread for each cluster is emulated using a RC by convolving the base band signal to be transmitted with the urban macrocell (UMa) or urban microcell (UMi) channel model tap delay line generated using a MATLAB program. The obtained Power Delay Profiles (PDPs) are verified by channel sounding based on a sliding correlation and show very good agreement to the theoretical 3GPP SCME UMi and UMa channel models. The work by Hansen [16] concentrates on demonstrating the ability of RCs to evaluate antenna correlations and to match the results obtained in an isotropic environment to those obtained from the classical definition. Clearly distinguishable capacity curves are also provided for the CTIA-approved good, nominal, and bad reference antennas.

The contributions related to ACs are equally interesting. Khatun et al. [17] clarify the very important and cost-related issue of the required number of probes for synthesizing the desired fields inside a multiprobe system. Rules are presented for the required number of probes as a function of the test zone size in wavelengths for certain chosen uncertainty levels of the 2D field synthesis in an AC. The work by Kyosti et al. [18] show that the creation of a propagation environment inside an AC with the ring of probes method requires unconventional radio channel modelling, namely, a specific mapping of the original models onto the probe antennas, with the geometric description being a prerequisite for the original channel model.

For the Two-Channel method, the works by Feng et al. [19] show that this method is well suited to distinguish good and bad devices using two new statistical figures of merit and

different realizations of two antennas in a distributed axis AC. Finally, the work by Jing et al. [20] describes the Two-Stage method in detail. This method takes a fundamentally different approach to the problem. Unlike all the other methods, which attempt to create some form of spatial channel model into which the device is placed for measurement, the two-stage method instead measures the 3D antenna pattern of the device in a traditional SISO AC and then convolves the antenna pattern inside a channel emulator in order to make throughput measurements using cabled connections to the DUT's temporary antenna ports. The conducted signal received by the DUT thus emulates what would have been received by the DUT had it been placed in the radio field created by the channel emulator. The orientation of the DUT relative to the channel model is changed synthetically within the channel emulator, and the time-consuming throughput measurements do not require use of an AC.

6. Future Work

In addition to the method-specific open issues briefly summarized in Table 1, CTIA, and 3GPP are collaborating on future studies in order to evaluate the most appropriate radio conditions in which to measure MIMO OTA performance as well as elaborating and evaluating the capabilities of the candidate methodologies to differentiate good and bad MIMO devices. The newly approved MIMO OTA work item in 3GPP [6] is targeting December 2012 for completion.

A key element of these works is the development of reference antennas by CTIA, which will be used both in simulation of expected performance in known channel conditions and actual measurements on real devices. These steps will provide the essential traceability required to finalize the development of conformance test methods and possible device minimum performance requirements. CTIA is also working on verification procedures to align the many environmental conditions that need to be controlled if measurements made using different equipment and methods are to be comparable. This effort will certainly minimise uncertainties in the final results provided by different MIMO OTA test methods. Furthermore, the use of the reference antennas, selected reference channel models, and other environmental considerations will provide important information required by 3GPP/CTIA to make a final decision for the selected standardised test methods.

Moray Rumney

Ryan Pirkel

Markus Herrmann Landmann

David A. Sanchez-Hernandez

References

- [1] European Cooperation in Science and Technology Action 259, "Wireless flexible personal communications," <http://www.lx.it.pt/cost259/>.
- [2] European Cooperation in Science and Technology Action 273, "Towards mobile broadband multimedia networks," http://www.cost.eu/domains_actions/ict/Actions/273.
- [3] CTIA ERP, Test Plan for Mobile Station Over the Air Performance v1.0, October 2001.
- [4] 3GPP, "Measurements of radio performances for UMTS terminals in speech mode," Tech. Rep. 25.914, 2006, v.7.0.0.
- [5] 3GPP, "Measurement of radiated performance for MIMO and multi-antenna reception for HSPA and LTE terminals," RP-090352, 2011.
- [6] 3GPP, "Verification of radiated multi-antenna reception performance of UEs in LTE/UMTS," RP-120368, 2012.
- [7] 3GPP, "Measurements of radiated performance for MIMO and multi-antenna reception for HSPA and LTE terminals," Tech. Rep. 37.976, 2012, v11.0.0.
- [8] Y. Kanemiyo, Y. Tsukamoto, H. Nakabayashi, and S. Kozono, "MIMO channel model with propagation mechanism and the properties of correlation and eigenvalue in mobile environments," Hindawi IJAP Special Issue on MIMO OTA, 2012.
- [9] H. Nguyen, V. D. Nguyen, T. K. Nguyen et al., "On the performance of the time reversal SM-MIMO-UWB system on correlated channels," Hindawi IJAP Special Issue on MIMO OTA, 2012.
- [10] R. Pirkel and K. A. Remley, "MIMO channel capacity in 2-D and 3-D isotropic environments," Hindawi IJAP Special Issue on MIMO OTA, 2012.
- [11] P. Hallbjörner, J. D. Sánchez-Heredia, and M. Antonio, "Mode-stirred chamber sample selection technique applied to antenna correlation coefficient," Hindawi IJAP Special Issue on MIMO OTA, 2012.
- [12] 3GPP, "MIMO OTA way forward," R4-122132, March 2012.
- [13] A. Marin-Soler, G. Ypina-Garcia, A. Belda-Sanchiz et al., "MIMO throughput effectiveness for basic MIMO OTA compliance testing," Hindawi IJAP Special Issue on MIMO OTA, 2012.
- [14] M. A. García-Fernández, C. Decroze, D. Carsenat et al., "On the relationship between the distribution of the field amplitude, its maxima, and field uniformity inside a mode-stirred reverberation chamber," Hindawi IJAP Special Issue on MIMO OTA, 2012.
- [15] N. Arsalane, M. Mouhamadou, C. Decroze et al., "3GPP channel model emulation with analysis of MIMO-LTE performances in reverberation chamber," Hindawi IJAP Special Issue on MIMO OTA, 2012.
- [16] T. B. Hansen, "Correlation and capacity calculations with reference antennas in an isotropic environment," Hindawi IJAP Special Issue on MIMO OTA, 2012.
- [17] A. Khatun, T. Laitinen, V. M. Kolmonen et al., "Dependence of error level on the number of probes in over-the-air multiprobe test systems," Hindawi IJAP Special Issue on MIMO OTA, 2012.
- [18] P. Kyosti, T. Jämsä, and J. P. Nuutinen, "Channel modelling for multiprobe over-the-air MIMO testing," Hindawi IJAP Special Issue on MIMO OTA, 2012.
- [19] Y. Feng, W. L. Schroeder, C. von Gagern et al., "Metrics and methods for evaluation of over-the-air performance of MIMO user equipment," Hindawi IJAP Special Issue on MIMO OTA, 2012.
- [20] Y. Jing, X. Zhao, H. W. Kong et al., "Two-stage over the air (OTA) test method for LTE MIMO device performance evaluation," Hindawi IJAP Special Issue on MIMO OTA, 2012.

Research Article

MIMO Channel Model with Propagation Mechanism and the Properties of Correlation and Eigenvalue in Mobile Environments

Yuuki Kanemiyo, Youhei Tsukamoto, Hiroaki Nakabayashi, and Shigeru Kozono

Department of Electrical, Electronics and Computer Engineering, Chiba Institute of Technology, 2-17-1 Tsudanuma, Narashino-shi, Chiba 275-0016, Japan

Correspondence should be addressed to Shigeru Kozono, kozono.shigeru@it-chiba.ac.jp

Received 29 November 2011; Revised 27 March 2012; Accepted 27 March 2012

Academic Editor: David A. Sanchez-Hernandez

Copyright © 2012 Yuuki Kanemiyo et al. This is an open access article distributed under the Creative Commons Attribution License, which permits unrestricted use, distribution, and reproduction in any medium, provided the original work is properly cited.

This paper described a spatial correlation and eigenvalue in a multiple-input multiple-output (MIMO) channel. A MIMO channel model with a multipath propagation mechanism was proposed and showed the channel matrix. The spatial correlation coefficient formula $\rho_{i-j, i'-j'}(bm)$ between MIMO channel matrix elements was derived for the model and was expressed as a directive wave term added to the product of mobile site correlation $\rho_{i-i'}(m)$ and base site correlation $\rho_{j-j'}(b)$ without LOS path, which are calculated independently of each other. By using $\rho_{i-j, i'-j'}(bm)$, it is possible to create the channel matrix element with a fixed correlation value estimated by $\rho_{i-j, i'-j'}(bm)$ for a given multipath condition and a given antenna configuration. Furthermore, the correlation and the channel matrix eigenvalue were simulated, and the simulated and theoretical correlation values agreed well. The simulated eigenvalue showed that the average of the first eigenvalue λ_1 hardly depends on the correlation $\rho_{i-j, i'-j'}(bm)$, but the others do depend on $\rho_{i-j, i'-j'}(bm)$ and approach λ_1 as $\rho_{i-j, i'-j'}(bm)$ decreases. Moreover, as the path moves into LOS, the λ_1 state with mobile movement becomes more stable than the λ_1 of NLOS path.

1. Introduction

To support realtime multimedia communication, future mobile communications will require a high-bit-rate transmission system with high utilization of the frequency spectrum in multipath channels with line-of-sight (LOS) and non-line-of-sight (NLOS) paths [1]. Systems capable of fulfilling this requirement, with features such as multiple-input multiple-output (MIMO) [2, 3] and orthogonal frequency division multiplexing (OFDM) [4, 5], have been studied extensively. MIMO is especially advantageous in high utilization of the frequency spectrum. In MIMO, transmission quality and capacity depend on the channel matrix, which consists of the complex transmission coefficients between MIMO antenna elements at a mobile terminal and at the base station. The channel matrix seems to be evaluated by the spatial correlation between matrix elements and the matrix eigenvalue, for which low correlation and a large eigenvalue are better [6]. The source of those properties is in the

MIMO channel model composed of multipath propagation and the conditions at the mobile and base sites, and many models have been proposed and studied analytically and experimentally [7–10]. As an analytical model that tries to produce the matrix with a given fixed spatial correlation between MIMO antenna elements, the stochastic MIMO channel model was analyzed on the basis of an independent and identically distributed (i.i.d) random matrix for one-side correlations at the mobile and base sites, and it has also been verified experimentally [11, 12]. However, the analysis method used in the model seems to have trouble interpreting the channel situation directly and visualizing the physical propagation in MIMO transmission studies. Moreover, most models proposed to date have been stationary and NLOS, and there has been little analytical work on the correlation between both sides and LOS, which is still being developed.

With this in mind, we proposed a MIMO channel model with a propagation mechanism composed of multipath propagation and mobile- and base-site antenna

configurations and created the channel matrix on the basis of the model. The channel matrix is allowed to consist of matrix elements with a given fixed theoretical correlation between antenna elements at the mobile and base sites because the propagation mechanism is known and we can calculate the correlation. Therefore, the matrix requires a formula for estimating the correlation between each pair of antenna elements at one side and at both sides under various multipath conditions and base- and mobile-site situations. So we derived the correlation formulas by using the matrix for indoors, outdoors, and so forth. Using the matrix, we could also calculate the matrix eigenvalue and we clarified its properties by simulation; moreover, it was possible to study the relation between the correlation and eigenvalue.

This paper is organized as follows. Section 2 covers the theoretical study. First, we describe the MIMO channel model with the propagation mechanism and antenna configurations and then show the channel matrix on the basis of the model. Next, we derive the correlation formulas between antenna elements at one side and between both sides in various site conditions and environments. Section 3 covers simulation. The simulation was done for the correlation and channel matrix eigenvalue with various parameter settings. The simulated and theoretical correlations are discussed and the eigenvalue's properties are described; moreover, the relation between the correlation and the eigenvalue is studied. Finally, Section 4 summarizes the results.

2. Theory

2.1. MIMO Channel Model. MIMO systems will be used in various areas: the cells are called pico, micro, and macro cells. The MIMO channel model, which consists of a delay profile measured around the base- and mobile-site origins and the antenna configurations with coordinate systems common to the profile's angle, is shown in Figure 1. The coordinate systems have the origin at the first antenna element center with $i = 1$ for mobile site and $j = 1$ for base site, respectively. The delay profile has both horizontal azimuth angles (ξ_n, ζ_n) incident to multipath scattering and to the receiving point [13–15], except for path data with an ordinary delay profile. Moreover, each arriving wave expresses a representative wave, which is the peak value in each cluster. The delay profile assumed the following conditions.

- (i) The number of arriving waves is $N + 1$, waves are independent of each other, and the n th-path wave is denoted by subscript n , where $n = 0$ means a directive wave and $n \geq 1$ means no directive waves.
- (ii) The waves have excess delay time τ_n relative to the shortest path between the two origins and maximum excess delay time τ_{\max} . The τ_n values are random over range $0 \leq \tau_n \leq \tau_{\max}$.
- (iii) The amplitude is h_n and independent of ξ_n and ζ_n , the power ratio of the directive and nondirective waves is denoted by k (K in dB: Rice factor k), and $k = 0$ ($K = -\infty$ dB) means NLOS. Furthermore, the nondirective wave's power is normalized to 1.

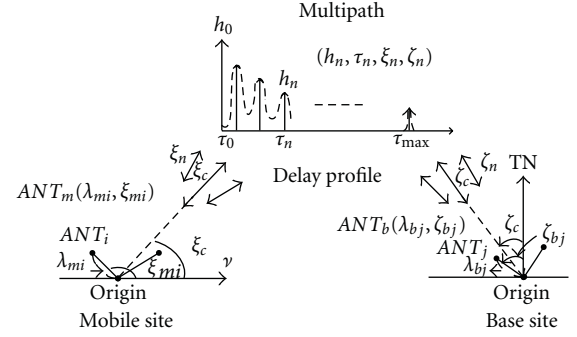


FIGURE 1: MIMO channel model.

- (iv) Whether a wave's arriving angle at the mobile or base is also the incident angle to multipath scattering from the mobile or base site depends on whether the site is receiving or transmitting. Here, the mobile-site angle is denoted by ξ_n and the base-site angle is denoted by ζ_n . The ξ_n and ζ_n are counterclockwise angles from TN (true north) at the origins on both sites; however, when the mobile station moves, ξ_n is the angle from the mobile's movement direction. The arriving wave's initial phase is ϕ_n and the values are random over $0 \leq \phi_n < 2\pi$.

On the other hand, assuming that all the antennas used have the same pattern with omnidirectionality and no mutual coupling, the antenna coordinates use a polar coordinate system centered at each site's origin, as shown in Figure 1. For the base site, the coordinates are denoted by $ANT_b(\lambda_{bj}, \zeta_{bj})$, where λ_{bj} and ζ_{bj} mean the radius normalized by wavelength λ and counterclockwise angle from TN for the j th antenna, respectively. For a mobile site, the coordinates are similarly denoted by $ANT_m(\lambda_{mi}, \xi_{mi})$; however, when the mobile station moves, ξ_{mi} is also the angle from the mobile's movement direction.

In this paper, we also assume that all antenna elements of each station have the same values of ξ_n and ζ_n , but strictly ξ_n and ζ_n differ slightly among the elements by value δ . The angular difference δ from ξ_n or ζ_n for the normalized distance (r/λ) between the origin and multipath scattering when the antenna element is set at spacing λ away from the origin is shown in Figure 2. This δ is less than 0.01 rad when $r/\lambda = 100$. As shown later, the spatial correlation is sensitive to ξ_n or ζ_n when the antenna is high and far away and when ξ_n and ζ_n have Gaussian distributions, but not so sensitive to ξ_n or ζ_n when r/λ is small and ξ_n and ζ_n are spread widely, as in the case with mobile stations or indoor cells.

2.2. MIMO Channel Matrix. Under the conditions described above and assuming a narrowband system such as OFDM, the MIMO channel, which is composed of the j th base- and i th mobile-station antenna elements, is denoted by MIMO

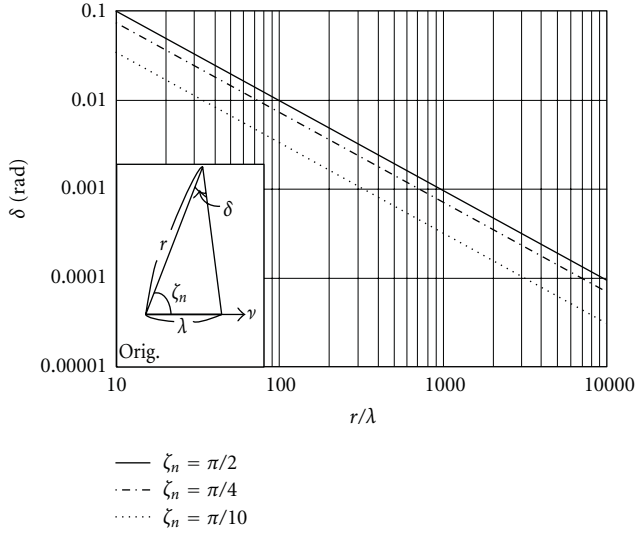


FIGURE 2: Angle difference δ from ξ_n or ζ_n (for space λ from origin).

$ch(i-j)$, and the complex received signal level $E_{i-j}(t, f_c)$ is given by

$$E_{i-j}(t, f_c) = \sum_{n=0}^N h_n e^{j\theta_{i-j,n}}, \quad (1)$$

$$\begin{aligned} \theta_{i-j,n} = 2\pi \left[f_c \tau_n - f_m t \cos \xi_n - \lambda_{mi} \cos(\xi_n - \xi_{mi}) \right. \\ \left. - \lambda_{bj} \cos(\zeta_n - \zeta_{bj}) \right] + \phi_n, \end{aligned} \quad (2)$$

where $\theta_{i-j,n}$ is the path phase of MIMO $ch(i-j)$ for the n th multipath wave, f_c is the radio frequency, and f_m is the maximum Doppler frequency. The third and fourth terms of $\theta_{i-j,n}$ in brackets depend on the mobile- and base-station antenna configurations and mean phase difference from mobile and base origins, respectively.

When the number of antenna elements at each station is M , the MIMO channel matrix E , which describes the connection between both stations, can be expressed as

$$E = \begin{bmatrix} E_{1-1} & E_{1-2} & \cdots & E_{1-M} \\ E_{2-1} & E_{2-2} & \cdots & E_{2-M} \\ \vdots & \vdots & \ddots & \vdots \\ E_{M-1} & E_{M-2} & \cdots & E_{M-M} \end{bmatrix}, \quad (3)$$

where E_{i-j} means $E_{i-j}(t, f_c)$ in (1).

2.3. Correlation between MIMO Channel Matrix Elements

2.3.1. General Formula. We start by studying the general spatial correlation between MIMO $ch(i-j)$ and $ch(i'-j')$; the complex correlation is denoted by $\rho_{i-j, i'-j'}(bm)$. With

variables x meaning $E_{i-j}(t, f_c)$ and y meaning $E_{i'-j'}(t, f_c)$ obtained by (1), $\rho_{i-j, i'-j'}(bm)$ is expressed by

$$\begin{aligned} \rho_{i-j, i'-j'}(bm) \\ = \frac{\langle (x - \langle x \rangle)^* (y - \langle y \rangle) \rangle}{\left[\langle (x - \langle x \rangle)^* (x - \langle x \rangle) \rangle \langle (y - \langle y \rangle)^* (y - \langle y \rangle) \rangle \right]^{1/2}}. \end{aligned} \quad (4)$$

Here, the symbols $\langle \rangle$ and $*$ mean ensemble average and conjugate complex, respectively. Under the conditions in Section 2.1, $\langle x \rangle$ and $\langle y \rangle$ are zero owing to the independence of h_n and $\theta_{i-j,n}$ (or $\theta_{i'-j',n}$) with random values from 0 to 2π . Therefore, the denominator in (4) is $k+1$, that is, received power. On the other hand, $\langle (x - \langle x \rangle)^* (y - \langle y \rangle) \rangle$ in the numerator of (4) is expressed by (5), where $\Delta\theta_0$ expresses the directive wave's path phase difference between MIMO $ch(i'-j')$ and $ch(i-j)$ (see Appendix A).

$$\begin{aligned} \langle (x - \langle x \rangle)^* (y - \langle y \rangle) \rangle \\ = \langle h_0^2 \exp(j\Delta\theta_0) \rangle \\ + \left\langle \sum_{n=1}^N h_n^2 \right\rangle \left\langle \sum_{n=1}^N \left[\cos(2\pi z_{i-i'} \cos(\xi_n - \psi_{i-i'})) \right. \right. \\ \left. \left. - j \sin(2\pi z_{i-i'} \cos(\xi_n - \psi_{i-i'})) \right] \right\rangle \\ \times \left\langle \sum_{n=1}^N \left[\cos(2\pi z_{j-j'} \cos(\zeta_n - \psi_{j-j'})) \right. \right. \\ \left. \left. - j \sin(2\pi z_{j-j'} \cos(\zeta_n - \psi_{j-j'})) \right] \right\rangle \end{aligned} \quad (5)$$

$$= k \exp(j\Delta\theta_0) + \rho_{i-i'}(m) \cdot \rho_{j-j'}(b). \quad (6)$$

Here, $z_{i-i'}$, $\Psi_{i-i'}$, and $z_{j-j'}$, $\Psi_{j-j'}$ in (5) are antenna construction parameters for the mobile and base sites, respectively. The $z_{i-i'}$ and $\Psi_{i-i'}$ are given by (7) and mean, respectively, the spacing between the i th and i' th antenna elements and the counterclockwise angle from TN or the movement direction to a line with both these elements.

$$z_{i-i'} = [a^2 + b^2]^{1/2}, \quad \psi_{i-i'} = \tan^{-1} \left(\frac{b}{a} \right) \quad (7)$$

$$a = \lambda_{mi'} \cos \xi_{mi'} - \lambda_{mi} \cos \xi_{mi}, \quad (8)$$

$$b = \lambda_{mi'} \sin \xi_{mi'} - \lambda_{mi} \sin \xi_{mi}.$$

The first and second terms in (5) are concerned with directive and nondirective waves. Moreover, three ensemble averages in the second term are nondirective wave power, that is, 1, mobile and base station factors, which are calculated independently of each other. Therefore, we denote them as

shown $\rho_{i-i'}(m)$ and $\rho_{j-j'}(b)$ in (6). Furthermore, we expand $\rho_{i-i'}(m)$ and $\rho_{j-j'}(b)$ to a Neumann expansion because the ensemble averages are integrated with respect to ξ_n and ζ_n [16], and we get (9) for the mobile site (see Appendix B).

$$\begin{aligned} \rho_{i-i'}(m) &= \left\langle \sum_{n=1}^N \left[\sum_{l=0}^{\infty} \varepsilon_l (-1)^l J_{2l}(2\pi z_{i-i'}) \cos(2l(\xi_n - \psi_{i-i'})) \right] \right\rangle \\ &\quad - j \left\langle \sum_{n=1}^N \left[2 \sum_{l=0}^{\infty} (-1)^l J_{2l+1}(2\pi z_{i-i'}) \cos((2l+1) \right. \right. \\ &\quad \left. \left. \times (\xi_n - \psi_{i-i'}) \right) \right] \right\rangle. \end{aligned} \quad (9)$$

Here, $\varepsilon_l = 1(l = 0)$, $\varepsilon_l = 2(l \geq 1)$, $J_{2l}(\cdot)$ is Bessel function of the first order. We can also get $\rho_{j-j'}(b)$ for the base site in a similar manner to that for $\rho_{i-i'}(m)$. From the above description, we can get finally the general formula for MIMO channel spatial correlation $\rho_{i-j, i'-j'}(bm)$ by rewriting (4) as

$$\rho_{i-j, i'-j'}(bm) = \frac{k \exp(j\Delta\theta_0) + \rho_{i-i'}(m) \cdot \rho_{j-j'}(b)}{k+1}, \quad (10)$$

where $\rho_{i-i'}(m)$ and $\rho_{j-j'}(b)$ are mobile and base site correlations without a directive wave. Though the value of the numerator in (10) depends strongly on the first term, that is, k and $\Delta\theta_0$, it becomes $\rho_{i-i'}(m)\rho_{j-j'}(b)$ without LOS, so $\rho_{i-j, i'-j'}(bm)$ is the product of $\rho_{i-i'}(m)$ and $\rho_{j-j'}(b)$. Moreover, (10) shows that $\rho_{i-j, i'-j'}(bm)$ is calculated from three items: the mobile- and base-site antenna configurations ($z_{i-i'}, z_{j-j'}, \Psi_{i-i'}, \Psi_{j-j'}$), the angle distribution for arriving and incident waves to multiple paths (ξ_n, ζ_n), and Rice factor k . By using (10), we can calculate $\rho_{i-j, i'-j'}(bm)$ for any MIMO channel matrix since i, i', j , and j' can be chosen freely within M . Here $i = i'$ and $j = j'$ mean $\rho_{i-i'}(m) = 1$ and $\rho_{j-j'}(b) = 1$, respectively.

2.3.2. Example of Correlation Coefficient $\rho_{i-j, i'-j'}(bm)$. The $\rho_{i-j, i'-j'}(bm)$ in (10) contains the product of $\rho_{i-i'}(m)$ and $\rho_{j-j'}(b)$, which depend on the site environments and are independent of each other, though these environments might sometimes be the same. Therefore, to get $\rho_{i-j, i'-j'}(bm)$, it is sufficient to prepare just one side for various situations because we can get $\rho_{i-j, i'-j'}(bm)$ by combining them. Therefore, we studied the correlation for two typical distributions with uniform ξ_n and Gaussian ζ_n .

(i) *For Uniform Distribution of ξ_n .* We first calculate $\rho_{i-i'}(m)$ by (9) when ξ_n has a uniform distribution centered at ξ_c over $\xi_c - \Delta\xi_n < \xi_n < \xi_c + \Delta\xi_n$ with the probability density function as $pdf(\xi_n) = 1/2\Delta\xi_n$. Assuming a large N , we can calculate

the ensemble average in (9) by integration with respect to ξ_n , and get (11) (see Appendix C).

$$\begin{aligned} \rho_{i-i'}(m) &= \sum_{l=0}^{\infty} \varepsilon_l (-1)^l J_{2l}(2\pi z_{i-i'}) \frac{1}{2l\Delta\xi_n} \sin(2l\Delta\xi_n) \\ &\quad \times \cos(2l(\xi_c - \psi_{i-i'})) \\ &\quad - j2 \sum_{l=0}^{\infty} (-1)^l J_{2l+1}(2\pi z_{i-i'}) \frac{1}{(2l+1)\Delta\xi_n} \\ &\quad \times \sin((2l+1)\Delta\xi_n) \cos((2l+1)(\xi_c - \psi_{i-i'})). \end{aligned} \quad (11)$$

(ii) *For Gaussian Distribution of ζ_n .* Next, we calculate $\rho_{j-j'}(b)$ when ζ_n has a Gaussian distribution centered at ζ_c with deviation σ . Similar to the uniform distribution case, we get (12) (see Appendix D).

$$\begin{aligned} \rho_{j-j'}(b) &= \sum_{l=0}^{\infty} \varepsilon_l (-1)^l J_{2l}(2\pi z_{j-j'}) \cos(2l(\zeta_c - \psi_{j-j'})) \\ &\quad \times \exp(-2l^2\sigma^2) \\ &\quad - j2 \sum_{l=0}^{\infty} (-1)^l J_{2l+1}(2\pi z_{j-j'}) \\ &\quad \times \cos((2l+1)(\zeta_c - \psi_{j-j'})) \exp\left(-\frac{(2l+1)^2\sigma^2}{2}\right). \end{aligned} \quad (12)$$

3. Simulation

3.1. Simulation Method. A computer simulation was performed to verify (10), (11), and (12) and to study the relation between the MIMO channel matrix correlation and eigenvalue. The simulation parameters are listed in Table 1, assuming pico, micro, and macro cells indoors and outdoors. As suggested by (10), we need to simulate two items for the correlation: mobile or base station one-side channel, that is, $\rho_{i-i'}(m)$ or $\rho_{j-j'}(b)$, and mobile and base stations both-side channel, that is, $\rho_{i-j, i'-j'}(bm)$. So we simulated the correlation with uniform-in- ξ_n and Gaussian-in- ζ_n distributions for each item. Concerning the eigenvalue, its dependence on the correlation was simulated while changing the mobile and base site conditions and environments. The radio frequency f_c was 3 GHz, and the channel model with the delay profile in Section 2.1 was used. The nondirective wave amplitude h_n exponentially decreases with increasing τ_n , and the effective amplitude is greater than -25 dB relative to the maximum one. The simulation was performed using (1), (2), (3), and (4); the incident and arriving angles (ξ_n, ζ_n) and antenna parameters ($\lambda_m, \xi_m, \lambda_b, \zeta_b$) were set as shown in Table 1. Each simulated value was calculated from an ensemble average for more than 10^6 delay profiles, except for eigenvalue variation with movement in Section 3.3.

TABLE 1: Simulation parameters.

MIMO channel Environment	Distribution	One-side channel				Correlation				Eigenvalue		
		Indoors	Outdoors	Indoors	Outdoors	Uniform	Gaussian	Uniform-uniform	Indoors	Outdoors	Uniform-uniform	Both-side channel
Incident/arriving angle	ξ_c	$0, 0 \sim \pi$	—	—	—	—	—	—	—	—	—	—
	$(\Delta \xi_n)$	$(\pi, \pi/2, \pi/4)$	—	—	—	—	—	—	—	—	—	—
Delay profile	ζ_c	—	$\pi/6, 0 \sim \pi$	0	0	0	$\pi/6$	0	0	0	0	0
	(σ)	—	$(\pi/90, \pi/36, \pi/18)$	$(\pi, \pi/2, \pi/4)$	$(\pi/90, \pi/36, \pi/18)$	$(\pi/90, \pi/36, \pi/18)$	$(\pi/90, \pi/36, \pi/18)$	(π)	(π)	(π)	(π)	$0, \pi/6, \pi/4, \pi/2$ $(\pi/90, \pi/36, \pi/18)$
Antenna	N	10 waves										
	h_n	Exponential distribution (effective amplitude greater than -25 dB)										
Components	K	$-\infty, 5\text{dB}$	$-\infty\text{dB}$	$-\infty, 5\text{dB}$	$-\infty\text{dB}$	$-\infty, 5\text{dB}$	$-\infty\text{dB}$	$-\infty, 5\text{dB}$	$-\infty, 5\text{dB}$	$-\infty, 5\text{dB}$	$-\infty\text{dB}$	$-\infty\text{dB}$
	$\lambda_m, (\xi_m)$	$0 \sim 5, 0.5, (0)$	—	$0 \sim 5, 0.5, (0)$	$0 \sim 20, 0.5, (0)$	$0 \sim 5, 0.5, (0)$	$0 \sim 20, 0.5, (0)$	$0 \sim 20, 0.5, (0)$	$0 \sim 5, 0.5, (0)$	$0 \sim 20, 0.5, (0)$	$0.07, 0.25, (0)$	$0.10, 0.21, 0.45, (0)$
Components	$\lambda_b, (\zeta_b)$	—	$0 \sim 20, 2, (0)$	$0 \sim 5, (0)$	$0 \sim 20, (0)$	$0 \sim 5, (0)$	$0 \sim 20, (0)$	$0 \sim 5, (0)$	$0 \sim 20, (0)$	$0.07, 0.25, (0)$	$0.07, 0.25, (0)$	$2, (0)$
	Components	1×2	1×2	2×2	2×2	2×2	2×2	2×2	2×2	2×2	4×4	4×4

3.2. Correlation Coefficient of MIMO Channel

3.2.1. Mobile or Base Station One-Side Channel. Figure 3 shows the absolute value of the simulated correlation for a mobile- or base-station one-side channel assuming a mobile station indoors for Figures 3(a) and 3(b) and a base station outdoors for Figure 3(c), when the antenna's spacing $z = z_{i-i'}(z_{j-j'})$ and setting angle $\Psi_{i-i'}(\Psi_{j-j'}) = 0$. Figures 3(a) and 3(b) have arriving angle ξ_n with uniform distribution and the parameter $\Delta \xi_n$ means the n th arriving wave uniformly from the direction $\xi_c - \Delta \xi_n < \xi_n < \xi_c + \Delta \xi_n$. Figures 3(a) and 3(b) are for NLOS and LOS with $K = 5$ dB and $\xi_0 = 5\pi/6$ paths, respectively, and the correlation of NLOS fluctuates less with increasing z , but that of LOS is higher than that of NLOS and is close to a fixed value $k/(k+1)$ fluctuating with increasing z . Figures 3(a) and 3(b) also show the theoretical value $|\rho_{i-i'}(m)|$ calculated by (10) with (11); the simulated and theoretical values agree well. The $\rho_{i-i'}(m)$ at $\Delta \xi_n = \pi$ in Figure 3(a) becomes $J_0(2\pi z_{i-i'})$, as is well known. Figure 3(c) shows the simulated correlation for arriving angle ζ_n with Gaussian distribution centered at $\zeta_c = \pi/6$ with standard deviation σ . The correlation value decreases monotonically with increasing z and the simulated values agree well with the theoretical values $|\rho_{j-j'}(b)|$ obtained by (10) using (12).

Figure 4 shows the dependence of the correlation on centered arriving angle in NLOS for a one-side channel. Figures 4(a) and 4(b) are the cases for angle ξ_n with uniform distribution centered on ξ_c with $\Delta \xi_n$, and angle ζ_n with Gaussian distribution centered on ζ_c with σ , respectively. The correlation in Figure 4(a) was simulated by changing ξ_c over the range from 0 to π while keeping $z_{i-i'} = 0.5$ and $\Psi_{i-i'} = 0$. The correlation values for $\Delta \xi_n = \pi/4$ and $\pi/2$ have minima at $\xi_c = \pi/2$ and become larger far away from $\xi_c = \pi/2$, but the value for $\Delta \xi_n = \pi$ does not depend on ξ_c since arriving waves arrive from all directions from 0 to 2π . The theoretical value $|\rho_{i-i'}(m)|$ was calculated using (10), that is, (11); the theoretical and simulated values agree well. The correlation $|\rho_{j-j'}(b)|$ in Figure 4(b) for the Gaussian distribution was also simulated in a similar way to Figure 4(a), except for $z_{j-j'} = 2$. Though $|\rho_{j-j'}(b)|$ has a minimum at $\xi_c = \pi/2$ and becomes larger far away from $\xi_c = \pi/2$ like in Figure 4(a), the values at $\xi_c = \pi/2$ depend on standard deviation σ , and the minimum value of $|\rho_{j-j'}(b)|$ is large when σ is small. The theoretical value was calculated using (10), that is, (12); the theoretical and simulated values agree well.

3.2.2. Mobile and Base Station Both-Side Channel. Figure 5 shows the simulated correlation coefficient $|\rho_{i-j,i'-j'}(bm)|$, that is, $i \neq i'$ at the mobile station and $j \neq j'$ at the base station for incident ζ_n and arriving ξ_n with the same value of $\Delta \xi_n = \Delta \zeta_n$ in the both-side uniform distribution, assuming that the mobile and base stations are indoors. Figure 5(a) shows the simulated correlation when changing $z = z_{i-i'} = z_{j-j'}$ and keeping $\Psi_{i-i'} = \Psi_{j-j'} = 0$. The correlation decreases faster than in Figure 3(a). The reason for this can be seen from the theory that the theoretical value $\rho_{i-j,i'-j'}(bm)$

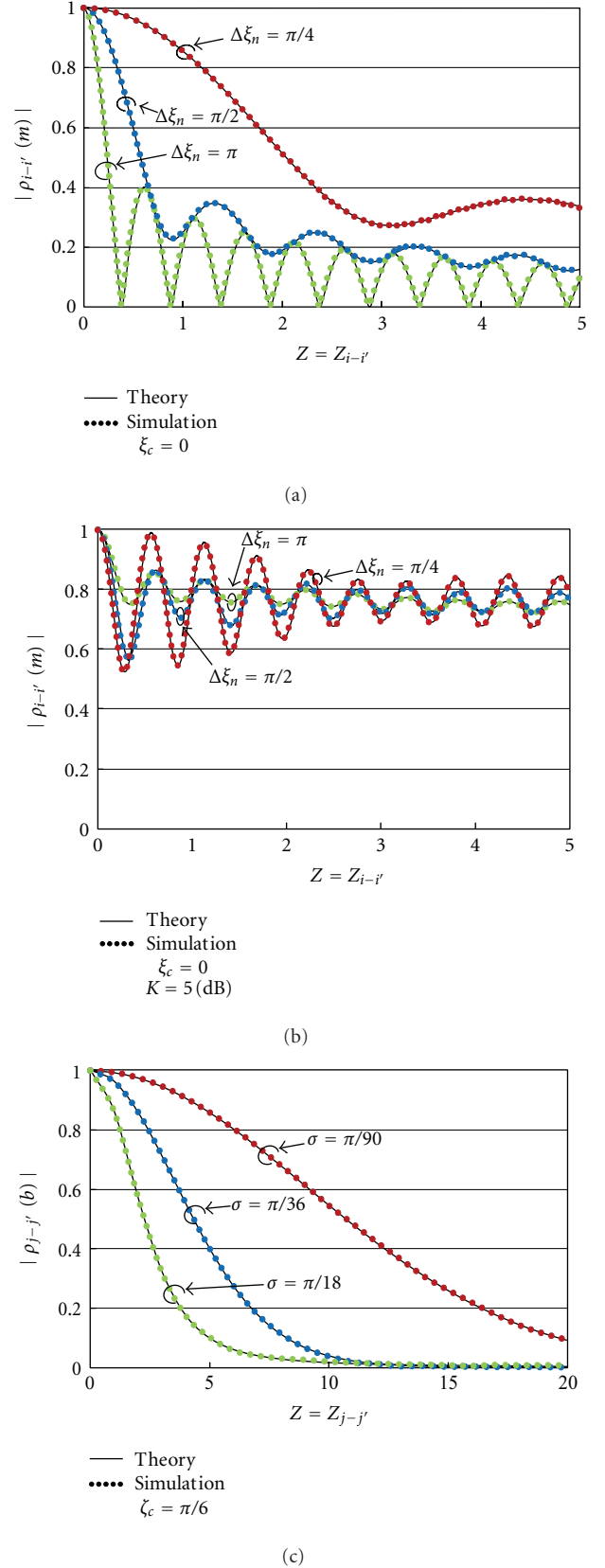


FIGURE 3: Correlation of one-side channel. (a) NLOS indoors (uniform distribution). (b) LOS indoors (uniform distribution). (c) NLOS outdoors (Gaussian distribution).

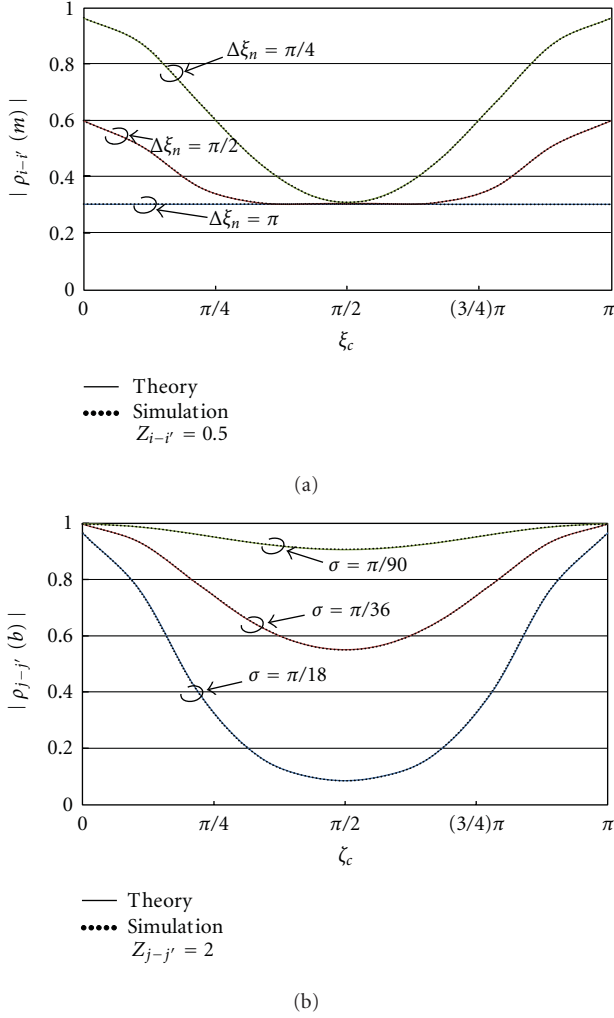


FIGURE 4: Correlation of dependence on arrival angle for one-side channel. (a) Uniform distribution. (b) Gaussian distribution.

from (10) is the product of $\rho_{i-i'}(m)$ and $\rho_{j-j'}(b)$, or here $|\rho_{i-j,i'-j'}(bm)| = |\rho_{i-i'}(m)|^2$. The simulated and theoretical values agree well. Figure 5(b) is the simulated value when changing $z = z_{j-j'}$, like Figure 5(a), except keeping $z_{i-i'} = 0.5$. So the value of the correlation at $z = 0$ is less than 1. The theoretical values from (10) at $z_{i-i'} = 0.5$ are also shown in Figure 5(b); the theoretical and simulated values agree well.

Figure 6 shows the simulated correlation $|\rho_{i-j,i'-j'}(bm)|$ for incident ξ_n with uniform distribution ($\xi_c = 0, \Delta\xi_n = \pi$) and arriving ζ_n with Gaussian distribution ($\zeta_c = \pi/6, \sigma$: parameter), assuming mobile and base sites outdoors. Figure 6(a) was simulated like Figure 5(a), that is, changing z and keeping σ fixed; compared with those in Figure 3(c), the simulated values become small rapidly with increasing z owing to the ξ_n with uniform distribution at another site. The theoretical value $\rho_{i-j,i'-j'}(bm)$ from (10) was calculated as corresponding to (11) for the mobile station $\rho_{i-i'}(m)$ and to (12) for the base station $\rho_{j-j'}(b)$, respectively. The theoretical and simulated values agree well. Figure 6(b) is the simulated correlation with changing $z = z_{j-j'}$ as in Figure 6(a), except

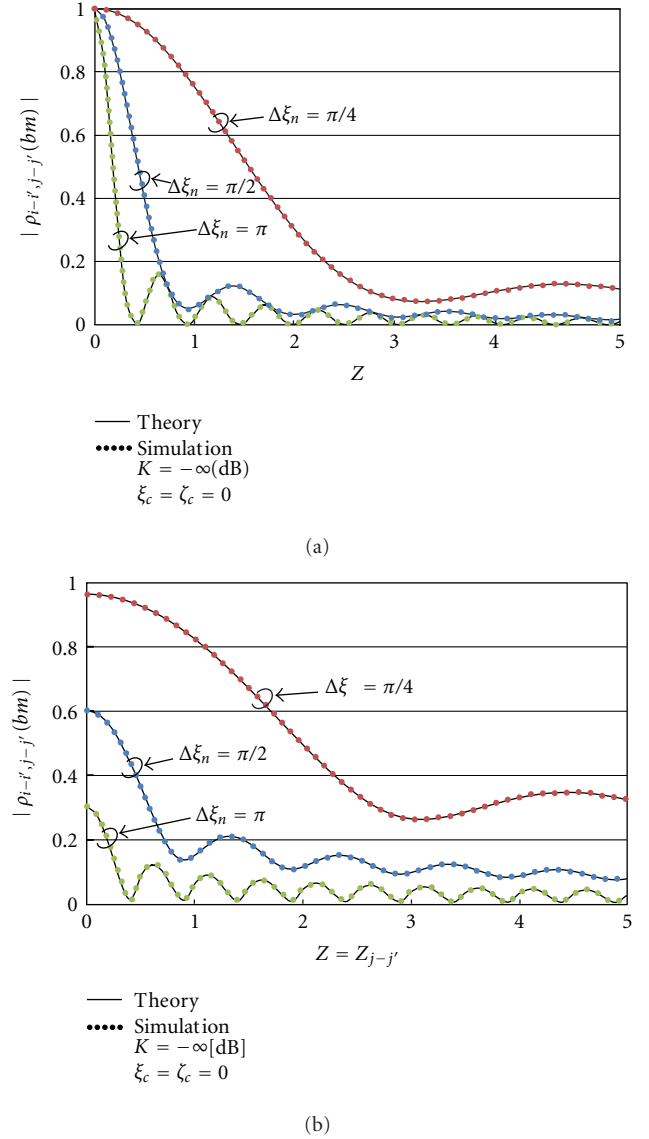


FIGURE 5: Correlation of both-side channel (uniform-uniform distribution). (a) $Z = Z_{i-i'} = Z_{j-j'}$. (b) $Z_{i-i'} = 0.5$.

keeping $z_{i-i'} = 0.5$. So the simulated value is less than 0.3 whenever z is small since we kept $z_{i-i'} = 0.5$. The theoretical value from (10) was also calculated; the theoretical and simulated values agree well.

3.3. Eigenvalue of MIMO Channel Matrix. All of the eigenvalues were simulated by a MIMO antenna with a 4×4 element configuration with elements placed with equal spacing and on a line in order to obtain the basic to eigenvalue properties.

3.3.1. Eigenvalue Property with Movement. Figure 7 shows an example of eigenvalue variation with movement of the mobile station calculated every 0.05 wavelength on the MIMO channel matrix by (3) in multipath fading. Figures 7(a) and 7(b) were simulated using the same delay profile

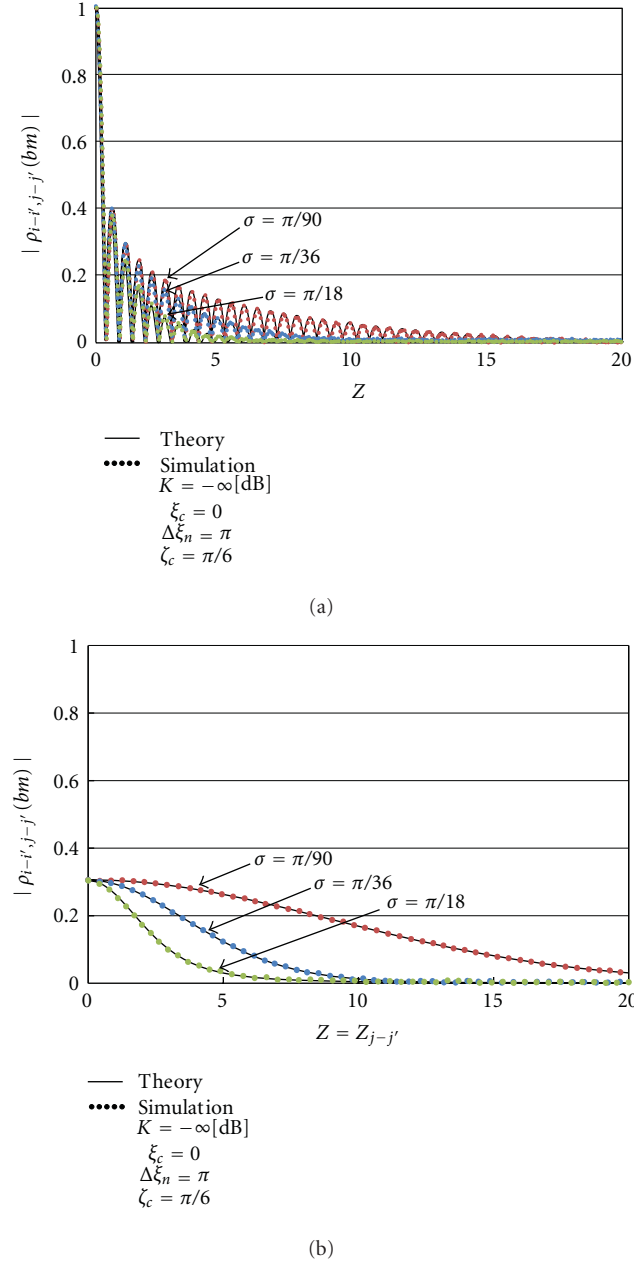


FIGURE 6: Correlation of both-side channel (uniform-Gaussian distribution). (a) $Z = Z_{i-i'} = Z_{j-j'}$. (b) $Z_{i-i'} = 0.5$.

with both-side uniform distribution with $\xi_c = 0$ and $\Delta\xi_n = \pi$ in NLOS; the only difference was the antenna radius $\lambda_{mi} = \lambda_{bj} = 0.25$ and 0.07 to make low and high correlations by (11) or the theoretical correlation between one MIMO antenna element and the next one $|\rho_{i-i+1}(m)| = |\rho_{j-j+1}(b)| = 0.45$ and 0.95 , respectively. Here, ρ in Figure 7 means $|\rho_{i-j, i'-j'}(bm)|$ from (10). Moreover, Figure 7(c) was simulated under the condition in Figure 7(a) with just the addition of a direct wave with $K = 5$ [dB] to the delay profile, when the total power of the profile was normalized to 1, and the ρ by (10) is 0.7 . Comparing Figures 7(a) and 7(b), we see that the first eigenvalue λ_1 at $\rho = 0.2$ in Figure 7(a) is almost

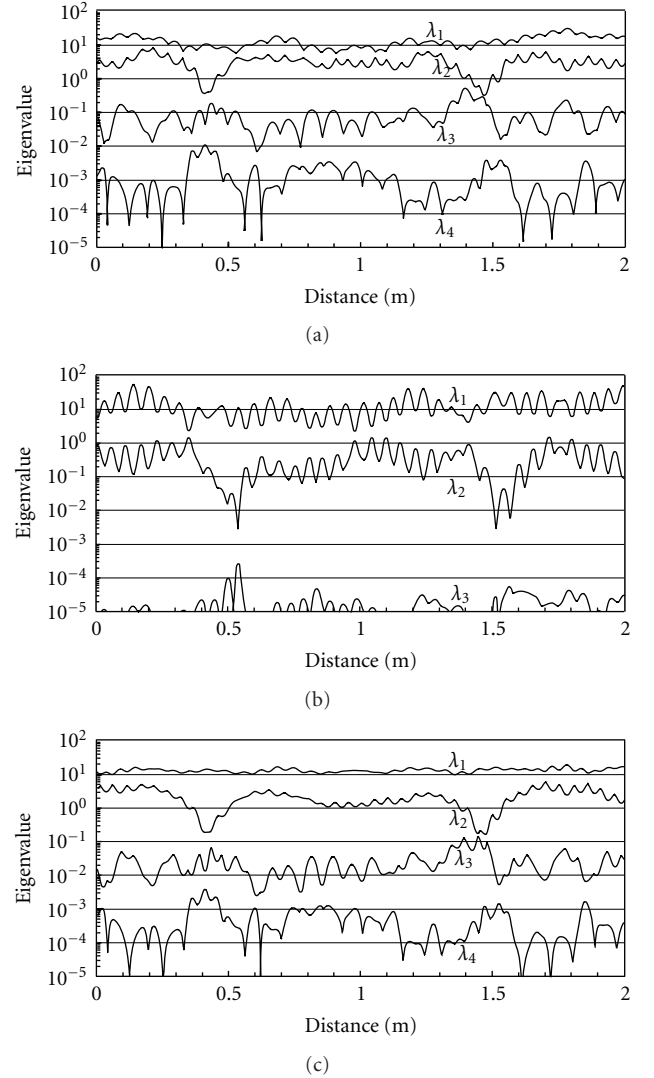


FIGURE 7: Example of eigenvalue variation with movement (4×4 MIMO, uniform distribution). (a) NLOS ($\rho = 0.2$). (b) NLOS ($\rho = 0.9$). (c) LOS ($K = 5$ [dB], $\rho = 0.7$).

equal to that at $\rho = 0.9$ in Figure 7(b) on average but that the other eigenvalues λ_2 , λ_3 , and λ_4 in Figure 7(a) are larger than that in Figure 7(b) (λ_4 is less than 10^{-5}). Moreover, each eigenvalue variation with movement in Figure 7(a) is smaller than the corresponding one in Figure 7(b). On the other hand, the average value of each eigenvalue in Figure 7(c) in LOS seems to be similar to that in Figure 7(a), but the state is more stable, especially for λ_1 , than that in NLOS.

3.3.2. Dependence of Eigenvalue on Correlation. Figure 8 shows the dependence of the eigenvalue on correlation with the property of antenna space and multipath channel by a cumulative distribution. All the eigenvalue curves in Figure 8(a), that is, at $\rho = 0.2$ and 0.9 in NLOS and at $\rho = 0.7$ in LOS, were simulated under the same conditions as in Figures 7(a), 7(b), and 7(c), respectively, except for the use of only one delay profile, or at this time the use of

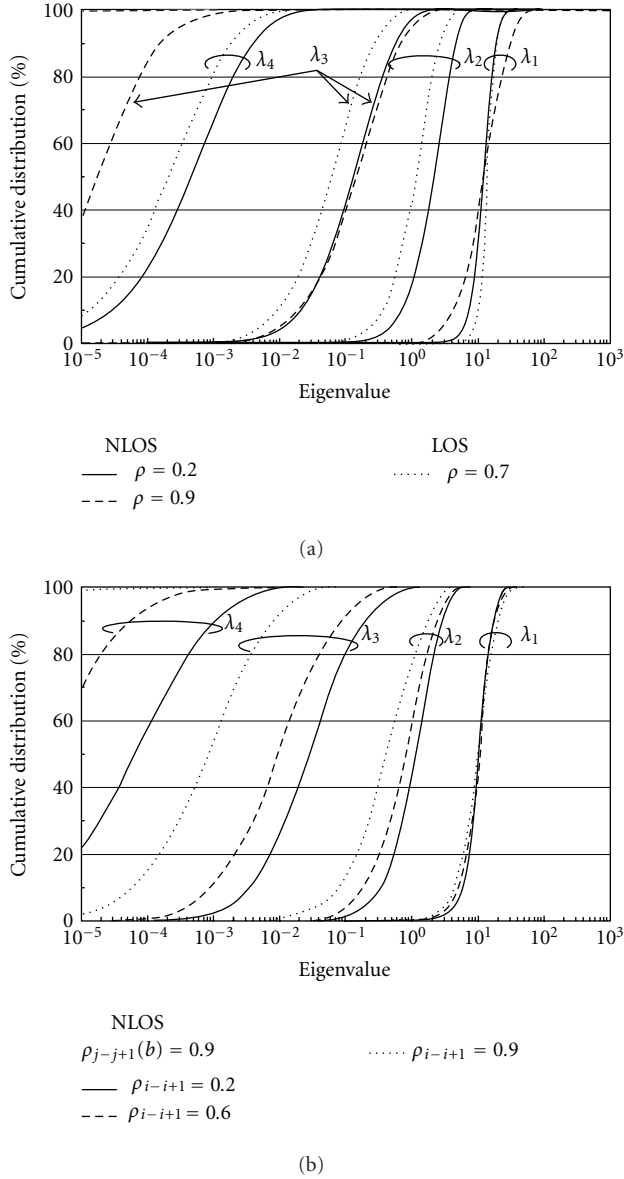


FIGURE 8: Dependence of eigenvalue on correlation (4×4 MIMO). (a) Uniform-uniform distribution. (b) Uniform-Gaussian distribution.

more than 10^6 profiles. As assumed in Figure 7, Figure 8(a) seems to suggest the following: though the 50% cumulative values in λ_1 are weakly dependent on ρ and almost equal, the other eigenvalues λ_2 , λ_3 , and λ_4 are dependent on ρ and K , and the λ_1 in LOS is the most stable. Figure 8(b) shows the dependence of the eigenvalue on correlation for $\rho_{i-j,i'-j'}(bm) = \rho_{i-i+1}(m)\rho_{j-j+1}(b)$ in NLOS, where the simulation was done changing antenna space correspondent to $|\rho_{i-i+1}(m)| = 0.2, 0.6, \text{ and } 0.9$ at the mobile station with a uniform distribution keeping a high $|\rho_{j-j+1}(b)| = 0.9$ at the base station in the Gaussian distribution with $\zeta_c = \pi/6$ and $\sigma = \pi/36$. Figure 8(b) also shows that the 50% cumulative values have little dependence on $\rho_{i-j,i'-j'}(bm)$ for λ_1 , but are dependent on $\rho_{i-j,i'-j'}(bm)$ for the other eigenvalues: the

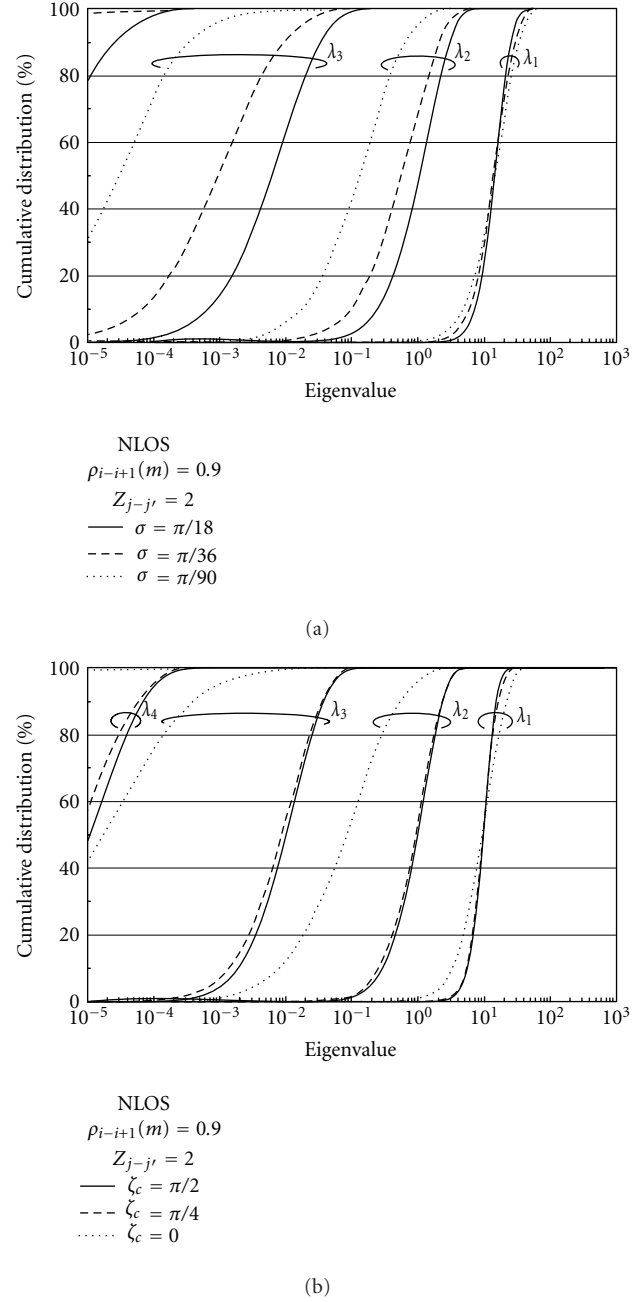


FIGURE 9: Dependence of eigenvalue on Gaussian distribution (4×4 MIMO). (a) Effect of standard deviation. (b) Effect of centering arriving angle.

smaller $\rho_{i-j,i'-j'}(bm)$ is, the closer the values are to λ_1 . All the eigenvalues tend to have a wider distribution with increasing $\rho_{i-j,i'-j'}(bm)$.

Figure 9 shows the dependence of the eigenvalue on correlation $\rho_{j-j+1}(b)$ with the properties of standard deviation σ and centering angle ζ_c in Gaussian distribution, as shown in Figure 4(b). Simulation was done for $\rho_{j-j+1}(b)$ with σ and ζ_c as parameters, while the mobile station condition was set to a constant at $|\rho_{i-i+1}(m)| = 0.9$ in a uniform distribution with $\zeta_c = 0$ and $\Delta\xi_n = \pi$. Figure 9(a) shows the influence

of σ on the eigenvalue with $\sigma = \pi/18, \pi/36$, and $\pi/90$ as parameters at $\zeta_c = \pi/6$ and $z_{j-j'} = 2$. These 50% cumulative values are also weakly dependent on σ for λ_1 , but do depend on σ for the other eigenvalues, and they become larger when σ becomes large, that is, $\rho_{j-j+1}(b)$ is small. Figure 9(b) shows the influence of ζ_c on the eigenvalue, when $\zeta_c = \pi/2, \pi/4$, and 0 at $\sigma = \pi/18$ and $z_{j-j'} = 2$. The dependence of the eigenvalues on ζ_c is similar to σ in Figure 9(a). Figure 9 suggests that the σ and ζ_c are parameters for eigenvalue property.

4. Conclusion

To study MIMO channel properties, we proposed a MIMO channel model with a propagating mechanism composed of multipath propagation and antenna configurations and then showed the MIMO channel matrix. Under this model, the spatial correlation formula $\rho_{i-j, i'-j'}(bm)$ between MIMO channel matrix elements was derived: the formula $\rho_{i-j, i'-j'}(bm)$ was expressed as a directive wave term added to the product of mobile site correlation $\rho_{i-i'}(m)$ and base site correlation $\rho_{j-j'}(b)$, which are calculated independently of each other, divided by $k+1$. This formula can be applied to create the channel matrix element with a fixed value of correlation estimated by $\rho_{i-j, i'-j'}(bm)$ for given multipath conditions and antenna configurations. Furthermore, simulation was done for the correlation and channel matrix eigenvalue indoors, outdoors, and for movement. The simulated and theoretical values of the correlation agree well. The simulated eigenvalue shows that the average of the first eigenvalue λ_1 is hardly dependent on the correlation $\rho_{i-j, i'-j'}(bm)$, but the other ones are dependent on $\rho_{i-j, i'-j'}(bm)$ and become close to λ_1 with decreasing $\rho_{i-j, i'-j'}(bm)$. Moreover, the λ_1 state with mobile movement in LOS path is more stable than the λ_1 of NLOS path. The MIMO channel model and derived $\rho_{i-j, i'-j'}(bm)$ make it possible to create a MIMO channel matrix with a fixed value correlation and furthermore to study the relation between the correlation and eigenvalue for various cell sites and environments.

Appendices

A. Derivation of (5)

Assuming that N is a large number for the delay profile in Section 2.1, then because τ_n and ϕ_n have random values, $\theta_{i-j,n}$ obtained by (2) is a random value over the range from 0 to 2π and independent of h_n . So we get $\langle x \rangle = \langle \sum_{n=0}^N h_n \rangle \langle \sum_{n=0}^N \exp(j\theta_{i-j,n}) \rangle = 0$ since the term $\langle \sum_{n=0}^N \exp(j\theta_{i-j,n}) \rangle$ becomes zero, that is, $\langle x \rangle$ and $\langle y \rangle$ in (4) are zero. Therefore, the denominator in (4) becomes $[\langle x^*x \rangle \langle y^*y \rangle]^{1/2}$, that is, $k+1$. On the other hand, $\langle (x - \langle x \rangle)^* (y - \langle y \rangle) \rangle$ in the numerator in (4) can be modified to $\langle x^*y \rangle = \langle E_{i-j}(t, f_c)^* E_{i'-j'}(t, f_c) \rangle$. As a result, the sum of products $E_{i-j}(t, f_c)^*$ and $E_{i'-j'}(t, f_c)$ remains the same for the n th arriving wave on MIMO $ch(i-j)$ and $ch(i'-j')$, but vanishes each other differences for the n th arriving wave on MIMO $ch(i-j)$ and $ch(i'-j')$ because

the values of $\theta_{i'-j',n'} - \theta_{i-j,n}$ are random; moreover, $h_n h_{n'}$ and $\theta_{i'-j',n'} - \theta_{i-j,n}$ are independent of each other. Therefore, we get (A.1) while considering h_n and $\Delta\theta_n$; moreover, mobile and base site factors are independent of each other, and the directive wave is deterministic and the amplitude h_0 is much larger than the others h_n .

$$\begin{aligned}
& \langle (x - \langle x \rangle)^* (y - \langle y \rangle) \rangle \\
&= \langle E_{i-j}(t, f_c)^* E_{i'-j'}(t, f_c) \rangle \\
&= \left\langle \sum_{n=0}^N h_n^2 \exp(j\Delta\theta_n) + \sum_{n=0}^N \sum_{n'=0}^N h_n h_{n'} \right. \\
&\quad \left. \times \exp(j(\theta_{i'-j',n'} - \theta_{i-j,n})) \right\rangle \\
&= \left\langle \sum_{n=0}^N h_n^2 \exp(j\Delta\theta_n) \right\rangle \\
&= \langle h_0^2 \exp(j\Delta\theta_0) \rangle \\
&\quad + \left\langle \sum_{n=1}^N h_n^2 \right\rangle \left\langle \sum_{n=1}^N \exp[-j2\pi\{\lambda_{mi'} \cos(\xi_n - \xi_{mi'}) \right. \\
&\quad \quad \quad \left. - \lambda_{mi} \cos(\xi_n - \xi_{mi})\}] \right\rangle \\
&\quad \times \left\langle \sum_{n=1}^N \exp[-j2\pi\{\lambda_{bj'} \cos(\zeta_n - \zeta_{bj'}) \right. \\
&\quad \quad \quad \left. - \lambda_{bj} \cos(\zeta_n - \zeta_{bj})\}] \right\rangle, \tag{A.1}
\end{aligned}$$

where $n \neq n'$ in $\sum_{n=0}^N \sum_{n'=0}^N$.

$$\begin{aligned}
\Delta\theta_n = & -2\pi \left[\lambda_{mi'} \cos(\xi_n - \xi_{mi'}) + \lambda_{bj'} \cos(\zeta_n - \zeta_{bj'}) \right. \\
& \left. - \lambda_{mi} \cos(\xi_n - \xi_{mi}) - \lambda_{bj} \cos(\zeta_n - \zeta_{bj}) \right]. \tag{A.2}
\end{aligned}$$

The $\Delta\theta_n$ yielded by (A.2) expresses the phase difference between MIMO $ch(i'-j')$ and $ch(i-j)$ for the n th arriving wave, or $\Delta\theta_n = \theta_{i'-j',n} - \theta_{i-j,n}$. Equation (A.1) has two terms, that is, directive and no directive wave terms. Moreover, since the second term can be classified into no directive power, mobile-site, and base-site factors, the classified factors are calculated independently of each other. So we used the ensemble average of mobile and base sites as $\rho_{i-i'}(m)$ and $\rho_{j-j'}(b)$, respectively, where $\langle \sum_{n=1}^N h_n^2 \rangle = 1$.

Furthermore, by continuously analyzing $\rho_{i-i'}(m)$, expanding $\cos(\xi_n - \xi_{mi'})$ and $\cos(\xi_n - \xi_{mi})$ in (A.1), and gathering terms of $\cos \xi_n$ and $\sin \xi_n$, and with a little modification we get (A.3) and express that as the third

ensemble average in (5).

$$\begin{aligned}
\rho_{i-i'}(m) &= \left\langle \sum_{n=1}^N \exp[-j2\pi\{\lambda_{mi'}\cos(\xi_n - \xi_{mi'}) - \lambda_{mi}\cos(\xi_n - \xi_{mi})\}] \right\rangle \\
&= \left\langle \sum_{n=1}^N \exp[-j2\pi\{(\lambda_{mi'}\cos \xi_{mi'} - \lambda_{mi}\cos \xi_{mi})\cos \xi_n \right. \\
&\quad \left. + (\lambda_{mi'}\sin \xi_{mi'} - \lambda_{mi}\sin \xi_{mi})\sin \xi_n\}] \right\rangle \\
&= \left\langle \sum_{n=1}^N \exp[-j2\pi z_{i-i'} \cos(\xi_n - \psi_{i-i'})] \right\rangle. \tag{A.3}
\end{aligned}$$

Here, $z_{i-i'}$ and $\Psi_{i-i'}$ are antenna construction parameters obtained from (7) for a mobile site. The $\rho_{j-j'}(b)$ for the base site is calculated in a similar manner to $\rho_{i-i'}(m)$.

B. Derivation of (9)

We expand the real and imaginary parts for $\rho_{i-i'}(m)$ in (5) into a Neumann expansion and get (9).

$$\begin{aligned}
\rho_{i-i'}(m) &= \left\langle \sum_{n=1}^N [\cos\{2\pi z_{i-i'} \cos(\xi_n - \psi_{i-i'})\} \right. \\
&\quad \left. - j \sin\{2\pi z_{i-i'} \cos(\xi_n - \psi_{i-i'})\}] \right\rangle \\
&= \left\langle \sum_{n=1}^N \left[\sum_{l=0}^{\infty} \varepsilon_l (-1)^l J_{2l}(2\pi z_{i-i'}) \cos(2l(\xi_n - \psi_{i-i'})) \right] \right\rangle \\
&\quad - j \left\langle \sum_{n=1}^N \left[2 \sum_{l=0}^{\infty} (-1)^l J_{2l+1}(2\pi z_{i-i'}) \right. \right. \\
&\quad \left. \left. \times \cos((2l+1)(\xi_n - \psi_{i-i'})) \right] \right\rangle. \tag{B.1}
\end{aligned}$$

C. Derivation of (11)

The real and imaginary parts of $\rho_{i-i'}(m)$ in (B.1) are denoted A and B . First, we calculate the real part A . Assuming a large N , when ξ_n has a uniform distribution centered at ξ_c over $\xi_c - \Delta\xi_n < \xi_n < \xi_c + \Delta\xi_n$, and the probability density function of ξ_n is $pdf(\xi_n) = 1/2\Delta\xi_n$, we can calculate the ensemble average in (9) by integration with respect to ξ_n , replacing variable $\xi_n - \Psi_{i-i'}$ by u .

$$\rho_{i-i'}(m) = A - jB,$$

$$\begin{aligned}
A &= \left\langle \sum_{n=1}^N \left[\sum_{l=0}^{\infty} \varepsilon_l (-1)^l J_{2l}(2\pi z_{i-i'}) \cos(2l(\xi_n - \psi_{i-i'})) \right] \right\rangle \\
&= \sum_{l=0}^{\infty} \varepsilon_l (-1)^l J_{2l}(2\pi z_{i-i'}) \frac{1}{2\Delta\xi_n} \\
&\quad \times \int_{\xi_c - \Delta\xi_n}^{\xi_c + \Delta\xi_n} \cos(2l(\xi_n - \psi_{i-i'})) d\xi_n \\
&= \sum_{l=0}^{\infty} \varepsilon_l (-1)^l J_{2l}(2\pi z_{i-i'}) \frac{1}{2\Delta\xi_n} \left[\frac{\sin(2lu)}{2l} \right]_{\xi_c - \psi_{i-i'} - \Delta\xi_n}^{\xi_c - \psi_{i-i'} + \Delta\xi_n} \\
&= \sum_{l=0}^{\infty} \varepsilon_l (-1)^l J_{2l}(2\pi z_{i-i'}) \frac{1}{2l\Delta\xi_n} \sin(2l\Delta\xi_n) \\
&\quad \times \cos(2l(\xi_c - \psi_{i-i'})). \tag{C.1}
\end{aligned}$$

The imaginary part B can be also calculated similarly to A ; we get (C.2):

$$\begin{aligned}
B &= 2 \sum_{l=0}^{\infty} (-1)^l J_{2l+1}(2\pi z_{i-i'}) \frac{1}{(2l+1)\Delta\xi_n} \sin((2l+1)\Delta\xi_n) \\
&\quad \times \cos((2l+1)(\xi_c - \psi_{i-i'})). \tag{C.2}
\end{aligned}$$

D. Derivation of (12)

The real and imaginary parts for $\rho_{j-j'}(b)$ in (5) are denoted A and B . We begin by calculating the real part A . Assuming that ζ_n has a Gaussian distribution centered at ζ_c with standard deviation σ by (D.1), first the real part A is expanded into a Neumann expansion and then the ensemble average is calculated by integration with respect to ξ_n as follows.

$$pdf : p(\zeta_n) = \frac{1}{\sqrt{2\pi\sigma^2}} \exp\left(-\frac{(\zeta_n - \zeta_c)^2}{2\sigma^2}\right), \tag{D.1}$$

$$\begin{aligned}
\rho_{j-j'}(b) &= \left\langle \sum_{n=1}^N \exp[-j2\pi z_{j-j'} \cos(\zeta_n - \psi_{j-j'})] \right\rangle \\
&= A - jB,
\end{aligned}$$

$$\begin{aligned}
A &= \left\langle \sum_{n=1}^N \cos(2\pi z_{j-j'} \cos(\zeta_n - \psi_{j-j'})) \right\rangle \\
&= \left\langle \sum_{n=1}^N \left[\sum_{l=0}^{\infty} \varepsilon_l (-1)^l J_{2l}(2\pi z_{j-j'}) \cos(2l(\zeta_n - \psi_{j-j'})) \right] \right\rangle \\
&= \sum_{l=0}^{\infty} \varepsilon_l (-1)^l J_{2l}(2\pi z_{j-j'}) \int_{\zeta_c - \pi}^{\zeta_c + \pi} \cos(2l(\zeta_n - \psi_{j-j'})) \\
&\quad \times p(\zeta_n) d\zeta_n. \tag{D.2}
\end{aligned}$$

Putting $\zeta_n - \zeta_c = u$, with an odd function of sine and assuming $(\pi/2\sigma)^2 \gg 1$ and with a little modification, we get

$$\begin{aligned}
A &= \frac{1}{\sqrt{2\pi\sigma^2}} \sum_{l=0}^{\infty} \varepsilon_l (-1)^l J_{2l}(2\pi z_{j-j'}) \\
&\quad \times \int_{-\pi}^{\pi} \cos(2l(u + \zeta_c - \psi_{j-j'})) \exp\left(-\frac{u^2}{2\sigma^2}\right) du \\
&= \frac{1}{\sqrt{2\pi\sigma^2}} \sum_{l=0}^{\infty} \varepsilon_l (-1)^l J_{2l}(2\pi z_{j-j'}) \cos(2l(\zeta_c - \psi_{j-j'})) \\
&\quad \times \int_{-\pi}^{\pi} \cos(2lu) \exp\left(-\frac{u^2}{2\sigma^2}\right) du \\
&= \sum_{l=0}^{\infty} \varepsilon_l (-1)^l J_{2l}(2\pi z_{j-j'}) \cos(2l(\zeta_c - \psi_{j-j'})) \\
&\quad \times \exp(-2l^2\sigma^2).
\end{aligned} \tag{D.3}$$

The imaginary part B can also be calculated in a similar manner to A . We get (D.4).

$$\begin{aligned}
B &= 2 \sum_{l=0}^{\infty} (-1)^l J_{2l+1}(2\pi z_{j-j'}) \cos((2l+1)(\zeta_c - \psi_{j-j'})) \\
&\quad \times \exp\left(-\frac{(2l+1)^2\sigma^2}{2}\right).
\end{aligned} \tag{D.4}$$

References

- [1] ITU Circular Letter 5/LCCE/2, "Radiocommunication Bureau," March 2008.
- [2] G. J. Foschini and M. J. Gans, "On limits of wireless communications in fading environments when using multiple antennas," *Wireless Personal Communications*, vol. 6, no. 3, pp. 311–335, 1998.
- [3] D. S. Shiu, G. J. Foschini, M. J. Gans, and J. M. Kahn, "Fading correlation and its effect on the capacity of multielement antenna systems," *IEEE Transactions on Communications*, vol. 48, no. 3, pp. 502–513, 2000.
- [4] R. Nee and R. Prasad, *OFDM for Wireless Multimedia Communications*, Artech House Publishers, London, UK, 1999.
- [5] T. Hwang, C. Yang, G. Wu, S. Li, and G. Y. Li, "OFDM and its wireless applications: a survey," *IEEE Transactions on Vehicular Technology*, vol. 58, no. 4, pp. 1673–1694, 2009.
- [6] M. Chiani, M. Z. Win, and A. Zanella, "On the capacity of spatially correlated MIMO Rayleigh-fading channels," *IEEE Transactions on Information Theory*, vol. 49, no. 10, pp. 2363–2371, 2003.
- [7] A. Abdi and M. Kaveh, "A space-time correlation model for multielement antenna systems in mobile fading channels," *IEEE Journal on Selected Areas in Communications*, vol. 20, no. 3, pp. 550–560, 2002.
- [8] A. F. Molisch, M. Steinbauer, M. Toeltsch, E. Bonek, and R. S. Thomä, "Capacity of MIMO systems based on measured wireless channels," *IEEE Journal on Selected Areas in Communications*, vol. 20, no. 3, pp. 561–569, 2002.
- [9] H. Xu, D. Chizhik, H. Huang, and R. Valenzuela, "A generalized space-time multiple-input multiple-output (MIMO) channel model," *IEEE Transactions on Wireless Communications*, vol. 3, no. 3, pp. 966–975, 2004.
- [10] H. Nishimoto, Y. Ogawa, T. Nishimura, and T. Ohgane, "Measurement-based performance evaluation of MIMO spatial multiplexing in a multipath-rich indoor environment," *IEEE Transactions on Antennas and Propagation*, vol. 55, no. 12, pp. 3677–3689, 2007.
- [11] J. P. Kermoal, L. Schumacher, K. I. Pedersen, P. E. Mogensen, and F. Frederiksen, "A stochastic MIMO radio channel model with experimental validation," *IEEE Journal on Selected Areas in Communications*, vol. 20, no. 6, pp. 1211–1226, 2002.
- [12] W. Weichselberger, M. Herdin, H. Özcelik, and E. Bonek, "A stochastic MIMO channel model with joint correlation of both link ends," *IEEE Transactions on Wireless Communications*, vol. 5, no. 1, pp. 90–99, 2006.
- [13] Q. H. Spencer, B. D. Jeffs, M. A. Jensen, and L. L. Swindlehurst, "Modeling the statistical time and angle of arrival characteristics of an indoor multipath channel," *IEEE Journal on Selected Areas in Communications*, vol. 18, no. 3, pp. 347–360, 2000.
- [14] J. B. Andersen and K. I. Pedersen, "Angle-of-arrival statistics for low resolution antennas," *IEEE Transactions on Antennas and Propagation*, vol. 50, no. 3, pp. 391–395, 2002.
- [15] K. N. Le, "On angle-of-arrival and time-of-arrival statistics of geometric scattering channels," *IEEE Transactions on Vehicular Technology*, vol. 58, no. 8, pp. 4257–4264, 2009.
- [16] S. Kozono and S. Sakagami, "Correlation coefficient on base station diversity for land mobile communication systems," *IEICE Communications Society: Transactions on Communications*, vol. 70, no. 4, pp. 476–482, 1987.

Research Article

Two-Stage Over-the-Air (OTA) Test Method for LTE MIMO Device Performance Evaluation

Ya Jing, Xu Zhao, Hongwei Kong, Steve Duffy, and Moray Rumney

Agilent Technologies, Santa Clara, CA 95051, USA

Correspondence should be addressed to Moray Rumney, moray_rumney@agilent.com

Received 11 February 2012; Accepted 28 March 2012

Academic Editor: Ryan J. Pirkl

Copyright © 2012 Ya Jing et al. This is an open access article distributed under the Creative Commons Attribution License, which permits unrestricted use, distribution, and reproduction in any medium, provided the original work is properly cited.

With MIMO technology being adopted by the wireless communication standards LTE and HSPA+, MIMO OTA research has attracted wide interest from both industry and academia. Parallel studies are underway in COST2100, CTIA, and 3GPP RAN WG4. The major test challenge for MIMO OTA is how to create a repeatable scenario which accurately reflects the MIMO antenna radiation performance in a realistic wireless propagation environment. Different MIMO OTA methods differ in the way to reproduce a specified MIMO channel model. This paper introduces a novel, flexible, and cost-effective method for measuring MIMO OTA using a two-stage approach. In the first stage, the antenna pattern is measured in an anechoic chamber using a nonintrusive approach, that is without cabled connections or modifying the device. In the second stage, the antenna pattern is convolved with the chosen channel model in a channel emulator to measure throughput using a cabled connection.

1. Introduction

OTA test has been standardized by CTIA and 3GPP to evaluate the end-to-end performance of SISO devices. Research results show that field performance of MIMO devices is more complex and depends on a number of factors, including self-desensitization, baseband processing, the propagation conditions, and the antenna performance. Of these, the propagation conditions and the antenna performance are paramount. With MIMO technology being adopted by the wireless communication standards LTE and HSPA+, cellular operators are pushing for the introduction of MIMO OTA performance requirements. A study of MIMO OTA for HSPA+ and LTE was proposed to 3GPP in [1]. Since then, MIMO OTA research has attracted wide interest from both industry and academia. Parallel studies are underway in COST2100 [2], CTIA [3], and 3GPP RAN WG4 [4]. 3GPP RAN WG4 has conducted a MIMO OTA measurement campaign using a common device pool. Some Agilent results in this paper come from the measurement campaign [5]. Due to the complexity of the problem, after about three-year study and discussion, there are still many issues unsolved, and further research work is required.

Unlike SISO, MIMO technology is designed to exploit a rich multipath channel. For MIMO OTA performance

evaluation, it is thus necessary to introduce a realistic MIMO channel model. The major challenge for testing MIMO OTA is how to emulate an RF environment which accurately reflects the MIMO device's performance in the real wireless propagation environment. The objective of the test is to get comparable performance between the field and the lab. Several methods for performing MIMO OTA test have been proposed to 3GPP RAN WG4, COST2100, and CTIA. These methods fall into four major categories [6]: the reverberation chamber, the two-stage method, the multiprobe anechoic chamber, and the two channel anechoic chamber. In this paper, we will introduce the two-stage MIMO OTA method and provide comparative measurement results with other methods. The paper is organized as follows. Section 2 provides a brief introduction of the two-stage MIMO OTA methodology and experimental procedure. In Section 3, the test results of the two-stage method using nonintrusive antenna pattern and throughput measurements are given. Section 4 provides a summary and some conclusions.

2. Two-Stage MIMO OTA Method

2.1. Two-Stage Method Description. The concept of the two-stage method is shown in Figure 1. The thorough

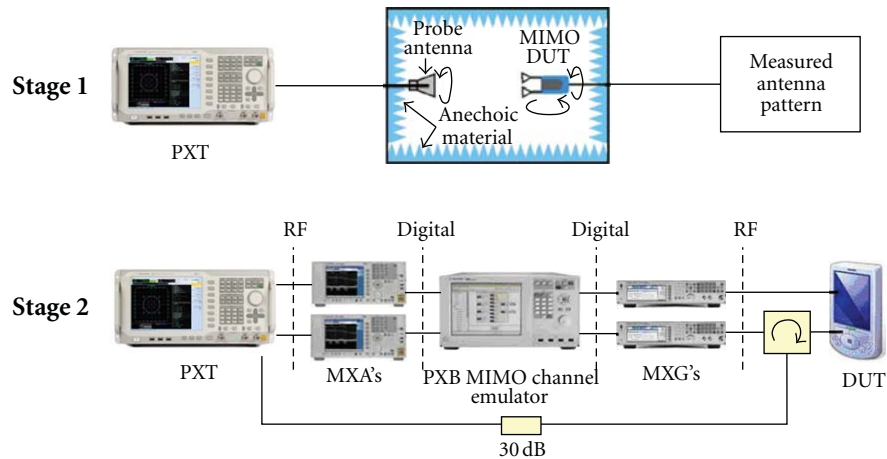


FIGURE 1: Concept of the two-stage method.

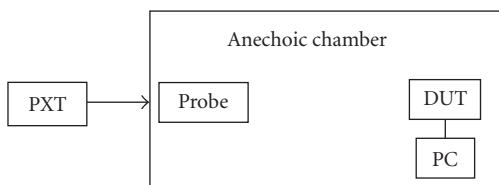


FIGURE 2: First-stage antenna pattern measurement.

introduction and analysis for this method can be found in [7]. This method divides the MIMO OTA test into two stages:

- (1) measuring the device antenna pattern inside an anechoic chamber;
- (2) using a commercial MIMO channel emulator, convolve the measured antenna pattern with the desired channel model to provide the stimulus for a conducted throughput test on the DUT.

The method is designed to provide a cost-effective MIMO OTA test solution by reusing the existing SISO OTA anechoic chamber for radiated antenna pattern measurements and then using a MIMO channel emulator to evaluate the DUTs throughput performance. [8, 9] give the power and relative phase definition for MIMO antenna pattern measurement. The chamber for antenna pattern measurement is set up as described in 3GPP TS 34.114 [10], where the DUT is put into a chamber, and each antenna element's far zone pattern is measured. The influence of human body loss can be measured by attaching the DUT to a SAM head and/or hand when doing the antenna pattern measurements. The MIMO antenna pattern and the desired multipath channel model are then convolved using a MIMO channel emulator like the Agilent N5106A to emulate the integrated channel. [11] explains how to apply measured antenna pattern to ray-based and correlation-based channel models for OTA test and also validates that combining with these two different models can get equivalent effects

by simulation results. To measure the DUT performance through this integrated channel, the base station (BS) emulator is connected to the MIMO channel emulator and then to the MIMO DUT's temporary antenna ports via approved RF cables. These DUT ports are the standard ones provided for conducted conformance tests. By controlling the power settings of the channel emulator and also the integrated channel, the end-to-end throughput with the MIMO antenna radiation influence can be measured. [5, 12, 13] provide detailed information on experiment setup and some LTE devices' performance results tested by this method. In [13], the capacity simulation results based on the measured antenna pattern are also given, and the test results show that the two-stage method throughput test results rank the devices consistently as compared with the capacity simulation results.

There are several advantages to this two-stage test method: the method can reuse existing SISO OTA anechoic chambers to make the antenna pattern measurements; only two-channel emulator outputs are required (to match the number of device receiver inputs) regardless of the complexity of the chosen channel model, the method is consequently easily scalable to higher order MIMO due to the reduced number of instruments required compared to some multi-probe methods; the channel models are highly accurate due to being implemented electronically and are also fully flexible and can be altered to suit any desired operating conditions such as indoor-outdoor, high or low Doppler spread, high or low delay spread, beam width, in 2D or full 3D, and so forth.

In order to accurately measure the antenna pattern of the intact device, the DUT needs to support amplitude and relative phase measurements of the antennas. This is not currently a standardized feature of devices although the concept has been prototyped and in principle is not dissimilar to other test features that have been standardized for other conformance tests such as loopback to enable receiver BER measurements. There is also further research being carried out to extend the first-stage pattern measurement to take account of DUT self-desensitization which otherwise is not measured.

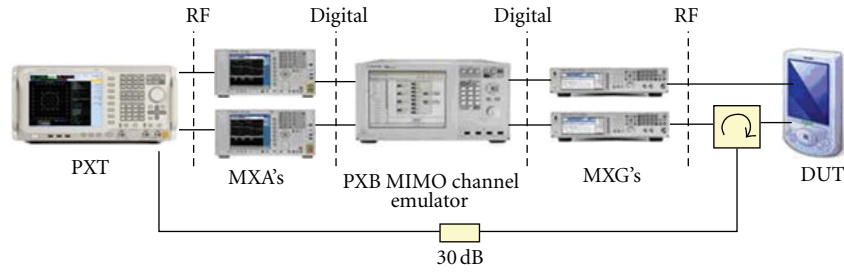


FIGURE 3: Second-stage conducted throughput measurement.

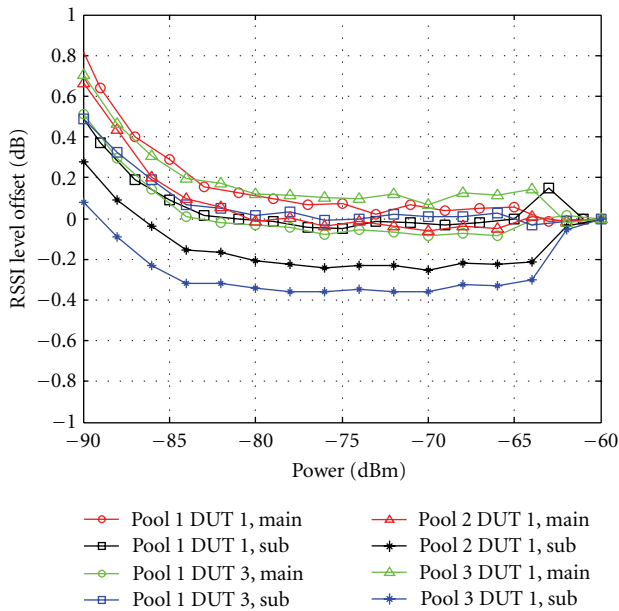


FIGURE 4: RSSI linearity measurement for DUTs from Company A.

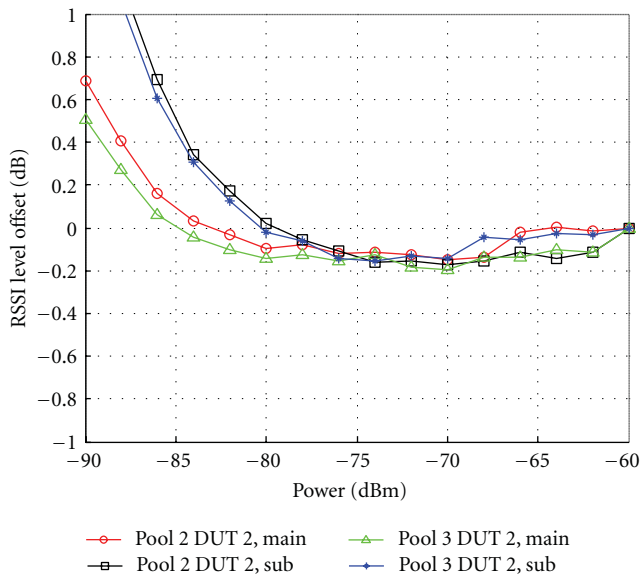


FIGURE 5: RSSI linearity measurement for DUTs from Company B.

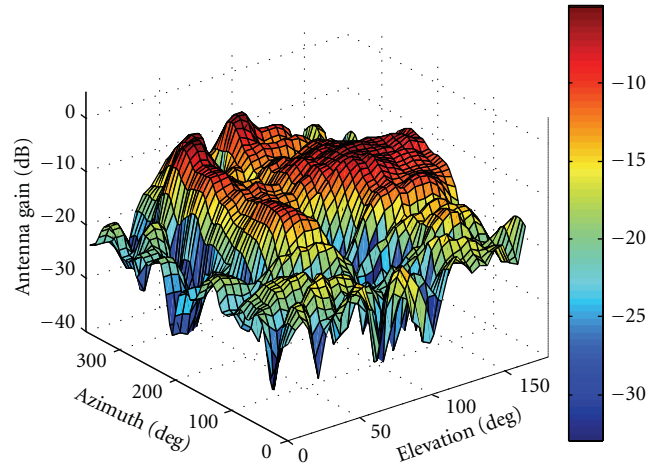


FIGURE 6: Pool 1 DUT 3 main antenna pattern on polarization V.

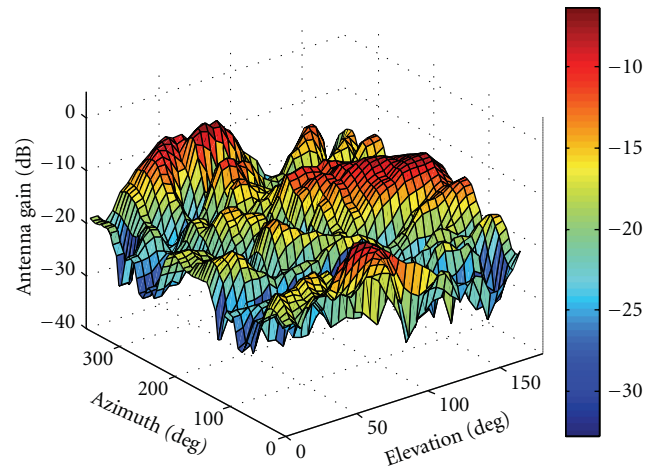


FIGURE 7: Pool 1 DUT 3 main antenna pattern on polarization H.

2.2. Experimental Setup and Procedure

2.2.1. *Active Pattern Measurement Setup.* Currently some LTE MIMO devices support a nonintrusive antenna pattern measurement function, which means that DUT can report amplitude, and relative phase measurements of the antennas [14, 15] validate the reported amplitude and phase's accuracy by designed experiments.

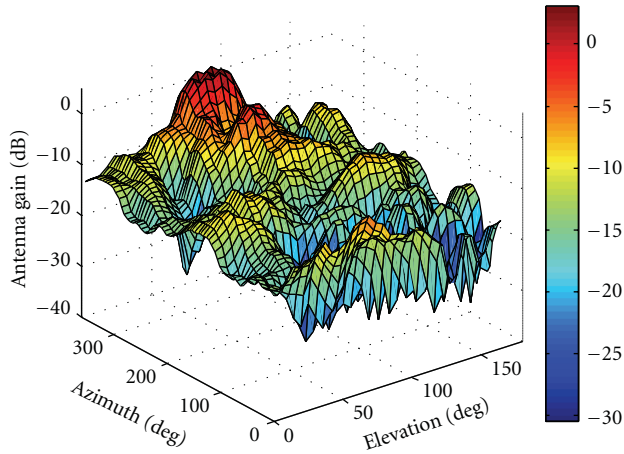


FIGURE 8: Pool 1 DUT 3 subantenna pattern on polarization V.

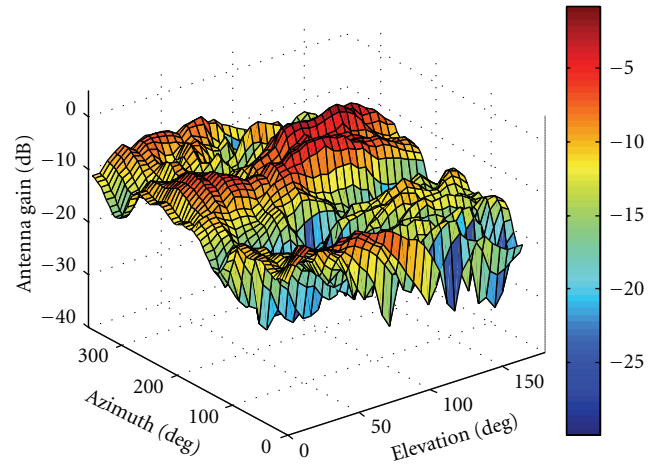


FIGURE 9: Pool 1 DUT 3 sub antenna pattern on polarization H.

We have done active 3D antenna pattern measurement on some devices in a SATIMO anechoic chamber. The antenna pattern measurement setup is shown in Figure 2. More information on these LTE devices and test setup can be found in [5]. There is software running on the laptop which controls the DUT to log the received power and phase per antenna. Before the antenna pattern measurement is carried out, the path loss between the reference antenna and DUT was calibrated to obtain the absolute power incident at the DUT. Agilent and SATIMO jointly defined a 3D antenna pattern measurement process. By using this process, the probe position and table rotation information can be correlated with the power and phase measurements in the UE log file. Agilent also developed a Matlab parser, which can extract the 3D antenna pattern data, and perform path loss, probe, and received signal strength indicator (RSSI) linearity calibration automatically from the logged file.

2.2.2. Pattern Power Linearity Calibration. Because the UE power measurement may not be completely linear, a further linearity calibration was performed using a calibrated signal in conducted mode. Using this correction, the antenna pattern was calibrated according to the measured power linearity curves. Section 3 will show some measured power linearity curves.

2.2.3. Throughput Test Setup. The throughput test configuration is shown in Figure 3. The Agilent E6621A PXT is used as the LTE BS emulator, the Agilent N5106A PXB is used as the channel emulator, and the Agilent MXG and MAX is used for RF upconversion and downconversion. The DUT has two antennas: the first antenna is the main antenna which acts as both transmitter and receiver. The second antenna is the supplementary antenna which acts only as a receiver. An RF circulator is used to separate the uplink and downlink of the main antenna. A 30 dB attenuator is used in the uplink to avoid interference between the uplink and the downlink at the BS emulator. The test setup is very similar to a typical cable conducted test for throughput

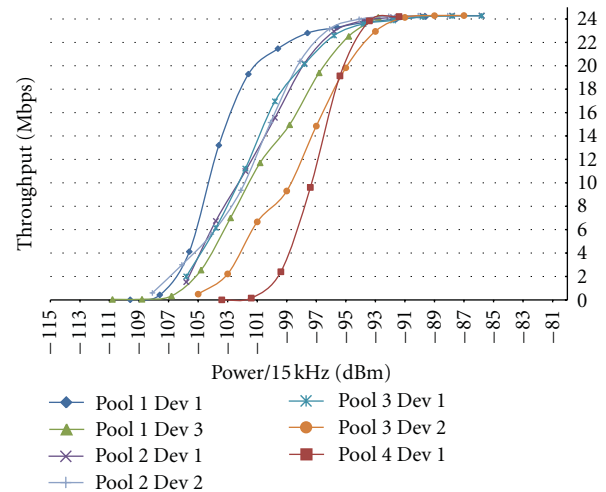


FIGURE 10: Throughput performance for single-cluster Umi channel model.

with fading. The difference is that in the MIMO OTA test, the measured antenna pattern of the DUT is loaded into the channel emulator and used together with the chosen MIMO channel model to emulate the influence of the DUT's antenna (correlation, power imbalance, and antenna gain) on the multipath fading. The detailed test procedure is referred to in Agilent proposal [12].

3. Experimental Results

This section gives the measurements results for Agilent's 3GPP measurements [5], including power linearity, 3D antenna pattern, and throughput. There is also other company which does the two-stage throughput test on same DUT. In the latest 3GPP MIMO OTA status report [16], it is summarized that under similar test conditions two companies get comparable results. [17] provides the throughput comparison with other methods. The comparison shows for some DUTs, the reverberation chamber method,

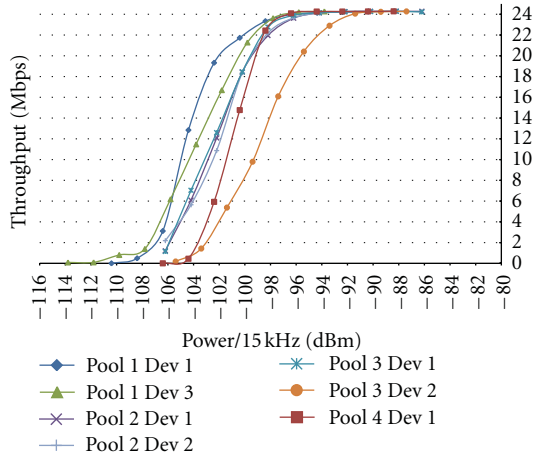


FIGURE 11: Throughput performance for multicluster Umi channel model.

the two-stage method, and the multi-probe anechoic chamber method can provide comparable results, but on some DUTs the results from different companies have big departures. The most key reason is that test environments from different companies are not completely same. Then, further investigation work is continued.

Power measurement linearity tests were performed on seven DUTs. In the experiment, we tune the signal power feed into DUTs from -60 dBm to -90 dBm in 2 dB steps and record the measured RSSI in each step. The RSSI recorded at -60 dBm signal power is chosen as the reference to calculate the RSSI linearity at different power levels. Figures 4 and 5 show RSSI linearity results for six DUTs from two different companies. These figures demonstrate that the uncorrected UE power measurement linearity was generally very good, and all DUTs have no more than 1 dB offset over a 30 dB power range. However, any linearity error is calibrated out from the measured antenna pattern in chamber before the throughput test.

Seven DUTs' 3D antenna patterns were measured in the SATIMO anechoic chamber. To save space, only one DUT pattern is given as an example from Figures 6, 7, 8, and 9. These figures demonstrate that the measured pattern is very smooth over the whole sphere, and we also performed the other experiments which validate the pattern measurement repeatability.

Throughput tests were performed on seven DUTs. Once the 3D antenna pattern is known, it is very simple using the two-stage method to calculate the 2D performance for any elevation angle to emulate the results obtained from the 2D multi-probe method. Here, we only show the throughput results for an elevation angle of 90 degrees, which is parallel to the ground. For each power level, eight uniform distributed orientation points were tested, and the overall results were the average. Figures 10, 11, and 12 show the throughput measurement results for single-cluster Umi, multi-cluster Umi, and multi-cluster Uma channel models [18].

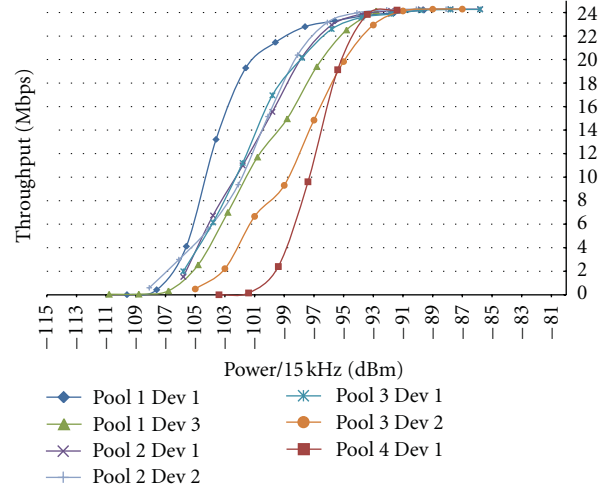


FIGURE 12: Throughput performance for multicluster Uma channel model.

These results show that:

- (1) no matter which of the three channel models is used, Pool 1 DUT 1 is the best DUT;
- (2) no matter which of the three channel models is used, Pool 2 DUT 1, Pool 2 DUT 2, and Pool 3 DUT 1 show very similar performance;
- (3) because the eNB antenna was set to be uncorrelated, the performance for multi-cluster Umi and multi-cluster Uma are similar;
- (4) the performance curves for the single-cluster channel models show wider spread than that for multi-cluster channel models, which demonstrates that a narrower angular spread makes the test more sensitive to DUT performance;
- (5) Pool 1 DUT 3's ranking sequence shows significant change between the single-cluster model and multi-cluster models, which demonstrates that Pool 1 DUT 3 is more sensitive to channel power angular spread;
- (6) Pool 4 DUT 1's ranking relative to Pool 3 DUT 2 changed when switching from single-cluster to multi-cluster, which also demonstrates Pool 4 DUT 1 is sensitive to channel power angular spread.

4. Summary

In this paper, the two-stage MIMO OTA test method is introduced. Using the antenna test mode of the DUT a nonintrusive 3D antenna pattern measurement is performed and verified by RSSI linearity calibration. The DUT's MIMO throughput is then measured using a conducted test by convolving the antenna pattern with the desired channel model. This approach enables the creation of arbitrarily complex 2D or 3D channel models including the antenna impact while only requiring a simple SISO anechoic chamber to measure the antenna pattern. The two-stage method can

thus provide a low-cost and accurate method for evaluating end-to-end MIMO performance.

Acknowledgments

The authors would like to thank SATIMO which provided access to its anechoic chamber laboratory to perform the OTA measurements.

References

- [1] Vodafone, "Study item proposal for MIMO OTA," 3GPP RAN4 R4-090903.
- [2] COST2100, <http://www.cost2100.org/>.
- [3] CTIA, <http://www.ctia.org/>.
- [4] 3GPP, <http://www.3gpp.org/>.
- [5] Agilent, "Results for two-stage LTE MIMO OTA Round Robin Testing," 3GPP R4-116046.
- [6] TR.37.976, "Measurement of radiated performance for MIMO and multiple antenna reception for HSPA and LTE terminals".
- [7] Agilent, "MIMO OTA test methodology proposal," 3GPP R4-091361.
- [8] Agilent, "Power and relative phase definition for antenna pattern measurement," 3GPP R4-115288.
- [9] Agilent, "Definition of UE pattern measurement function based on RSRP definition," 3GPP R4-116105.
- [10] 3GPP TS 34.114, User Equipment (UE)/Mobile Station (MS) Over The Air (OTA) Antenna Performance Conformance Testing.
- [11] Agilent, "Applying measured MIMO antenna patterns to MIMO channel models for OTA analysis," 3GPP R4-091949.
- [12] Agilent, "Preliminary LTE MIMO OTA test results using two-stage method," 3GPP R4-112184.
- [13] Agilent, "LTE MIMO OTA test results and analysis," R4-114188.
- [14] Qualcomm, "TP on including antenna pattern based test procedure for LTE MIMO OTA test plan," 3GPP R4-104154.
- [15] Agilent, "Experimental validation on handset antenna pattern measurement accuracy," 3GPP R4-111742.
- [16] 3GPP RP-111541, "MIMO OTA status reports".
- [17] Agilent, "Summary of two-stage measurement results," 3GPP R4-116104.
- [18] 3GPP TR 25.996, Spatial channel model for MIMO simulation.

Research Article

Metrics and Methods for Evaluation of Over-The-Air Performance of MIMO User Equipment

Yifei Feng,¹ Werner L. Schroeder,¹ Christoph von Gagern,²
Adam Tankielun,² and Thomas Kaiser³

¹RF and EMC Department, RheinMain University of Applied Sciences, Am Brückweg 26, 65428 Rüsselsheim, Germany

²Rohde & Schwarz GmbH & Co. KG, Mühldorfstraße 15, 81671 Munich, Germany

³Fachgebiet Digitale Signalverarbeitung, Universität Duisburg-Essen, Bismarckstraße 81, 47057 Duisburg, Germany

Correspondence should be addressed to Yifei Feng, yifei.feng@hs-rm.de

Received 15 January 2012; Accepted 2 April 2012

Academic Editor: Markus Landmann

Copyright © 2012 Yifei Feng et al. This is an open access article distributed under the Creative Commons Attribution License, which permits unrestricted use, distribution, and reproduction in any medium, provided the original work is properly cited.

Commercial User Equipment (UE) testing and certification has become more complex for state-of-the-art mobile communication standards such as 3rd Generation Partnership Project (3GPP) Long-Term Evolution (LTE) due to the extensive use of Multiple Input-Multiple Output (MIMO) transmission techniques. The variety of different MIMO operating modes and the almost unlimited choice of possible multipath channel conditions under which UE performance may be evaluated are not accounted for by established Single Input-Single Output (SISO) Over-The-Air (OTA) performance metrics like Total Isotropic Sensitivity (TIS) and Total Radiated Power (TRP). As pointed out in this contribution, meaningful metrics and cost-effective, low-complexity measurement methods can, nevertheless, be derived by focusing on characterization of the physical attributes of UE and by adopting statistical metrics. Starting from a brief review of the most important MIMO operating modes in the 3GPP LTE standard, the relation between UE properties and UE performance, which is observed in these operating modes, is discussed. Two complementary metrics and corresponding measurement procedures for evaluation of MIMO OTA performance are presented in order to address the diversity of possible propagation scenarios. Measurement results from preliminary implementations of the two proposed measurement procedures, including comparison between different LTE devices, are presented.

1. Introduction

Since the early years of mobile communication development, a method to reliably predict in-the-field performance of a mobile device is highly demanded. OTA test methods were first introduced when Mobile Network Operators (MNOs) experienced that devices with comparable conducted performance exposed significantly different in-the-field performance, including increased rates of dropped connections. Since most small form-factor SISO devices have inherently omni-directional patterns, especially in the low frequency bands, the focus of traditional OTA test is on total antenna efficiency [1].

State-of-the-art mobile communication standards such as 3GPP LTE bear the promise of significantly enhanced cell capacity and per-user throughput. Whether the performance of commercial UE holds up to the promise has become more

intricate to predict because MIMO performance depends strongly on UE antenna properties. New OTA measurement methods and performance metrics are necessary. After an initial request by 3GPP RAN4 to address this issue [2], directed to COST 2100 and CTIA, several OTA test method proposals have been made by participants of COST 2100, 3GPP RAN4 and CTIA. The proposals differ significantly in terms of measurement setup and equipment because each approach is trying to solve the issue from a different perspective. Some initial comparison between methods has been conducted in two large-scale Round-Robin Measurement Campaigns [3] without arriving at definite conclusions with respect to advantages and drawbacks of each method [4, 5]. Further measurement campaigns and comparison to simulation [6] and a decision on a suitable test methodology or several methodologies are planned in the near future [7].

2. Goals and Requirements for MIMO OTA Measurements

The goal of a MIMO OTA measurement is to evaluate UE with respect to in-the-field performance for various MIMO transmission modes and an almost infinite choice of multipath channel conditions. An agreed test method should, nevertheless, clearly discriminate between “good” and “bad” devices without footnotes stating “under certain conditions.” Excellent reproducibility of results is mandatory. Consistent results should be obtained by every test lab.

A further important requirement is low complexity because tests are to be performed for large number of E-UTRA frequency bands and for a variety of different near-field conditions (e.g., with head or hand phantoms), a fact which increases test time substantially. The time required for each measurement should not exceed typical measurement time for established SISO OTA measurement procedures like TIS and TRP. Additional cost for the certification process would have to be transferred to the end-user.

3. MIMO-Operating Modes in LTE

So as to design an OTA test method for MIMO UE, it is mandatory to have a basic understanding of the underlying communication standard. State-of-the-art communication standards employ an aggressive switching strategy in adaptation to the ever-changing multipath channel. LTE is a perfect example to illustrate this issue. The Downlink (DL) of LTE Rel-8 features already 7 basic transmission modes. Further modes are added in Rel-9 and Rel-10. The most relevant MIMO modes are the DL Transmit Diversity (TD) mode and Open-Loop and Closed-Loop Spatial Multiplexing (SM) modes. Apart from the different transmission modes, there are 15 unique combinations of modulation order and coding rate, each referred to in the following context as a Modulation and Coding Scheme (MCS) (note this is different to the definition of parameter I_{MCS} in LTE). In reality, transmission mode and MCS are adaptively selected by the evolved Node-B (eNB), taking into account, at its own discretion, feedback from the UE.

Among the different indicators, which are returned by the UE and provide Channel State Information (CSI) feedback to the eNB, the Rank Indication (RI) is fundamental for the selection of the appropriate MIMO transmission mode. SM is possible only as long as the current rank of the channel is larger than one. If the channel is in addition not too rapidly varying over time, the eNB can select Closed-Loop Spatial Multiplexing (CL-SM) mode and use the Precoding Matrix Indicator (PMI) information from the UE to select from a predefined set of precoding matrices the one which optimizes the condition number of the channel matrix. Otherwise, if the channel exposes rapid time variation, not allowing for timely update of PMI, the eNB may switch to Open-Loop Spatial Multiplexing (OL-SM) mode. In this case, random precoding is employed in order to assure an at least statistically, on average, good condition number of the channel matrix. In OL-SM mode, Large-delay Cyclic Delay

Diversity (LD-CDD) is in addition introduced as a means to enhance diversity of the channel.

If the rank of the channel or the Signal-to-Noise Ratio (SNR) do not allow for either of the SM modes, DL TD is available as a robust fallback mode, which maximally exploits the diversity of the channel for reliable transmission of single stream. Note that DL TD mode is, nevertheless, a MIMO transmission mode. Space-Frequency Block Coding (SFBC) is used to transmit orthogonal replicas of a single stream from different Basestation (BS) antennas based on the Alamouti scheme [8]. In reality, DL TD is the most important mode as it allows for reliable transmission under poor channel conditions.

A further aspect of adaptivity is MCS selection. Based on Channel Quality Indication (CQI), feedback from the UE the eNB continuously adapts the MCS to current channel conditions. By means of the CQI, the UE indicates allowance for a higher MCS if the current Block Error Rate (BLER) drops below a threshold and requests a lower MCS if the BLER exceeds the threshold.

The above overview is admittedly superficial but considered necessary here to emphasize the role of the interaction between the eNB and the UE in MIMO transmission. Any performance figure like, for example, throughput observed in a real network is a system property, which includes not only UE receive performance and UE feedback reporting quality but also the response of the scheduler in the eNB. It is of uttermost importance to be aware of this fact so as not to arrive at a simplistic and erroneous idea of a realistic test case. To be realistic a time-variant, faded multipath channel is always to be combined with a fully adaptive system comprising not only the UE but also the mode switching and MCS adaptation functionality of the eNB's scheduler. This functionality is, however, neither supported by presently available test equipment nor is there a standardized scheduler at all. Measurements are presently rather performed under conditions of a Fixed Reference Channel (FRC), which predefines transmission mode and MCS. Exposing UE to a random channel under these fixed settings is all but realistic.

The way out of this difficulty is to characterize the physical UE attributes which determine the UE's contribution to overall performance. Part of this task requires for OTA measurements, other properties are more easily and reliably characterized by conducted measurements.

4. Relevant Physical Attributes of MIMO UE

4.1. Antenna Properties. A passive N -port antenna can be fully characterized by its *compound polarimetric pattern*, the $N \times 2$ complex matrix function

$$\mathbf{T}(\Omega) = \begin{pmatrix} T_{\theta,1}(\Omega) & T_{\phi,1}(\Omega) \\ \vdots & \vdots \\ T_{\theta,N}(\Omega) & T_{\phi,N}(\Omega) \end{pmatrix} \quad (1)$$

with $\Omega = (\theta, \phi)$, and its *scattering matrix* \mathbf{S} . With \mathbf{a} and \mathbf{b} denoting the vectors of incoming (TX \rightarrow antenna) and

outgoing (antenna \rightarrow RX) wave quantities at the N ports, the receive mode is described by

$$\mathbf{b}(\Omega) = \mathbf{S}\mathbf{a} + \mathbf{b}_0(\Omega), \quad \mathbf{b}_0(\Omega) = \frac{\lambda_0}{\sqrt{4\pi Z_0}} \mathbf{T}(\Omega) \mathbf{E}(\Omega) \quad (2)$$

and the transmit mode by

$$\mathbf{E}(\Omega) = j\sqrt{\frac{Z_0}{4\pi}} \frac{e^{-jk_0 r}}{r} \mathbf{T}^\top(\Omega) \mathbf{a}, \quad \mathbf{b} = \mathbf{S}\mathbf{a}. \quad (3)$$

Radiated power can be written as

$$P_{\text{rad}} = \frac{1}{2} \mathbf{a}^\dagger \mathbf{R} \mathbf{a}, \quad (4)$$

where

$$\mathbf{R} = \frac{1}{4\pi} \iint_{\Omega} \mathbf{T}^*(\Omega) \mathbf{T}^\top(\Omega) d\Omega \quad (5)$$

is referred to as the *radiation matrix*. Superscripts $(\cdot)^\top$, $(\cdot)^*$, and $(\cdot)^\dagger$ denote transposed, conjugate, and Hermitian transposed, respectively.

A closer look at this $N \times N$ Hermitian matrix is mandatory because it contains all relevant information about the performance of the antenna system in a statistically isotropic environment. Although the isotropic scattering environment is of rare occurrence, the concept takes its justification from the fact that the orientation of UE in space may be random. We shall see that the radiation matrix is one of the UE attributes to be characterized. To understand its meaning, consider the case that only port n is fed, that is, $\mathbf{a} = (0, \dots, 0, a_n, 0, \dots, 0)^\top$. Available power is then given by $P_{\text{avail},n} = (1/2)a_n^* a_n$ and radiated power by $P_{\text{rad},n} = (1/2)a_n^* R_{nn} a_n$ with

$$R_{nn} = \frac{1}{4\pi} \int_{\Omega} \left(|T_{\vartheta,n}(\Omega)|^2 + |T_{\varphi,n}(\Omega)|^2 \right) d\Omega, \quad (6)$$

the norm of the n th pattern. Obviously the diagonal element R_{nn} is equal to the ratio of radiated over available power from port n , that is, to per-port (total) efficiency,

$$\eta_{\text{tot},n}^{\text{port}} = \frac{P_{\text{rad},n}}{P_{\text{avail},n}} = R_{nn}. \quad (7)$$

Different per-port efficiencies correspond to the different expectation values of received power in a statistically isotropic environment and are, therefore, linked to the concept of *antenna imbalance*. But we shall see below that a deeper look into this concept is necessary.

The off-diagonal elements of the radiation matrix contain the scalar products between patterns associated with different ports,

$$R_{mn} = \frac{1}{4\pi} \int_{\Omega} \left(T_{\vartheta,m}^*(\Omega) T_{\vartheta,n}(\Omega) + T_{\varphi,m}^*(\Omega) T_{\varphi,n}(\Omega) \right) d\Omega, \quad (8)$$

from which the traditional pattern correlation coefficient is obtained as

$$\rho_{mn} = \frac{R_{mn}}{\sqrt{R_{mm} R_{nn}}}. \quad (9)$$

The correlation corresponds to the expectation value of the observed Complex Envelope Correlation Coefficient (CECC) at the antenna ports in a statistically isotropic environment.

It would not have been worthwhile to introduce the radiation matrix just to come back to familiar parameters like per-port efficiencies and correlation between per-port patterns. It is important to understand that the traditional parameters “antenna imbalance” and “antenna correlation” are actually meaningless for MIMO transmission if considered separately.

A simple thought experiment reveals why. Consider an N -port antenna, which receives N uncorrelated paths of equal power coming in with different Angle of Arrival (AOA) and isotropic Power Angular Spectrum (PAS). The received signal vector \mathbf{b}_0 will contain components with different amplitudes and some correlation between the components will be observed. The noise contributions in each component may be considered uncorrelated and of equal power because they are dominated by receiver noise figure. The MIMO detector now basically applies an approximate inverse of the channel matrix to the received signal vector in order to recover the transmitted signal vector, that is, to remove the correlation. The quality of this approximation depends solely on the condition number of the channel matrix. In the present setting, the expectation value of the channel matrix is just the radiation matrix of the antenna. Consequently, the relevant property of the radiation matrix is the attainable rank, which in fact is the number of eigenvalues (assumedly ordered in sequence of decreasing magnitude) for which the ratio of largest to smallest magnitude does not exceed some threshold.

Moreover, in case of CL-SM, the eNB’s precoder and the UE’s MIMO detector make a joint attempt to diagonalize the channel matrix. In either case, unitary transforms are applied to the channel matrix. Hence only those properties of the radiation matrix, which are invariant under unitary transforms, are relevant: the eigenvalues of \mathbf{R} . The radiation matrix is Hermitian and hence has real eigenvalues, which correspond to the *modal efficiencies* of the N orthogonal radiation modes, which are supported by the antenna system. The discussion can be summarized as follows.

- (a) The MIMO performance of an N -port antenna in a statistically isotropic environment is described by the N modal efficiencies $\eta_1 \geq \eta_2, \dots, \geq \eta_n$, the eigenvalues of the radiation matrix.
- (b) *Total antenna system efficiency* is described by the invariant property

$$\overline{\eta}_{\text{tot}} = \frac{1}{N} \text{tr}(\mathbf{R}). \quad (10)$$

This figure is equal to the ratio of transmitted over available power in case that the total available power is evenly distributed over N uncorrelated feed port signals [9].

- (c) *Modal imbalance* is a relevant parameter, whereas conventional per-port “antenna imbalance” is not. The attainable rank of MIMO transmission is

restricted by the number of modal efficiencies with value η_n not less than a given (power dependent) fraction of η_1 . An *imbalance figure* can be introduced as the ratio of the arithmetic over the geometric mean of modal efficiencies

$$\beta = \frac{\overline{\eta_{\text{tot}}}}{\sqrt[n]{\eta_1 \eta_2 \cdots \eta_n}}. \quad (11)$$

A perfectly balanced antenna system with $\eta_1 = \eta_2 = \cdots = \eta_n = \overline{\eta_{\text{tot}}}$ will have $\beta = 1$. An antenna system with higher modal imbalance has larger β .

- (d) “Antenna correlation,” that is, pattern correlation with respect to different port patterns does not convey useful information. We note in passing that antenna correlation is anyway always small if the antenna system is properly matched (Hermitian match with respect to impedance matrix) and if dissipative losses are small [10]. For a lossless antenna system (no dissipation), power balance in fact implies that radiated power is equal to power incident at the ports minus power scattered back from the ports, that is,

$$\mathbf{R} = \mathbf{I} - \mathbf{S}^\dagger \mathbf{S}. \quad (12)$$

If a multi-port antenna is correctly matched (at a given frequency), then all elements of the scattering matrix \mathbf{S} are small in magnitude. The off-diagonal elements of the radiation matrix \mathbf{R} (corresponding to pattern correlation) are then obviously also small. This statement applies irrespective of the spatial separation between different antenna elements. The latter may have an influence on the bandwidth over which a good multi-port match is attainable but is otherwise not directly related to pattern correlation. Generalization to lossy antennas is straightforward by adding a loss matrix term to the power balance relation.

After having identified the eigenvalues of the radiation matrix, that is, the efficiencies of the N orthogonal radiation modes supported by the antenna system as the relevant parameters, a brief look into their physical behaviour is indicated.

Each radiation mode (orthogonal pattern) comes with an individual *radiation quality factor* defined as the ratio of average reactive energy stored in its near-field over radiated energy per period. As opposed to what the term “quality” suggests, a high radiation quality factor is detrimental. It corresponds to narrow matching bandwidth and high dissipation, that is, the modal efficiency of the respective mode is acceptable only over a small bandwidth and may be still poor even there. Reduction of radiation quality factors is the goal of antenna design but unfortunately is subject to fundamental physical limits. When adding further antennas to small form-factor devices, the radiation quality factors of the additional radiation modes typically take increasingly large values. An example for the frequency dependence of modal efficiencies for a simulated 2-port antenna system in

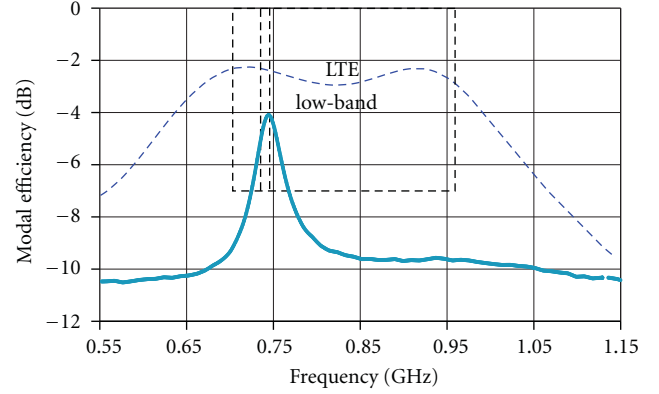


FIGURE 1: Frequency dependence of modal efficiencies for a simulated 2-port MIMO antenna example.

a USB dongle is shown in Figure 1. Cyan and blue curves represent efficiencies of the two modes versus frequency. It can be seen that total antenna system efficiency (10) and modal imbalance can be strongly dependent on frequency, which should be considered in test design.

4.2. Reconfigurable and Adaptive Antennas. The above-mentioned physical limitations in antenna design are reasons for introduction of tunable and reconfigurable or even adaptively matched antenna systems (so as to compensate for antenna detuning in a variable near-field environment, e.g., due to user’s head and hand). As a consequence, the antenna system can in principle no longer be treated as a linear system block and, in case of adaptive matching, not even as time invariant. It should be noted in particular that with a tunable antenna system the first nonlinear system block appears in the receive chain before the band filter. New test cases may, therefore, be necessary. Moreover, the benefit (or malfunction) of adaptive matching will not be assessed correctly without a properly chosen set of test cases with phantoms, possibly accounting also for time dependence of the adaptation algorithm. A thorough discussion of these issues is beyond the scope of the present paper. It should be obvious, however, that MIMO OTA test methods, which build on a separate characterization of an assumedly linear and time invariant antenna system in combination with conducted measurements, are not suitable for this situation.

4.3. Self-Interference and Cross-Interference. Self-interference is in reality often the most important cause of poor device performance. Conducted measurements are not capable to detect problems caused by coupling of an interfering signal to the antennas. Cross-interference is important for devices that are connected to a host device such as datacards or USB dongles. Interference from the host computer may differ dramatically between, for example, different laptop models. A standard mock-up is necessary to make comparable measurement for this type of devices.

4.4. Receiver Noise Figure. The noise figure of a receiver is defined as the additional noise power level at a receiver’s

output as compared to an ideal receiver. If the effect of nonlinear distortion is approximated as Additive White Gaussian Noise (AWGN), it may be subsumed under the noise figure and the latter be taken as a quality measure for the analog and mixed signal system blocks in the UE's receive chain. In an "end-to-end" measurement, it is not possible to separate receiver noise figure from antenna efficiency. It is, therefore, necessarily included in MIMO OTA measurements.

4.5. Baseband Algorithms. The quality of the algorithms implemented in the digital baseband of UE is crucial for receiver performance and reporting quality (CSI). These aspects, however, can at much lower cost and with superior repeatability be tested in conducted measurements with the full flexibility to apply time-dependent faded channels, different Doppler spectra, and birth-death scenarios with the help of today's sophisticated fading emulators. In the sequel, it is therefore silently assumed that such conducted tests have been performed separately and the digital baseband is not considered in the context of MIMO OTA measurement.

5. Multipath Channels and UE Properties

5.1. Generic Multipath Scenario, Constellations. In communication theory, the radio channel comprises the propagation channel and the antennas at either side of the link. The topic of this section is the interaction of a multipath scenario with the UE antenna system. Consider a single subcarrier frequency of an OFDM DL supporting M parallel data streams. The complex amplitudes of the M sinusoids can be described by a vector $\mathbf{s} = (s_0, s_1, \dots, s_{M-1})^\top$, which is normalized to unit power according to $1/2\|\mathbf{s}\|^2 = 1$. In addition, L interfering signals may be present and are described in the same fashion by a vector $\mathbf{w} = (w_0, w_1, \dots, w_{L-1})^\top$.

Conceptually, we define the Device Under Test (DUT) as the combination of the UE under test and any possible objects in the near-field such as head or hand phantoms. This allows to consider the DUT as being immersed into a superposition of K plane waves, incident from AOA $\Omega_k = (\theta_k, \phi_k)$, $k = 0, \dots, K-1$. This superposition is described in terms of the distribution

$$\hat{\mathbf{E}}(\Omega) = \begin{pmatrix} \hat{E}_\theta(\Omega) \\ \hat{E}_\phi(\Omega) \end{pmatrix} = E_0 \hat{\mathbf{C}}(\Omega) \mathbf{s} + E_0 \hat{\mathbf{D}}(\Omega) \mathbf{w}, \quad (13)$$

where E_0 is a calibration factor (see below) and $\hat{\mathbf{C}}$ and $\hat{\mathbf{D}}$ are, respectively, $2 \times M$ and $2 \times L$ matrices of distributions, referred to as constellations below, which describe the multipath channel for the wanted signals and the interferers, respectively. Both have the same form, namely, $\hat{\mathbf{C}} = (\hat{\mathbf{C}}_0, \dots, \hat{\mathbf{C}}_{M-1})$ with

$$\hat{\mathbf{C}}_m = \sum_{k=0}^{K-1} \begin{pmatrix} c_{\theta,k,m} \\ c_{\phi,k,m} \end{pmatrix} \delta(\Omega, \Omega_k) \quad (14)$$

and likewise for $\hat{\mathbf{D}}$. This is a generic description, which covers any real-world scenario as well as any test case. In the context

of OFDM, it is sufficient to identify the coefficients in (14) with complex numbers provided that path delays do not exceed the guard period.

The received signal vector at the antenna ports is then, in absence of interferers, given by

$$\mathbf{b}_0 = \frac{\lambda E_0}{\sqrt{4\pi Z_0}} [\mathbf{T}, \hat{\mathbf{C}}] \mathbf{s}, \quad (15)$$

where

$$[\mathbf{T}, \hat{\mathbf{C}}] = \iint_{S_1(0)} \mathbf{T}(\Omega) \hat{\mathbf{C}}(\Omega) d\Omega. \quad (16)$$

The integral over the unit sphere $S_1(0)$ evaluates to an $N \times M$ matrix for an N -port antenna system. A similar term with $\hat{\mathbf{D}}$ exchanged for $\hat{\mathbf{C}}$ is to be added to include external interferers.

In order to obtain the channel matrix in real-world units, the factor E_0 in (13) must be quantified, that is, the measurement must be calibrated. As usual in anechoic chamber measurements we express E_0 in terms of the power P_{iso} , fictitiously received by an ideal isotropic antenna in the center of the UE position without the UE (and phantom) in place when subject to a single co-polarized plane wave. In this setting, (1) reduces to unity and

$$P_{\text{iso}} = \frac{1}{2} \|\mathbf{b}_0\|^2 = \frac{\lambda^2 E_0^2}{4\pi Z_0} \frac{1}{2} \|\mathbf{s}\|^2 = \frac{\lambda^2 E_0^2}{4\pi Z_0} \quad (17)$$

(due to the normalization of the signal vector) from which E_0 can be calculated. The operation $\|\cdot\|$ denotes the Frobenius norm. Since the channel matrix is conventionally referenced to the "inner antenna ports" in the form

$$\mathbf{r} = \mathbf{H} \mathbf{s} + \text{noise and interference}, \quad (18)$$

where $\mathbf{r} = (r_1, \dots, r_{N-1})^\top$ is the received signal vector at the input of the detector, it is convenient to scale the received signal vector according to $\mathbf{r} := (1/\sqrt{F}) \mathbf{b}$, where F denotes receiver noise figure. The correct SNR is thus maintained when we simply substitute an AWGN signal \mathbf{n} with thermal noise power $P_{N,0} = k_B T B$ per component for the noise contribution on the right-hand-side (RHS) of (18). The resulting expression for the channel matrix is

$$\mathbf{H} = \sqrt{\frac{P_{\text{iso}}}{F}} [\mathbf{T}, \hat{\mathbf{C}}]. \quad (19)$$

An analogous expression can be written for the external interferers to yield upon combination

$$\mathbf{r} = \sqrt{\frac{P_{\text{iso}}}{F}} [\mathbf{T}, \hat{\mathbf{C}}] \mathbf{s} + \sqrt{\frac{P_{\text{iso}}}{F}} [\mathbf{T}, \hat{\mathbf{D}}] \mathbf{w} + \mathbf{r}_S + \mathbf{n}. \quad (20)$$

The additional term \mathbf{r}_S accounts for self-interference.

Any MIMO OTA test case obviously amounts to the realization of a sequence of channel matrices (19) and therefore to the selection of a sequence of constellations, each containing K incoming (polarized) paths. In an anechoic chamber, each constellation can be realized by means of K dual-polarized test antennas. It is understood that the K test

antennas are either movable over the sphere or selectable from a larger set of fixed test antennas to allow for a sequence of different constellations.

Each choice of $\hat{\mathbf{C}}$ amounts to the definition of a *sampling operator*, which is applied to the compound pattern \mathbf{T} as described by the projection $[\mathbf{T}, \hat{\mathbf{C}}]$ in (19). The question arises, how to select these operators so as to obtain on the one hand a sufficient characterization of \mathbf{T} but on the other hand to avoid an overly complex approach. The options range from simply assigning each of the M downlink streams to a single test antenna at a time to complex schemes, where pre-faded superpositions of all downlink streams are routed to a large number of test antennas. A large number of antennas allows for emulation of geometrically realistic propagation scenarios as described by Geometry-Based Stochastic Channel Models (GSCMs), for example, the 3GPP Spatial Channel Model Extended (SCME) [11]. Related proposals have been made by several groups [3, 12, 13], and there is a tendency to emulate a GSCM in as much detail as possible, including multiple pre-faded copies of the DL signals, time dependence of the channel, and geometrical detail such as the angular spread of incoming clusters.

The following subsections are devoted to a discussion of these aspects.

5.2. Number of Test Antennas. The number of test antennas has a large impact on cost, complexity, and thereby reproducibility of a MIMO OTA test method. It is, therefore, important to clarify whether a larger number of test antennas will correspond to a better test method or not.

There is an obvious lower bound on the number of test antennas. To investigate UE performance in an $M \times N$ MIMO scheme at least $\min(M, N)$ test antennas are required to realize a channel of maximum possible rank. Below we assume $M = N$. The minimum number of test antennas is then $K_{\min} = N = M$. Use of a larger number of test antennas makes sense only if also additional uncorrelated DL signals are generated. This is possible by applying different time-variant delays or phase shifts and distributing these newly generated signals to different antennas. The resulting $K > K_{\min}$ paths will superimpose in the UE's antenna system to yield again N received signals. We refer to this effect as *in situ fading*, which (as opposed to pre-fading, see below) is a physical effect and relates to physical attributes of the UE antenna system. Formally, in situ fading is a consequence of the linearity and projection property of the sampling operator $[\mathbf{T}, \hat{\mathbf{C}}]$ showing up in (19). In fact, for any constellation $\hat{\mathbf{C}}^{(K)}$ with $K > K_{\min}$ incoming paths the channel matrix can be represented as a superposition of channel matrices for constellations with only K_{\min} antennas in the form

$$\mathbf{H} = \sqrt{\frac{P_{\text{iso}}}{F}} [\mathbf{T}, \hat{\mathbf{C}}^{(K)}] = \sqrt{\frac{P_{\text{iso}}}{F}} \sum_i a_i [\mathbf{T}, \hat{\mathbf{C}}_i^{(K_{\min})}]. \quad (21)$$

From the perspective of characterizing physical attributes of the UE, the question is, whether we can obtain significant additional information about the compound pattern \mathbf{T} by applying superpositions of the constellations $\hat{\mathbf{C}}_i^{(K_{\min})}$ instead

of considering them individually. Although the finally recorded metric (e.g., throughput) is not a linear function of the channel matrix, the answer is negative. It will be shown in Section 6 that a setup with K_{\min} antennas is sufficient to characterize the relevant properties of a UE antenna system, in particular total antenna system efficiency and modal imbalance.

5.3. Pre-Fading. In connection with MIMO OTA test approaches that use more than K_{\min} test antennas, it may be tempting to generate signals for the additional antennas by emulation of a channel model. A common way to do so is to use a fading emulator to apply a multi-tap delay line model to a signal before routing it to a test antenna. We refer to this approach as pre-fading. It corresponds to common functionality of fading emulators. Pre-fading is valuable for conducted measurements where it substitutes for the lack of in situ fading in the UE antenna system. It must be emphasized, however, that the introduction of pre-fading in a MIMO OTA test method, where in situ fading is already present, is unphysical and represents an arbitrary deterioration of the channel, which does not correspond to reality. Consider, for instance, the case of several paths which superimpose in space to create a spatial interference pattern with maxima and minima of available receive power. The diversity performance of a UE antenna system depends on how well it exploits this spatial interference pattern. If the paths are pre-combined before routing them to a test antenna, that is, generated by means of a tapped delay line filter, the spatial interference pattern is lost and replaced by a purely temporal fading characteristic, which is basically sensed in identical form by all UE antennas. Since such proposals, nevertheless, exist [3], it is worthwhile to take a brief look at the main effect of a pre-faded signal when applied under conditions of a fixed MCS.

To this end, it is sufficient to consider a single receiver. Without fading, we shall observe a sudden drop of throughput from nearly 100% to 0% in a small region about the threshold power of the selected MCS as available receive power is reduced below the threshold. This behaviour is approximated by a step function (dashed line) in Figure 2 (the width of the transition region is in the order of 1 dB to 2 dB and not relevant for our argument here). The threshold radiated power level at which this transition occurs, assumedly $P_{\text{thr}} = -85$ dBm in Figure 2, uniquely describes the receive quality of the UE in this situation. It reflects antenna efficiency, receiver noise figure, and possibly self-interference. In a Rayleigh scenario, the probability that the instantaneous receive power P_r exceeds P for a given average available receive power \bar{P} is

$$\text{Prob}\{P_r > P\} = \exp\left(-\frac{P}{\bar{P}}\right). \quad (22)$$

A fading emulator has to emulate exactly this behaviour. The observed average relative throughput $t(\bar{P})$ as a function of average power is then basically given by the convolution of

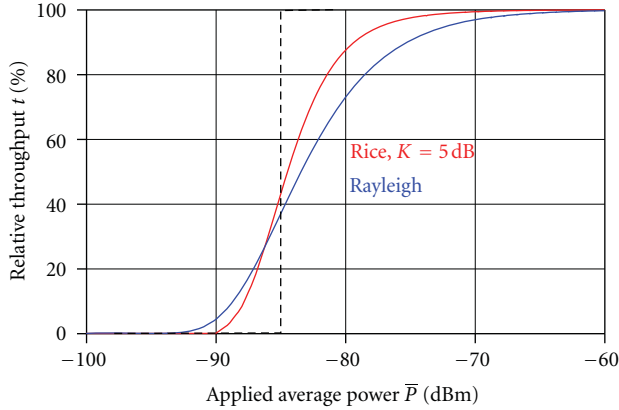


FIGURE 2: Illustration of the effect of Rayleigh fading (blue curve) and Rician fading ($K = 5$ dB, red curve) on observed throughput for an MCS threshold power of -85 dBm. See text for details.

the Probability Density Function (PDF) corresponding to (22) with the step function resulting in

$$t(\bar{P}) = \exp\left(-\frac{P_{\text{thr}}}{\bar{P}}\right). \quad (23)$$

This dependency is shown in blue in Figure 2. The red curve displays the analogous result for Rician fading with a K -factor of 5 dB. We observe that the desired information about the UE receive quality is just blurred by the statistics of the channel. Differences between results obtained this way are characteristic for the measurement setup (channel) but not for the UE.

5.4. GSCM, Adaptivity and Averages. The common starting point of any GSCM is the definition of UE velocity. It is directly translated into Doppler shifts. But in addition it is also used to introduce time dependence into the channel, resulting in time-dependent fading where the UE velocity determines the rate of change. Any MIMO OTA measurement performed under these conditions necessarily amounts to the measurement of a time average, for example, of average throughput. It is tempting to consider such time average to be a particularly “realistic” indicator of UE performance. But there are two major issues with this approach if combined with an FRC.

- (a) The condition number of the channel is varied over time in a poorly predictable way, that is, the rank of the channel may change up to the situation that it is in disagreement with a pre-selected MIMO operating mode.
- (b) Fading becomes time-dependent and the available receive power is spread out statistically about its average value with the effect that the SNR may be in disagreement with a pre-selected MCS during extended portions of the measurement interval.

Either effect potentially renders the recorded average values meaningless with respect to in-the-field results. In

reality, that is, in a fully adaptive system with a real eNB, the UE would have reported the current rank of the channel and the eNB would have switched to a more appropriate transmission mode (such as TD and OL-SM or CL-SM). During a measurement with time-dependent fading, the UE under test may also have desperately reported over parts of the measurement period that it could still attain appreciable throughput if CQI was decremented (i.e., the eNB should switch to a lower order modulation scheme or lower coding rate). But it is not heard. Instead zero throughput is recorded. Similarly, the UE may have reported over parts of the measurement period that the channel is good enough for the next higher order modulation scheme or higher coding rate (CQI increment), but the measurement under conditions of an FRC fails to account for the true performance of the UE.

We conclude that time averages taken with respect to a time-variant channel do not correspond to any real situation if taken under conditions of an FRC. But as opposed to average values, empirical outage probabilities may still convey useful information.

5.5. GSCM and Near-Field Impact. A lot of attention has been given to accurate emulation of geometrical detail of the SCME models such as Angular Spread (AS) in Anechoic Chambers (AC) [14]. In reality, however, such “free-space detail” is seldom visible to the UE at all. It is rather masked and strongly modified by the near-field environment of the UE, in case of hand-held devices, for example, by the user’s hand or head. Measurements with appropriate phantoms are well established in existing OTA test plans (e.g., [1]). Since the performance of MIMO UE is potentially more susceptible to the near-field environment than that of a single antenna UE, the quest for realistic test conditions will have to include them.

6. MIMO OTA Metrics and Measurement Methods

6.1. Towards a Direct Device Characterization Method. Based on the discussion and models presented in the previous sections, metrics and methods for MIMO OTA testing are proposed below. The selection of test cases is guided by the following principles.

- (i) OTA test cases are selected to correspond to those physical UE attributes, which cannot be characterized by conducted measurements but must be characterized by OTA measurements.
- (ii) The discretionary introduction of features from channel models for which a UE antenna system is transparent, in particular time-dependent fading, is to be avoided. Such features are likely to dominate measurement results and obliterate differences between devices.
- (iii) In order to assure reproducibility and accurate calibration, each test case should be stripped down in complexity to what is essential for the result.

- (iv) The influence of the measurement setup on results must be clearly understood and traceable.
- (v) Test setups that allow for reuse of existing OTA chambers are preferred.

Meaningful and realistic test cases can only be defined in agreement with the fundamental features of a MIMO communication standard, the most important of which is adaptation of the MIMO transmission mode to the channel properties.

The investigation of throughput in SM transmission mode is not meaningful unless it is assured that both the rank of the channel is larger than one and the SNR is sufficiently high. Otherwise, the result will just show that a poor channel is applied, a situation in which TD transmission mode would be invoked in reality. A MIMO-favourable channel is mandatory to evaluate MIMO performance in SM transmission modes.

Conversely, diversity performance cannot be evaluated if the channel is good enough to achieve constant maximum throughput with a single antenna. Diversity performance is best described by sensitivity under poor channel conditions. The MIMO transmission mode which in reality is used in the low SNR regime is TD and hence should also be used for testing in this context.

Two basic test cases are derived from the above consideration, which will be shown to cover the relevant physical attributes of UE:

- (1) evaluation of noise limited performance in TD mode using a sensitivity-based metric,
- (2) evaluation of peak performance in SM mode using a throughput-based metric.

They correspond to poor and MIMO-favourable channel conditions, respectively [15–17].

The definition of the metrics must in either case follow the purpose to provide a criterion for in-the-field performance. The UE should perform reasonably well in a virtually unlimited variety of propagation scenarios. Hence performance can only be described statistically. Average quantities are not sufficient to characterize the UE in this respect. Appropriate statistical metrics are *outage probabilities* with respect to given sensitivity or throughput levels. Statistical metrics allow for a comparison of the UE in terms of the probability that a prescribed minimum performance will be achieved or, conversely, in terms of outage probability of a given transmission mode and MCS [18]. The probabilities are directly related to user experience and network efficiency.

As opposed to averages, observed *outage probabilities* relative to some performance figure gathered over a set of fixed, identically reproducible propagation scenarios, also remain meaningful under conditions of an FRC.

6.2. Sensitivity in Noise-Limited Scenarios. DL TD mode is meant to provide fair link reliability and throughput under non-optimum channel conditions. The appropriate test case amounts to a characterization of UE sensitivity in a noise-limited scenario, akin to traditional TIS measurements for

SISO devices. Differences to traditional TIS measurements arise (i) from the fact that at least $M = 2$ orthogonal DL signals are available in DL TD mode which carry the same information and (ii) from the presence of multiple receive antennas and the possible support of Receive Diversity (RD) in the UE. Note that TD and RD are completely independent methods for improvement of link quality. TD is in general based on the Alamouti scheme, in LTE, for instance, in form of SFBC. RD can be realized by Maximum Ratio Combining (MRC), which is the optimum approach and is taken as reference case below. Both schemes work together so as to combine the total available power from all M downlink signals and all N UE antennas in order to maximize the SNR. The sensitivity is recorded in terms of the received power, which is required for not exceeding a specified BLER threshold. Based on the discussion in Section 5, an explicit model expression for the SNR is readily obtained. Assuming DL TD mode, a power-normalized signal vector \mathbf{s} (see Section 5.1) and an N -antenna UE with MRC (if $N > 1$), the effective SNR is given by

$$\text{SNR} = \text{SNR}_0 \left\| \left[\mathbf{T}, \hat{\mathbf{C}} \right] \right\|^2 \quad (24)$$

with

$$\text{SNR}_0 = \frac{P_{\text{iso}}}{P_{N,0}F}. \quad (25)$$

$\|[\mathbf{T}, \hat{\mathbf{C}}]\|$ denotes the Frobenius norm of the matrix (16). We note in passing that the Shannon capacity formula can be rewritten in terms of the above-introduced symbols as

$$C_{\text{MRC}} \approx B \log_2 \left(1 + \text{SNR}_0 \left\| \left[\mathbf{T}, \hat{\mathbf{C}} \right] \right\|^2 \right), \quad (26)$$

where B denotes bandwidth.

If a sequence of different constellations $\hat{\mathbf{C}}$ is applied, different values of SNR are observed. The distribution of these SNR values and hence the statistics of sensitivity observed over the sequence of constellations characterizes important features of the compound pattern of the UE's antenna system.

To describe the proposed test procedure in more detail, we consider DL TD mode with $M = 2$ (two orthogonal DL signals), and a sequence of constellations $\mathcal{C} = \{\hat{\mathbf{C}}_i\}$ whose elements are, apart from irrelevant phase factors, of the form

$$\hat{\mathbf{C}}_i = \begin{pmatrix} 1 & 0 \\ 0 & 1 \end{pmatrix} \delta(\Omega, \Omega_i), \quad (27)$$

that is, only a single AOA Ω_i is encountered per measurement [19]. The factor $\|[\mathbf{T}, \hat{\mathbf{C}}]\|^2$ on the RHS of (24), therefore simplifies to $\|\mathbf{T}(\Omega_i)\|^2$ in the i -th measurement. The setting resembles a conventional sensitivity measurement with the modification that two DL signals are routed to the two orthogonal polarizations of a dual-polarized test antenna.

Let SNR_{thr} denote the threshold SNR level on the Left-Hand-Side (LHS) of (24) below which the specified BLER threshold is exceeded for the selected FRC. The corresponding value $P_{\text{iso}} = P_{\text{iso,thr}}$ on the RHS of (25)

gives the sensitivity at AOA Ω_i , the *directional compound sensitivity*

$$\frac{1}{P_{\text{iso,thr}}(\Omega_i)} = \frac{1}{\text{SNR}_{\text{thr}} P_{N,0}} \frac{\|\mathbf{T}(\Omega_i)\|^2}{F}. \quad (28)$$

Note that the RHS of (28) is essentially the compound antenna gain over receiver noise figure at given AOA Ω_i . The average of (28) over the unit sphere is the Total Compound Isotropic Sensitivity (TCIS)

$$\frac{1}{\overline{P_{\text{iso,thr}}}} = \frac{1}{\text{SNR}_{\text{thr}} P_{N,0}} \frac{\text{tr}(\mathbf{R})}{F} = \frac{1}{\text{SNR}_{\text{thr}} P_{N,0}} \frac{N \overline{\eta_{\text{tot}}}}{F}. \quad (29)$$

\mathbf{R} is the radiation matrix (5), $\overline{\eta_{\text{tot}}}$ denotes total antenna system efficiency after (10), and N is the number of UE antenna ports. Note that (29) completely characterizes the most important UE attribute: the ratio of total antenna system efficiency over receiver noise figure. The result can be approximated by choosing AOAs from a proper regular grid in the same way as in conventional SISO OTA test plans. Moreover, this test case can be realized in a conventional OTA test chamber equipped with a single dual-polarized test antenna, for example, a quad-ridged horn antenna. Two output ports of the MIMO Basestation Emulator (BSE), carrying the two orthogonal DL TD signals are routed to the two polarizations of the test antenna simultaneously and with equal power.

It is to the authors' opinion remarkable that the most relevant MIMO OTA performance figure, TCIS, equivalent to total antenna system efficiency over receiver noise figure, can be obtained with actually less effort than suggested in existing SISO OTA test plans, which require separate measurements for each polarization. But the test procedure, which has been sketched above, is suitable also to obtain a more significant statistical metric at no additional cost. As well known from income statistics, average values do not tell the full story. A UE with the same value of TCIS may still exhibit different outage probabilities. Receive diversity performance will be rated the better the less it depends on the accidental directions of the incoming paths, that is, on the variation of the total power received from both polarizations over all possible AOAs. The Figure of Merit (FOM) to be reported, is therefore, the empirical Cumulative Distribution Function (CDF) of sensitivity, which is readily obtained from recorded directional sensitivity values (28). The proposed metric is formally introduced as a function of applied power P_{iso} by

$$\text{CDF}_{\text{sensitivity}}(P_{\text{iso}}; \mathcal{C}, \text{FRC}, \text{BLER}) = \text{Prob}\{P_{\text{iso,thr}} < P_{\text{iso}}\} \quad (30)$$

and of course depends on choice of FRC, threshold BLER, and applied sequence of constellations \mathcal{C} . The CDF (30) allows for comparison of devices in terms of outage probability of a given FRC at given power level for arbitrary AOA, a quantity which is expected to bear a close relation to the probability of dropped service in an arbitrary propagation scenario.

For illustration, Figure 3 displays sensitivity patterns of a High-Speed Packet Access (HSPA) dongle plugged into

a laptop. Figures 3(a) and 3(b) display the conventional separate sensitivity patterns for a φ -polarized wave and θ -polarized wave, respectively. The result of Figure 3(c) corresponds to the above-described procedure with uncorrelated signals of half the total power applied to the two polarizations simultaneously. It can be observed that the deep troughs in Figures 3(a) and 3(b) do not show up in Figure 3(c), which approaches a more spherical shape indicating an effective receive diversity.

The CDFs (30) of three different LTE devices of different form-factor (and operating in different bands) are presented in Figure 4. A measurement resolution of 30° is used. The CDFs have been generated with a weight correction for each individual sensitivity measurement corresponding to the relative fraction of the surface of the unit sphere, which is represented by the corresponding AOA. As illustrated by the shaded regions in Figure 4, an MNO may decide to define a rejection region in the CDF plot. A device might for instance be rated acceptable if it exposes a compound sensitivity better than -124 dBm (RS EPRE) with a probability of at least 33% and still better than -120 dBm with a probability of at least 66%. Note that the numerical values here are just for illustration and arbitrarily selected. Actual values are likely to be obtained only by comparison of (30) against in-the-field results.

6.3. Peak Performance in MIMO-Favourable Scenarios. The capability of a device to benefit from multipath propagation by providing high throughput can only be tested if the propagation environment is suitable for such transmission. MIMO peak performance is to be measured for SM modes under conditions of a full rank propagation channel and high SNR. A throughput-based metric is appropriate to evaluate whether the UE antenna system meets the performance target. The metric and accompanying test procedure, which is proposed below, covers the physical UE attributes modal efficiencies and modal imbalance and is therefore complementary to what was obtained by sensitivity measurement in a noise-limited scenario in the previous section.

Figure 5 depicts the concept of a test setup with two dual-polarized horns, which can independently be set to AOA Ω_i and AOA Ω_j , respectively. For each pair of AOAs, all possible combinations of polarizations can be realized. The setup, therefore, allows for full characterization of the UE with $N = 2$ antennas. In this context, it can accommodate for a 2×2 MIMO scheme. For evaluation of the UE with more antennas, additional test antennas may be added to the setup. For the presently proposed approach, we consider the simple case of a 2×2 MIMO transmission in SM mode. Among all possible constellations that can be realized with the setup after Figure 5, we restrict ourselves to those which are of the simple form

$$\hat{\mathbf{C}} = \begin{pmatrix} c_{\vartheta,0} & 0 \\ c_{\varphi,0} & 0 \end{pmatrix} \delta(\Omega, \Omega_i) + \begin{pmatrix} 0 & c_{\vartheta,1} \\ 0 & c_{\varphi,1} \end{pmatrix} \delta(\Omega, \Omega_j) \quad (31)$$

with exactly one element in either matrix on the RHS of (31) equal to one and the other zero. Each of the two orthogonal, equal power downlink signals is then routed to exactly one

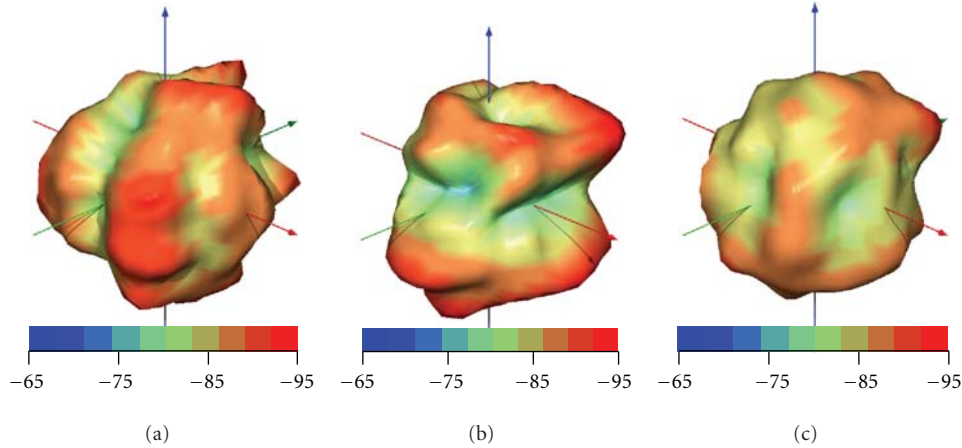


FIGURE 3: 3D sensitivity pattern (dBm) of an HSDPA dongle: (a) φ polarised DL signal only, (b) ϑ polarized DL signal only, (c) decorrelated copies of the DL signal with half power each on either polarization.

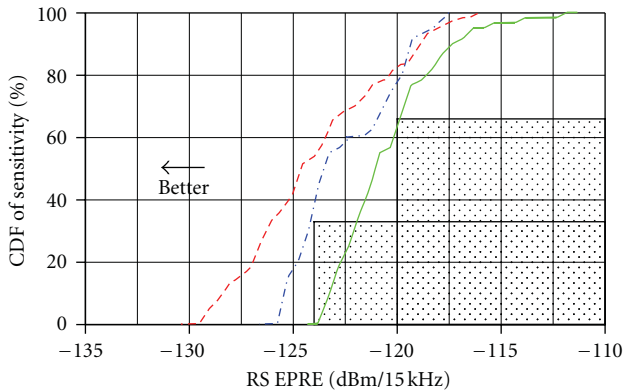


FIGURE 4: Measured CDF of sensitivity for three different commercially available LTE devices. Shaded regions illustrate potential rejection criteria (see text).

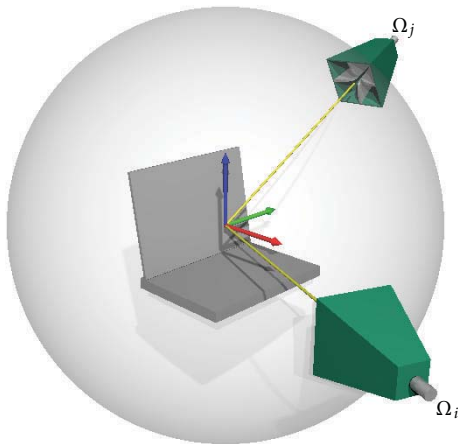


FIGURE 5: Test setup for, for example, a 2×2 MIMO scheme using two dual-polarized test antennas. The AOA's Ω_i and Ω_j are independently selected on the unit sphere.

out of the 4 available ports at a time. The measurement procedure involves a sequence of such constellations with Ω_i and Ω_j taken from a predefined grid on the unit sphere for all possible combinations of polarization, that is, (ϑ, ϑ) , (ϑ, φ) , (φ, ϑ) , and (φ, φ) . Throughput is recorded for each measurement.

Before going into further detail of the procedure, let us briefly consider which UE antenna attributes can in principle be characterized with this approach. LTE offers a CL-SM and an OL-SM DL transmission mode. Provided that “good” channel information is available at the receiver, a situation which would be assumed as a prerequisite for CL-SM mode, the Shannon capacity formula can be approximated by

$$C_{SM} \approx B \log_2 \left(\det \left(\mathbf{I} + \text{SNR}_0 [\mathbf{T}, \hat{\mathbf{C}}]^\dagger [\mathbf{T}, \hat{\mathbf{C}}] \right) \right) \quad (32)$$

for a given constellation. Assume now that we apply a sequence of constellations of the form (31), which corresponds to a (doubly) isotropic PAS for both polarizations and both downlink signals. Such sequence can be obtained by choosing Ω_i and Ω_j from a proper regular grid on the unit sphere. Obviously then, as angular resolution is increased, the average of the term $[\mathbf{T}, \hat{\mathbf{C}}]^\dagger [\mathbf{T}, \hat{\mathbf{C}}]$ approaches the radiation matrix \mathbf{R} . In the limit, we would obtain the isotropic average of (32) in the form

$$\overline{C_{SM}} \approx B \log_2 (\det(\mathbf{I} + \text{SNR}_0 \mathbf{R})). \quad (33)$$

Since we intend to test in the high SNR regime, we may assume that the SNR is high enough to neglect the identity matrix \mathbf{I} in (33) as proposed in [20]. The isotropic average (33) can then be approximated by

$$\begin{aligned} \overline{C_{SM}} &\approx B \log_2 (\text{SNR}_0^N \cdot \det(\mathbf{R})) \\ &= BN \log_2 (\text{SNR}_0 \overline{\eta_{\text{tot}}}) + B \sum_{n=1}^N \log_2 \left(\frac{\eta_n}{\overline{\eta_{\text{tot}}}} \right). \end{aligned} \quad (34)$$

The first term on the RHS of (34) corresponds to the isotropic average of capacity in the optimum case of a balanced

N -port MIMO antenna system with total antenna system efficiency $\overline{\eta}_{\text{tot}}$. The second term on the RHS (34) describes the capacity degradation due to modal imbalance. It is always nonpositive and equal to zero if and only if the antenna system is perfectly balanced with equal modal efficiencies $\eta_1 = \eta_2 = \dots = \overline{\eta}_{\text{tot}}$. The approximation (34) can be rewritten in the form

$$\overline{C}_{\text{SM}} \approx 3.322BN \left(\text{SNR}_0^{(\text{dB})} + \overline{\eta}_{\text{tot}}^{(\text{dB})} - \beta^{(\text{dB})} \right), \quad (35)$$

where superscript (dB) indicates a quantity given in decibels and

$$\beta^{(\text{dB})} = 10 \text{ dB} \log_{10} \left(\frac{\overline{\eta}_{\text{tot}}}{\sqrt[n]{\eta_1 \eta_2 \dots \eta_n}} \right) \quad (36)$$

is the *imbalance figure* of the UE antenna system as introduced in (11). Note that both $\overline{\eta}_{\text{tot}}$ and β are invariant properties of the radiation matrix as discussed in Section 4.1. We conclude that with diligent choice of SNR_0 , such that $\text{SNR}_0 \overline{\eta}_{\text{tot}}$ would allow for almost the maximum throughput supported by a given FRC, an observed degradation of the isotropic average of throughput can be attributed to modal imbalance, that is, the latter attribute can be characterized by the proposed measurement approach.

The above derivation has been made only for the purpose of a qualitative interpretation of the significance of throughput measurements in the high SNR regime. It is neither necessary nor feasible to choose the AOAs Ω_i, Ω_j from a grid on the unit sphere with resolution fine enough to accurately approximate \mathbf{R} in (33). Even for a setup with 2 test antennas only, there are 4 degrees of freedom ($\theta_1, \phi_1, \theta_2, \phi_2$). Hence, at an angular resolution comparable to traditional TIS/TRP measurement, instead of say $2K$ samples (2 polarizations times K grid points on the unit sphere), $2K^2 - K$ samples would be required. It must be emphasized that this observation holds equally for measurements in an anechoic chamber and in a reverberation chamber. The number of samples, that is, different constellations required for sampling with a prescribed resolution, can also *not* be reduced by employing more antennas. It should be clearly understood that with a larger number of test antennas we can only generate linear combinations of those constellations, which were also realizable with the smaller number of test antennas. Only when taking a larger number of samples, that is, resorting to a longer sequence of different constellations, further independent samples can be obtained. It is, therefore, inevitable, but as to presently available experimental evidence also sufficient, to resort to a sequence of constellations, which is just large enough to deliver trustworthy statistics of throughput. There are some minimum requirements on the selection of such sequence of constellations, which are experimentally confirmed and will be illustrated with examples below.

- (a) It is mandatory to consider both polarizations in all cases, that is, for each pair of AOA Ω_i, Ω_j all 4 possible combinations of polarizations must be accounted for.

- (b) It is mandatory to achieve a fair representation of the assumed PAS. An “economization” of MIMO OTA measurement by, for example, restriction to AOAs, which are exclusively in the azimuthal plane may yield grossly misleading results.

Before turning to the proposed statistical metric for the present test case, some considerations with respect to the MIMO transmission modes, which may be selected for the measurement, that is, CL-SM or OL-SM, are necessary. In view of the above discussion, CL-SM appears to be well suited for the intended characterization. It comes with the additional advantage to minimize possible bias introduced through the test scenario by virtue of adaptive precoding. Investigation of CL-SM performance, however, makes sense only if the eNB emulator supports adaptive precoding based on the UE’s PMI report and adaptive per-stream CQI-based MCS selection. It must further allow to have the UE’s RI report ignored. These features are not yet in general supported by test equipment. OL-SM comes with an inherent randomization of the channel via LD-CDD and random precoding. As a consequence, throughput observed in each particular constellation represents by itself a statistical average of different channel realizations. Furthermore, when using OL-SM mode meaningful statistics can be gathered under conditions of an FRC provided that the power level P_{iso} is selected properly. In view of the limitations of presently available test equipment, OL-SM mode is therefore assumed below.

The proposed metric is the empirical Complementary Cumulative Distribution Function (CCDF) of observed relative throughput t_{obs} written as function of relative throughput t in the form

$$\text{CCDF}_{\text{throughput}}(t; \mathcal{C}, \text{FRC}, P_{\text{iso}}) = 1 - \text{Prob}\{t_{\text{obs}} < t\}, \quad (37)$$

where \mathcal{C} denotes the set of applied constellations and P_{iso} is the applied power level.

Figure 7 shows an example for this metric. It relates to a commercially available LTE device, a USB dongle for E-UTRA band class 7. The device has connectors for two external antennas (Figure 6). For this proof-of-concept example, it was decided to use external antennas to facilitate interpretation of results. Two dipoles were used in different arrangements:

- (a) collinear placement with half-wavelength separation (“canonical dual dipole arrangement”) as shown in Figure 6(a),
- (b) orthogonal placement with half-wavelength separation (“crossed dipoles”) as shown in Figure 6(b),
- (c) similar to (a) and (b) but with 45° inclination between the axes of the two dipoles.

The theoretical patterns of these antenna arrangements are of course disturbed by the presence of the laptop and connecting cables.

The CCDF of throughput for the 3 antenna arrangements were recorded for an FRC with 16QAM and a 10 MHz bandwidth (DL 2655 MHz, UL 2535 MHz) at a power level

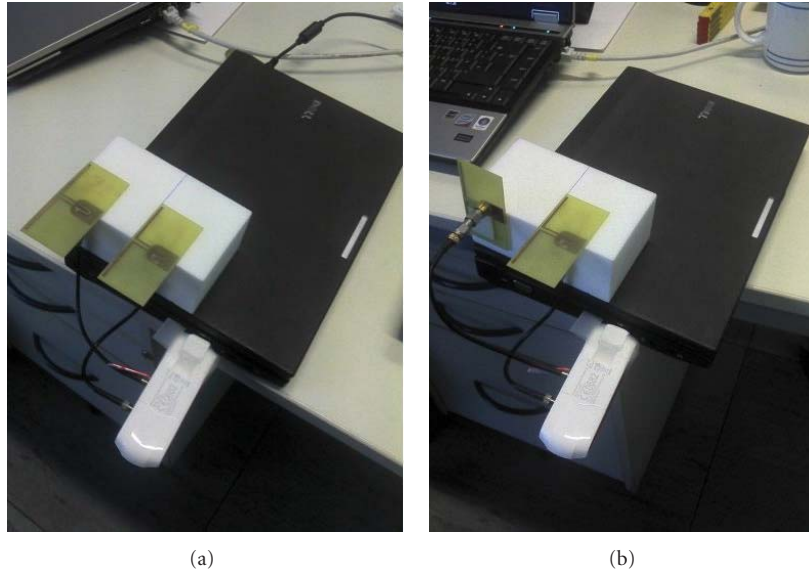


FIGURE 6: Band 7 dongle in a test setup with 2 external antennas, (a) collinear dipole arrangement and (b) cross-polarized dipoles.

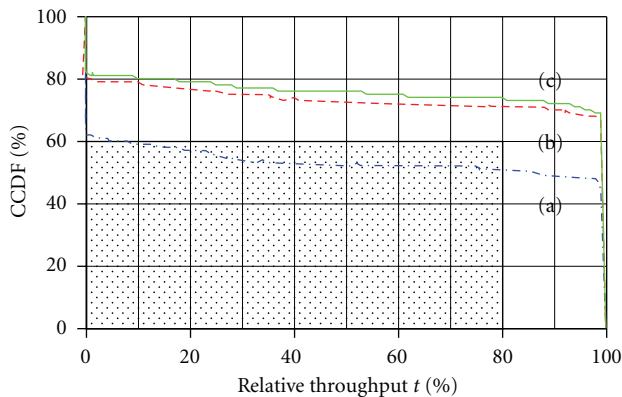


FIGURE 7: Measured CCDFs of throughput for a Band 7 dongle with external antennas: (a) collinear dipoles arrangement (blue), (b) cross-polarized dipoles setup (red), and (c) 45° polarization inclination (green) at RS EPRE = -100 dBm/15 kHz. The shaded region indicates a possible rejection criterion (see text).

P_{iso} corresponding to RS EPRE = -100 dBm/15 kHz. A sequence of only 488 constellations (including different combinations of polarization) was applied in this example with a resolution of 30° in θ_1 and ϕ_1 but fixed $\theta_2 = 90^\circ$ and only the two cases $\phi_2 = \phi_1 + 45^\circ$ and $\phi_2 = \phi_1 + 90^\circ$. The choice of θ_2 and ϕ_2 was restricted by the chamber used for this measurement, which did not allow moving the second antenna automatically. The throughput observed for each constellation is weighted in the CCDF with the relative fraction of the surface of the unit sphere it represents, that is, the data reflect a two-path uniform PAS. Despite the fact that the sequence of applied constellations appears insufficient for a full characterization, the results in Figure 7 confirm that we can already clearly distinguish the three arrangements (a), (b), and (c). The arrangement (a) (collinear dipoles)

performs worst and one may assume that this observation carries over to in-the-field performance where cross-polarized antennas are employed at the basestation.

One way to make use of the FOM in Figure 7 is to introduce again a “rejection region” as performance criterion. The shaded box in Figure 7 is given for illustration. It corresponds to the criterion that “UE should provide at least 80% throughput in 60% of all test cases.” The MNO can specifically tailor this requirement based on network quality requirements and user expectation.

Suitable chamber setups to be used in automated commercial test systems are presented in Figure 8. These two setups have extensions made to distributed axis chambers with an additional boom mounted at the opposite wall or the ceiling. The example presented in Figure 7 corresponds to a rudimentary implementation after Figure 8(b).

Further measurement results that were obtained in a chamber setup after Figure 8(a) are given in Figure 9. The figure displays the CCDF of throughput for 4 LTE devices of different form-factors (and operating in different bands). Results were recorded for an FRC with 16QAM and a 10 MHz bandwidth at a power level P_{iso} corresponding to RS EPRE = -102 dBm/15 kHz. A sequence of constellations (including different combinations of polarization), which have their AOA components limited to the azimuthal plane of the DUT, was applied in this example. The result permits to discriminate the devices although constellations with elevated AOAs are desirable in further investigations.

The question remains, how many constellations are actually required to sufficiently characterize a device. The question has been addressed by simulation, and results are presented in Figure 11. The simulation is based on a realistic compound pattern of an LTE datacard in a laptop with two antennas, operating in OL-SM mode in a 2×2 MIMO configuration. The patterns are indicated in Figure 10 (colored and gray pattern, resp.). The simulation tool [6]

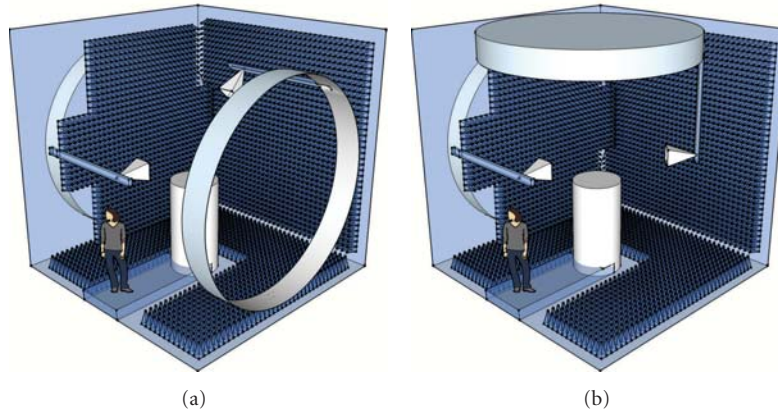


FIGURE 8: Examples for realization of 2-test-antenna setups in a distributed axis chamber.

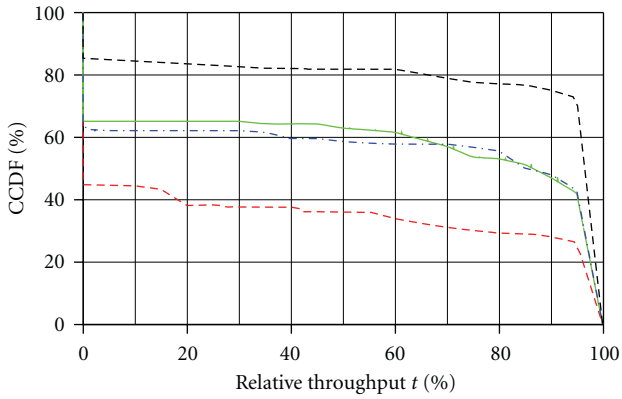


FIGURE 9: Measured CCDF of throughput for 4 different LTE devices with different form-factors and operating frequencies at RS EPRE = -102 dBm/15 kHz using only constellations in the azimuthal plane.

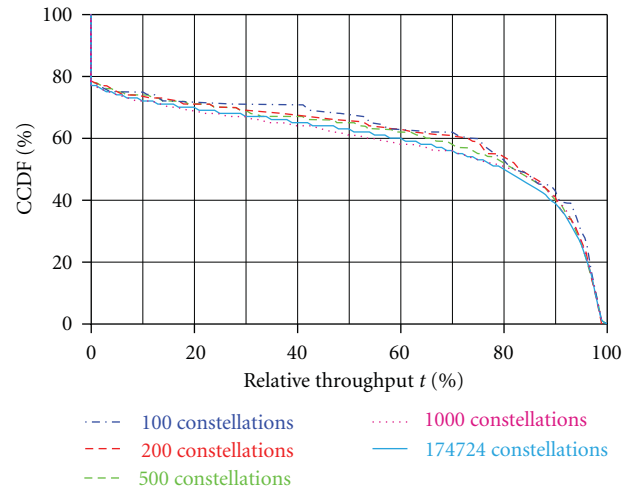


FIGURE 11: Simulated throughput statistics for a 2-antenna LTE datacard in a laptop in OL-SM mode with FRC using two dual-polarized test antennas. CCDFs of estimated throughput are presented for $SNR_0 = 7$ dB for different numbers of randomly selected constellations.

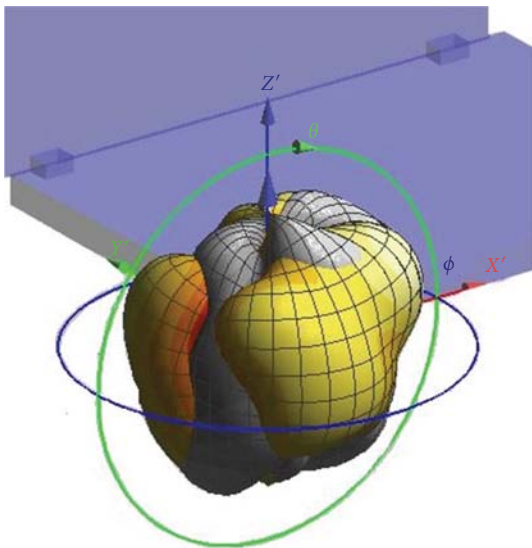


FIGURE 10: Compound pattern of a simulated datacard with 2 antennas in a laptop [6, 18]. The magnitude of the patterns are shown separately colored/black-and-white.

is based on the LTE simulator developed by the Institute of Communications and Radio-Frequency Engineering of TU Vienna [21]. The MCS corresponds to CQI = 4, that is, QPSK with coding rate of 30%. The maximum number of HARQ transmissions was set to 4. The DL channel bandwidth was chosen to be 5 MHz (25 Resources Blocks (RBs)). To save simulation time, received signals were captured after the Zero Forcing (ZF) receiver to estimate throughput for the selected MCS based on Error Vector Magnitude (EVM).

CCDFs of estimated throughput for $SNR_0 = 7$ dB for different numbers of randomly selected constellations are given in Figure 11. The throughput observed for each constellation is weighted in the CCDF with the relative fraction of the surface of the unit sphere it represents, that is, the data reflect a two-path uniform PAS. It is observed that a level of hundreds of constellations is already sufficient for

convergence of the CCDF even for a complicated pattern as in Figure 10.

7. Conclusion

In this paper, a straightforward test approach is presented, which focuses on the characterization of the physical attributes of UEs. Statistical metrics are adopted to adequately represent the variety of possible propagation scenarios. The approach is of low complexity and allows for reuse of existing test sites and equipment. The relevant device properties are covered by two test cases.

The first test case covers total antenna system efficiency, receiver noise figure, and self-interference. It bears similarity to traditional TIS measurement for SISO devices. The statistical metric that is reported maps directly to in-the-field outage probability. The second test case covers modal imbalance, pattern and polarization selectivity. The measurement setup in this case realizes a maximum rank channel. The statistical metric, which is reported here, describes the probability of attaining theoretical peak performance in SM mode.

The examples that have been presented support the conclusion that the approach is suitable to distinguish very well between good and bad devices. Final validation of the predictive power of MIMO OTA test approaches, however, requires a thorough comparison between lab results and in-the-field observations, which has to be the program of future work.

Abbreviations

3GPP:	3rd Generation Partnership Project
AC:	Anechoic Chamber
AOA:	Angle of Arrival
AS:	Angular Spread
AWGN:	Additive White Gaussian Noise
BLER:	Block Error Rate
BS:	Basestation
BSE:	Basestation Emulator
CCDF:	Complementary Cumulative Distribution Function
CDF:	Cumulative Distribution Function
CECC:	Complex Envelope Correlation Coefficient
CL-SM:	Closed-Loop Spatial Multiplexing
CQI:	Channel Quality Indication
CSI:	Channel State Information
DL:	Downlink
DUT:	Device Under Test
eNB:	evolved Node-B
E-UTRA:	Evolved Universal Terrestrial Radio Access
EVM:	Error Vector Magnitude
FOM:	Figure of Merit
FRC:	Fixed Reference Channel
GSCM:	Geometry-Based Stochastic Channel Model
HARQ:	Hybrid Automatic Repeat Request
HSDPA:	High-Speed Downlink Packet Access
HSPA:	High-Speed Packet Access

LD-CDD:	Large-Delay Cyclic Delay Diversity
LHS:	Left-Hand-Side
LTE:	Long-Term Evolution
MCS:	Modulation and Coding Scheme
MIMO:	Multiple Input-Multiple Output
MNO:	Mobile Network
MRC:	Maximum Ratio Combining
OFDM:	Orthogonal Frequency Division Multiplex
OL-SM:	Open-Loop Spatial Multiplexing
OTA:	Over-The-Air
PAS:	Power Angular Spectrum
PDF:	Probability Density Function
PMI:	Precoding Matrix Indicator
QAM:	Quadrature Amplitude Modulation
QPSK:	Quaternary Phase-Shift Keying
RB:	Resource Block
RD:	Receive Diversity
RHS:	Right-Hand-Side
RI:	Rank Indication
SCME:	3GPP Spatial Channel Model Extended
SFBC:	Space-Frequency Block Coding
SISO:	Single Input-Single Output
SM:	Spatial Multiplexing
SNR:	Signal-to-Noise Ratio
TCIS:	Total Compound Isotropic Sensitivity
TD:	Transmit Diversity
TIS:	Total Isotropic Sensitivity
TRP:	Total Radiated Power
UE:	User Equipment
UL:	Uplink
ZF:	Zero Forcing.

Acknowledgments

The authors would like to thank Mr. Aleksander Krewski for kindly supplying the simulation results in Figures 1 and 10. Part of the measurements presented in Figure 7 was conducted in the test lab of CETECOM GmbH, Essen, Germany. The authors gratefully acknowledge support by Mr. Rachid Acharkaoui. The research project on which this paper is based was funded by the German Ministry for Education and Research (BMBF) under project no. 17N1408. Responsibility for the contents is with the authors.

References

- [1] *Test Plan for Mobile Station Over the Air Performance Rev 3.1*, CTIA—The Wireless Association Std., 2011.
- [2] RP-080766, LS on status of radiated testing methods for MIMO/multiple receive antenna terminals http://www.3gpp.org/LiaisonsDocs/Outgoing_Ls/Rp-41-meeting.htm, 2008.
- [3] *Measurement of radiated performance for MIMO and multi-antenna reception for HSPA and LTE terminals (Release 10)*, 3GPP TR 37.976, Rev. 1.5.0, May 2011.
- [4] W. L. Schroeder and Y. Feng, "A critical review of MIMO OTA test concepts—lessons learned from actual measurements," in *Proceedings of the 30th URSI General Assembly and Scientific Symposium (URSIGASS '11)*, pp. 1–4, URSI, Istanbul, Turkey, August 2011.

- [5] R4-103763, COST2100 MIMO OTA Round Robin Measurement Campaign, summer 2010—first results & conclusions from measurements performed at RheinMain University of Applied Sciences, <http://www.3gpp.org/>, 2010.
- [6] Y. Feng, A. Krewski, and W. L. Schroeder, "Simulation based comparison of metrics and measurement methodologies for OTA test of MIMO terminals," in *Proceedings of the 4th European Conference on Antennas and Propagation (EuCAP '10)*, pp. 1–5, Barcelona, Spain, April 2010.
- [7] Vodafone Group, RP-120272: Verification of radiated multi-antenna reception performance of UEs in LTE/UMTS, <http://www.3gpp.org/>, 2010.
- [8] S. M. Alamouti, "A simple transmit diversity technique for wireless communications," *IEEE Journal on Selected Areas in Communications*, vol. 16, no. 8, pp. 1451–1458, 1998.
- [9] W. L. Schroeder and A. Krewski, "Total multi-port return loss as a figure of merit for MIMO antenna systems," in *Proceedings of the 40th European Microwave Conference (EuMC '10)*, pp. 1742–1745, Paris, France, September 2010.
- [10] J. W. Wallace and M. A. Jensen, "Termination-dependent diversity performance of coupled antennas: network theory analysis," *IEEE Transactions on Antennas and Propagation*, vol. 52, no. 1, pp. 98–105, 2004.
- [11] "Spatial channel model for multiple input multiple output (MIMO) simulations (Release 7)," 3GPP Technical Report TR 25.996, Rev. 7.0.0, 2007, <http://www.3gpp.org/>, 2010.
- [12] P. Kyösti, J.-P. Nuutinen, and M. Falck, "Proposal for standardized test procedure for OTA testing of multi-antenna terminals," in *Proceedings of the 7th MCM, COST2100*, Braunschweig, Germany, February 2009, TD(09)766, <http://www.cost2100.org/>.
- [13] J. Takada, "Handset MIMO antenna testing using a RF-controlled spatial fading emulator," in *Proceedings of the 7th MCM, COST2100*, Braunschweig, Germany, February 2009, TD(09)742, <http://www.cost2100.org/>.
- [14] Y. Okano, "Impact of number of probe antennas for MIMO OTA spatial channel emulator," in *Proceedings of the 9th MCM, COST2100*, Vienna, Austria, September 2009, TD(09)929, <http://www.cost2100.org/>.
- [15] Y. Feng, C. von Gagern, A. Tankielun, R. Acharkaoui, W. Richter, and W. L. Schroeder, "Test plan for DL 2×2 MIMO OTA testing—part I: concepts for straightforward characterization measurements and statistical metrics," in *Proceedings of the 1st MCM, COST IC1004*, Lund, Sweden, January 2011, TD(11)01045, <http://www.ic1004.org/>.
- [16] C. von Gagern, A. Tankielun, Y. Feng, W. L. Schroeder, R. Acharkaoui, and W. Richter, "Test plan for DL 2×2 MIMO OTA testing—part II: test plan description and examples," in *Proceedings of the 1st MCM, COST IC1004*, Lund, Sweden, January 2011, TD(11)01044, <http://www.ic1004.org/>.
- [17] E. Böhler, C. von Gagern, A. Tankielun, Y. Feng, and W. L. Schroeder, "Measurements of over-the-air performance of MIMO UE," in *Proceedings of the 33rd Annual Symposium of the Antenna Measurement Techniques Association (AMTA '11)*, Englewood, Colo, USA, October 2011.
- [18] Y. Feng, J. Jonas, and W. L. Schroeder, "Discussion of statistical metrics for MIMO over-the-air (OTA) performance based on empirical results," in *Proceedings of the 5th European Conference on Antennas and Propagation (EuCAP '11)*, pp. 1233–1237, Rome, Italy, April 2011.
- [19] Y. Feng and W. L. Schroeder, "Extending the definition of total isotropic sensitivity (TIS) and total radiated power (TRP) for application to MIMO over-the-air (OTA) testing," in *Proceedings of the 8th MCM, COST 2100*, Valencia, Spain, May 2009, TD(09)866, <http://www.cost2100.org/>.
- [20] R. Tian, B.K. Lau, and Z. Ying, "Multiplexing efficiency of MIMO antennas," *IEEE Antennas and Wireless Propagation Letters*, vol. 10, Article ID 5727906, pp. 183–186, 2011.
- [21] C. Mehlführer, M. Wrulich, J. C. Ikuno, D. Bosanska, and M. Rupp, "Simulating the long term evolution physical layer," in *Proceedings of the 17th European Signal Processing Conference (EUSIPCO '09)*, Glasgow, UK, August 2009, http://publik.tuwien.ac.at/files/PubDat_175708.pdf.

Research Article

On the Performance of the Time Reversal SM-MIMO-UWB System on Correlated Channels

Hieu Nguyen,¹ Van Duc Nguyen,² Trung Kien Nguyen,¹ Kiattisak Maichalernnukul,¹ Feng Zheng,³ and Thomas Kaiser³

¹*Institute of Communications Technology, Leibniz University of Hannover, 30167 Hannover, Germany*

²*School of Electronics and Telecommunications, Hanoi University of Science and Technology, 1 Dai Co Viet, Hanoi 10000, Vietnam*

³*Institute of Digital Signal Processing, Faculty of Engineering, University of Duisburg-Essen, 47057 Duisburg, Germany*

Correspondence should be addressed to Hieu Nguyen, hieunth@gmail.com

Received 3 January 2012; Revised 9 March 2012; Accepted 9 March 2012

Academic Editor: David A. Sanchez-Hernandez

Copyright © 2012 Hieu Nguyen et al. This is an open access article distributed under the Creative Commons Attribution License, which permits unrestricted use, distribution, and reproduction in any medium, provided the original work is properly cited.

The impact of spatial correlation on the multi-input multi-output ultrawide band (MIMO-UWB) system using the time reversal (TR) technique is investigated. Thanks to TR, several data streams can be transmitted by using only one antenna in a system named virtual MIMO-TRUWB. Since the virtual MIMO-TR-UWB system is not affected by the transmit correlation, under the condition of the high spatial correlation, it outperforms the true MIMO-UWB system with multiple transmit antennas. The channel measurements are performed in short-range indoor environment, both line-of-sight and non-line-of-sight to verify the adopted correlated channel model.

1. Introduction

An ultrawide band (UWB) communication system, whose relative bandwidth is usually defined as greater than twenty-five percents, has become a promising candidate for high data rate and short-range communication systems, which have attracted great interests from both academic and industrial aspects recently [1, 2]. Impulse radio UWB is however designed with low complexity and low power consumption applications such as in many application such as wireless sensor networks, sensing and positioning systems, interchip communication, contact less wireless, biological or biomedical networks, imaging systems, health monitoring, and body-area networks [3]. However, due to the wide bandwidth property, UWB systems suffer from a very long delay spread by multipath effect [4–6]. One has to deploy RAKE receivers to combat the intersymbol interference (ISI).

The time reversal (TR) technique, which is originated from under-water acoustics and ultrasonic [7, 8], now has been used in many applications such as localization, imaging and green wireless communications [9–14]. TR also has shown its potential in dealing with the ISI problems in UWB [15, 16]. In a TR system, the time-reversed channel impulse

response (CIR) is implemented as a filter at the transmitter side. This process leads to a very narrow focus of power at the receiver at one specific time instant, and one specific space position if the CIRs between any two communication pairs at different locations are de-correlated. In other words, a TR-UWB prefiltering system has a unique feature of space-time domain focusing.

The space-time focusing feature is also beneficial in a MIMO spatial multiplexing scheme [17, 18]. Several studies have applied the TR technique to multiple antennas beamforming systems. In [19–21], the same stream of data is beamformed by a TR filter and transmitted over transmit antennas. In [22, 23], a joint ZF and TR pre-equalizer is designed to minimize the ISI and maximize the received power at the intended receiver. This proposal only deals with the ISI problem for beamforming schemes. The potential of a MIMO UWB system using spatial multiplexing scheme is considered in [24], where the matching filter plays the role of a passive time reversal filter and the maximum likelihood (ML) detector is used to deal with the multistream interference (MSI) but ignores the ISI. The SM-MIMO-UWB system using TR is introduced in [25] with the capability of transmit

antenna selection. The TR technique and preequalizer are proposed in [26] for the so-called virtual MIMO UWB system.

As shown in [26], with the help of the TR prefilter and a properly designed preequalizer, the system with only one transmit antenna can deliver several independent data streams at the same time. However, the spatial correlation among the transmit and receive antennas has not been investigated. We have taken the spatial correlation into account in [27], where a constant spatial correlation model for MIMO UWB with linear array structure has been applied. In this paper, the performance of system over both correlated line-of-sight (LOS) and non-line-of-sight (NLOS) channels is investigated with the same correlation model. In order to verify the adopted correlation model, the correlated channels are measured in both scenarios NLOS and LOS in indoor environment. These scenarios are referred to as channel models CM1 and CM2, respectively, in the IEEE 802.15.3a standard [28]. The BER results on the adopted correlated channel model with an appropriate value of correlation coefficient are shown closely matching with those on the measured indoor channel.

It is well known that the MIMO-TR-UWB system can achieve transmit diversity [26], but it suffers from penalty caused by both transmit and receive antenna correlations. Meanwhile, the single-input multiple-output TR-UWB (SIMO-TR-UWB) or virtual MIMO-TR-UWB does not face the transmit antenna correlation because it has only one transmit antenna. It will be shown that, under some conditions, the virtual MIMO outperforms the true MIMO system in term of the BER performance.

The remainder of the paper is organized as follows: in Section 2, the correlated MIMO channel model is shown, and then the virtual MIMO-UWB-TR system is presented in Section 3; UWB channel measurement is described in Section 4; in Sections 5 and 6, numerical simulation results and conclusions are presented, respectively.

2. Correlated MIMO Channel Model

In order to achieve the high data rate without expanding the bandwidth, the spatial multiplexing scheme with multiple transmit antennas is introduced. In the spatial multiplexing (SM) system, several streams of data are transmitted over several transmit antennas at the same time. The channel capacity can be increased proportionally to the number of antennas. Let us consider an SM-MIMO UWB system with M transmit and N receive antennas as shown in Figure 1, where the preequalizer and prefilter blocks will be discussed in the next section. We assume that the maximum length of each channel realization is L . The CIR between transmit antenna j and receive antenna i is

$$h_{i,j}(t) = \sum_{l=1}^L \alpha_l^{i,j} \delta(t - \tau_l^{i,j}), \quad i = 1, \dots, N, \quad j = 1, \dots, M. \quad (1)$$

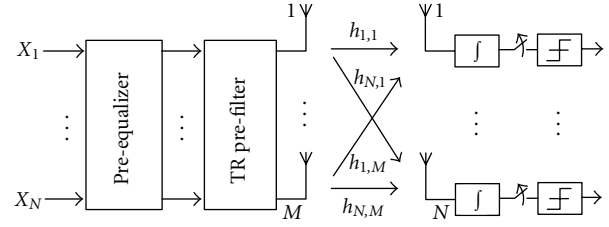


FIGURE 1: Block diagram of an SM-MIMO UWB system.

We can arrange these channels in a matrix form as follows:

$$\mathbf{H}(t) = \begin{pmatrix} h_{1,1}(t) & h_{1,2}(t) & \cdots & h_{1,M}(t) \\ h_{2,1}(t) & h_{2,2}(t) & \cdots & h_{2,M}(t) \\ \vdots & \vdots & \ddots & \vdots \\ h_{N,1}(t) & h_{N,2}(t) & \cdots & h_{N,M}(t) \end{pmatrix}. \quad (2)$$

Generally, the entries of the MIMO channel matrix \mathbf{H} are assumed to be independent of each other. In the real world, however, the spatial correlation among antennas (transmit or receive antennas) exists. In other words, the individual channels of \mathbf{H} are correlated [29, 30]. The correlation is caused by a variety of reasons such as inadequate antenna spacing.

The correlation can be included into the MIMO UWB channel model by introducing fixed transmit and receive correlation matrices following the well-known Kronecker model. The transmit and receive correlation can be represented by an $M \times M$ matrix \mathbf{R}_{Tx} and an $N \times N$ matrix \mathbf{R}_{Rx} , respectively [31]. The correlated channel is represented by equation

$$\mathbb{H} = \mathbf{R}_{Rx}^{1/2} \mathbf{H}_w \mathbf{R}_{Tx}^{1/2}, \quad (3)$$

where \mathbf{H}_w is the channel matrix of independent channel realization.

For the fixed correlation matrix in the Kronecker model, there are some variations in terms of whether or not the impact of interelement distance is considered [32, 33]. In this paper, the exponential decay model for the correlation is deployed [30, 32]. The transmit and receive correlation matrices are

$$\mathbf{R}_{Tx} = \begin{pmatrix} 1 & \rho_{Tx} & \rho_{Tx}^2 & \cdots & \rho_{Tx}^{M-1} \\ \rho_{Tx} & 1 & \rho_{Tx} & \cdots & \rho_{Tx}^{M-2} \\ \vdots & \vdots & \vdots & \ddots & \vdots \\ \rho_{Tx}^{M-1} & \rho_{Tx}^{M-2} & \rho_{Tx}^{M-3} & \cdots & 1 \end{pmatrix}, \quad (4)$$

$$\mathbf{R}_{Rx} = \begin{pmatrix} 1 & \rho_{Rx} & \rho_{Rx}^2 & \cdots & \rho_{Rx}^{N-1} \\ \rho_{Rx} & 1 & \rho_{Rx} & \cdots & \rho_{Rx}^{N-2} \\ \vdots & \vdots & \vdots & \ddots & \vdots \\ \rho_{Rx}^{N-1} & \rho_{Rx}^{N-2} & \rho_{Rx}^{N-3} & \cdots & 1 \end{pmatrix},$$

where ρ_{Tx} and ρ_{Rx} are the correlation coefficients of transmit and receive antennas, respectively.

3. Virtual MIMO-UWB-TR System

In this paper, a TR prefilter combined with a zero forcing (ZF) preequalizer, which has been proposed in [26, 27], is adopted to combat the ISI and the MSI in the SM-MIMO UWB system.

The TR prefilter matrix of the MIMO system is given by [27]

$$\bar{\mathbf{H}}(t) = \begin{pmatrix} h_{1,1}(-t) & h_{2,1}(-t) & \cdots & h_{N,1}(-t) \\ h_{1,2}(-t) & h_{2,2}(-t) & \cdots & h_{N,2}(-t) \\ \vdots & \vdots & \ddots & \vdots \\ h_{1,M}(-t) & h_{2,M}(-t) & \cdots & h_{N,M}(-t) \end{pmatrix}, \quad (5)$$

which is based on the original CIR matrix reversed in time and transposed in space. The CIR matrix of the equivalent channel is

$$\hat{\mathbf{H}}(t) = \begin{pmatrix} \hat{h}_{1,1}(t) & \hat{h}_{1,2}(t) & \cdots & \hat{h}_{1,N}(t) \\ \hat{h}_{2,1}(t) & \hat{h}_{2,2}(t) & \cdots & \hat{h}_{2,N}(t) \\ \vdots & \vdots & \ddots & \vdots \\ \hat{h}_{N,1}(t) & \hat{h}_{N,2}(t) & \cdots & \hat{h}_{N,N}(t) \end{pmatrix}, \quad (6)$$

where each component of the equivalent composite channel (which we will call equivalent channel in the sequel for simplicity) is calculated by

$$\hat{h}_{i,j}(t) = \sum_{k=1}^M h_{i,k}(t) \otimes h_{j,k}(-t), \quad i, j = 1, \dots, N. \quad (7)$$

Some remarks can be drawn from the matrix of the equivalent channel. Firstly, the maximum number of independent data streams the system can achieve is N , which is the number of receive instead of transmit antennas. Secondly, the matrix of the equivalent channel is a square matrix with the entries in the main diagonal being the summation of the autocorrelation of the original CIRs and other entries being the summation of the cross-correlation of the original CIRs between the transmit and receive antennas. Third, the TR technique in MIMO-UWB can exploit M order transmit diversity, and the diversity gain depends on the number of transmit antennas.

Let us consider the special case of MIMO-TR-UWB system, where the data is transmitted over only one antenna, that is, $M = 1$. The channel matrix is thus only a column vector $\mathbf{H}(t) = [h_1(t), h_2(t), \dots, h_N(t)]^T$ and the TR filter matrix is a row vector $\bar{\mathbf{H}}(t) = [h_1(-t), h_2(-t), \dots, h_N(-t)]$. The equivalent channel, however, is still a square $N \times N$ matrix as presented in (6). Each entry of equivalent matrix is

$$\hat{h}_{i,j}(t) = h_i(t) \otimes h_j(-t), \quad i, j = 1, \dots, N. \quad (8)$$

In this case, N data stream are multiplexed to be transmitted over one antenna. In other words, the data are seen to be transmitted over N virtual antennas. Hence, the system is named virtual MIMO-TR-UWB.

In the true MIMO-TR-UWB system, when the separation distance between antenna elements is small, the spatial correlation appears at both transmit and receive sides. These correlation will doubly degrade the performance of the system. Meanwhile, in the virtual MIMO-TR-UWB system, the correlation appears only at the receiver side and the degradation is caused only by receiver correlation. The virtual MIMO-TR-UWB system can mitigate the impact of the transmit correlation. However, it cannot achieve the transmit diversity gain as the true one does.

The CIR can also be reused by the preequalizer design at the transmitter side for further multistream interference (MSI) mitigation. Here, we assume that a ZF preequalizer is deployed. A simple TR filter focuses the energy into a short-time duration in the equivalent CIR, so we can use the shortened equivalent channels to design the preequalizer. Suppose that the maximum length of the equivalent channel is L_e . As shown in [27], we can choose L_s ($L_s \ll L_e$) capturing most of the energy to compute the linear preequalizer.

We assume that the channels do not change when a block of $K + L_s - 1$ data symbols is transmitted. The new equivalent channel matrix can be represented by a block Toeplitz matrix

$$\hat{\mathbf{H}}_s = \begin{pmatrix} \hat{\mathbf{H}}[L_s - 1] & \cdots & \hat{\mathbf{H}}[0] & 0 & \cdots & 0 \\ 0 & \hat{\mathbf{H}}[L_s - 1] & \cdots & \hat{\mathbf{H}}[0] & \cdots & 0 \\ \vdots & \ddots & \ddots & \ddots & \ddots & \vdots \\ 0 & \cdots & 0 & \hat{\mathbf{H}}[L_s - 1] & \cdots & \hat{\mathbf{H}}[0] \end{pmatrix}, \quad (9)$$

where each block matrix is

$$\hat{\mathbf{H}}[k] = \begin{pmatrix} \hat{h}_{1,1}[k] & \hat{h}_{1,2}[k] & \cdots & \hat{h}_{1,N}[k] \\ \hat{h}_{2,1}[k] & \hat{h}_{2,2}[k] & \cdots & \hat{h}_{2,N}[k] \\ \vdots & \vdots & \ddots & \vdots \\ \hat{h}_{N,1}[k] & \hat{h}_{N,2}[k] & \cdots & \hat{h}_{N,N}[k] \end{pmatrix}. \quad (10)$$

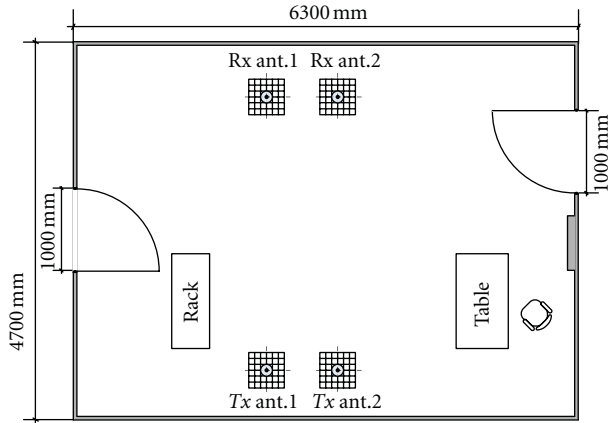
The preequalizer matrix \mathbf{G}_{ZF} is the inverse of the shortened equivalent channels matrix, given by [27, 34]

$$\mathbf{G}_{ZF} = \alpha \hat{\mathbf{H}}_s^\dagger = \alpha (\hat{\mathbf{H}}_s^H \hat{\mathbf{H}}_s)^{-1} \hat{\mathbf{H}}_s^H, \quad (11)$$

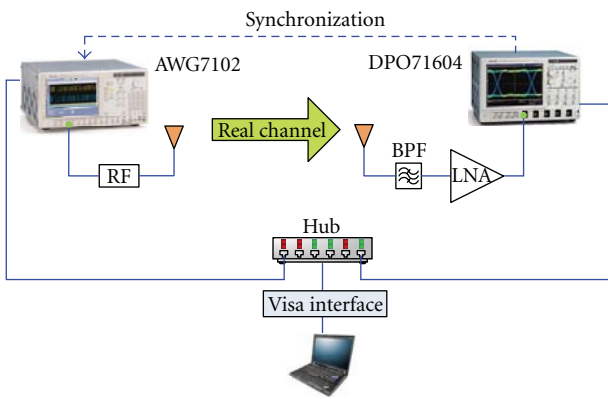
where \dagger denotes the Moore-Penrose pseudoinverse of a matrix. The coefficient α , which can be found from [34], is introduced for the power constraint of the transmit signal.

4. UWB Channel Measurement

We generate the channel realizations for comparison using both the adopted correlated channel model and those obtained from our indoor measurements. The indoor UWB channels are measured in time domain within a 4.7 m \times 6.3 m room with a table, a chair, a wooden rack, and different kinds of smaller scattering objects as shown in Figure 2(a). The floor and walls of this room are constructed from concrete materials. The ceiling (3.2 m above the floor) is composed of iron sheets and metallic beams.



(a) Floor plan and measurement configuration



(b) A sketch of system

FIGURE 2: Setup of UWB channel measurement.

The sketch of the whole system is illustrated in Figure 2(b). The major components used in the measurements are a Tektronix AWG7102 arbitrary waveform generator (AWG) and a Tektronix DPO71604 digital phosphor oscilloscope (DPO) which are synchronized by the reference clock signal and connected to the processing computer via Ethernet. The AWG supports two channels with sampling rates of up to 10 GSamples/s (GS/s) and 3.5 GHz bandwidth or one channel with sampling rates of up to 20 GS/s and 5.8 GHz analog bandwidth using interleaving. The DPO provides four channels with sampling rates of up to 50 GS/s and 16 GHz frequency span. The small-size omnidirectional UWB patch antennas are used. On the receiver side, each antenna is connected to the DPO through a bank of bandpass filters (1.5 GHz bandwidth) and +55 dB low-noise amplifiers for reliable signal acquisition under harsh SNR conditions. The transmit and receive antennas are placed at the same height of 1.1 m. The probe UWB pulse used in all measurements is a second-order derivative Gaussian pulse with the symbol duration $T = 250$ ns.

The common scenario for applications of UWB systems is in a small office or home environment. Therefore, we focus on the short-range indoor environment, both NLOS and LOS. These scenarios are referred to as CM1 (for LOS)

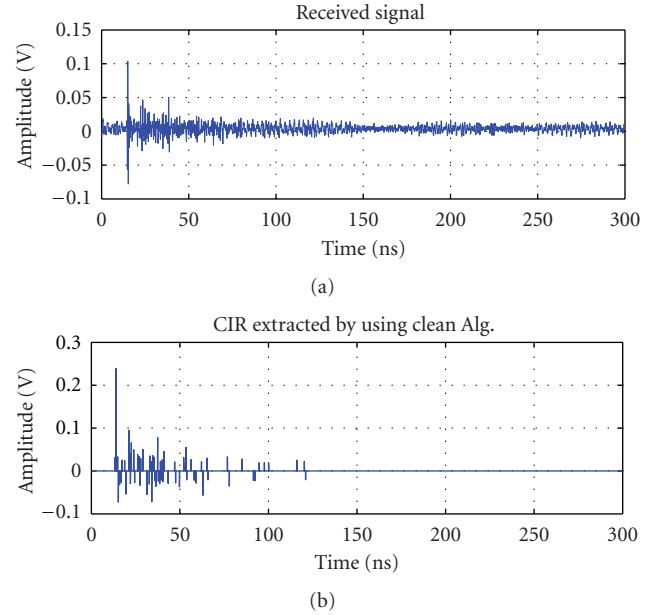


FIGURE 3: An example of the received signal and the extracted CIR.

and CM2 (for NLOS) in the IEEE 802.15.3a UWB channel models [28]. In our measurement, the blockage for the NLOS scenario is created by vertically placing a large iron sheet in the direct propagation path.

The temporal stationarity of the environment is ensured by the absence of mobile objects/persons, thus allowing us to assume that the channels for the links are quasistatic over the duration of data transmissions. For the MIMO channels, the spatial antenna arrays at both transmitter and receiver are synthesized by sequential measurements exploiting such temporal stationarity. Due to this array synthesis, our measurement results do not include the effects of antenna coupling. A (2×2) virtual MIMO channel, corresponding to 4 SISO channels (49 realizations for each), are measured in our campaign. The adjacent antennas are separated by 0.2 m, and the mean separation between transmit and receive antennas is kept at 4 m.

In order to extract the CIR from received signals, we use the well-known deconvolution technique, the so-called Clean Algorithm [35]. A realization of the SISO channel which is extracted from the received signal by using Clean Algorithm is shown in Figure 3.

5. Numerical Results and Discussions

In our simulations, the binary data is modulated to the binary phase-amplitude modulation format. The UWB monocycle waveform is the 2nd derivative Gaussian pulse, represented by

$$p(t) = \left[1 - 4\pi \left(\frac{t - t_c}{w} \right)^2 \right] e^{-2\pi((t-t_c)/w)^2}, \quad (12)$$

where w is a parameter corresponding to pulse, width, t_c is a time shifting of the pulse and T is the symbol duration. In our simulations, $w = 1$ ns, $t_c = w/2$, and $T = 2$ ns.

Simulation results are based on the UWB channel model in the IEEE 802.15.3a standard [28] and those obtained from measurements. Results are followed by descriptions of the channel models. The correlated MIMO channel model is generated by modifying the channel models in the IEEE 802.15.3a standard, which is formulated for SISO UWB, then included with the correlation matrices in (5). For the simulation results based on the standard model, the correlation of receive antennas affects in the same way on SIMO and MIMO-TR-UWB systems and the receive correlation coefficient is fixed at $\rho_{Rx} = 0.2$. For the fair comparison, we shorten the equivalent channel when designing the ZF preequalizer with the same ratio $L_s/L_e = 0.2$ for standard channels and measured channels.

Figure 4 shows the BER performance of a 2×2 MIMO system operating in the modified CM1, CM2 channels with the matched transmit correlation coefficient and in the measured LOS and NLOS channels. The value of correlation coefficient matched with the measurement result is found by exhaustive search and is then rounded to one decimal place. It can be seen that the average BERs based on realizations of CM1 and CM2 with the selected value of $\rho_{Tx} = 0.2$ are closely matched with those based on the corresponding measured channels. It is noted that this correlation value is specific to our measurement setting. Also observed from this figure that the system performance in the LOS environment is better than in the NLOS environment for standard channels as well as measured channels. Transmission through walls and obstructions in NLOS environment leads to additional delay before arriving at the receiver and significant additional attenuation, which reduce the received strength and lead to increased errors in estimation [36].

In Figures 5 and 6, the effect of the transmit correlation coefficient on the BER performance of the system is presented. In both figures, two data streams are transmitted over $M = 1, 2$, and 4 transmit antennas, respectively. The transmit correlation coefficient ρ_{Tx} varies from 0 (no correlation) to 0.95 (strong correlation), and the SNR = 12 dB.

It can be seen from Figure 5, for the LOS environment, that, when ρ_{Tx} increases, the average BER of the SIMO or virtual MIMO-TR-UWB system keeps unchanged while it increases in the true MIMO case. This can be explained by that the SIMO system is impacted by only the spatial correlation between receive antennas, so the BER performance of such system does not change with variation of the transmit correlation. Meanwhile, the spatial correlation appears at both transmit and receive sides in the MIMO system and it will doubly degrade the performance of the system. The BER performance of the MIMO system will be worse than the SIMO system if the transmit correlation coefficient is greater than a critical value. For example, the performance of the 2×2 MIMO system is worse than the 1×2 SIMO system if $\rho_{Tx} \geq 0.7$, and the performance of the 4×2 MIMO system is worse than the 1×2 SIMO system if $\rho_{Tx} \geq 0.6$.

At low transmit correlation regime, the more the transmit antennas, the better the BER performance that the system can achieve. This is the advantage of the transmit diversity possessed by the MIMO-TR-UWB system [34]. However, if the correlation is strong, more transmit antenna

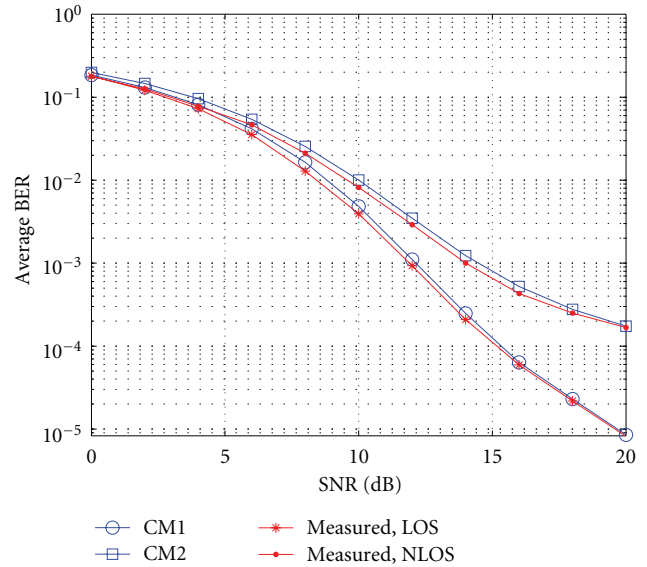


FIGURE 4: BER performance comparison, for standard channels with $\rho_{Tx} = 0.2$ and for measured indoor channels.

will greatly degrade the performance of MIMO systems since the rank of the MIMO channel reduces, leading to destroy the diversity. As shown in Figure 5, when the transmit correlation coefficient ρ_{Tx} is greater than 0.45, the performance of the 2×2 MIMO system outperforms the performance of the 4×2 MIMO system. It has been shown in Figure 5 that, at high correlation, the BER increases from 0.002 to 0.0024. This trend is also observed in Figure 6 for the NLOS environment. In CM1 channel, BER degradation of MIMO system in comparison with SIMO system is about 0.0005, while, in CM2 channel, this value is 0.0015.

The BER performance of 1×2 SIMO and 2×2 MIMO systems operating in the CM1 and CM2 with some values of ρ_{Tx} is illustrated in Figures 7 and 8. As can be seen from these figures, if there is no correlation, the MIMO-TR-UWB system achieves very good BER performance. However, if the correlation appears, the average BER will reach an error floor at the high SNR. Particularly, the performance of the MIMO system will be worse than the SIMO system if the transmit correlation is too high (e.g., $\rho_{Tx} = 0.9$). In Figure 7, at BER = 10^{-3} , the SNR of the MISO scheme 3 dB worse than the MIMO scheme without correlation but 1 dB better than the high correlation MIMO scheme. In Figure 8, these values are 5 dB and 3 dB, respectively. This is also agreed with results in Figures 5 and 6.

6. Conclusion

We have investigated the impact of the spatial correlation on the performance of the SM-MIMO UWB systems where the TR prefilter and the ZF preequalizer are adopted to mitigate the interferences. It is shown that the SIMO-TR-UWB system can work as a virtual MIMO system when several data streams are transmitted over only one transmit antenna. The SIMO system suffers from only the receive correlation,

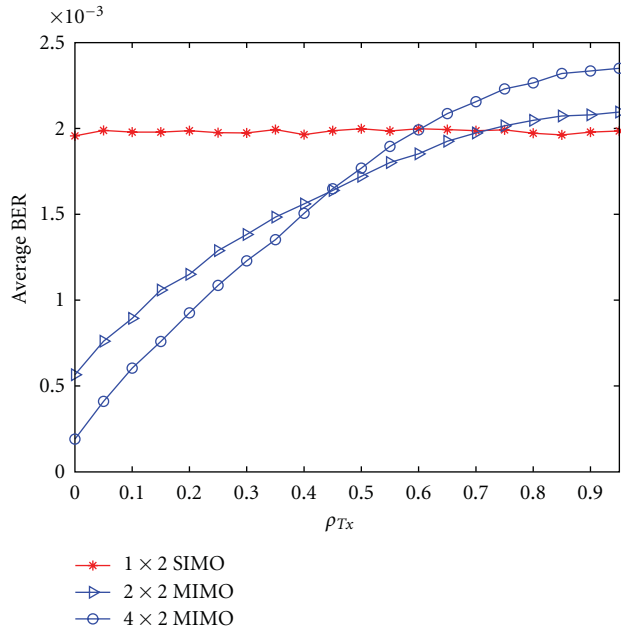


FIGURE 5: BER performance versus transmit correlation coefficient, for CM1 channels.

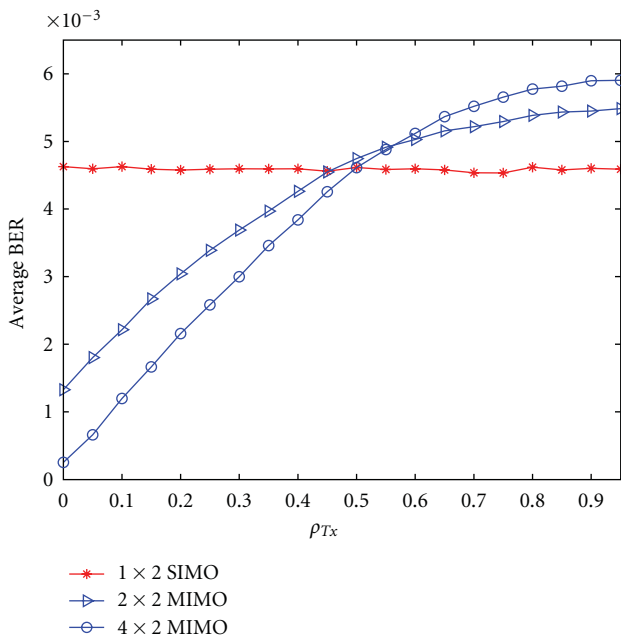


FIGURE 6: BER performance versus transmit correlation coefficient, for CM2 channels.

while both the transmit and receive correlation affect the performance of the real MIMO system. The simulation results show that, at the low transmit correlation regime, the MIMO-TR-UWB systems outperform the SIMO-TR-UWB systems in the BER performance. However, when the transmit correlation becomes large, the performance of the MIMO systems is worse than that of the SIMO systems.

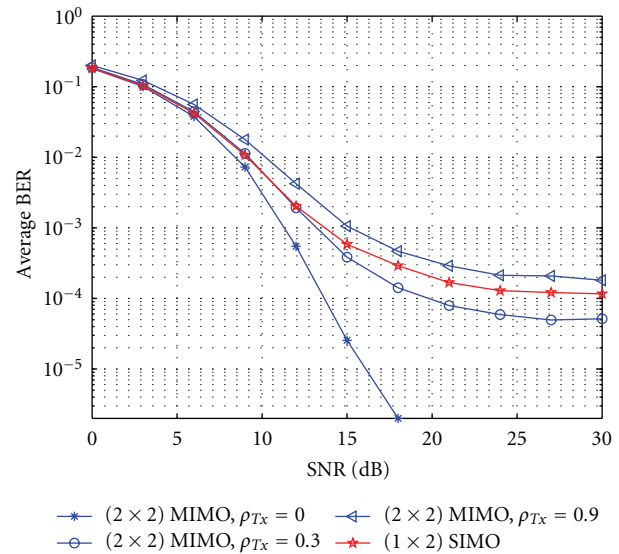


FIGURE 7: BER performance of 2×2 MIMO and 1×2 SIMO systems, for CM1 channels.

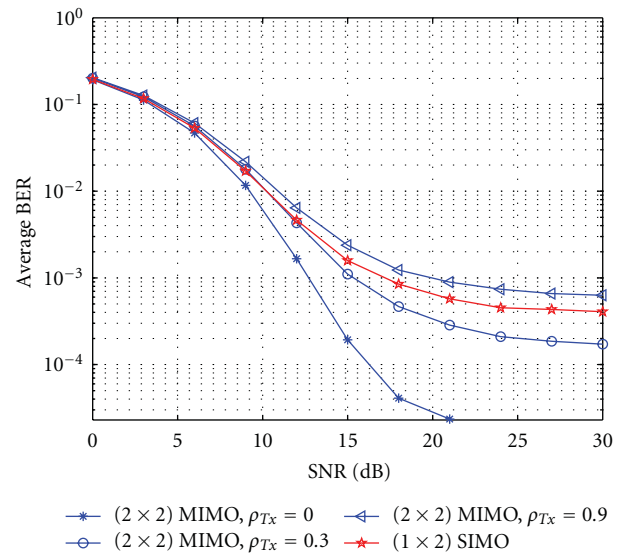


FIGURE 8: BER performance of 2×2 MIMO and 1×2 SIMO systems, for CM2 channels.

The BER performance based on the fixed correlation model generated from the standard UWB channel models is compared with those based on the MIMO UWB channels measured in indoor environment and the matched value of the spatial correlation coefficient is found.

Additionally, we would like to point out that it is interesting to combine the design of the TR prefilter and the preequalizer into one-step design since both designs use the same information. It is not clear yet whether or not the integrate design can reduce the complexity in the system

implementation. However, how to exploit the nice property of the composite TR channel remains an issue in the integrate design.

Acknowledgment

This paper is carried out under the framework of the Project number 102.02.07.09 funded by the Vietnamese National Foundation for Science and Technology Development (NAFOSTED).

References

- [1] M. Di Benedetto, T. Kaiser, D. Porcino, A. Molisch, and I. Opperman, *UWB Communication Systems A Comprehensive Overview*, Hindawi Publishing Corporation, New York, NY, USA, 2006.
- [2] R. J. Fontana, "Recent system applications of short-pulse ultra-wideband (UWB) technology," *IEEE Transactions on Microwave Theory and Techniques*, vol. 52, no. 9, pp. 2087–2104, 2004.
- [3] J. R. Fernandes and D. Wentzloff, "Recent advances in IR-UWB transceivers: an overview," in *Proceedings of the IEEE International Symposium on Circuits and Systems: Nano-Bio Circuit Fabrics and Systems (ISCAS '10)*, pp. 3284–3287, June 2010.
- [4] R. J. M. Cramer, R. A. Scholtz, and M. Z. Win, "Evaluation of an ultra-wide-band propagation channel," *IEEE Transactions on Antennas and Propagation*, vol. 50, no. 5, pp. 561–570, 2002.
- [5] A. F. Molisch, K. Balakrishnan, D. Cassioli et al., "IEEE 802.15.4a Channel model final report," Tech. Rep., 2005, <http://www.ieee802.org/15/pub/04/15-04-0662-02-004a-channel-model-final-report-r1.pdf>.
- [6] F. Zheng and T. Kaiser, "On the evaluation of channel capacity of multi-antenna UWB indoor wireless systems," in *Proceedings of the 8th IEEE International Symposium on Spread Spectrum Techniques and Applications (ISSSTA '04)*, pp. 525–529, September 2004.
- [7] M. Fink, "Time reversal of ultrasonic fields. I: basic principles," *IEEE Transactions on Ultrasonics, Ferroelectrics, and Frequency Control*, vol. 39, no. 5, pp. 555–566, 1992.
- [8] A. Derode, P. Roux, and M. Fink, "Robust acoustic time reversal with high-order multiple scattering," *Physical Review Letters*, vol. 75, no. 23, pp. 4206–4209, 1995.
- [9] F. Foroozan and A. Asif, "Time reversal based active array source localization," *IEEE Transactions on Signal Processing*, vol. 59, no. 6, pp. 2655–2668, 2011.
- [10] M. H. S. Sajjadih and A. Asif, "Unsupervised time reversal based microwave imaging for breast cancer detection," in *Proceedings of the 24th Canadian Conference Electrical and Computer Engineering (CCECE '11)*, pp. 411–415, 2011.
- [11] B. Wang, Y. Wu, F. Han, Y.-H. Yang, and K. J. R. Liu, "Green wireless communications: a time-reversal paradigm," *IEEE Journal on Selected Areas in Communications*, vol. 29, no. 8, pp. 1698–1710, 2011.
- [12] M. Rice and M. Saquib, "MIMO equalization for helicopter-to-ground communications," in *Proceedings of the Military Communications Conference (MILCOM '11)*, pp. 501–506, 2011.
- [13] T. Shimura, H. Ochi, Y. Watanabe, and T. Hattori, "Time-reversal communication in deep ocean Results of recent experiments," in *Proceedings of the IEEE Symposium on Underwater Technology (UT) and Workshop on Scientific Use of Submarine Cables and Related Technologies (SSC '11)*, April 2011.
- [14] B. Van Damme, K. Van Den Abeele, and O. Bou Matar, "The vibration dipole: a time reversed acoustics scheme for the experimental localisation of surface breaking cracks," *Applied Physics Letters*, vol. 100, no. 8, Article ID 084103, 3 pages, 2012.
- [15] T. Strohmer, M. Emami, J. Hansen, G. Papanicolaou, and A. J. Paulraj, "Application of time-reversal with MMSE equalizer to UWB communications," in *Proceedings of the IEEE Global Telecommunications Conference (GLOBECOM '04)*, vol. 5, pp. 3123–3127, December 2004.
- [16] M. Emami, M. Vu, J. Hansen, A. J. Paulraj, and G. Papanicolaou, "Matched filtering with rate back-off for low complexity communications in very large delay spread channels," in *Conference Record of the 38th Asilomar Conference on Signals, Systems and Computers*, vol. 1, pp. 218–222, November 2004.
- [17] G. J. Foschini, "Layered space-time architecture for wireless communication in a fading environment when using multi-element antennas," *Bell Labs Technical Journal*, vol. 1, no. 2, pp. 41–59, 1996.
- [18] J. H. Winters, "On the capacity of radio communication systems with diversity in a Rayleigh fading environment," *IEEE Journal on Selected Areas in Communications*, vol. 5, no. 5, pp. 871–878, 1987.
- [19] P. Kyritsi, G. Papanicolaou, P. Eggers, and A. Oprea, "IMISO time reversal and delay-spread compression for FWA channels at 5 GHz," *IEEE Antennas and Wireless Propagation Letters*, vol. 3, no. 1, pp. 96–99, 2004.
- [20] R. C. Qiu, C. Zhou, N. Guo, and J. Q. Zhang, "Time reversal with MISO for ultrawideband communications: experimental results," *IEEE Antennas and Wireless Propagation Letters*, vol. 5, no. 1, pp. 269–273, 2006.
- [21] R. C. Qiu, "A theory of time-reversed impulse Multiple-Input Multiple-Output (MIMO) for Ultra-Wideband (UWB) communications," in *Proceedings of the IEEE International Conference on Ultra-Wideband (ICUWB '06)*, pp. 587–592, September 2006.
- [22] P. Kyritsi, G. Papanicolaou, and C. Tsogka, "Optimally designed time reversal and zero forcing schemes," in *Proceedings of the International Symposium on Wireless Personal Multimedia Communications (WPMC '05)*, pp. 105–109, September 2005.
- [23] P. Kyritsi, P. Stoica, G. Papanicolaou, P. Eggers, and A. Oprea, "Time reversal and zero-forcing equalization for fixed wireless access channels," in *Proceedings of the 39th Asilomar Conference on Signals, Systems and Computers*, pp. 1297–1301, November 2005.
- [24] M. Weisenhorn and W. Hirt, "Performance of binary antipodal signaling over the indoor UWB MIMO channel," in *Proceedings of the International Conference on Communications (ICC '03)*, vol. 4, pp. 2872–2878, May 2003.
- [25] H. Nguyen, F. Zheng, and T. Kaiser, "Antenna selection for time reversal MIMO UWB systems," in *Proceedings of the 69th IEEE Vehicular Technology Conference (VTC '09)*, April 2009.
- [26] H. Nguyen, Z. Zhao, F. Zheng, and T. Kaiser, "On the MSI mitigation for MIMO UWB time reversal systems," in *Proceedings of the IEEE International Conference on Ultra-Wideband (ICUWB '09)*, pp. 295–299, September 2009.
- [27] T. K. Nguyen, H. Nguyen, F. Zheng, and T. Kaiser, "Spatial correlation in SM-MIMO-UWB systems using a pre-equalizer and pre-Rake filter," in *Proceedings of the IEEE International Conference on Ultra-Wideband (ICUWB '10)*, pp. 540–543, September 2010.

- [28] J. Foerster, "Channel modeling sub-committee report final," IEEE, Document IEEE P802.15-02/490r1-SG3a, 2003, http://www.ieee802.org/15/pub/2003/Mar03/02490r1P802-15_SG3a-Channel-Modeling-Subcommittee-Report-Final.zip.
- [29] W. Q. Malik, "Spatial correlation in ultrawideband channels," *IEEE Transactions on Wireless Communications*, vol. 7, no. 2, pp. 604–610, 2008.
- [30] T. Kaiser, F. Zheng, and E. Dimitrov, "An overview of ultrawide-band systems with MIMO," *Proceedings of the IEEE*, vol. 97, no. 2, pp. 285–312, 2009.
- [31] A. Paulraj, R. Nabar, and D. Gore, *Introduction to Space-Time Wireless Communications*, Cambridge University Press, 2003.
- [32] S. L. Loyka, "Channel capacity of MIMO architecture using the exponential correlation matrix," *IEEE Communications Letters*, vol. 5, no. 9, pp. 369–371, 2001.
- [33] A. V. Zelst and J. Hammerschmidt, "A single coefficient spatial correlation model for Multiple-input Multiple-output radio channels," in *27th General Assembly of the International Union of Radio Science*, 2002.
- [34] H. Nguyen, Z. Zhao, F. Zheng, and T. Kaiser, "Preequalizer design for spatial multiplexing SIMO-UWB TR systems," *IEEE Transactions on Vehicular Technology*, vol. 59, no. 8, pp. 3798–3805, 2010.
- [35] R. M. Buehrer, A. Safaai-Jazi, W. Davis, and D. Sweeney, "Ultrawideband propagation measurements and modeling, final report," in *DARPA NETEX Program*, Virginia Tech, 2004.
- [36] I. Oppermann, M. Hmlinen, and J. Iinatti, *UWB Theory and Applications*, John Wiley & Sons, 2004.

Research Article

Correlation and Capacity Calculations with Reference Antennas in an Isotropic Environment

Thorkild B. Hansen

Consultant, Azimuth Systems, Inc., 35 Nagog Park, Acton, MA 01720, USA

Correspondence should be addressed to Thorkild B. Hansen, thorkild.hansen@att.net

Received 5 January 2012; Revised 10 March 2012; Accepted 21 March 2012

Academic Editor: Moray Rumney

Copyright © 2012 Thorkild B. Hansen. This is an open access article distributed under the Creative Commons Attribution License, which permits unrestricted use, distribution, and reproduction in any medium, provided the original work is properly cited.

A reverberation chamber is a convenient tool for over-the-air testing of MIMO devices in isotropic environments. Isotropy is typically achieved in the chamber through the use of a mode stirrer and a turntable on which the device under test (DUT) rides. The quality of the isotropic environment depends on the number of plane waves produced by the chamber and on their spatial distribution. This paper investigates how the required sampling rate for the DUT pattern is related to the plane-wave density threshold in the isotropic environment required to accurately compute antenna correlations. Once the plane-wave density is above the threshold, the antenna correlation obtained through isotropic experiments agrees with the antenna correlation obtained from the classical definition, as has been proven theoretically. This fact is verified for the good, nominal, and bad reference antennas produced by CTIA. MIMO channel capacity simulations are performed with a standard base station model and the DUT placed in a single-tap plane-wave reverberation chamber model. The capacity curves obtained with the good, nominal, and bad reference antennas are clearly distinguishable.

1. Introduction

The reverberation chamber [1] is a cost-efficient and convenient tool for creating an isotropic environment in which wireless devices can be tested. The field in a rectangular reverberation chamber can be described in terms of chamber modes that each can be expressed as a sum of eight plane waves [2, 3]. The chamber typically contains a mode stirrer and a turn table on which the device under test (DUT) rides. At any fixed turntable and stirrer position, the DUT sees a certain collection of plane waves. By rotating the stirrer and turntable, a new collection of plane waves illuminates the DUT (the turntable causes the DUT to see each plane wave from different angles). The isotropic test environment is thus achieved by rotating both the stirrer and turntable to illuminate the DUT with many different collections of plane waves. One can determine if a given reverberation chamber at a given frequency is isotropic by evaluating anisotropy coefficients obtained from three-axis dipole experiments [23, Annex J] and [4].

In the present paper we investigate the use of reverberation chambers for over-the-air testing of MIMO devices.

Both antenna correlation (a quantity that is critically important for MIMO system performance) and MIMO capacity will be simulated in a plane-wave reverberation chamber model [5–9]. The simulations will be performed with a pair of Hertzian dipoles and with good, nominal, and bad reference antennas [10]. The classical antenna correlation is compared to the isotropic antenna correlation, and it is verified numerically that the two are equivalent, as proven by De Doncker and Meys [11].

To ensure accurate and reliable over-the-air test results, the test system must produce an accurate test environment in the entire physical region that contains the DUT. For example, in conventional 2D anechoic tests, the number of antennas in the ring surrounding the DUT must be large enough to accurately reproduce the desired channel conditions in the region occupied by the DUT. Similarly, the reverberation chamber must be large enough to supply enough plane waves to achieve an isotropic environment in the region occupied by the DUT.

By expressing the DUT pattern in terms of a spherical expansion (with a recently derived formula for truncation limit), we determine how closely the DUT pattern must

be sampled to properly capture its variation. Using this sampling rate, we obtain rules that determine both the required number of antennas in the anechoic test and the required plane-wave density in the reverberation chamber test. As a byproduct of this investigation, we present accurate Fourier expansions of the DUT pattern that have been used in spherical near-field scanning for many years but appear to be relatively unknown in wireless communications.

The paper is organized as follows. Section 2 introduces the truncated spherical-wave expansion and derives the sampling theorems and Fourier expansions for the pattern of an arbitrary DUT. Section 3 deals with antenna correlations in both the reverberation chamber test and in a 2D anechoic chamber test. This section also relates the accuracy of simulated correlations to the sampling rate required for the pattern. In Section 4 we investigate the plane-wave distribution for realistic reverberation chambers by using the dyadic Green's function for the rectangular box. We further simulate antenna correlations and compute anisotropy coefficients. Section 5 presents MIMO channel capacity simulations using a standard base station model and the plane-wave reverberation chamber model. Section 6 presents conclusions. Throughout, we assume time-harmonic fields that have $e^{-i\omega t}$ time dependence with $\omega > 0$.

2. Plane-Wave Receiving Characteristic and Far-Field Pattern

In this section we introduce the plane-wave receiving characteristic and far-field pattern of an arbitrary DUT-mounted antenna. (The term “pattern” will be used to refer to both the plane-wave receiving characteristic and to the far-field antenna pattern). A spherical expansion determines the spatial sampling rate required to “capture” the pattern of the antenna and provides a Fourier series expansion useful for computing any quantity involving the pattern. The standard spherical coordinates (r, θ, ϕ) with unit vectors given by

$$\begin{aligned}\hat{\mathbf{r}}(\theta, \phi) &= \hat{\mathbf{x}} \cos \theta \sin \phi + \hat{\mathbf{y}} \sin \theta \sin \phi + \hat{\mathbf{z}} \cos \theta, \\ \hat{\boldsymbol{\theta}}(\theta, \phi) &= \hat{\mathbf{x}} \cos \theta \cos \phi + \hat{\mathbf{y}} \cos \theta \sin \phi - \hat{\mathbf{z}} \sin \theta, \\ \hat{\boldsymbol{\phi}}(\theta, \phi) &= -\hat{\mathbf{x}} \sin \phi + \hat{\mathbf{y}} \cos \phi\end{aligned}\quad (1)$$

will be used throughout. Here, the unit vectors for the rectangular coordinates (x, y, z) are $\hat{\mathbf{x}}$, $\hat{\mathbf{y}}$, and $\hat{\mathbf{z}}$. Note that $\hat{\mathbf{r}}(\theta, \phi)$ with $0 \leq \theta \leq \pi$ and $0 \leq \phi < 2\pi$ covers the unit sphere once. Figure 1 shows the spherical coordinates.

The DUT with a mounted antenna is shown in Figure 2 inside the minimum sphere with radius R_{\min} , defined such that the maximum value of the coordinate r for all points on the DUT equals R_{\min} . Note that R_{\min} depends not only on the size of the DUT but also on its location with respect to the coordinate system. For example, a Hertzian dipole located at \mathbf{r}_0 has $R_{\min} = |\mathbf{r}_0|$ despite the fact that its physical extent is vanishing. Also, even if the physical dimension of a DUT-mounted antenna is much smaller than the dimensions of the DUT (as in Figure 2), the antenna interacts with the DUT and therefore it is the entire DUT size that must be used when computing R_{\min} .

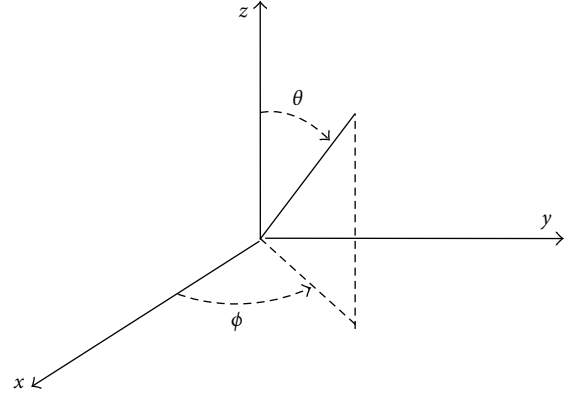


FIGURE 1: Spherical coordinates.

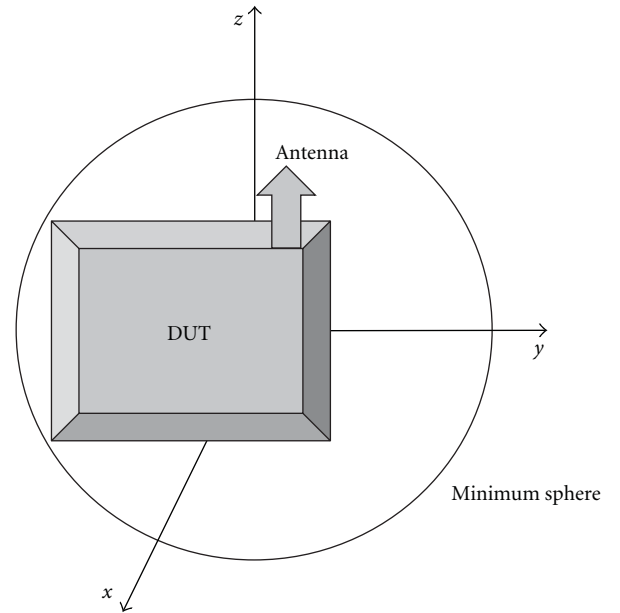


FIGURE 2: The DUT with mounted antenna contained in the minimum sphere of radius R_{\min} .

The plane-wave receiving characteristic is defined as follows. Assume that the incident plane wave $\mathbf{E}(\mathbf{r}) = \mathbf{E}_0 e^{i\mathbf{k}_0 \cdot \mathbf{r}}$ with propagation direction $\hat{\mathbf{k}}_0$ illuminates the DUT. The direction of propagation is $\hat{\mathbf{k}}_0 = -\hat{\mathbf{r}}(\theta_0, \phi_0)$, and the constant vector \mathbf{E}_0 satisfies $\mathbf{E}_0 \cdot \hat{\mathbf{k}}_0 = 0$. With this notation, the incident plane wave “comes” from the direction (θ_0, ϕ_0) . For example, if $\theta_0 = 0$, the plane wave is $\mathbf{E}(\mathbf{r}) = \mathbf{E}_0 e^{-ikz}$ and propagates in the direction of the negative z -axis. When the DUT is illuminated by this plane-wave field, its output is by definition $V = \mathcal{R}(\theta_0, \phi_0) \cdot \mathbf{E}_0$, where $\mathcal{R}(\theta_0, \phi_0)$ is the plane-wave receiving characteristic satisfying $\hat{\mathbf{k}}_0 \cdot \mathcal{R}(\theta_0, \phi_0) = 0$.

If the DUT-mounted antenna satisfies reciprocity, its plane-wave receiving characteristic can be expressed in terms of its normalized far-field pattern $\mathcal{F}_0(\theta, \phi)$ as [12, equation (6.60)] (The spherical angles determining the plane-wave

directions of propagation in [12] are different from those used in the present paper):

$$\mathcal{R}(\theta_0, \phi_0) = \sqrt{\frac{\epsilon}{\mu}} \frac{i}{kY_p} \mathcal{F}_0(\theta_0, \phi_0), \quad (2)$$

where μ and ϵ are the free-space permeability and permittivity, respectively. Moreover, $k = \omega\sqrt{\mu\epsilon}$ is the wavenumber and Y_p is the characteristic admittance of the propagating mode of a wave-guide feed assumed attached to the DUT antenna; see [12, Chapter 6]. In general, if the antenna is not reciprocal, the receiving characteristic can be related to the pattern of an adjoint antenna [13].

The electric far field of the DUT, when it is fed by an input voltage-amplitude V_0 , is [12, equation (6.35)] (The nonnormalized far-field pattern $\mathcal{F}(\theta, \phi)$ is defined in [12, equation (3.31)] in terms of the electric field through the limit $\mathcal{F}(\theta, \phi) = \lim_{r \rightarrow \infty} r e^{-ikr} \mathbf{E}(r, \theta, \phi)$. The normalized far-field pattern $\mathcal{F}_0(\theta, \phi)$ is in turn defined by $V_0 \mathcal{F}_0(\theta, \phi) = \mathcal{F}(\theta, \phi)$, where V_0 is the input voltage amplitude of the signal that feeds the antenna. Note that the symbol “ \sim ” in (3) means “asymptotically equal to” in the limit $r \rightarrow \infty$.)

$$\mathbf{E}(r, \theta, \phi) \sim V_0 \mathcal{F}_0(\theta, \phi) \frac{e^{ikr}}{r}. \quad (3)$$

The far-field pattern $\mathcal{F}(\theta_0, \phi_0)$ determines the far field in the direction (θ_0, ϕ_0) whereas $\mathcal{R}(\theta_0, \phi_0)$ determines the output due to a plane wave “coming in” from the direction (θ_0, ϕ_0) . Hence, this incident plane wave propagates in the direction $(\pi - \theta_0, \pi + \phi_0)$. Also, the normalized far-field pattern $\mathcal{F}_0(\theta, \phi)$ is dimensionless and the plane-wave receiving characteristic $\mathcal{R}(\theta, \phi)$ is a length.

These statements fully define the plane-wave receiving characteristic for any propagating plane wave that may illuminate the DUT. If the source of the incident field is close to the DUT, one must also specify the plane-wave receiving characteristic for evanescent plane waves [12, Chapters 3 and 6]. However, in this paper we consider only sources that are at least a few wavelengths away from the DUT so that evanescent waves are negligible.

Using (2) in conjunction with standard spherical-wave theory [14, 15] shows that the receiving characteristic can be expressed in terms of the transverse vector-wave functions \mathbf{M}_{nm} and \mathbf{N}_{nm} as

$$\mathcal{R}(\theta, \phi) = \sum_{n=1}^N \sum_{m=-n}^n [A_{nm} \mathbf{M}_{nm}(\theta, \phi) + B_{nm} \mathbf{N}_{nm}(\theta, \phi)], \quad (4)$$

where A_{nm} and B_{nm} are spherical expansion coefficients satisfying $A_{nm} = 0$ and $B_{nm} = 0$ when $|m| > n$. The truncation number N is determined from the radius of the minimum sphere as

$$N = \text{int}(kR_{\min} + \gamma(kR_{\min})^{1/3}), \quad (5)$$

where the constant γ determines the number of digits of accuracy achieved [16, Section 3.4.2] and “int” denotes the

integral part. The formula (5) is especially useful for small sources where the second term is on the same order of magnitude as the first term. (In older literature the following truncation formula is often used with the second term left unspecified: “ $N = \text{int}(kR_{\min} + n_1)$ where n_1 is a small integer.”)

The transverse vector-wave functions can be expressed in terms of the spherical harmonic $Y_{nm}(\theta, \phi)$ [15, page 99] as [15, pages 742–746]

$$\mathbf{M}_{nm}(\theta, \phi) = \hat{\theta} \frac{imY_{nm}(\theta, \phi)}{\sqrt{n(n+1)} \sin \theta} - \hat{\phi} \frac{(\partial/\partial\theta)Y_{nm}(\theta, \phi)}{\sqrt{n(n+1)}}, \quad (6)$$

and $\mathbf{N}_{nm}(\theta, \phi) = \hat{\mathbf{r}} \times \mathbf{M}_{nm}(\theta, \phi)$. The orthogonality relations [15] for the transverse vector-wave functions give the following well-known expressions for the spherical expansion coefficients A_{nm} and B_{nm} :

$$\begin{aligned} A_{nm} &= \int_0^{2\pi} \int_0^\pi \mathcal{R}(\theta, \phi) \cdot \mathbf{M}_{nm}^*(\theta, \phi) \sin \theta \, d\theta \, d\phi, \\ B_{nm} &= \int_0^{2\pi} \int_0^\pi \mathcal{R}(\theta, \phi) \cdot \mathbf{N}_{nm}^*(\theta, \phi) \sin \theta \, d\theta \, d\phi, \end{aligned} \quad (7)$$

where $*$ indicates complex conjugation. The formula (4) makes it possible to compute the plane-wave receiving characteristic in any direction from the spherical expansion coefficients A_{nm} and B_{nm} . However, in this paper we shall use (4) to derive Fourier expansions and sampling theorems that are useful for computing quantities like correlations that involve the plane-wave receiving characteristic.

The expressions for the transverse vector-wave functions $\mathbf{M}_{nm}(\theta, \phi)$ and $\mathbf{N}_{nm}(\theta, \phi)$ show that the θ and ϕ components of $\mathcal{R}(\theta, \phi) = \mathcal{R}_\theta(\theta, \phi)\hat{\theta} + \mathcal{R}_\phi(\theta, \phi)\hat{\phi}$ in (4) have the Fourier series (The expressions [15, page 98] for the associated Legendre function show that both the derivative $(\partial/\partial\theta)Y_{nm}(\theta, \phi)$ and the fraction $mY_{nm}(\theta, \phi)/\sin \theta$ can be expanded in terms of $e^{im\phi}e^{iq\theta}$ with $q = -n, \dots, n$):

$$\begin{aligned} \mathcal{R}_\theta(\theta, \phi) &= \sum_{q=-N}^N \sum_{m=-N}^N \mathcal{D}_{qm}^\theta e^{im\phi} e^{iq\theta}, \\ \mathcal{R}_\phi(\theta, \phi) &= \sum_{q=-N}^N \sum_{m=-N}^N \mathcal{D}_{qm}^\phi e^{im\phi} e^{iq\theta}, \end{aligned} \quad (8)$$

where \mathcal{D}_{qm}^θ and \mathcal{D}_{qm}^ϕ are Fourier coefficients. The Fourier expansions (8) define functions that are 2π -periodic in both θ and ϕ . Hence, the Fourier coefficients cannot be determined from the sampling theorem for periodic spatially bandlimited functions when $\mathcal{R}(\theta, \phi)$ is known only over the standard sphere $0 \leq \theta \leq \pi$, $0 \leq \phi \leq 2\pi$. We shall overcome this problem by continuing $\mathcal{R}(\theta, \phi)$ to the interval $0 \leq \theta \leq 2\pi$ (see [17, 18], and [19, pages 111–113, 140–144]).

Since $\hat{\mathbf{r}}(\theta, \phi) = \hat{\mathbf{r}}(2\pi - \theta, \phi + \pi)$, the two points (θ, ϕ) and $(2\pi - \theta, \phi + \pi)$ correspond to the same point in space. Moreover, since the tangential spherical unit vectors satisfy $\hat{\theta}(\theta, \phi) = -\hat{\theta}(2\pi - \theta, \phi + \pi)$ and $\hat{\phi}(\theta, \phi) = -\hat{\phi}(2\pi - \theta, \phi + \pi)$,

we can analytically continue $\mathcal{R}(\theta, \phi)$ into a 2π -periodic in both θ and ϕ by use of

$$\begin{aligned}\mathcal{R}_\theta(\theta, \phi) &= -\mathcal{R}_\theta(2\pi - \theta, \phi + \pi), \\ \mathcal{R}_\phi(\theta, \phi) &= -\mathcal{R}_\phi(2\pi - \theta, \phi + \pi).\end{aligned}\quad (9)$$

One can show that the conditions (9) imply that the Fourier coefficients satisfy $\mathcal{D}_{qm}^\theta = (-1)^{m+1} \mathcal{D}_{-q,m}^\theta$ and $\mathcal{D}_{qm}^\phi = (-1)^{m+1} \mathcal{D}_{-q,m}^\phi$.

Assume that $\mathcal{R}_\theta(\theta, \phi)$ and $\mathcal{R}_\phi(\theta, \phi)$ are known over the standard sphere $0 \leq \theta \leq \pi$, $0 \leq \phi \leq 2\pi$ at $\theta = (t-1)\Delta\theta$, $t = 1, \dots, N_\theta$ and $\phi = (p-1)\Delta\phi$, $p = 1, \dots, N_\phi$, where the sample rates are $\Delta\theta = \pi/(N_\theta-1)$ and $\Delta\phi = 2\pi/N_\phi$, with $N_\theta \geq N+2$ and $N_\phi \geq 2N+1$. Then the Fourier coefficients can be computed from the sampling theorem for periodic spatially bandlimited functions in conjunction with (9) as [19] and [20, Section IV]:

$$\begin{aligned}\mathcal{D}_{qm}^\theta &= \frac{1}{N_\phi(2N_\theta-2)} \sum_{p=1}^{N_\phi} e^{-im(p-1)\Delta\phi} \\ &\quad \times \left[\sum_{t=1}^{N_\theta} \mathcal{R}_\theta([t-1]\Delta\theta, [p-1]\Delta\phi) e^{-iq(t-1)\Delta\theta} \right. \\ &\quad \left. + (-1)^{m+1} \sum_{t=2}^{N_\theta-1} \mathcal{R}_\theta([t-1]\Delta\theta, [p-1]\Delta\phi) e^{iq(t-1)\Delta\theta} \right], \\ \mathcal{D}_{qm}^\phi &= \frac{1}{N_\phi(2N_\theta-2)} \sum_{p=1}^{N_\phi} e^{-im(p-1)\Delta\phi} \\ &\quad \times \left[\sum_{t=1}^{N_\theta} \mathcal{R}_\phi([t-1]\Delta\theta, [p-1]\Delta\phi) e^{-iq(t-1)\Delta\theta} \right. \\ &\quad \left. + (-1)^{m+1} \sum_{t=2}^{N_\theta-1} \mathcal{R}_\phi([t-1]\Delta\theta, [p-1]\Delta\phi) e^{iq(t-1)\Delta\theta} \right].\end{aligned}\quad (10)$$

Of course, (10) hold only for functions that satisfy (9). We summarize the results (which also hold for the antenna pattern $\mathcal{F}_0(\theta, \phi)$) as follows.

- (i) The plane-wave receiving characteristic $\mathcal{R}(\theta, \phi)$ should be sampled over the sphere $0 \leq \theta \leq \pi$ and $0 \leq \phi < 2\pi$ at a rate of at least $\Delta\theta = \Delta\phi = \pi/(N+1)$, where N , given by (5), depends on frequency, physical DUT size, and DUT location.
- (ii) The plane-wave receiving characteristic $\mathcal{R}(\theta, \phi)$ can be expressed in terms of the Fourier series (8) with Fourier coefficients computed through (10) from sampled values of $\mathcal{R}(\theta, \phi)$.
- (iii) Integrals of the form

$$I = \int_0^{2\pi} \int_0^\pi \mathbf{U}(\theta, \phi) \cdot \mathcal{R}(\theta, \phi) \sin \theta \, d\theta \, d\phi, \quad (11)$$

where $\mathbf{U}(\theta, \phi)$ is a known function, occur in many places. For example, the expressions (7) for the spherical expansion coefficients have this form. Such

integrals can be computed accurately by inserting the Fourier expansions (8) for $\mathcal{R}(\theta, \phi)$. One can often compute the contribution from each Fourier term explicitly. Alternatively, by use of the Fourier series one can resample $\mathcal{R}(\theta, \phi)$ to a finer grid and then compute I through numerical integration.

- (iv) In contrast, brute-force approximations of the form (with the original sampling rate retained)

$$\begin{aligned}I &\simeq \sum_{t=1}^{N_\theta} \sum_{p=1}^{N_\phi} \mathbf{U}([t-1]\Delta\theta, [p-1]\Delta\phi) \\ &\quad \times \mathcal{R}([t-1]\Delta\theta, [p-1]\Delta\phi) \\ &\quad \times \sin([t-1]\Delta\theta)\Delta\theta\Delta\phi\end{aligned}\quad (12)$$

are often inaccurate, especially when the sampling is sparse (the antenna is electrically small). The lack of accuracy is caused by the fact that the integral over θ does not involve a periodic spatially bandlimited function, so the trapezoidal rule is not guaranteed to work well [19, pages 111–113, 140–144, 372].

3. Antenna Correlation in Isotropic Environment

In this section we describe the concept of antenna correlation in an isotropic environment like the one observed in a reverberation chamber. However, first we state the classical definition of antenna correlation in terms of the plane-wave receiving characteristics introduced in Section 2.

Consider two receiving antennas, possibly mounted on the same DUT, with plane-wave receiving characteristics $\mathcal{R}_1(\theta, \phi)$ and $\mathcal{R}_2(\theta, \phi)$. The classical definition of the correlation ρ between the two receiving antennas is

$$\rho = \frac{\int_0^{2\pi} \int_0^\pi \mathcal{R}_1(\theta, \phi) \cdot \mathcal{R}_2^*(\theta, \phi) \sin \theta \, d\theta \, d\phi}{\sqrt{\int_0^{2\pi} \int_0^\pi |\mathcal{R}_1(\theta, \phi)|^2 \sin \theta \, d\theta \, d\phi} \sqrt{\int_0^{2\pi} \int_0^\pi |\mathcal{R}_2(\theta, \phi)|^2 \sin \theta \, d\theta \, d\phi}}.\quad (13)$$

In accordance with Section 2, the correlation (13) can be computed by inserting Fourier series expansions for $\mathcal{R}_1(\theta, \phi)$ and $\mathcal{R}_2(\theta, \phi)$ with Fourier coefficients obtained from sampled values.

A general specification of the isotropic environment can be found in Hill's book [1, Section 7.1] and in the paper by De Doncker and Meys [11]. Here we consider a specific embodiment [5–9] involving plane waves propagating in a set of fixed directions. The points (θ_s, ϕ_s) , $s = 1, 2, \dots, S$, are roughly evenly distributed on the unit sphere as shown in Figure 3. More specifically, the points are on constant- θ rings with the number of points on each ring dependent on θ . In particular, the top and bottom rings $\theta = 0$ and $\theta = \pi$ consist of just one point each.

Assume that two plane waves are incoming in each of the directions (θ_s, ϕ_s) . One of them is θ -polarized with amplitude

$\alpha_s^{(j)}$; the other is ϕ -polarized with amplitude $\beta_s^{(j)}$, where $j = 1, 2, \dots, J$. For a particular j , the incident field is thus given by

$$\mathbf{E}^{(j)}(\mathbf{r}) = \sum_{s=1}^S \left[\alpha_s^{(j)} \hat{\boldsymbol{\theta}}_s e^{-ik\hat{\mathbf{r}}_s \cdot \mathbf{r}} + \beta_s^{(j)} \hat{\boldsymbol{\phi}}_s e^{-ik\hat{\mathbf{r}}_s \cdot \mathbf{r}} \right], \quad (14)$$

where $\hat{\mathbf{r}}_s$, $\hat{\boldsymbol{\theta}}_s$, and $\hat{\boldsymbol{\phi}}_s$ are the spherical unit vectors evaluated at $(\theta, \phi) = (\theta_s, \phi_s)$. The plane-wave amplitudes $\alpha_s^{(j)}$ and $\beta_s^{(j)}$ are uniformly distributed independent complex random variables with zero mean, and the corresponding outputs of the two receiving antennas are

$$\begin{aligned} V_1^{(j)} &= \sum_{s=1}^S \left[\alpha_s^{(j)} \hat{\boldsymbol{\theta}}_s \cdot \mathcal{R}_1(\theta_s, \phi_s) + \beta_s^{(j)} \hat{\boldsymbol{\phi}}_s \cdot \mathcal{R}_1(\theta_s, \phi_s) \right], \\ V_2^{(j)} &= \sum_{s=1}^S \left[\alpha_s^{(j)} \hat{\boldsymbol{\theta}}_s \cdot \mathcal{R}_2(\theta_s, \phi_s) + \beta_s^{(j)} \hat{\boldsymbol{\phi}}_s \cdot \mathcal{R}_2(\theta_s, \phi_s) \right]. \end{aligned} \quad (15)$$

The isotropic environment is obtained as the collection of incident fields $\mathbf{E}^{(j)}(\mathbf{r})$ for $j = 1, 2, \dots, J$, with a new set of amplitudes $\alpha_s^{(j)}$ and $\beta_s^{(j)}$ selected for each j . Thus, we can compute the outputs $V_1^{(j)}$ and $V_2^{(j)}$ for each of the two receiving antennas for $j = 1, 2, \dots, J$. Section 5 presents MIMO capacity simulations with a receiving DUT placed in this isotropic environment.

It was shown by De Doncker and Meys [11] that the correlation between the outputs V_1 and V_2 in the isotropic environment is equal to the classical correlation (13):

$$\rho = \text{corr}(V_1, V_2). \quad (16)$$

We shall now demonstrate through numerical simulations that this result is indeed correct and investigate the sampling rate (density of incident plane waves) required in the isotropic environment to make (16) accurate.

3.1. Two Hertzian Dipoles. Consider two z -directed Hertzian dipoles on the x -axis at $\mathbf{r}_1 = (-d/2, 0, 0)$ and $\mathbf{r}_2 = (d/2, 0, 0)$ so that the radius of the minimum sphere is $R_{\min} = d/2$; see Figure 4. The output of a Hertzian dipole is proportional to the incident electric field in the direction of the dipole. Hence,

$$\begin{aligned} \mathcal{R}_1(\theta, \phi) &= L \hat{\boldsymbol{\theta}} \sin \theta e^{ik(d/2) \cos \phi \sin \theta}, \\ \mathcal{R}_2(\theta, \phi) &= L \hat{\boldsymbol{\theta}} \sin \theta e^{-ik(d/2) \cos \phi \sin \theta}, \end{aligned} \quad (17)$$

where L is a constant length. The correlation between the dipoles is found from (13) to be

$$\rho(d) = \frac{3}{2} \left[\frac{\sin(kd)}{kd} - \frac{1}{(kd)^2} \left(\frac{\sin(kd)}{kd} - \cos(kd) \right) \right]. \quad (18)$$

Hill [1, equation (7.63)] confirms the general result (16) that the classical correlation (18) is the correlation obtained in an isotropic environment.

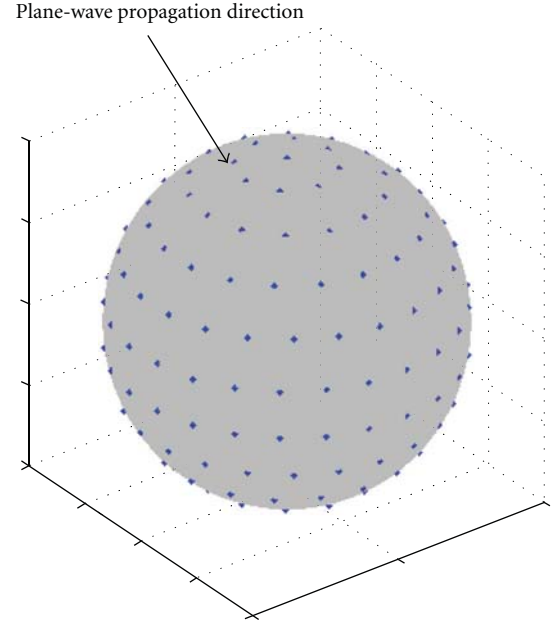


FIGURE 3: A selection of points (θ_s, ϕ_s) , $s = 1, 2, \dots, S$, evenly distributed on the unit sphere. Each point defines a direction of propagation for two plane waves. One plane wave is θ -polarized, the other is ϕ -polarized.

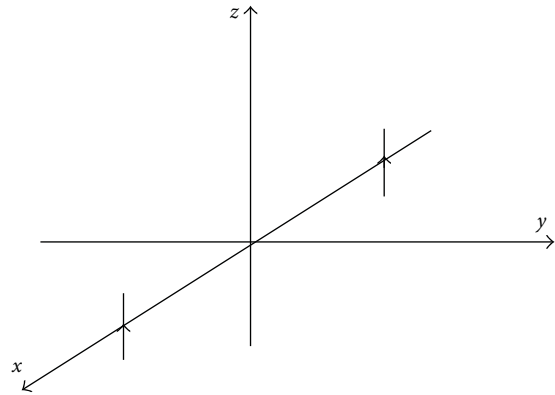


FIGURE 4: Two z -directed Hertzian dipoles on the x -axis at $\mathbf{r}_1 = (-d/2, 0, 0)$ and $\mathbf{r}_2 = (d/2, 0, 0)$.

We compute the correlation from (16) for $d = \lambda/2$ and $d = 2\lambda$ with varying S . Throughout, $J = 10000$. As a measure of the density of incident plane waves, we use the ‘‘isotropic’’ spacing Δ_i between constant- θ rings on the unit sphere. Specifically, if there are \mathcal{N} constant- θ rings (including the two at $\theta = 0$ and $\theta = \pi$), we have $\Delta_i = \pi/(\mathcal{N} - 1)$.

Unlike the points (θ_i, ϕ_i) with $\Delta\theta$ and $\Delta\phi$ spacing used in computing the Fourier coefficients in Section 2, the points (θ_s, ϕ_s) do not lie on a rectangular grid. Hence, the number of plane-wave directions of incidence in the isotropic environment (denoted by S) is smaller than the number of grid points used to compute the Fourier coefficients in Section 2, even if $\Delta_i = \Delta\theta$.

TABLE 1: Correlations computed from the classical formula (13) and from the isotropic simulation formula (16) with 180 plane-wave directions of propagation. The data is collected at 751 MHz.

	Good antenna	Nominal antenna	Bad antenna
Classical formula (13)	$-0.0381 + 0.0009i$	$-0.5749 - 0.0054i$	$-0.9042 + 0.0172i$
Isotropic simulation formula (16)	$-0.0367 - 0.0020i$	$-0.5740 - 0.0040i$	$-0.9066 + 0.0130i$

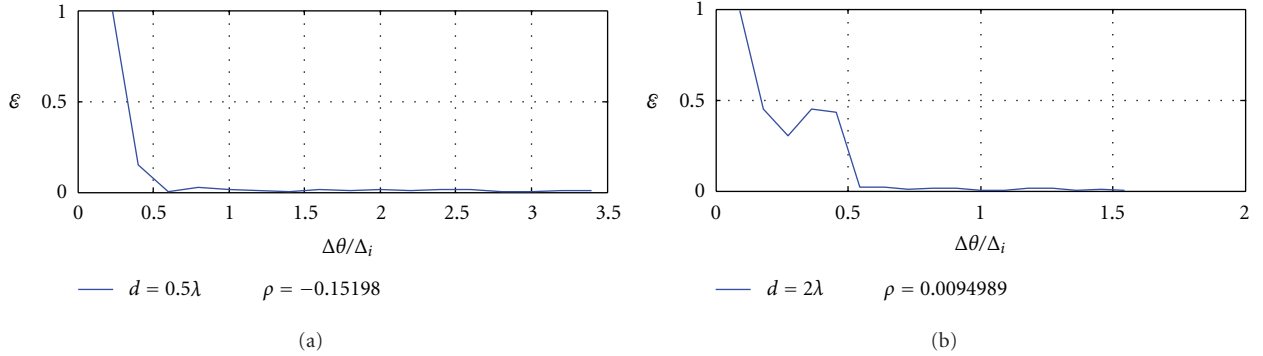


FIGURE 5: The error \mathcal{E} in (19) as a function of $\Delta\theta/\Delta_i$ where $\Delta\theta = \pi/(N+1)$. N is computed from (5) with $\gamma = 2$. Large values of $\Delta\theta/\Delta_i$ correspond to dense plane-wave distributions in the isotropic environment.

Figure 5 shows the error:

$$\mathcal{E} = |\rho(d) - \text{corr}(V_1, V_2)|, \quad (19)$$

where $\rho(d)$ is the exact correlation (18) and $\text{corr}(V_1, V_2)$ is the correlation obtained from the isotropic environment, as a function of $\Delta\theta/\Delta_i$. We set $\gamma = 2$ in the computation of N in (5) and use $\Delta\theta = \pi/(N+1)$.

For both $d = \lambda/2$ and $d = 2\lambda$, the error becomes negligible when the ratio $\Delta\theta/\Delta_i$ is about 0.7. In other words, accurate correlations are obtained when the isotropic sampling distance Δ_i is about 1.4 times the sampling distance $\Delta\theta$ required to compute the Fourier coefficients in Section 2 with ($\gamma = 2$). It is not surprising that accurate correlations are obtained in the isotropic environment when $\Delta_i > \Delta\theta$ since the correlation (13) is an ‘‘average-over-an-entire-sphere’’ quantity whereas the expression for $\Delta\theta$ is derived to achieve the more demanding ‘‘point-by-point’’ accuracy.

To accurately reproduce the isotropic field conditions in a reverberation chamber, one must choose a chamber size large enough to ensure enough plane-wave directions of incidence for a given DUT size. We also note that these numerical simulations validate the general theorem by De Doncker and Meys [11].

Before leaving this section we investigate the sampling required for a 2D configuration where the correlation is based on incident fields from a small region of the unit sphere. This type of model will be used in Section 5 to simulate a transmitting base station that broadcasts according to a Laplacian distribution.

The two z -directed Hertzian dipoles are still on the x -axis at $\mathbf{r}_1 = (-d/2, 0, 0)$ and $\mathbf{r}_2 = (d/2, 0, 0)$ as shown in Figure 6. The dipoles are now illuminated by a collection of plane waves that all propagate in the x - y plane. 180 directions of incidence are selected according to the approximate Laplacian distribution [21, equation (18)] with $\sigma_\theta = 35^\circ$

centered on $\phi = 90^\circ$, as indicated in Figure 6. At any instant, each of the 180 plane waves is multiplied by a random phase to create a particular incident field. We achieve 10000 different incident fields by applying 10000 independent sets of random phases. The outputs $V_1^{(j)}$ and $V_2^{(j)}$ are thus obtained for $j = 1, 2, \dots, 10000$, and the exact correlation in this experiment is $\text{corr}(V_1, V_2)$.

We also compute an approximate correlation based on a fixed set of equally spaced directions of incidence illustrated by the ring in Figure 6. The angular spacing between two directions of incidence on this ring is Δ_r . We simply replace the directions of incidence from the Laplacian distribution by the closest direction of incidence on this ring. The sampling theorem derived in Section 2 states that the angular spacing between these directions of incidence should be $\Delta\phi = \pi/(N+1)$ with N computed from (5).

Figure 7 shows the error of the approximate correlation as a function of the ratio $\Delta\phi/\Delta_r$. We see that the error in this case with a limited range of directions of incidence only vanishes when Δ_r is roughly equal to the spacing $\Delta\phi$ required by the sampling theorem. Hence, to accurately reproduce the model-specified field conditions in an anechoic-chamber tests system consisting of a ring of antennas, one must supply enough antennas to satisfy the sampling theorem.

3.2. CTIA Reference Antennas. To expedite the baseline between laboratories participants of CTIA LTE round robin, a set of MIMO 2×2 reference antennas has been developed [10]. A subset of these antennas has dimension $240 \times 80 \times 1$ mm and operate at 751 MHz corresponding to $R_{\min} = 0.12$ m and $kR_{\min} = 1.89$. Hence, (5) gives $N = 4$ when $\gamma = 2$, and the required sampling is therefore $\Delta\theta = \Delta\phi = 36^\circ$.

We compute the isotropic correlation with 180 plane-wave directions of propagation corresponding to an isotropic sampling of $\Delta_i = 16.3^\circ$. Table 1 shows the resulting

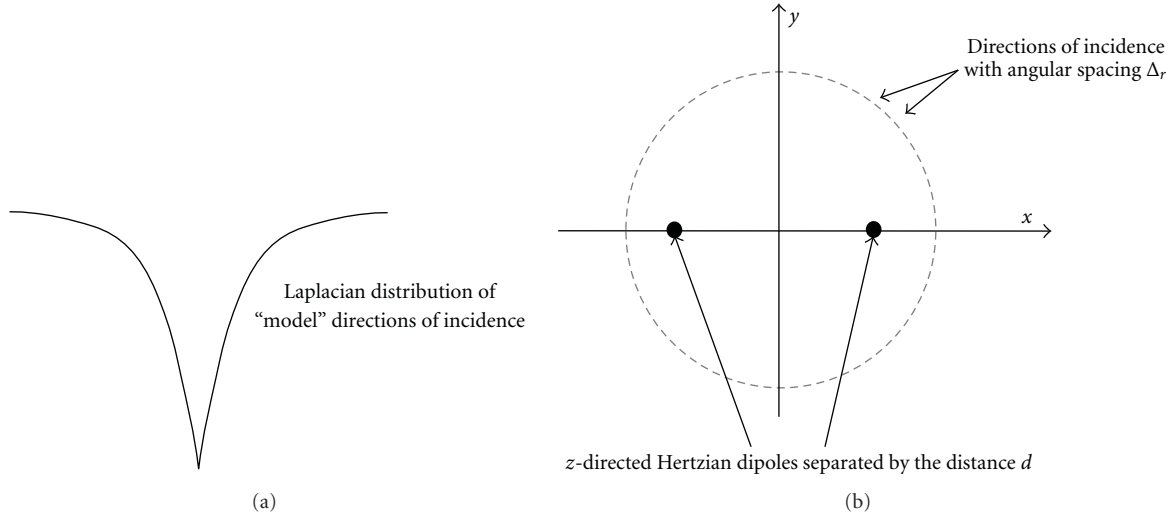


FIGURE 6: Two z -directed Hertzian dipoles on the x -axis at $\mathbf{r}_1 = (-d/2, 0, 0)$ and $\mathbf{r}_2 = (d/2, 0, 0)$ with surrounding plane-wave directions of propagation and Laplacian distribution. All directions of incidence are in the x - y plane.

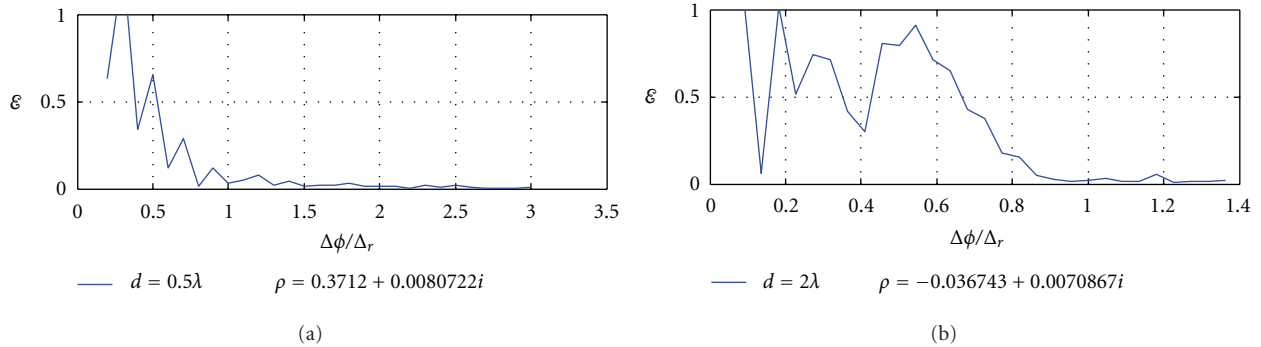


FIGURE 7: The error ε as a function of $\Delta\phi/\Delta_r$, where $\Delta\phi = \pi/(N + 1)$. N is computed from (5) with $\gamma = 2$. Large values of $\Delta\phi/\Delta_r$ correspond to dense plane-wave distributions along in the ring in Figure 6.

correlations for three antennas: (i) good antenna with low correlation, (ii) nominal antenna with average correlation, and (iii) bad antenna with high correlation. The table validates the general theorem by De Doncker and Meys [11] in (16).

These results have also been verified experimentally in a reverberation chamber at NIST [5–9].

4. Isotropic Environment of a Rectangular Reverberation Chamber

A reverberation chamber provides a rich scattering environment that is ideal for over-the-air testing of wireless devices. The chamber typically contains a number of wall-mounted transmitting antennas, a mechanical mode stirrer, and a turntable on which the DUT is placed; see Figure 8. The turntable provides so-called platform stirring [22]. As we shall see, at any given position of stirrer and turntable, the DUT is illuminated by a large number of plane waves whose directions of propagation are determined by the modes of the chamber [1, 2]. We assume that the chamber is excited by a Hertzian dipole with frequency f (as usual $\omega = 2\pi f$).

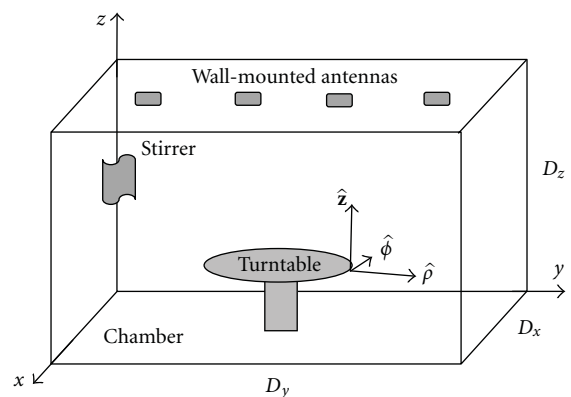


FIGURE 8: Rectangular reverberation chamber with dimensions D_x , D_y , and D_z . The chamber contains four wall-mounted transmitting antennas, a mechanical stirrer, and a turntable. The DUT position is near the edge of the turntable.

4.1. Modes in Terms of Plane Waves. Let the rectangular chamber have the dimensions D_x , D_y , and D_z as shown in Figure 8. The dyadic Green’s function (field due to a Hertzian

dipole source) can be expressed as a superposition of modes determined such that the tangential electric field vanishes on the chamber walls [3, pages 383-384]. Specifically, each rectangular field component can be expressed as a sum of terms of the form (we use the z component for illustration purposes; the x and y components have similar expressions):

$$\begin{aligned} E_z(x, y, z, x', y', z', n_x, n_y, n_z) \\ = E_0(x', y', z', n_x, n_y, n_z) \\ \times \sin\left(\frac{n_x \pi x}{D_x}\right) \sin\left(\frac{n_y \pi y}{D_y}\right) \cos\left(\frac{n_z \pi z}{D_z}\right), \end{aligned} \quad (20)$$

where $E_0(x', y', z', n_x, n_y, n_z)$ is independent of the observation point (x, y, z) but dependent on the source location (x', y', z') , the source strength, and the mode indices n_x , n_y , and n_z , which can take on any nonnegative value.

There is one additional term (called an irrotational mode) that goes with the mode in (20) to ensure that the field satisfies the wave equation with wave number that corresponds to the medium in the chamber. The irrotational mode has an identical plane-wave representation, so analyzing (20) is sufficient. Also, the sum over n_z can be performed in closed form to obtain a formula that involves just a double sum [3, page 384] and [1, page 34]. As usual, all losses (including wall losses) are accounted for by an effective lossy medium [3, page 389] and [1, page 35].

We associate a frequency f_{n_x, n_y, n_z} and a propagation constant k_{n_x, n_y, n_z} with each mode:

$$f_{n_x, n_y, n_z} = \frac{c}{2} \sqrt{\left(\frac{n_x}{D_x}\right)^2 + \left(\frac{n_y}{D_y}\right)^2 + \left(\frac{n_z}{D_z}\right)^2}, \quad (21)$$

$$\begin{aligned} k_{n_x, n_y, n_z} &= \sqrt{\left(\frac{n_x \pi}{D_x}\right)^2 + \left(\frac{n_y \pi}{D_y}\right)^2 + \left(\frac{n_z \pi}{D_z}\right)^2} \\ &= \sqrt{k_x^2 + k_y^2 + k_z^2}, \end{aligned} \quad (22)$$

where $k_x = n_x \pi / D_x$, $k_y = n_y \pi / D_y$, and $k_z = n_z \pi / D_z$. Note that $\sin(x) = (e^{ix} - e^{-ix}) / (2i)$ and $\cos(x) = (e^{ix} + e^{-ix}) / 2$ to convert (20) to

$$\begin{aligned} E_z(x, y, z, x', y', z', n_x, n_y, n_z) \\ = - \frac{E_0(x', y', z', n_x, n_y, n_z)}{8} \\ \times \left[e^{i(k_x x + k_y y + k_z z)} + 7 \text{ more terms} \right], \end{aligned} \quad (23)$$

where “7 more terms” indicate that the square bracket contains seven additional terms of the form $e^{i(\pm k_x x \pm k_y y \pm k_z z)}$. Hence, each mode can be expressed as the sum of eight plane waves with propagation vectors $\pm k_x \hat{\mathbf{x}} \pm k_y \hat{\mathbf{y}} \pm k_z \hat{\mathbf{z}}$. The excitation factor can be written as

$$E_0(x', y', z', n_x, n_y, n_z) = \frac{F_0(x', y', z', n_x, n_y, n_z)}{(1 - 2i/Q) f_{n_x, n_y, n_z}^2 - f^2}, \quad (24)$$

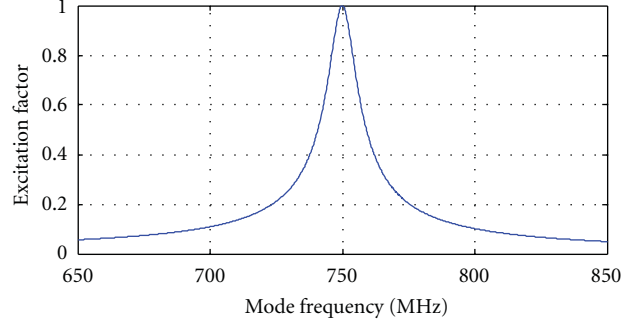


FIGURE 9: Normalized magnitude of the excitation factor as function of mode frequency for a 750 MHz driving signal and a 30 ns RMS delay. Only modes in a “3 dB” region near the peak get effectively excited.

where $F_0(x', y', z', n_x, n_y, n_z)$ is independent of frequency f and Q is the quality factor that accounts for wall and other losses in the chamber. Q is related to the RMS power delay time τ through $\tau = Q/\omega$. The 8 directions of incidence for a single mode are

$$\hat{\mathbf{k}}^i = \frac{\pm \hat{\mathbf{x}}(n_x/D_x) \pm \hat{\mathbf{y}}(n_y/D_y) \pm \hat{\mathbf{z}}(n_z/D_z)}{\sqrt{(n_x/D_x)^2 + (n_y/D_y)^2 + (n_z/D_z)^2}}, \quad (25)$$

with the corresponding mode frequency given by (21).

The magnitude of the excitation factor $1/[(1 - 2i/Q) f_{n_x, n_y, n_z}^2 - f^2]$ (normalized) as a function of mode frequency f_{n_x, n_y, n_z} for a 750 MHz driving signal and a 30 ns RMS delay is shown in Figure 9. We see that this factor has a peak at the driving frequency and that it falls off fairly slowly away from this frequency. For a chamber to work well, it must support a significant number of plane waves, which translates into the requirement that there must be a significant number of modes in the region where the excitation factor is significantly nonzero. One typically sets the threshold point where modes are considered “unexcitable” at the point where the excitation factor has fallen 3 dB. Notice that the width of the excitation factor depends on the quality factor. One of the benefits of using multiple wall-mounted transmitting antennas is that all excitable modes do actually get excited.

Let us now show the actual plane-wave directions of incidence for two reverberation chambers with 30 ns RMS delay that are driven by a 750 MHz source. One is electrically large ($D_x = 3$ m, $D_y = 2$ m, and $D_z = 1.5$ m) at 750 MHz; the other is electrically small ($D_x = 1$ m, $D_y = 0.9$ m, and $D_z = 0.8$ m) at 750 MHz. We include modes that lie in a 50 MHz band around 750 MHz. Figure 10(a) shows the plane-wave directions of incidence for the large chamber. The directions of incidence are nonuniformly distributed over the unit sphere with a maximum distance between points of 22° and an average distance of 6° . The largest gaps occur near the north and south poles.

As the stirrer in the reverberation chamber rotates, the amplitudes and phases of the plane waves change to produce an isotropic environment as discussed in the previous

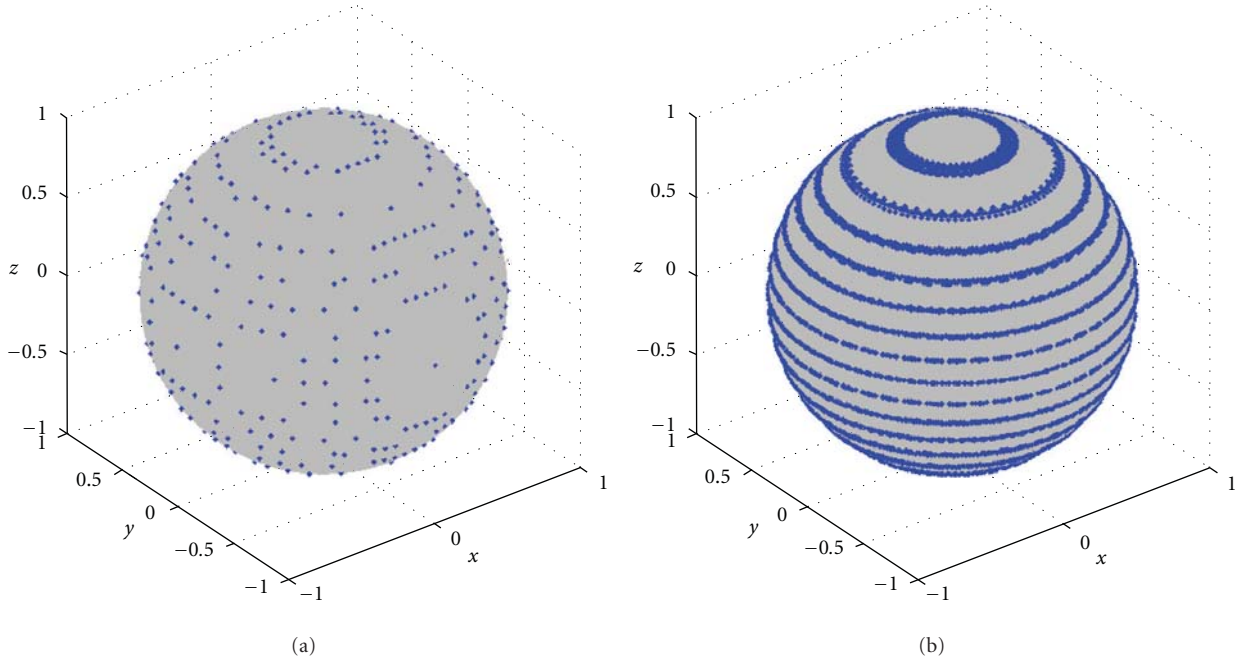


FIGURE 10: Plane-wave directions of incidence for modes in a 50 MHz band around 750 MHz in a large chamber with dimensions $D_x = 3$ m, $D_y = 2$ m, and $D_z = 1.5$ m. (a) Without turntable. (b) With turntable rotating around a z -directed axis. Without the turntable, the maximum distance between directions of incidence is 22° and the average distance is 6° .

section. In addition to the stirrer, the chamber contains a turntable on which the DUT rides. As the turntable rotates, the DUT sees the plane waves from different angles, effectively creating additional directions of incidence. Figure 10(b) shows all the directions of incidence (see from the point of view of the DUT) for a turntable that rotates around a z -directed axis, as illustrated in Figure 8. The turntable thus multiplies the effective number of plane waves available. Of course, only plane waves corresponding to a single rotated version of Figure 10(a) are available at any instant.

Figure 11(a) shows the plane-wave directions of incidence for the small chamber. The directions of incidence are sparsely distributed with a maximum distance between points of 48° and an average distance of 27° . There are large gaps throughout the unit sphere. Figure 11(b) shows all the directions of incidence (see from the point of view of the DUT) for the turntable in Figure 8. Again, only plane waves corresponding to a single rotated version of Figure 11(a) are available at any instant.

4.2. Correlation Simulations. Let us now investigate how these reverberation chambers perform when evaluating the correlation between the two z -directed Hertzian dipoles in Figure 4. The exact correlation is given by (18), and the error \mathcal{E} in (19) for the large chamber is shown in Figure 12 as a function of dipole separation. The “turntable off” simulation is performed by randomly changing the phase and amplitude of incident plane waves with directions of incidence in Figure 10(a) (the plane waves are given by $\mathbf{E}_0 \exp(-ik\hat{\mathbf{k}}^i \cdot \mathbf{r})$ with $\hat{\mathbf{k}}^i$ given by (25) and $\hat{\mathbf{k}}^i \cdot \mathbf{E}_0 = 0$). The “turntable

on” simulation is performed by repeating the “turntable off” simulation with the plane-wave directions of incidence rotated by a fixed amount. In other words, the “turntable on” simulation accurately replicates the actual situation encountered by the DUT in a real reverberation chamber where only one set of plane waves (corresponding to a rotated version of the plane waves for a fixed DUT orientation) is available at any given instant. Figure 12 demonstrates that the turntable dramatically improves the accuracy of the computed correlation between the dipoles. This improved accuracy is achieved by illuminating the two dipoles from additional directions.

The error \mathcal{E} in (19) for the small chamber is shown in Figure 13 as a function of dipole separation. With the sparse coverage of plane-wave directions of incidence (Figure 11(a)), the correlation obtained with the turntable off is very inaccurate. The error is above 0.3 for certain values of the dipole separation. Remarkably, with the turntable on, the error falls dramatically to an almost tolerable level.

4.3. Anisotropy Coefficients. One of the most important statistical properties of the field in the chamber is the degree to which it is isotropic, that is, how evenly distributed are the directions of propagation and polarizations of the incoming plane waves at the location of the DUT. With the isotropy test developed by the international standards committee (ICE) [23], field anisotropy coefficients measure the bias of the average direction of polarization of the electric field in the chamber. The bias is computed by comparing three components of the electric field obtained from dipole-antenna measurements. The degree of isotropy

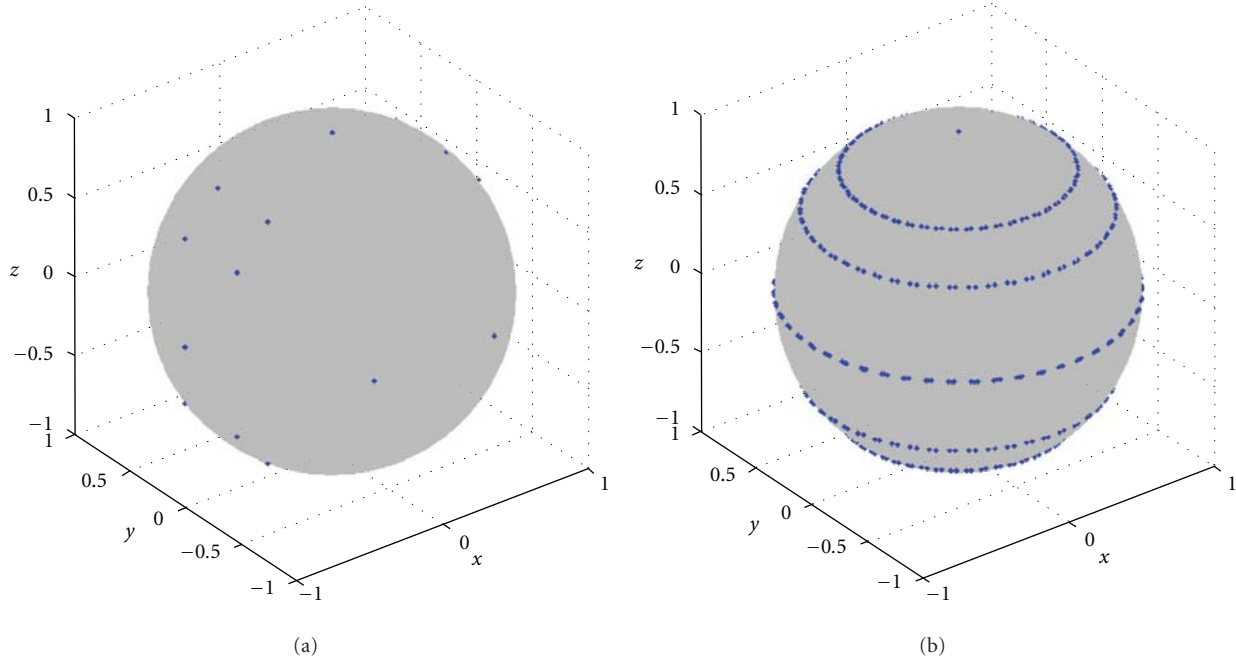


FIGURE 11: Plane-wave directions of incidence for modes in a 50 MHz band around 750 MHz in a small chamber with dimensions $D_x = 1$ m, $D_y = 0.9$ m, and $D_z = 0.8$ m. (a) Without turntable. (b) With turntable rotating around a z -directed axis. Without the turntable, the maximum distance between directions of incidence is 48° and the average distance is 27° .

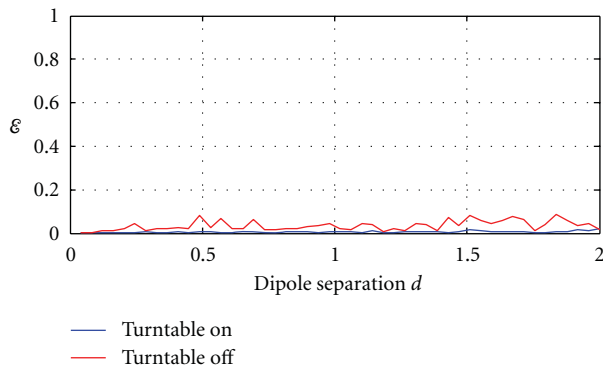


FIGURE 12: The error \mathcal{E} as a function of dipole separation d for the large chamber with dimensions $D_x = 3$ m, $D_y = 2$ m, and $D_z = 1.5$ m operating around 750 MHz.

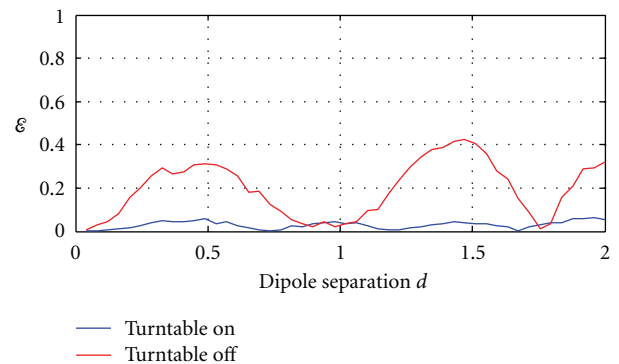


FIGURE 13: The error \mathcal{E} as a function of dipole separation d for the small chamber with dimensions $D_x = 1$ m, $D_y = 0.9$ m, and $D_z = 0.8$ m operating around 750 MHz.

of an actual chamber is determined by comparing the observed and ideal (known from theory) distributions of the anisotropy coefficients. We shall next compute the anisotropy coefficients for the large and small reverberation chambers introduced above.

Three orthogonal components of the electric field recorded at the location of the DUT are required to compute the field anisotropy coefficients [23]:

$$A_{\alpha\beta}(n) = \frac{|E_\alpha(n)|^2/P_i(n) - |E_\beta(n)|^2/P_i(n)}{|E_\alpha(n)|^2/P_i(n) + |E_\beta(n)|^2/P_i(n)}, \quad (26)$$

where α and β denote the three orthogonal directions. The quantity $P_i(n)$ is the net input power (forward minus

reflected) injected into the chamber, and n is an index that determines the position of the turntable, the position of the mechanical stirrer, and the active transmit antenna. In addition to the three anisotropy coefficients defined by (26), the test in [23] also employs a total anisotropy coefficient that we shall not investigate here. For a perfectly isotropic chamber, $A_{\alpha\beta}(n)$ is uniformly distributed between -1 and 1 . Pages 195 and 196 of [23] show plots of anisotropy coefficients for well-stirred and poorly stirred reverberation chambers.

When the DUT is placed near the edge of the turntable in Figure 8, the three relevant orthogonal directions for the isotropy test are (i) the direction \hat{z} normal to the turn table, (ii) the direction $\hat{\phi}$ tangential to the edge of the turntable, and (iii) the direction $\hat{\rho}$ radial to the turntable. Hence, in a

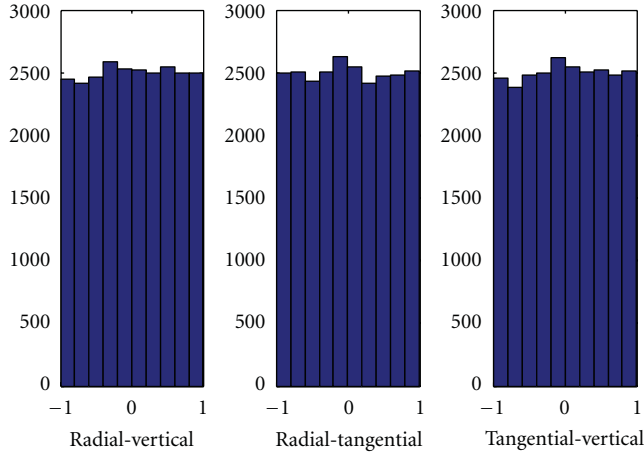


FIGURE 14: Histograms of anisotropy coefficients for large chamber with dimensions $D_x = 3$ m, $D_y = 2$ m, and $D_z = 1.5$ m operating around 750 MHz.

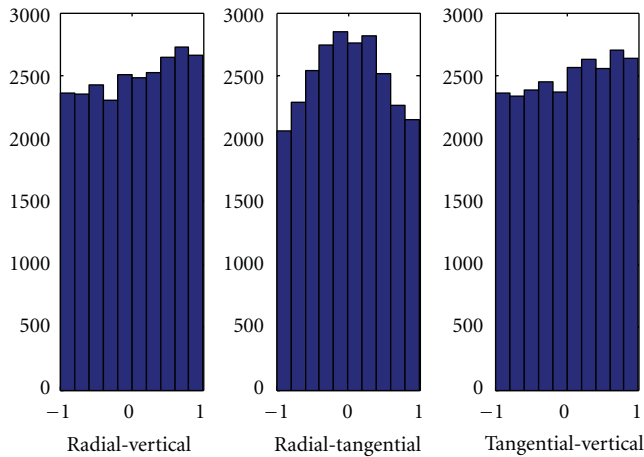


FIGURE 15: Histograms of anisotropy coefficients for small chamber with dimensions $D_x = 1$ m, $D_y = 0.9$ m, and $D_z = 0.8$ m operating around 750 MHz.

standard cylindrical coordinate system (ρ, ϕ, z) centered on the turntable, α and β can take the values ρ , ϕ , and z .

Figures 14 and 15 show the histograms for the anisotropy coefficients of the large ($D_x = 3$ m, $D_y = 2$ m, and $D_z = 1.5$ m) and small ($D_x = 1$ m, $D_y = 0.9$ m, and $D_z = 0.8$ m) reverberation chambers (both with the turntable active). We see that the anisotropy coefficients for the large chamber closely follow a uniform distribution, whereas the anisotropy coefficients for the small chamber show a significant deviation from a uniform distribution. We conclude that the small chamber does not produce enough plane waves, even though the turntable is active.

4.4. Remarks. We have now described the plane-wave environment in a reverberation chamber using the mode expansion of the dyadic Green's function for the rectangular box. We have seen how the plane-wave directions of incidence as seen from the DUT depend on the dimensions of the

chamber and on whether or not a turntable is active. Through numerical simulations, we evaluated the accuracy of correlation experiments in the chamber. It would be nice to have a theory that explicitly determined the accuracy of the chamber as a function of chamber dimension and chamber loading (quality factor Q). Such a theory does not exist, and at the present moment the accuracy can only be determined by numerical simulations like the ones presented here. Moreover, if a precise theory existed, it would have to be fairly complicated because accuracy depends not only on mode density (which is largely determined by chamber volume [1, page 30]) but also on the actual plane-wave directions of incidence, which depend on all 3 rectangular chamber dimensions. For example, a large chamber may have a large "plane-wave gap" near the poles, which in turn can make it less accurate than a smaller chamber.

5. MIMO Capacity Simulations

In this section we perform MIMO capacity simulations with a two-antenna DUT receiver in an isotropic environment. The transmitter is a standard two-antenna base station. We employ the good, nominal, and bad reference antennas described in Section 3.2 and show that they produce clearly distinguishable throughput curves. The approach taken in this section was inspired by [5–9].

A schematic of the channel model is shown in Figure 16. The base station employs two antennas separated by $D = 4\lambda$ and radiating through a standard 3-sector pattern $\mathcal{A}(\Theta)$ [24, page 9]. The voltage input amplitudes for the two base station antennas are denoted V_1^T and V_2^T . Each base station antenna broadcasts in the directions Θ_s , $s = 1, 2, \dots, S$, according to the Laplacian distribution approximation [21, equation (18)] with $\sigma_\theta = 5^\circ$. We have now S complex numbers for base station antenna 1,

$$U_s^{(1)} = V_1^T \mathcal{A}(\Theta_s) e^{ik(D/2) \sin \Theta_s}, \quad (27)$$

and S complex numbers for base station antenna 2,

$$U_s^{(2)} = V_2^T \mathcal{A}(\Theta_s) e^{-ik(D/2) \sin \Theta_s}. \quad (28)$$

In practice, the two-antenna 2D Laplacian base station output would be fed to the reverberation chamber through two or more wall antennas. The directions of propagation from the base station are thus distributed randomly into plane waves in the chamber, and the Laplacian distribution is not preserved. In other words, the chamber does not reproduce the Laplacian distribution. However, the correlation imposed on the two information streams by the base station is preserved. Further, one often feeds a reverberation chamber from a channel emulator that is programmed to produce advanced spatial channel models, which can include both Doppler spectra, long time delays (much longer than the one produced by the chamber alone), and specified directions of incidence. When such channel models are fed to the reverberation chamber, the channel model is said to be evaluated isotropically. In such situations, the specified directions of propagation dictated by the channel model are not preserved. However, if the emulator and reverberation

chamber are adjusted properly, the time delays and Doppler spectra of the channel model are preserved in the chamber. The use of advanced channel models adds a lot of flexibility to the reverberation chamber as an over-the-air test tool.

Next we select a set of evenly distributed points (θ_s, ϕ_s) , $s = 1, 2, \dots, S$, on the unit sphere as described in Section 3 to obtain S incoming plane-wave propagation directions for illuminating the DUT. For $j = 1, 2, \dots, J$ we compute a set of random permutations of the numbers $1, 2, \dots, S$ given by $s' = p(j, s)$. In addition, for $j = 1, 2, \dots, J$, we compute two sets of uniformly distributed random variables $v_\theta(j, s)$ and $v_\phi(j, s)$ in the range from 0 to 2π . The permutations $s' = p(j, s)$ facilitate the random pairing between point on the base station pattern and plane-wave directions of incidence. The variables $v_\theta(j, s)$ and $v_\phi(j, s)$ provide random phase adjustments for each pair.

We now have J different propagation channels that result in the following DUT antenna outputs:

$$\begin{aligned} V_1^{(j)} &= \sum_{s=1}^S [U_{p(j,s)}^{(1)} + U_{p(j,s)}^{(2)}] \\ &\quad \times [e^{iv_\theta(j,s)} \hat{\theta}_s \cdot \mathcal{R}_1(\theta_s, \phi_s) + e^{iv_\phi(j,s)} \hat{\phi}_s \cdot \mathcal{R}_1(\theta_s, \phi_s)], \\ V_2^{(j)} &= \sum_{s=1}^S [U_{p(j,s)}^{(1)} + U_{p(j,s)}^{(2)}] \\ &\quad \times [e^{iv_\theta(j,s)} \hat{\theta}_s \cdot \mathcal{R}_2(\theta_s, \phi_s) + e^{iv_\phi(j,s)} \hat{\phi}_s \cdot \mathcal{R}_2(\theta_s, \phi_s)], \end{aligned} \quad (29)$$

which can be written in matrix form as

$$\begin{bmatrix} V_1^{(j)} \\ V_2^{(j)} \end{bmatrix} = \bar{\mathbf{H}}^{(j)} \begin{bmatrix} V_1^T \\ V_2^T \end{bmatrix}, \quad (30)$$

where $\bar{\mathbf{H}}^{(j)}$ is the 2×2 channel matrix. The corresponding channel capacities are

$$C^{(j)} = \log_2 \left[\det \left(\bar{\mathbf{I}} + \frac{P_t}{2N_0} \bar{\mathbf{H}}^{(j)} (\bar{\mathbf{H}}^{(j)})^H \right) \right], \quad (31)$$

where the superscript H indicates the transpose complex conjugate, N_0 is the receiver noise, and P_t the transmitter power.

Figure 17 shows the capacity curves as functions of the signal to noise ratio (SNR) for the good, nominal, and bad reference antennas computed with $S = 180$ and $J = 10000$. These curves are obtained by computing the mean capacity for varying SNR. The mean is taken over all $J = 10000$ propagation channels. To achieve a capacity of 7 bps/Hz, the three reference antennas require very different SNR values: the bad reference antenna requires an SNR of 19 dB, whereas the good reference antenna requires only an SNR of 13 dB. The difference in SNR between good and bad reference antennas is in this case 6 dB. Similarly, to achieve a capacity of 12.5 bps/Hz, the difference in SNR between good and bad reference antennas is 7 dB. Hence, the capacity curves are clearly distinguishable, thereby confirming the capability of the isotropic environment for over-the-air MIMO testing. However, given the large variation in correlation of the three

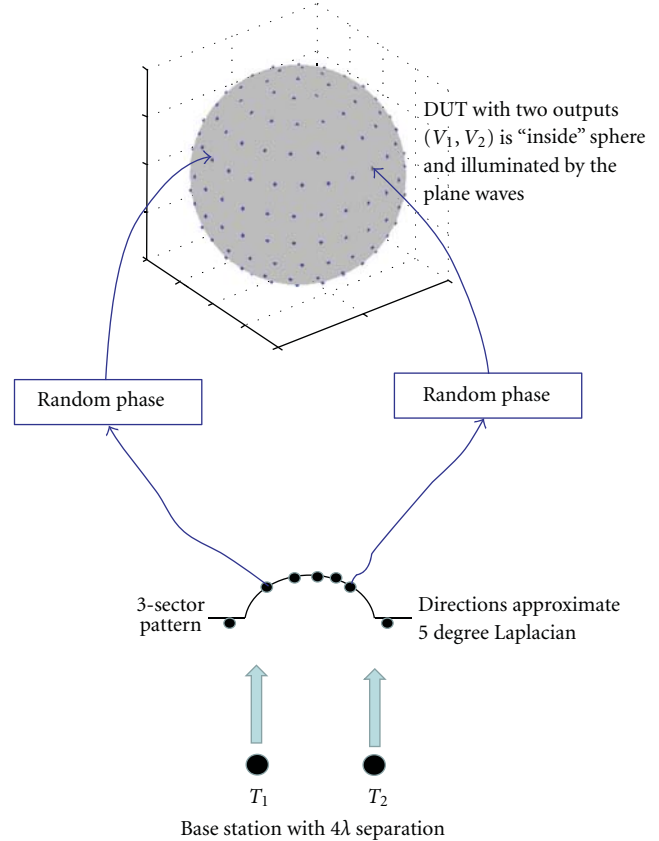


FIGURE 16: Channel model employing an isotropic environment. Each point on the base station pattern is randomly paired with a plane-wave propagation direction illuminating the DUT. In addition, each "pairing" is supplied by a random phase. The multiple states of the model are obtained by changing the pairing and the random phases.

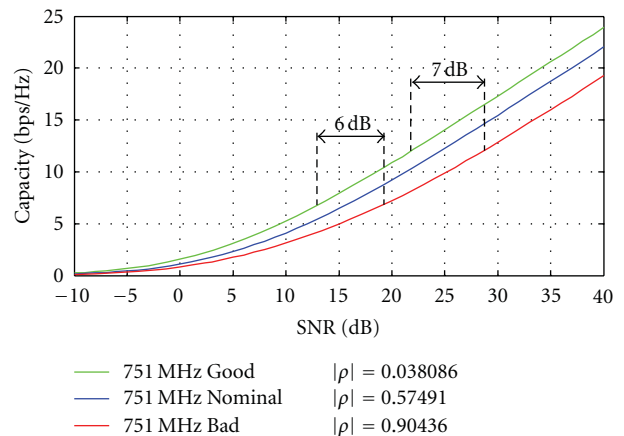


FIGURE 17: Capacity curves as functions of SNR for the "good," "nominal," and "bad" reference antennas in an isotropic environment. To achieve a capacity of 7 bps/Hz, the three reference antennas require very different SNR values: the bad reference antenna requires an SNR of 19 dB, whereas the good reference antenna requires only an SNR of 13 dB. The difference in SNR between good and bad reference antennas is in this case 6 dB. Similarly, to achieve a capacity of 12.5 bps/Hz, the difference in SNR between good and bad reference antennas is 7 dB.

antennas (see Table 1), it is no surprise that the capacity curves are very different. Most practical antennas would likely fall in the nominal category.

6. Conclusions

We investigated the use of reverberation chambers for over-the-air testing of MIMO devices by examining antenna correlation and throughput in isotropic environments. A truncated spherical-wave expansion was used to derive sampling theorems and the Fourier expansions for the pattern of an arbitrary DUT. The required sampling rate of the pattern depends on the frequency, the physical size of the entire DUT (not just its antenna), and the relative location of the DUT to the spherical coordinate system.

Through numerical investigations involving Hertzian dipoles, it was shown how the sampling rate for the pattern determines the plane-wave density required in the isotropic environment to obtain accurate values for the correlation between antennas. It was also demonstrated that antenna correlation in the isotropic environment is equivalent to the classical definition of antenna correlation, as was proven theoretically by De Doncker and Meys [11]. In particular, the correlations computed for the CTIA reference antennas [10] in isotropic simulations agree with the correlations obtained from the classical definition.

Using the dyadic Green's function for the rectangular box, we computed the plane-wave distribution for realistic reverberation chambers, which were in turn used in simulations of antenna correlations and anisotropy coefficients. No general theory that explicitly determined the accuracy of the chamber as a function of chamber dimension and chamber loading was found. Instead we explained how one can determine accuracy estimates through simulations.

We performed MIMO channel capacity simulations using a standard base station model and the DUT (employing the CTIA reference antennas) placed in a single-tap plane-wave reverberation chamber model. The capacity curves obtained with the good, nominal, and bad reference antennas were clearly distinguishable, as would be expected given the vast difference between the correlations of these antennas; see Table 1.

Hence, we conclude that isotropic tests performed in a reverberation chamber can distinguish between DUTs that employ the different CTIA reference antennas. It would be interesting to perform link-level simulations with multitap isotropic channel models to further investigate this over-the-air test method.

Acknowledgments

The author would like to thank R. J. Pirkl and K. A. Remley of the NIST for numerous helpful discussions. I. Szini of Motorola is thanked for providing the patterns for the reference antennas.

References

- [1] D. A. Hill, *Electromagnetic Fields in Cavities*, John Wiley & Sons, New York, NY, USA, 2009.

- [2] K. Rosengren and P. S. Kildal, "Study of distributions of modes and plane waves in reverberation chambers for the characterization of antennas in a multipath environment," *Microwave and Optical Technology Letters*, vol. 30, no. 6, pp. 386–391, 2001.
- [3] R. E. Collin, *Field Theory of Guided Waves*, IEEE Press, New York, NY, USA, 2nd edition, 1991.
- [4] Azimuth Systems, "Isotropy and rayleighness of emulator-chamber system," White Paper, 2011.
- [5] R. J. Pirkl and K. A. Remley, "A study of channel capacity in 2-D and 3-D isotropic environments," CTIA Contribution MOSG110805, 2011.
- [6] R. J. Pirkl and K. A. Remley, "A study of channel capacity in 2-D and 3-D isotropic environments: comparison between MIMO reference antennas," CTIA Contribution MOSG110906, 2011.
- [7] R. J. Pirkl and K. A. Remley, "A study of channel capacity in 2-D and 3-D isotropic environments: effect of gain imbalance," CTIA Contribution MOSG111008, 2011.
- [8] R. J. Pirkl, E. Engvall, and K. A. Remley, "Measurements of correlation coefficients and capacity CDFs for MIMO reference antennas," CTIA Contribution MOSG111009, 2011.
- [9] R. J. Pirkl and K. A. Remley, "Dependence of antenna orientation on correlation, average gain, and capacity in 2-D isotropic environments," CTIA Contribution MOSG111010, 2011.
- [10] I. Szini, "Reference antenna proposal for MIMO OTA," CTIA Contribution MOSG110504R1, 2011.
- [11] P. De Doncker and R. Meys, "Statistical response of antennas under uncorrelated plane wave spectrum illumination," *Electromagnetics*, vol. 24, no. 6, pp. 409–423, 2004.
- [12] T. B. Hansen and A. D. Yaghjian, *Plane-Wave Theory of Time-Domain Fields*, IEEE Press, New York, NY, USA, 1999.
- [13] D. M. Kerns, "Plane-wave scattering-matrix theory of antennas and antenna-antenna interactions," NBS Monograph 162, U.S. Government Printing Office, Washington, DC, USA, 1981.
- [14] W. W. Hansen, "A new type of expansion in radiation problems," *Physical Review*, vol. 47, no. 2, pp. 139–143, 1935.
- [15] J. D. Jackson, *Classical Electrodynamics*, John Wiley & Sons, New York, NY, USA, 2nd edition, 1975.
- [16] W. C. Chew, J. M. Jin, E. Michielssen, and J. Song, Eds., *Fast and Efficient Algorithms in Computational Electromagnetics*, Artech-House, Boston, Mass, USA, 2006.
- [17] L. J. Ricardi and M. L. Burrows, "A recurrence technique for expanding a function in spherical harmonics," *IEEE Transactions on Computers*, vol. 21, no. 6, pp. 583–585, 1972.
- [18] P. F. Wacker, "Non-planar near-field measurements: spherical scanning," NBS Internal Report 75–809, 1975.
- [19] J. E. Hansen, J. Hald, F. Jensen, and F. H. Larsen, Eds., *Spherical Near-Field Antenna Measurements*, Peter Peregrinus, London, UK, 1988.
- [20] T. B. Hansen, "Formulation of spherical near-field scanning for electromagnetic fields in the time domain," *IEEE Transactions on Antennas and Propagation*, vol. 45, no. 4, pp. 620–630, 1997.
- [21] M. Patzold and Q. Yao, "A study of stochastic and deterministic procedures for the design of simulation models for spatial channels," in *Proceedings of the IEEE International Symposium on Personal, Indoor and Mobile Radio Communications (PIMRC '02)*, pp. 1924–1931, September 2002.
- [22] K. Rosengren, P. S. Kildal, C. Carlsson, and J. Carlsson, "Characterization of antennas for mobile and wireless terminals in reverberation chambers: improved accuracy by platform

stirring,” *Microwave and Optical Technology Letters*, vol. 30, no. 6, pp. 391–397, 2001.

- [23] International Standard, *Testing and measurement techniques-Reverberation chamber test methods*, IEC 61000-4-21, 2003.
- [24] 3rd Generation Partnership Project, Technical Specification Group Radio Access Network, “Spatial channel model for Multiple Input Multiple Output (MIMO) simulations,” 3GPP TR 25.996 V8.0.0, 2008.

Research Article

Channel Modelling for Multiprobe Over-the-Air MIMO Testing

Pekka Kyösti, Tommi Jämsä, and Jukka-Pekka Nuutinen

Elektrobit Corporation, Wireless Business Segment, Tutkijantie 8, 90590 Oulu, Finland

Correspondence should be addressed to Pekka Kyösti, pekka.kyosti@elektrobit.com

Received 28 December 2011; Accepted 20 March 2012

Academic Editor: Moray Rumney

Copyright © 2012 Pekka Kyösti et al. This is an open access article distributed under the Creative Commons Attribution License, which permits unrestricted use, distribution, and reproduction in any medium, provided the original work is properly cited.

This paper discusses over-the-air (OTA) test setup for multiple-input-multiple-output (MIMO) capable terminals with emphasis on channel modelling. The setup is composed of a fading emulator, an anechoic chamber, and multiple probes. Creation of a propagation environment inside an anechoic chamber requires unconventional radio channel modelling, namely, a specific mapping of the original models onto the probe antennas. We introduce two novel methods to generate fading emulator channel coefficients; the prefaded signals synthesis and the plane wave synthesis. To verify both methods we present a set of simulation results. We also show that the geometric description is a prerequisite for the original channel model.

1. Introduction

To meet the increased consumer demand on high data rate applications—such as music and video downloading, web browsing, and multimedia sharing—multiantenna technology will be widely utilized in mobile terminals near future. New standards such as the 3rd Generation Partnership Project (3GPP) High Speed Downlink Packet Access (HSDPA), Long Term Evolution (LTE), LTE-Advanced, and IEEE 802.16m specify multiple antenna technology also at mobile terminal, and IEEE 802.11n and 802.11ac specify multiple antennas in Wireless Local Area Network (WLAN) devices. Multiple-input-multiple-Output (MIMO) technology in wide sense covers any multi antenna technique, such as spatial multiplexing, beam forming, and spatial diversity. MIMO offers significant increases in data throughput, quality of service (QoS), and cell coverage without additional bandwidth or transmit power. Communication performance is improved by exploiting the characteristics of the propagation channel in which the device is operating.

In MIMO systems, spatial correlation plays a key role. It depends on both antenna and propagation characteristics. Neither can determine the correlation alone. Therefore, it is necessary to include both antenna and propagation effects at the same time when testing multiantenna terminals. MIMO over-the-air (OTA) testing provides solution for that demand. Due to the complexity of multiple antenna setups,

flexible, fast, and accurate testing solution is needed to speed up the development process and to ensure the real performance of the terminal. Foegelle [1] identified the need for a new approach for OTA testing of multiantenna terminals to complement the existing OTA test methodologies for single antenna terminals.

Recently, several different MIMO OTA test methodologies have been proposed in research and standardization forums. European Cooperation in Science and Technology (COST) action COST2100 [2] has been finished and the final report will be published soon [3]. Follower of COST2100, new COST IC1004 action continues the work, and the final results are expected in year 2015 [4]. 3GPP MIMO OTA Study Item is almost finished, and the work will potentially continue in a Work Item [5]. CTIA [6] discusses MIMO OTA as well. In all of these groups, three fundamentally different categories of methodologies have been proposed. The methodologies in the first category are based on anechoic chamber and a number of probe antennas, in which the signals are controlled by for example a fading emulator. The second category provides angular dispersion of multipath signals via a reverberation chamber. The power angular spectrum is 3D uniform. By using an external fading emulator, longer delay spread can be achieved. Third, multistage methodology is based on a number of measurement steps to evaluate the OTA performance. In the first stage the complex antenna pattern is measured by a

traditional anechoic chamber-based antenna measurement system, single-input-single-output (SISO) OTA. The second stage combines the antenna pattern information and the channel model to calculate the MIMO correlation matrices and antenna power imbalances, which are implemented in a channel emulator to make a conductive measurement or theoretical capacity calculation. The two first MIMO OTA methodologies provide a possibility to measure the true mobile terminal performance without using artificial cabling in the test setup. On the contrary, conductive test requires an RF cable connection, which affect the terminal RF and antenna performance.

MIMO OTA testing based on an anechoic chamber and a fading emulator (the first methodology) enables true evaluation of the end-user experience of the final product against realistic radio channel conditions. It also makes it possible to change the channel model (scenario) flexibly via software, for example signal angle-of-arrival (AoA) and angle spread are controllable. All critical parts of the mobile terminal design (antennas, RF front end, baseband processing) are tested at once. In traditional conductive testing, as in LTE conformance tests, only certain baseband processing is tested with predefined correlation characteristics, which omits the antenna effect in testing.

Anechoic chamber-based MIMO OTA enables to test off-the-shelf products (i.e., end products) in equivalent radio propagation conditions to provide unquestionable comparisons between the devices under test. In practice, the performance differences between “golden samples” and mass products may be large, thus there is a need for end device test system that can be used for mass production device testing without any cable connections.

This paper describes the anechoic chamber and fading emulator-based MIMO OTA test methodology. In Section 2 the overall system is described. Section 3 discusses and proposes channel models for MIMO OTA. Section 4 describes how the desired channel model is mapped onto the limited number of probe antennas. Two novel methods, namely, prefaded signals synthesis and plane wave synthesis, are explained. Section 5 shows simulation results, and Section 6 concludes this paper.

2. Anechoic Chamber and Fading Emulator-Based System

The MIMO OTA test setup, originally described in [7], is based on a fading emulator, an anechoic chamber and a number of OTA antennas. The purpose of the setup is to reproduce time variant electromagnetic field around the device under test (DUT) imitating the target MIMO radio channel model, as accurately as possible. The idea is to apply widely approved channel models like TGN model [8], SCM(E) [9], WINNER [10], or IMT-Advanced [11] on a radiated testing of DUT performance.

The components of OTA performance test setup are illustrated in Figure 1. DUT is in the centre of the anechoic chamber, in an area called test zone or test area, and transmitting antennas are arranged, for example, uniformly

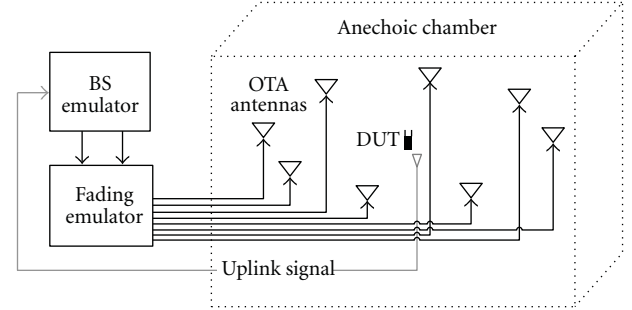


FIGURE 1: Fading emulator and anechoic chamber based MIMO OTA test set-up.

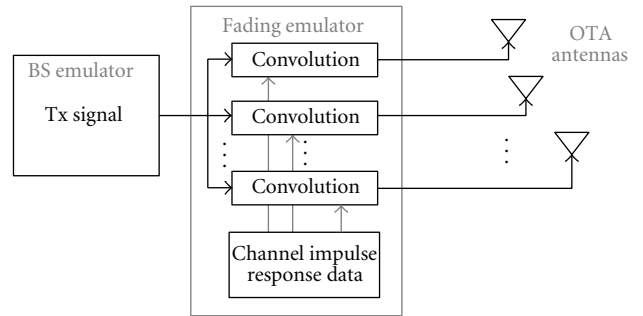


FIGURE 2: Convolution of Tx signal and radio channel impulse response data in the fading emulator.

around the DUT in two or three dimensions. Each of the transmitting antennas is connected to an output port of the fading emulator. Typically a power amplifier, between a fading emulator output and an OTA probe, is required to compensate path loss between the OTA probe and DUT. The communication tester (BS emulator) creates the test signal, which is fed to the multichannel fading emulator. The emulator creates the multipath environment including path delays, Doppler spread and fast fading. A fading emulator performs convolution of Tx signals with channel model impulse responses as described in Figure 2. The channel models containing directions of departures and arrivals are mapped to emulator so that model allocation corresponds to physical antenna installation in the chamber. Phantom heads, hands, and so forth can be easily added to the measurement. DUT is assumed to be in the far field region of the OTA antenna radiation.

In the actual MIMO OTA test of a multiantenna terminal an appropriate performance metric, for example throughput, is collected as a figure of merit. DUT may be rotated around one, two, or three rotation axis and the final performance may be the average performance over different DUT orientations. The performance averaged over a number of DUT orientations is effectively different to, for example, the performance in 3D isotropic scattering environment of a reverberation chamber. From mathematics it is well known that in general case an average of function values is different to a function value of averaged function argument.

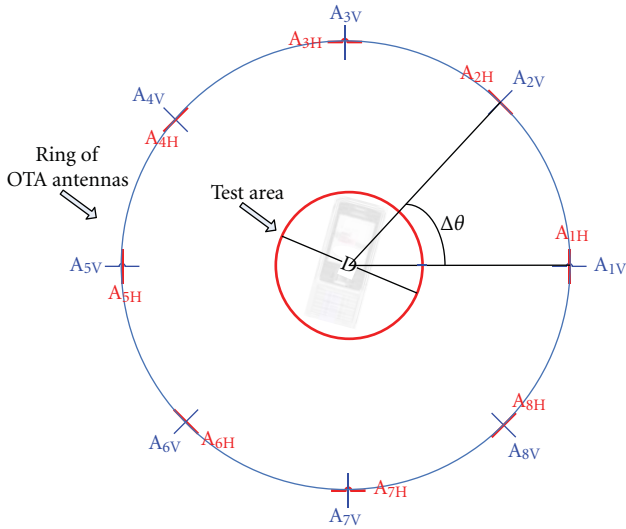


FIGURE 3: Ring of OTA antennas and the test zone.

Typically both downlink and uplink transmissions are required in the measurement. An uplink communication antenna is located inside the anechoic chamber so that it does not cause interference problems to downlink. A proper uplink antenna would be a circularly polarized antenna with high directivity. The antenna is connected to a base station (BS) emulator with a coaxial cable. In the simplest case no fading or multipath effects are emulated in the uplink. In time division duplex (TDD) systems the uplink radio channel should be reciprocal to downlink, but TDD case is not discussed in this paper. A system diagram for TDD MIMO OTA test setup is presented in [12].

OTA antennas must be dual-polarized if also polarization dimension of the radio channel is considered. Both elements of a single OTA antenna, radiating orthogonally polarized signals, have to be connected to different fading emulator outputs. This will guarantee independent fading on different polarizations as specified, for example in SCM and WINNER channel models [10, 13]. An example layout of eight dual-polarized OTA antennas is illustrated in Figure 3 with uniformly spaced probes on a circle, resulting to angular spacing $\Delta\theta = 45^\circ$.

The example layout in Figure 3 is of 2D setup. Most of the standardized radio channel models are two dimensional (2D) in the sense that they use only geometrical xy -coordinates (azimuth plane) [14]. Elevation dimension has been left out because the power angular spectrum is typically confined close to the horizon. The MIMO OTA setup can be extended to 3D by installing antennas on, for example, cylindrical or spherical formation. A 3D addendum for IMT-advanced channel models is given in [14].

The number of required OTA antennas has been discussed in [15, 16] and in various COST 2100 contributions. The final formula is still missing, but the number depends on the DUT size, the centre frequency, the channel model, the

OTA antenna locations, and the acceptable error level. The following rule of thumb is given in [15]:

$$K = 2 \left\lceil \frac{\pi D}{\lambda} \right\rceil + 1, \quad (1)$$

where K is a number of OTA antennas, $\lceil \cdot \rceil$ denotes round up operation, D is diameter of the test area as in the Figure 3, and λ is the wavelength.

In a practical setup there may be unintentional reflections of transmitted downlink signals from other OTA antennas. Preliminary measurements of [17] indicate that the reflections are not a serious problem for the field synthesis. The average scattering level was 35 dB below the line-of-sight path power with a directive Vivaldi type of OTA antenna design. In the measurement the observed frequency range was 1.35–7.25 GHz and the distance from OTA antenna to the centre of the test area was at minimum 1 metre.

3. Geometric Channel Models

There exists a high variety of different kinds of MIMO radio channel models. An overview of models is given in [18]. MIMO radio channel models typically have to cover all the four dimensions of the radio channel, namely, time, frequency, space, and polarization. Thus the models are time variant, wideband, double directional, and polarimetric. The two most popular classes of MIMO channel models are so-called geometry-based models and correlation matrix based models. Models for example in [10, 11, 13] belong to the geometric family and in [8] to the family of correlation matrix based models. In many cases also the correlation matrix based models have geometric description as an initial starting point. This is the case also in TGN model.

Geometry based modelling enables separation of propagation and antennas. Antenna geometries and field patterns can be defined independent of propagation parameters. Channel realisations are generated with the geometrical principle by summing contributions of rays (plane waves) with specific small scale parameters like for example delay, power, angle of arrival (AoA), and angle of departure (AoD). Superposition results to correlation between antenna elements and temporal fading with geometry-dependent Doppler spectrum [10].

A widely approved concept in spatial channel modelling is the concept of “cluster.” A number of rays constitute a cluster. In a common terminology the cluster is understood as a propagation path diffused in space, either or both in delay and angle domains. Typically a cluster is composed of a fixed number of rays (sub paths) and has a specific shaped power angular spectrum, for example, Laplacian function, defined by nominal AoA/AoD and angular spread of arrival and departure (ASA/ASD). A physical propagation mechanism creating clusters is reflection, scattering, or diffraction on a limited sized object in the physical environment, for example on a corner of a building. A cluster can be composed of, for example, a high number of scattering points on surface of a building. Each scatterer has characteristics like AoA, AoD, and complex attenuation coefficients. A single

ray of geometric model represents scattering (or reflection or diffraction) on a single scattering point.

A geometry-based channel model can be composed from the following propagation parameters: cluster powers, delays, nominal arrival and departure angles, and angle spreads of clusters on both arrival and departure ends, and cluster cross-polarization power ratios (XPRs). In addition, information of the receiver and transmitter antenna arrays including both array geometry and antenna field patterns is required. (Note that Rx antennas are not specified in MIMO OTA.) Also either the terminal velocity vector or the cluster Doppler frequency components have to be defined.

In the following we define a system model for horizontal plane (2D) MIMO radio channel based on [10, 13]. Transfer matrix of the MIMO channel is

$$\mathbf{H}(t, \tau) = \sum_{l=1}^L \mathbf{H}_l(t, \tau). \quad (2)$$

It is composed of antenna array response matrices $\mathbf{F}_{tx}(\text{Tx})$, $\mathbf{F}_{rx}(\text{Rx})$, and impulse response matrices \mathbf{h}_l for rays l as follows:

$$\mathbf{H}_l(t, \tau) = \iint \mathbf{F}_{rx}^T(\varphi) \mathbf{h}_l(t, \tau, \phi, \varphi) \mathbf{F}_{tx}(\phi) d\phi d\varphi. \quad (3)$$

The channel impulse response of the l th ray is a 2×2 polarimetric matrix

$$\begin{aligned} & \mathbf{h}_l(t, \tau, \phi, \varphi) \\ &= \begin{bmatrix} \alpha_l^{VV}(t) & \alpha_l^{VH}(t) \\ \alpha_l^{HV}(t) & \alpha_l^{HH}(t) \end{bmatrix} \delta(\tau - \tau_l) \delta(\phi - \phi_l) \delta(\varphi - \varphi_l). \end{aligned} \quad (4)$$

Now we introduce the clustered structure of a propagation channel and replace ray index l with cluster index n and cluster sub path index m . The channel coefficient for a channel from Tx antenna element s to Rx antenna element u for the cluster n can be modelled as

$$\begin{aligned} & H_{u,s,n}(t, \tau) \\ &= \sum_{m=1}^M \begin{bmatrix} F_{rx,u,V}(\varphi_{n,m}) \\ F_{rx,u,H}(\varphi_{n,m}) \end{bmatrix}^T \mathbf{A} \begin{bmatrix} F_{tx,s,V}(\phi_{n,m}) \\ F_{tx,s,H}(\phi_{n,m}) \end{bmatrix} \\ & \cdot \exp(j2\pi\nu_{n,m}t) \delta(\tau - \tau_n), \end{aligned} \quad (5)$$

where $\nu_{n,m}$ is the Doppler shift of sub path n, m and 2×2 polarization matrix of scattering coefficients is

$$\mathbf{A} = \begin{bmatrix} \alpha_{n,m}^{VV} & \alpha_{n,m}^{VH} \\ \alpha_{n,m}^{HV} & \alpha_{n,m}^{HH} \end{bmatrix}. \quad (6)$$

For example, the coefficient $\alpha_{n,m}^{HV}$ contains phase rotation and attenuation for vertically polarized incident wave and horizontally polarized scattered wave of ray m of cluster n . Coefficients α are modelled as time invariant in cluster based geometric models. Phases are typically random and amplitudes are determined by the XPR. Random phases

result always to elliptical polarization. For a line-of-sight path with linear polarization the off-diagonal elements of \mathbf{A} are zeros and diagonal elements have equal phase.

The presented 2D model can be extended to 3D, by interpreting angles φ and ϕ as composed of azimuth and elevation components like, for example, $\varphi = (\varphi_{az}, \varphi_{el})$. Elevation angular parameters to extend the model are; elevation angle of arrival (EoA) and departure (EoD), and elevation angle spread of arrival (ESA) and departure (ESD).

Cross-polarization power ratio (XPR) has different definitions. Here we follow and clarify the definition of [10], where XPR is a pure propagation parameter. XPR for vertically polarized Tx signals is

$$\text{XPR}_V = \frac{S^{VV}}{S^{HV}} = \frac{|\alpha^{VV}|^2}{|\alpha^{HV}|^2}, \quad (7)$$

respectively, XPR for horizontally polarized Tx signals is

$$\text{XPR}_H = \frac{S^{HH}}{S^{VH}} = \frac{|\alpha^{HH}|^2}{|\alpha^{VH}|^2}, \quad (8)$$

where

- (a) S^{VV} is the coefficient for scattered power on V -polarization and incident power on V -polarization of an interacting object (cluster),
- (b) S^{VH} is the coefficient for scattered power on V -polarization and incident power on H -polarization of an interacting object (cluster),
- (c) S^{HV} is the coefficient for scattered power on H -polarization and incident power on V -polarization of an interacting object (cluster),
- (d) S^{HH} is the coefficient for scattered power on H -polarization and incident power on H -polarization of an interacting object (cluster).

Even though XPR_V and XPR_H are defined separately, it is often assumed that $\text{XPR}_V = \text{XPR}_H$. This is the assumption, for example, in [10, 11].

3.1. Channel Model Prerequisites for MIMO OTA. Geometric description of the propagation and the separation of antennas and propagation are essential requirements for the basic radio channel model to be reconstructed to a MIMO OTA test setup. Pure correlation matrix models are not realizable with a MIMO OTA setup, because they do not fulfil these prerequisites. At least the DUT end of the channel model has to be specified by angular propagation parameters. If some antenna characteristics are embedded to the channel model, which is the case in pure correlation matrix-based model, the model itself assumes some DUT antennas. Thus it is not feasible to measure the real DUT antenna performance anymore.

TGn channel model [8] is a correlation matrix-based model, but it contains also geometric description. It is possible to reconstruct TGn model to MIMO OTA environment with specified Tx (base station) antenna correlation matrices and specified, nongeometry-based, Doppler spectra. This

can be done with the method of prefaded signals, but not with the method of plane wave synthesis. Both methods are discussed in the next section.

The clustered modelling principle of many MIMO channel models is a benefit for the method of prefaded signals. It is not a prerequisite, but it makes the method more efficient. With clustered channel models the individual rays are not essential, but the clusters they compose. In other words, it is not necessary to create a high number of rays with specific characteristics, but instead to model the sum effects, like spatial correlation, Doppler spectrum, power delay profile, XPR, and so forth, accurately.

4. Synthesis of Propagation Environment

This section describes two alternative methods to generate channel impulse response data (see Figure 2), to a fading emulator, to create desired radiated propagation environment within the test volume. The methods are prefaded signals synthesis and plane wave synthesis. Both methods can create statistically equal radiated propagation environment within the test volume. The plane wave synthesis has a point of view in individual rays (plane waves) while the prefaded signals synthesis focuses on clusters. The basic component created by the plane wave synthesis is a single plane wave with a specific angle of arrival, Doppler shift and magnitude. With the prefaded signals synthesis the basic component is a single cluster with parameters like nominal AoA, ASA, Doppler spectrum, and XPR. Methods are described in details in the following sub-sections.

4.1. Prefaded Signals Synthesis. Idea of the prefaded signals synthesis is to transmit Rayleigh or any other kind of faded signals separately from multiple OTA antennas. Fading sequences are created independently for each cluster. Clusters are mapped to OTA antennas based on cluster power angular spectrum (PAS) and OTA antenna directions. A single cluster is composed by a number of OTA antennas. Each OTA antenna contributing to the cluster has independent fading coefficient sequences with identical statistics. For example Doppler spectra of fading patterns of different OTA antennas are identical for a single cluster. Discrete PAS of the single cluster is formed by allocating power weights on top of OTA antennas i.i.d. fading patterns.

As a summary, Doppler spectrum, amplitude distribution, and Tx antenna and directional characteristics are created to the prefaded sequences. XPR and Rx directional characteristics are created by allocating i.i.d. prefaded sequences to a set of OTA antennas with specific power weights.

The principle of creating clusters, applying a number of OTA antennas, by superposition of independent fading patterns with direction-dependent powers approximate physical reality. We may consider OTA antennas as subareas of an scattering object creating the cluster. It is assumed that each subarea contributes to the cluster fading patterns with identical statistics. Assuming uncorrelated scattering (US) the subareas create independent fading patterns. Thus we

can create the cluster effect with a set of spatially separated OTA antennas as far as the DUT antenna aperture is small with respect to the OTA antenna angular distance. More precisely, the angular resolution of DUT antenna array has to be smaller than $\Delta\theta$ in Figure 3.

This approach has at least one unrealistic element. In a real environment the Doppler spectrum should be angle dependent within the cluster. With the proposed method the Doppler spectrum is equal on all the OTA antennas composing the cluster. This effect may be observed by a DUT with directional antenna in the case of cluster with a high angular spread. We assume that this effect has negligible effect on DUT performance.

Details of creating fading patterns and power weights are described in the following. Here we present purely geometry-based method of creating Rayleigh fading coefficients. Anyhow it is possible to apply some other method too, as far as the Rx side directional and polarization characteristics are known. For example, noise filtering method can be applied for Rayleigh fading. Also, for example, fluorescent light effects of TGn model can be included in the prefaded coefficients. The Doppler spectrum may be based on some other definition than geometric.

4.1.1. Per Antenna Fading Patterns. On the prefaded signals synthesis the fading coefficients are generated based on (5). Now the Rx antenna is unknown, thus F_{rx} is substituted by an ideal OTA antenna pattern. The approximation is valid if we use OTA antennas with a high polarization isolation and a flat radiation pattern to the direction of the test zone. A Rayleigh fading pattern for cluster n for a channel from Tx (BS) antenna s to vertically polarized element of OTA antenna k is

$$\begin{aligned} H_{k,s,n}^V(t, \tau) &= \gamma_n \sum_{m=1}^M \begin{bmatrix} 1 \\ 0 \end{bmatrix}^T \mathbf{A} \begin{bmatrix} F_{tx,s,V}(\phi_{n,m}) \\ F_{tx,s,H}(\phi_{n,m}) \end{bmatrix} \\ &\cdot \exp(j2\pi\gamma_{n,m}t) \delta(\tau - \tau_n) \sqrt{g_{k,n}}, \end{aligned} \quad (9)$$

where γ_n is an amplitude of cluster n , \mathbf{A} is a polarization matrix and, $g_{k,n}$ is an antenna power weight. The fading pattern for the horizontally polarized element is obtained by changing Rx antenna pattern of (9) to $[F_{rx,k,V} \ F_{rx,k,H}] = [0 \ 1]$ as

$$\begin{aligned} H_{k,s,n}^H(t, \tau) &= \gamma_n \sum_{m=1}^M \begin{bmatrix} 0 \\ 1 \end{bmatrix}^T \mathbf{A} \begin{bmatrix} F_{tx,s,V}(\phi_{n,m}) \\ F_{tx,s,H}(\phi_{n,m}) \end{bmatrix} \\ &\cdot \exp(j2\pi\gamma_{n,m}t) \delta(\tau - \tau_n) \sqrt{g_{k,n}}. \end{aligned} \quad (10)$$

Antenna power weights determine, together with OTA antenna directions, a discrete power angular spectrum to the

test area, as will be discussed subsequently. The polarization matrix

$$\mathbf{A} = \begin{bmatrix} \frac{\exp(\Phi_{n,m,k}^{VV})}{1 + 1/\kappa_{n,m}^V} & \frac{\exp(\Phi_{n,m,k}^{VH})}{1 + \kappa_{n,m}^H} \\ \frac{\exp(\Phi_{n,m,k}^{HV})}{1 + \kappa_{n,m}^V} & \frac{\exp(\Phi_{n,m,k}^{HH})}{1 + 1/\kappa_{n,m}^H} \end{bmatrix} \quad (11)$$

is composed of random, independent and identically distributed initial phases $\Phi \sim \text{Uni}(0, 2\pi)$, and cross-polarization power ratios κ^V and κ^H for vertically and horizontally transmitted signals, respectively.

With a Rayleigh fading channel it is commonly assumed, for example in [10], that polarization components are independently fading [19] and polarization is practically always elliptical [20]. In the existing geometric channel models the XPR is specified, but the actual polarization states are not controlled. In MIMO OTA the propagation channel XPR is determined by coefficients κ in (11). Strengths of radiated vertically and horizontally polarized fields are determined by channel coefficient $H_k^V(t)$ and $H_k^H(t)$.

The radio channel dimensions, like delay, Doppler, polarization, and Tx side spatial characteristics, are modelled by other terms of (9) than $g_{k,n}$. For DUT antennas, the essential dimension is Rx side PAS denoted as $P(\Omega)$, defined as power P received from direction Ω . OTA antennas power weights $g_{k,n}$ determine PAS around the test area. A method is discussed in the following to form a discrete PAS, with power weights, such that the resulting field follows the continuous PAS specified by the channel model.

4.1.2. Antenna Power Weights. Purpose of the MIMO OTA system is to create a specific propagation environment within the test area. A channel model specifies continuous PAS on RX side, which may be composed of a number of spatial clusters with PAS $P_n(\Omega)$. Typically $P_n(\Omega)$ is defined by a nominal AoA and a root mean squared (rms) angular spread. The shape of $P_n(\Omega)$ may follow, for example, uniform, Gaussian, or Laplacian functions. With a limited number of OTA antennas we can only *approximate* the continuous PAS.

A straight forward method to obtain power weights would be to define $g_{k,n} = P_n(\theta_k)$, where θ_k is direction of the k th OTA antenna. This is not an optimal method, because it does not consider, for example, the size of the test area. This is analogous to a conventional filter design, where the method of sampling continuous impulse response does not produce optimal filter coefficients with a limited number of taps. A method to optimally utilize limited OTA antenna resources is needed.

The power angular spectrum is a Fourier transform pair with the spatial correlation function [21]. Instead of directly sampling the continuous PAS, it is beneficial to determine the discrete PAS by utilizing the spatial correlation function. Our proposed method to find optimal power weights is to sample the test area with an virtual array of ideal isotropic antennas. The target is to find power weights that minimize the mean squared error between theoretical correlations and

correlations resulting from a discrete PAS, between elements of the virtual array.

Let us spatially sample the test area with a number of virtual antennas such that the antennas compose M pairs. Theoretical correlation between m th pair (u, v) of antenna elements can be determined according to [20], omitting polarization, as

$$\rho_m = \frac{\int F_u(\Omega)F_v^*(\Omega)P(\Omega)d\Omega}{\sqrt{\int |F_u(\Omega)|^2P(\Omega)d\Omega \cdot \int |F_v(\Omega)|^2P(\Omega)d\Omega}}, \quad (12)$$

where $()^*$ denotes complex conjugate operation, F_u and F_v are complex radiation patterns of antennas u and v , respectively, with a common phase center. For virtual antennas the amplitude $|F_u(\Omega)| \equiv 1$. Phase is determined by the wavelength and relative positions of elements u and v .

Respectively, the correlation for m th antenna pair (u, v) with discrete PAS composed by K OTA antennas in directions Θ and with power weights \mathbf{G} is

$$\tilde{\rho}_m(\Theta, \mathbf{G}) = \frac{\sum_{k=1}^K F_u(\theta_k)F_v^*(\theta_k)g_k}{\sqrt{\sum_{k=1}^K |F_u(\theta_k)|^2g_k \cdot \sum_{k=1}^K |F_v(\theta_k)|^2g_k}}, \quad (13)$$

where $\Theta = \{\theta_k\}$, $\theta_k \in [0, 2\pi]$ is a vector of OTA antenna directions and $\mathbf{G} = \{g_k\}$, $g_k \in [0, 1]$, is a vector of OTA antenna power weights. The cost function to be minimized with respect to weights \mathbf{G} for fixed directions Θ is defined as

$$E_\rho(\Theta, \mathbf{G}) = \sum_{m=1}^M |\rho_m - \tilde{\rho}_m(\Theta, \mathbf{G})|^2. \quad (14)$$

Optimal vector of OTA antenna power weights \mathbf{G} for (9) and (10), minimizing (14), can be solved applying some numerical optimization method. Polarization is omitted from the described method, because we assume identically *shaped* PAS for both vertical and horizontal polarizations. The assumption is aligned, for example, with [10, 13].

4.2. Plane Wave Synthesis. This section describes a method to generate channel impulse responses, to the system depicted in Figure 2, applying the plane wave synthesis. Components of the setup are shown in Figure 1. At first we describe the creation of a single static plane wave, from an arbitrary direction, with complex antenna weights. Then the method is extended for creation of frequency and spatially selective fading radio channel model.

The plane wave synthesis for MIMO OTA is an extension to disciplines of acoustics and electromagnetic plane wave synthesis [22]. The following principle is applied in the plane wave synthesis; a closed curve in 2D case or a closed surface in 3D determines the field within the curve/surface when no sources are present inside [22]. In other words, the right target field is generated inside the test zone, if such a field is generated, that the components of both the electric and magnetic fields tangential to the surface of the test zone field are equal to those of the target field [15].

Nyquist sampling of at least two samples per wavelength on edge of the test zone, implies an approximation of

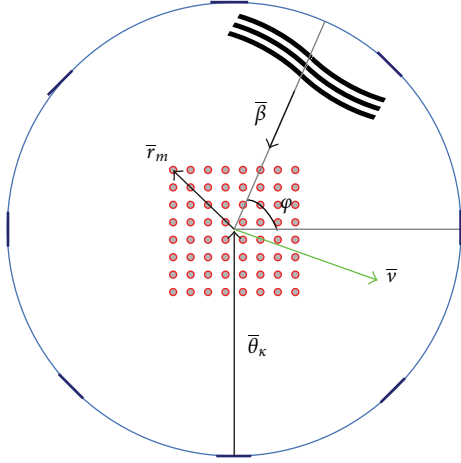


FIGURE 4: A single plane wave from AoA φ observed in location \bar{r}_m .

required probe numbers [15]. A waveform, observed within a test zone as a single plane wave from an arbitrary direction (angle of arrival AoA), can be created if the angular sampling by OTA antennas is dense enough. This is approximated by the rule of thumb of (1).

4.2.1. Single Static Plane Wave. As in Figure 4 a plane wave from an arbitrary AoA φ is created by setting appropriate complex antenna weights g_k to the CW (continuous wave on carrier frequency) transmitted from OTA antenna k , $k = 1, \dots, K$. Each OTA antenna may contribute by radiating waves. Superposition of waves within the test area is then observed as a single plane wave with a specific AoA φ . Weights g_k can be obtained, for example, by a numerical optimization. The numerical optimization may, for example, minimize the difference between the target field and the resulting field on the edge of the test area or some other sampling points within the test area. There are various procedures to perform the optimization. Here we present a method based on matrix inversion. The presented method is for vertically polarized (z -polarized) fields only, but it can be extended to any polarizations.

Weights g_k for a single plane wave can be obtained by solving OTA antenna weight vector \mathbf{G} from the following matrix equation

$$\mathbf{F}\mathbf{G} = \mathbf{T}, \quad (15)$$

where:

- $\mathbf{F} = \{\alpha_{m,k}\} \in \mathbb{C}^{M \times K}$ is a transfer matrix of coefficients from k th OTA antenna to m th location \bar{r}_m ;
- $\mathbf{G} = \{g_k\} \in \mathbb{C}^{K \times 1}$ is a vector of OTA antenna complex weights;
- $\mathbf{T} = \{e_z(\bar{r}_m)\} \in \mathbb{C}^{M \times 1}$ is a vector of complex target field values in locations \bar{r}_m (of a plane wave with AoA φ);
- \bar{r}_m is a location vector, pointing from the origin to m th sample point.

The transfer coefficient from k th OTA antenna to m th location \bar{r}_m is composed of path loss term L and a phase term as

$$\alpha_{m,k} = L(d_{k,m}) \exp(-j\|\bar{\beta}\|d_{k,m}), \quad (16)$$

where $d_{k,m} = \|\bar{\theta}_k + \bar{r}_m\|$ is the distance from the k th OTA antenna to m th location, $\bar{\theta}_k$ is a vector from k th OTA antenna to centre of the test area, $\bar{\beta}$ is the wave vector pointing from AoA direction as in Figure 4, $\|\bar{\beta}\| = 2\pi/\lambda_0$, and λ_0 is the wavelength at f_c . The target field for a plane wave is

$$e_z(\bar{r}_m) = E_0 \exp(-j\bar{\beta} \cdot \bar{r}_m), \quad (17)$$

where field strength $E_0 \equiv 1$ for the target field and \cdot denotes the scalar product operation.

When both \mathbf{F} and \mathbf{T} are constructed the vector \mathbf{G} can be solved. If $M = K$, the solution can be computed by matrix inversion

$$\mathbf{G} = \mathbf{F}^{-1}\mathbf{T}. \quad (18)$$

In some cases $M > K$ sample points within the test area may be specified. This leads to an overdetermined optimization problem. In this case the target is to minimize squared L2 norm [23]

$$\min_{\mathbf{G}} \|\mathbf{F}\mathbf{G} - \mathbf{T}\|, \quad (19)$$

which results to solving \mathbf{G} by the pseudo inverse

$$\mathbf{G} = (\mathbf{F}^H\mathbf{F})^{-1}\mathbf{F}^H\mathbf{T}. \quad (20)$$

Creation of vertical polarizations in 2D MIMO OTA configuration can be done with the discussed principles. For other polarizations or 3D environment the coefficient \mathbf{G} have to be determined for three orthogonal polarizations instead of just one polarization. The mathematics to derive the cost function and the optimization for the multipolarized case is excluded from this paper.

4.2.2. Doppler Shift. In the previous we described how to find channel coefficients to create a single static plane wave with an arbitrary AoA. Now we introduce Doppler shift to the plane wave to enable time variant radio channels. A virtual motion of DUT creates Doppler shifts to plane waves. The Doppler shift to a plane wave with AoA φ resulting from virtual motion to direction \bar{v} , as illustrated in Figure 4, is

$$\omega_d = -\bar{\beta} \cdot \bar{v}. \quad (21)$$

The Doppler shift can be introduced to the plane wave by multiplying Doppler frequency component $\omega_d (= 2\pi f_d)$ to the complex weights. That is by making the complex weights time dependent as follows:

$$w_k(t) = g_k \exp(-j t \omega_d). \quad (22)$$

Now the received field on an arbitrary location m within the test area, neglecting the path loss, is

$$\begin{aligned} E_z(t, \bar{r}_m) &= \sum_{k=1}^K w_k(t) \exp(-j (\|\bar{\beta}\| d_{k,m} + t\omega_c)) \\ &= \sum_{k=1}^K g_k \exp(-j \|\bar{\beta}\| d_{k,m}) \exp(-jt(\omega_d + \omega_c)). \end{aligned} \quad (23)$$

Even though the complex weights $w_k(t)$ are time dependent, the AoA dependent part (g_k) has to be determined only once. Temporal behaviour is generated by multiplying fixed weight with rotating phasor as in (22).

4.2.3. Power Angular Spectrum. A specific power angular density function can be formed within the test zone by introducing a number of plane waves with an appropriate AoA and magnitude. The AoA range may be, for example, sampled uniformly, as in Figure 5(a), with Q plane waves. Appropriate powers P_q , $q = 1, \dots, Q$, can be allocated to plane waves according to the target PAS. Another option is to fix powers and sample the angular space nonuniformly such that the target PAS is created as illustrated in Figure 5(b). In both cases each plane wave q has a specific AoA φ_q and power P_q . Also the Doppler shift $\omega_{d,q}$ will be unique for each plane wave depending on AoA and velocity vector of the virtual motion, as specified in (21).

Now the the complex weight of k th OTA antenna will be a sum of contributions to Q plane waves as follows:

$$w_k(t) = \sum_{q=1}^Q \sqrt{P_q} g_{k,q} \exp(-jt\omega_{d,q}), \quad (24)$$

where $g_{k,q}$ is solved separately for each plane wave q by minimization of (19).

4.2.4. Delay Dispersion. Delay dispersion is straightforward to implement in the fading emulator-based setup. Assuming uncorrelated scattering (UC) the fading of each discrete delay component is independent. Thus channel coefficients for different delay taps are generated applying same principles as when creating a single plane wave and an arbitrary power angular spectrum.

Polarization characteristics, Tx (base station) antenna effects, and Tx side spatial characteristics can be included in the channel impulse responses generated with the plane wave synthesis. Description of the method to model the mentioned effects is excluded from this paper, but the principle is similar to the prefaded signals synthesis.

5. Simulation Results

Measurement and simulation results to verify the concept of anechoic chamber and fading emulator-based multiprobe MIMO OTA setup are reported in numerous COST 2100, COST IC1004 and 3GPP contributions. Paper [24] presents

experimental and simulated results applying the prefaded signals method. Verification of a created radio channel with all its dimensions and characteristics is an extensive task. Here we show only a selection of simulation figures to demonstrate the two channel synthesis methods. The simulated characteristics are spatial correlation function (SCF), XPR, Doppler power spectrum (DPS), and temporal correlation function (TCF). Power delay profile (PDP) is excluded from the simulations, because creation of PDP is a trivial task with a digital fading emulator. Although the XPR simulation result illustrates a special case of a PDP.

In the simulations we had 16 uniformly spaced OTA antennas with 22.5° angular spacing. OTA antennas were assumed as omnidirectional vertically polarized probes with an isotropic radiation pattern. Additional horizontally polarized probes, co-located with vertically polarized OTA probes, were present in the XPR simulation. Transmitter antenna (base station) was assumed as ideal omnidirectional vertically polarized element. In XPR case the target channel model contained nine equal power clusters, with 200 ns spacing in delay, and XPRs from -20 dB to $+20$ dB with a 5 dB increment. In the other cases the channel model was a single cluster model with AoA = 10° and ASA = 15° . The direction of travel was 40° and sampling was four samples per wavelength. At total 50,000 samples was simulated. An exception was the Doppler power spectrum and the temporal correlation, where 20 samples per wavelength and 250,000 samples was used to make the curves smoother.

5.1. Spatial Correlation. Figure 6 depicts the theoretical spatial correlation function for a Laplacian function shaped PAS and SCF calculated from channel impulse responses generated with the plane wave synthesis (PWS) and the prefaded signals synthesis (PFS). A time series of channel impulse responses for each OTA antenna was generated with the both methods. Then the field $E_z(t, \bar{r}_m)$ over time, along a segment of line of locations \bar{r}_m was composed. Correlation between locations was calculated as the correlation between field coefficients $E_z(t, \bar{r}_m)$ in different locations over time. The examined correlation is an absolute value of a complex correlation coefficient. The simulation setup was similar to the measurement reported in [24].

Spatial correlation is an appropriate measure of the spatial dimension. Power angular spectrum observed by a DUT is inherently discontinuous and any power cannot be received from directions in between probes. Thus AoA or PAS estimation is not necessarily a meaningful technique to evaluate the created PAS. On the other hand, spatial correlation, as a fourier transform pair of PAS [21], is a continuous function and a good metric to assess the created spatial field.

The PWS curve (solid red) follows well the theoretical curve (blue circles) up to the simulated 1.5 wavelength spatial separation, as we can observe from the Figure 6. The PFS curve (solid green) follows the theoretical curve up to the simulated 1.2 wavelength spatial separation and deviates slightly after that. Anyhow the theoretical correlation on the area of deviation is low, 0.2, or below, and the deviation

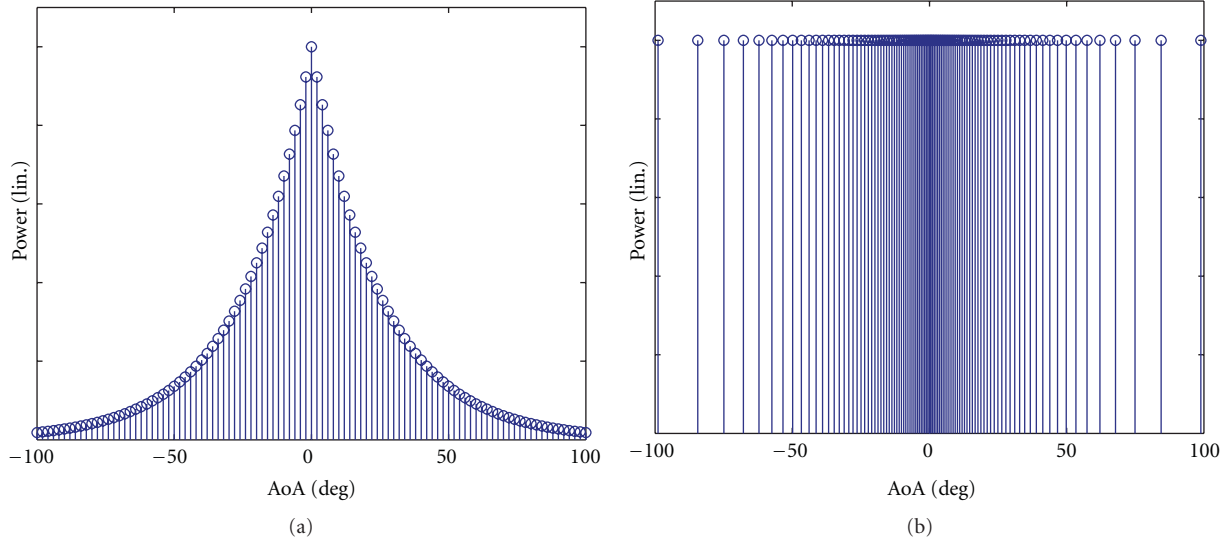


FIGURE 5: Uniform (a) and non-uniform (b) sampling of Laplacian function shaped PAS.

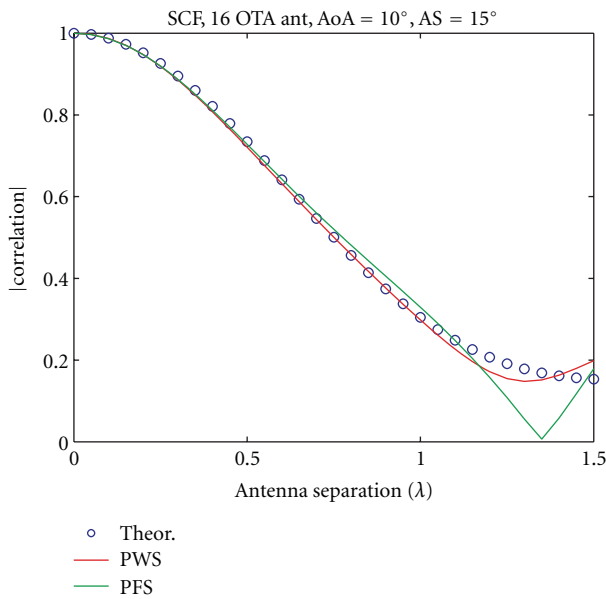


FIGURE 6: Simulated spatial correlations with 16 probes, AoA = 10°, and ASA = 15°.

should have only marginal effect on, for example, channel capacity. We may conclude that the both channel mapping methods are capable of creating spatial radio channel characteristics according to the target model in the simulated case.

5.2. XPR. The polarization dimension is evaluated by investigating XPR values. With this type of geometric models the exact polarization state is not specified, as discussed earlier. Thus it is not feasible to simulate and compare polarization states. In the simulation a nine-cluster target model was defined, with different per cluster XPR values. The

average power, received by an ideal vertically polarized DUT antenna, is the simulation result. Because Tx (base station) antenna was also vertically polarized ideal element, we get the simulated XPR directly by observing the Rx power and compensating out the path loss.

The simulated XPR values, achieved with the PFS method, and the target values are presented in the Figure 7. Also the deviation between target and simulation per cluster XPR values is shown. The maximum deviation in this simulation was below 0.2dB. In practical measurement the antenna nonidealities typically preclude this accurate results. The PWS method was excluded from the polarization simulation.

5.3. Doppler and Temporal Correlation. Simulated Doppler spectra from channel fading patterns generated with the PWS method (solid red) and the PFS method (solid green) are shown in Figure 8. The both spectra have similar spiky shape. Due to the nature of ray based geometric modelling it is difficult to compare the Doppler spectra directly. Especially any numerical comparison is practically impossible. Equivalent to the angular dimension, it is beneficial to transform spiky Doppler spectrum to a continuous domain of temporal correlation function.

TCF is a Fourier transform pair with the Doppler spectrum [21]. The transformation results to continuous function, which can be directly compared to a theoretical TCF. Such a comparison is depicted in the Figure 9, where real values of the complex temporal correlation coefficient are plotted. Temporal separation (delay) $\Delta\tau$ in the figure has a normalized unit of $1/2f_{\max}$, where f_{\max} is the maximum Doppler frequency component of the fading pattern. We can observe that the main lobe of the correlation resulting from both PWS (solid red) and PFS (solid green) methods follows almost perfectly the theoretical correlation (blue circles). PWS curve starts to deviate at the second peak of TCF while

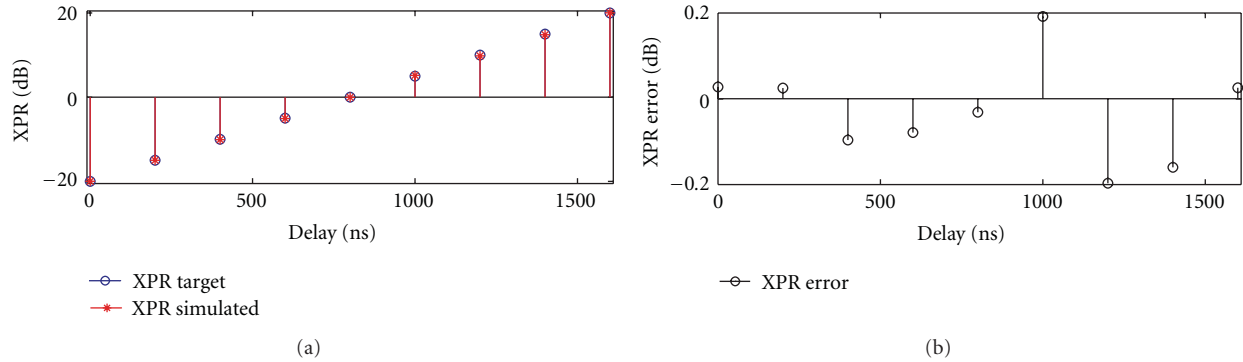


FIGURE 7: Simulated XPR with prefaded signals synthesis, target XPR is from -20 to $+20$ dB with 5 dB increments.

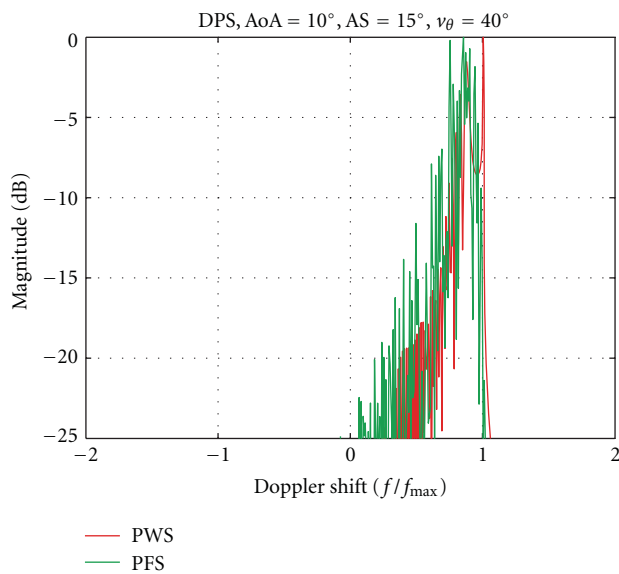


FIGURE 8: Simulated Doppler power spectra with 16 probes, AoA = 10° , and ASA = 15° .

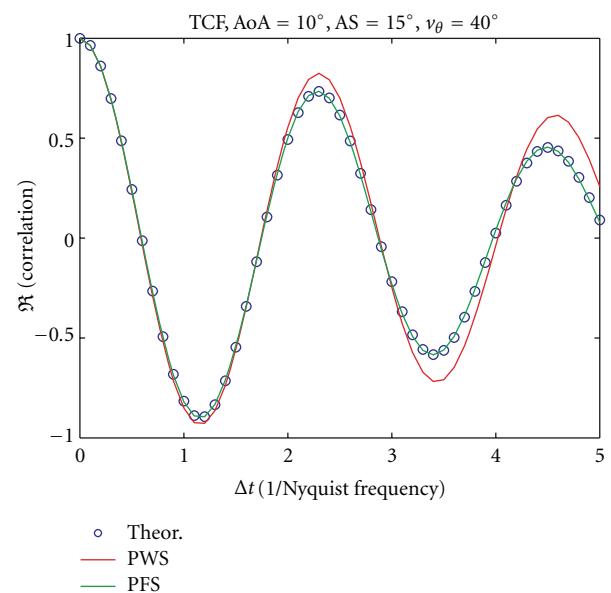


FIGURE 9: Simulated temporal correlations with 16 probes, AoA = 10° , and ASA = 15° .

PFS curve has excellent match over the range of simulated $\Delta\tau$.

In the simulation we created clusters by a set of plain waves having uniform arrival angles. Arrival angles determine Doppler shifts by relation $\nu = f_{\max} \cos(\varphi - \theta_\nu)$. The selection of 1° uniform angular sampling was probably not the optimal choice for creating accurate TCF. Some other angular sampling may have been better. Anyhow, the exact Doppler modelling is not the main focus of our contribution. The topic of defining parameters for a sum of rays based on temporal modelling is widely investigated by Pätzold, for example, in [25].

6. Discussion

In this paper we discussed the multiprobe MIMO OTA test system. We presented two alternatives to create radio propagation environment to MIMO OTA system, (1) prefaded approach and (2) plane wave approach. Both approaches

are feasible to generate given radio propagation environment and we conclude the paper to highlight the pros and cons of each approach.

Benefits of the prefaded signals synthesis are; phase calibration is not required, simplicity, and possibility to create non-geometrical Doppler spectra. We recommend prefaded signals synthesis for standard models with wide clusters and Rayleigh fading or Rician fading with a single LOS component. The LOS component, typically with a linear polarization state, can be created by rounding its AoA to the nearest dual polarized OTA probe. For that purpose the orthogonally polarized OTA antenna elements have to be colocated.

Main benefits of the plane wave synthesis for MIMO OTA compared to the prefaded signals synthesis are; support for LOS paths between OTA antennas, support for controlled polarization of paths (e.g., linear, circular, elliptic), and possibly more flexible support for dynamic (non stationary)

channel models. Plane wave synthesis may also compensate distortion effect resulting from limited physical dimensions of an OTA antenna ring. These effects are, for example, distortion due to varying path loss and curved phase fronts, as discussed in [26]. A drawback of the plane wave synthesis is the requirement of phase calibration.

Complex weights g_k for the plane wave synthesis are function of AoA and OTA antenna configuration only. For a fixed OTA antenna configuration it is possible to pre-calculate weights g_k , for example, for one degree grid of AoA values. In the actual generation of impulse response data the weights could be taken from a table and it would not be necessary to calculate them again. This would be a remarkable reduction of computing time in the case of dynamic channel models with time variant AoA and other propagation parameters.

Simulation results indicate that the spatial, polarimetric, and temporal dimensions of a target channel model can be created with the both methods. Delay dimension is a trivial modelling with a digital fading emulator applying either of PWS or PFS methods.

Acknowledgments

The research was partly conducted in the framework the CELTIC Project CP5-026 WINNER+ and partly of a research project, abbreviated MIMOTA, funded by the Finnish Funding Agency for Technology and Innovation (Tekes). The authors would like to acknowledge the contributions of their colleagues, especially Mr. Lassi Hentilä.

References

- [1] M. D. Foegelle, "Over-the-air performance testing of wireless devices with multiple antennas," *RF Design*, pp. 44–52, 2006.
- [2] <http://www.cost2100.org/>.
- [3] R. Verdone and A. Zanella, Eds., *Pervasive Mobile and Ambient Wireless Communications: COST Action 2100*, Springer, 2012.
- [4] <http://ic1004.org/>.
- [5] Vodafone, "Proposed SID revision for study item: measurement of radiated performance for MIMO and multi-antenna reception for HSPA and LTE terminals," 3GPP TSG-RAN 54, RP-111754, Berlin, Germany, 2011.
- [6] <http://www.ctia.org/>.
- [7] P. Kyösti, J. Nuutinen, J. Kolu, and M. Falck, "Channel modelling for radiated testing of MIMO capable terminals," in *Proceedings of the ICT-Mobile Summit*, Santander, Spain, June 2009.
- [8] V. Erceg, L. Schumacher, P. Kyritsi et al., "TGN channel models, IEEE P802.11 wireless LANs, <http://www.802wirelessworld.com:8802/>," Tech. Rep., IEEE, 2004.
- [9] D. S. Baum, J. Hansen, G. del Galdo, M. Milojevic, J. Salo, and P. Kyösti, "An interim channel model for beyond-3G systems: extending the 3GPP spatial channel model (SCM)," in *Proceedings of the IEEE 61st Vehicular Technology Conference (VTC '05)*, vol. 5, pp. 3132–3136, Stockholm, Sweden, May 2005.
- [10] P. Kyösti, J. Meinilä, L. Hentilä et al., "IST-4-027756 WINNER II deliverable 1.1.2. v.1.2, WINNER II channel models," Tech. Rep. IST-WINNER2, 2007.
- [11] "Guidelines for evaluation of radio interface technologies for IMTAdvanced, ITU-R Report M.2135," Tech. Rep., 2008, ITU-R.
- [12] J. P. Nuutinen, P. Kyösti, Y. Gao, and M. D. Foegelle, "On the MIMO OTA test system," in *Proceedings of the 5th International ICST Conference on Communications and Networking in China (ChinaCom '10)*, Beijing, China, August 2010.
- [13] 3GPP/3GPP2 TR 25.996 V6.1.0, "Spatial channel model for multiple input multiple output (MIMO) simulations," Tech. Rep., 2003, 3rd Generation Partnership Project.
- [14] L. Hentilä, P. Kyösti, and J. Meinilä, "Elevation extension for a geometry-based radio channel model and its influence on MIMO antenna correlation and gain imbalance," in *Proceedings of the 5th European Conference on Antennas and Propagation (EUCAP '11)*, pp. 2175–2179, Rome, Italy, April 2011.
- [15] T. Laitinen, P. Kyösti, and J. Nuutinen, "On the number of OTA antenna elements for plane-wave synthesis," in *Proceedings of the 4th European Conference on Antennas and Propagation (EuCAP '10)*, Barcelona, Spain, April 2010.
- [16] T. Imai, Y. Okano, K. Koshiro, K. Saito, and S. Miura, "Theoretical analysis of adequate number of probe antennas in spatial channel emulator for mimo performance evaluation of mobile terminals," in *Proceedings of the 4th European Conference on Antennas and Propagation (EuCAP '10)*, Barcelona, Spain, April 2010.
- [17] M. Sonkki, V. Hovinen, D. Sánchez-Escuderos, E. Salonen, and M. Ferrando-Bataller, "Scattering properties of wideband dual-polarized vivaldi antenna for MIMO OTA," in COST IC1004 TD(12) 03058, Barcelona, Spain, 2012.
- [18] P. Almers, E. Bonek, A. Burr et al., "Survey of channel and radio propagation models for wireless MIMO systems," *Eurasip Journal on Wireless Communications and Networking*, vol. 2007, Article ID 19070, 2007.
- [19] S. R. Saunders, *Antennas and Propagation for Wireless Communication Systems*, John Wiley & Sons, Chichester, UK, 1999.
- [20] R. Vaughan and J. B. Andersen, *Channels, Propagation and Antennas for Mobile Communications*, IET, London, UK, 2003.
- [21] M. Pätzold, "System function and characteristic quantities of spatial deterministic Gaussian uncorrelated scattering processes," in *Proceedings of the 57th IEEE Semiannual Vehicular Technology Conference (VTC '03)*, pp. 256–261, April 2003.
- [22] W. A. T. Kotterman, A. Heuberger, and R. S. Thomä, "On the accuracy of synthesised wave-fields in MIMO-OTA set-ups," in *Proceedings of the 5th European Conference on Antennas and Propagation (EUCAP '11)*, pp. 2560–2564, Rome, Italy, April 2011.
- [23] G. H. Golub and C. F. van Loan, *Matrix Computations*, The Johns Hopkins University Press, Baltimore, Md, USA, 3rd edition, 1996.
- [24] P. Kyösti, J. P. Nuutinen, and T. Jämsä, "MIMO OTA test concept with experimental and simulated verification," in *Proceedings of the 4th European Conference on Antennas and Propagation (EuCAP '10)*, Barcelona, Spain, April 2010.
- [25] M. Pätzold, *Mobile Fading Channels*, John Wiley & Sons, Chichester, UK, 2002.
- [26] P. Kyösti and L. Hentilä, "Criteria for physical dimensions of MIMO OTA multi-probe test setup," in *Proceedings of the 6th European Conference on Antennas and Propagation (EuCAP '12)*, Prague, Czech Republic, March 2012.

Research Article

Dependence of Error Level on the Number of Probes in Over-the-Air Multiprobe Test Systems

Afroza Khatun, Tommi Laitinen, Veli-Matti Kolmonen, and Pertti Vainikainen

*Department of Radio Science and Engineering SMARAD, Aalto University School of Electrical Engineering,
P.O. Box 13000, 00076 Aalto, Finland*

Correspondence should be addressed to Afroza Khatun, afroza.khatun@aalto.fi

Received 2 December 2011; Revised 9 March 2012; Accepted 19 March 2012

Academic Editor: Markus Landmann

Copyright © 2012 Afroza Khatun et al. This is an open access article distributed under the Creative Commons Attribution License, which permits unrestricted use, distribution, and reproduction in any medium, provided the original work is properly cited.

Development of MIMO over-the-air (OTA) test methodology is ongoing. Several test methods have been proposed. Anechoic chamber-based multiple-probe technique is one promising candidate for MIMO-OTA testing. The required number of probes for synthesizing the desired fields inside the multiprobe system is an important issue as it has a large impact on the cost of the test system. In this paper, we review the existing investigations on this important topic and end up presenting rules for the required number of probes as a function of the test zone size in wavelengths for certain chosen uncertainty levels of the field synthesis.

1. Introduction

The multiple-input multiple-output (MIMO) is a key technology for evolving wireless technologies including LTE and LTE-Advanced (or IMT-Advanced) [1]. It involves multiple antennas to enhance the capacity and throughput in multipath propagation environments. The MIMO performance in a multiantenna communication system depends on the antenna placement and design at the terminal and on the channel environment. Furthermore, since the MIMO radio channel is a combination of the antenna characteristics and the radio propagation conditions, the antenna performance metrics, such as gain, radiation efficiency, and the difference of gain between the multiple antennas, do not directly point towards the MIMO performance.

At the moment, development on measurement methodologies and figures of merit for assessing the overall MIMO performance is being conducted by Radio Access Networks working group 4 (RAN4) of 3GPP [2] in Europe and by CTIA [3] in the North America. Over-the-air (OTA) testing, which has been used for single-input single-output (SISO) performance evaluation [4, 5], is an obvious choice also for MIMO performance evaluation; additionally radiopropagation channel must be taken into account. Several test methods have been proposed [6–14]. A strong candidate for the MIMO performance metrics is throughput [15].

The three main candidates MIMO-OTA test methods [6–14] are (1) anechoic chamber and fading emulator-based multiprobe methods [6–9], (2) reverberation chamber based methods [10–13], and (3) multistage method, often refers to the “two-stage” method [14]. In the latter one the first stage involves the pattern measurement of the device under test (DUT) over the air, and the second stage involves combining of the DUT patterns with the radio-propagation channel data and performing the MIMO performance test conductively.

It is now noted that geometric reference channel models with well-defined characteristics such as complex amplitudes, directions of arrival (DoA), directions of departure (DoD), the delays, and polarizations of the multipath components constitute a good means to describe the radio-propagation channel. These channel models are well accepted by 3GPP [2], and the use of such well-defined channel models in the MIMO OTA performance evaluation is very well justified for the sake of the repeatability of testing [15]. Several reference models have been proposed by [15], such as SCME TDL and WINNER II CDL models, as well as simplified single spatial cluster models.

The difficulty with reverberation chamber-based methods is that they are not well suited for synthesizing such channel conditions that would be in line with any geometric radio channel model. The two-stage method on the other hand has the problem with the cable connection to the

antenna ports it requires, which means that the test is never performed in the realistic usage conditions of the DUT. From these technical points of view the anechoic chamber and fading emulator-based multiprobe methods appear to be the most promising method for MIMO performance evaluation.

One of the key issues addressed in anechoic chamber and fading emulator-based multiprobe systems is the number of required probes. Due to the fact that the cost for such a multiprobe system increases rapidly with the required number of probes, it becomes important to analyze in detail what the required number of probes is. The purpose of this paper is to establish accurate rules for the number of probes required for synthesizing the radio propagation channel inside the multiprobe system as a function of the size of the DUT in wavelengths and the uncertainty level of the field synthesis. These rules concern particularly 2D circular multiprobe systems, and hence they support well the development of test methods relying on 2D channel models like SCME and WINNER II. Here, the synthesis of the electromagnetic fields is conducted using the spherical wave theory which has been widely used in the spherical near-field as well as far-field antenna measurements to model the 3D radiation from antennas [16].

First, a review on existing studies on the required number of probes is presented in Section 2. The well-known general rules for the number of probes are first presented in Section 3, and the accurate rules are established in Section 4. Conclusions are given in Section 5.

2. Review of the Existing Investigations on the Number of Probes

2.1. General. Anechoic chamber- and fading emulator-based multiprobe methods involve several probes placed on a circle in 2D case or on a sphere in 3D case, and the DUT is in the center of the circle or sphere [6–9, 17]. An illustration of a 2D MIMO OTA test system based on multiprobe technology is in Figure 1.

The base station emulator creates the test signal which is fed to the fading emulator to create delay dispersion, Doppler spectra, and fast fading behavior. The emulator is connected to the probes inside the anechoic chamber with the prefaded signal. To achieve a high level of accuracy, more probes are needed to emulate the desired power azimuth spectra (PAS) around the test zone (the test zone is the geometrical volume inside which the DUT is located during the measurement) of the DUT.

In [17–22] studies have been done which directly provide rules for or discuss theoretically how to determine the required number of probes and the test zone size with a given accuracy. Two different ways for determining the required number of probes as well as the test zone size can be identified: (i) through spatial correlation function [18–20] and (ii) through plane wave synthesis [17, 21, 22]. The analysis is done (a) for the multiple cluster 2D channel model with uniform distributed PAS, where the probes are assumed to be placed equidistantly in 360° angular region in φ ($\theta = 90^\circ$) and (b) for the single cluster spatial 2D channel model with the Laplacian distributed PAS when

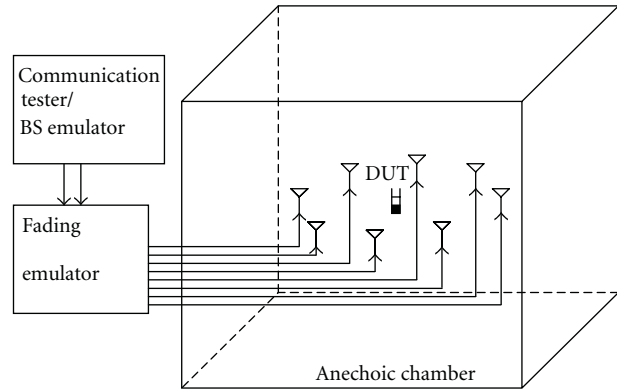


FIGURE 1: Illustration of a MIMO-OTA test system based on multiprobe technology.

the freedom of placing the probes in an optimum angular sector is considered. In this section we review those concepts reported in [17–22] and make a comparison between the obtained results.

2.2. Spatial Correlation Function. Spatial correlation characteristics, which influence the MIMO transmission performance, depend on the PAS of the radio channel. These characteristics are often expressed using the Bessel series of the Fourier spectrum of the PAS as coefficients. In [18–20] investigations have been performed on the required number of probes through spatial correlation function of the PAS for both the multiple-cluster model and the single-cluster model with the criterion that the correlation deviation, as defined in [18–20], should be less than 0.1.

2.3. Plane Wave Synthesis. The plane wave synthesis technique reported in [17, 21, 22] is based on the synthesis of the electromagnetic field environment using the spherical wave theory [16]. In [17, 21, 22] the influence of the number of probes on the geometrical size of the test zone and the quietness of the test-zone field in terms of an equivalent reflectivity level has been investigated for the 2D case. Here, the equivalent reflectivity level means the maximum relative error between the synthesized plane-wave field and a target plane-wave field on the circumference of the test zone. Hence, the given reflectivity level values are the worst case values. In [17, 21, 22], the required number of probes is calculated as a function of different accuracy level and test zone size. It is noted that the number of probes required to synthesize the incoming plane waves with a fixed accuracy is dictated by the radius of the test zone and not affected by the number of incoming plane waves of the channel model.

2.4. Comparison between the Obtained Results of Required Number of Probes and Test Zone Size. The comparisons of the results for the required number of probes as a function of test zone size obtained by different methods given in [17–21] are presented in Figures 2 and 3. The results in Figure 2 are for the multiple-cluster model with uniform distributed PAS where the probes are assumed to be placed equidistantly

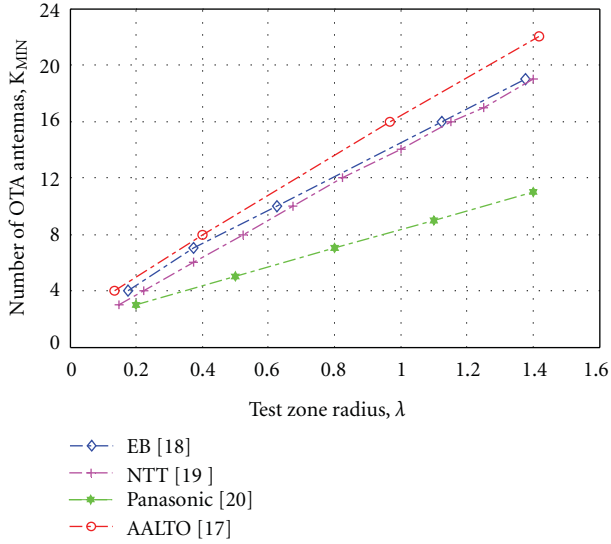


FIGURE 2: The number of probes as a function of the test zone radius for the multiple cluster model with uniform distributed PAS when the probes are placed equidistantly over the 360° angular region in φ .

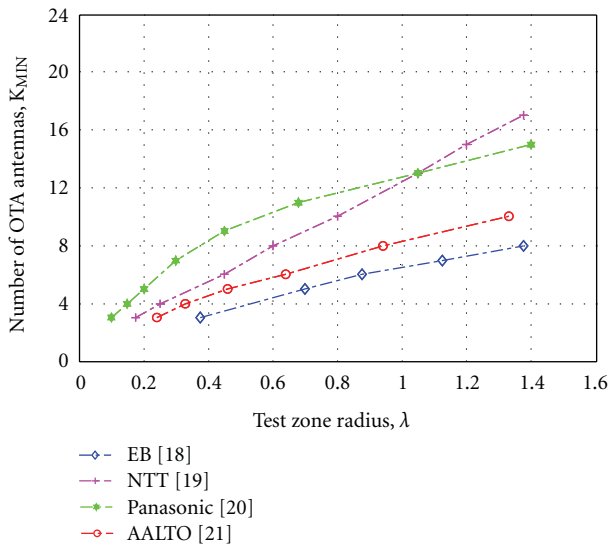


FIGURE 3: The number of probes as a function of the test zone radius for the single cluster model with the Laplacian distributed PAS with the angular spread of 35° when the probes are placed in an optimum azimuth region.

in 360° angular region in φ . The results in Figure 3 are for the single cluster model with the Laplacian distributed PAS with the power angular spread of 35° when the probes are placed in an optimum azimuth region. In [18–20] the number of probes is determined with the correlation deviation of 0.1. For the plane wave synthesis technique [17, 21], a -15 dB equivalent reflectivity level is considered here for the comparison which gives the correlation deviation between the target and synthesis fields of 0.1 approximately.

For the multiple-cluster model, the results obtained from [17–19] show the similar trend with just a small difference, but the results in [20] clearly provide different values compared to the others. For the single-cluster model with the Laplacian distributed PAS with the angular spread of 35° , the results obtained from [19, 20] show some difference from the other results obtained from [18, 21]

Based on the analysis, the same conclusion is drawn in [17–19, 21]; that is, for the synthesis of the multiple-cluster model, a higher number of probes is needed than for the single-cluster model with the Laplacian distributed PAS when the probes are placed in an optimum azimuth region. From the simulated results presented in [20], a remarkable difference on the number of probes for synthesizing the Laplacian-distributed PAS is observed. It is stated in [20] that the number required for the Laplacian distributed PAS is higher than that for the uniform distributed PAS. The likely reason is that the weights for the probes are obtained by directly synthesizing the PAS rather than the field.

Although there are some differences in the results between the two techniques, we have chosen to go deeper to the theory with the plane wave synthesis technique in the next section of this paper. The reason for this is that the plane wave synthesis technique provides a straightforward way for the theoretical justification of the number of probes through the plane wave to spherical wave expansion (SWE) and the well-known cut-off properties of the spherical wave functions. In the following section we will present the plane wave synthesis technique in more detail in a similar fashion as presented in [17, 21, 22].

3. General Rules for the Required Number of Probes

3.1. Introduction. The electromagnetic fields in the test zone, which are synthesized by the probes located either on a 2D circle around the DUT or on a 3D spherical surface, may be considered for composing plane wave fields arriving from different spatial directions at the centre of the test zone. Any radio channel conditions may as well be considered as a sum of plane waves by additionally taking into account, for example, the delay spread and Doppler effects, by using proper RF electronics.

The purpose of this section is to briefly review the spherical wave theory in the context of plane wave fields and to present the well-known general rules for the number of required probes for the plane wave synthesis. These general rules provide the basis for establishing the accurate rules for the number of required probes later in Section 4.

3.2. Spherical Wave Expansion of the Plane Wave Field. The electric field $\vec{E}_0 e^{i\vec{k}_0 \cdot \vec{r}}$ of a time-harmonic plane wave coming from a direction (θ_0, φ_0) in free space can be represented by an infinite sum of SWE modes as [16]

$$\vec{E}_0 e^{i\vec{k}_0 \cdot \vec{r}} = \frac{k}{\sqrt{\eta}} \sum_{s=1}^2 \sum_{n=1}^{\infty} \sum_{m=-n}^n Q_{smn}^{(1)} \vec{F}_{smn}^{(1)}(r, \theta, \varphi). \quad (1)$$

Here \bar{E}_0 describes the amplitude and complex polarization of the wave, $\bar{k}_0 = -k \sin \theta_0 \cos \varphi_0 \bar{u}_x - k \sin \theta_0 \sin \varphi_0 \bar{u}_y - k \cos \theta_0 \bar{u}_z$ is the propagation vector, k is the wave number, η is the wave admittance of the medium, s , m , and n are the spherical mode indices, $Q_{smn}^{(1)}$ are the spherical vector wave coefficients for spherical standing waves, and $\bar{F}_{smn}^{(1)}(r, \theta, \varphi)$ represent the corresponding power normalized spherical vector wave functions in standard spherical coordinates (r, θ, φ) [16].

3.3. Cut-Off Property and General Rules for Minimum Number of Probes. It is known that the spherical vector wave functions $\bar{F}_{smn}^{(1)}(r, \theta, \varphi)$ are separated into radial, elevation, and azimuth functions, where the radial functions are the spherical Bessel functions and their derivative functions, the elevation functions are the associated Legendre functions, and the azimuth functions are the exponential functions [16]. Importantly, due to the cut-off property of the spherical-wave functions, in particular that of the spherical Bessel function and its derivative function, the expansion in (1) can be truncated appropriately at a finite $n = N$. Hence the expansion of the plane wave field with the truncated series of spherical wave functions becomes

$$\bar{E}_0 e^{i\bar{k}_0 \cdot \bar{r}} = \frac{k}{\sqrt{\eta}} \sum_{s=1}^2 \sum_{n=1}^N \sum_{m=-n}^n Q_{smn}^{(1)} \bar{F}_{smn}^{(1)}(r, \theta, \varphi), \quad (2)$$

where the truncation number N is

$$N = [kr_0 + n_1]. \quad (3)$$

In (3) r_0 is the radius of the spherical test zone, n_1 is a small integer number, and the square brackets indicate the nearest integer number greater than or equal to the number inside the brackets. Typically, n_1 varies from $n_1 = 0$ to 10 [16] depending on the desired accuracy of the field characterization (or synthesis). The triple summation over $n = 1 \cdot \dots \cdot N$, $m = -n \cdot \dots \cdot n$ and $s = 1, 2$ in (2) has in total $J = 2N(N + 2)$ terms. Hence, with (3) the number of spherical wave modes J can be written as

$$J = 2N(N + 2) = 2([kr_0 + n_1])^2 + 4([kr_0 + n_1]). \quad (4)$$

Now, in theory, for synthesizing all J modes, the minimum number of probes, K_{MIN} , is equal to the number of modes J . Hence, the general rules for required number of probes becomes

$$K_{\text{MIN}} = 2([kr_0 + n_1])^2 + 4([kr_0 + n_1]). \quad (5)$$

The noticeable issue in (5) is that the number of the probes K_{MIN} is proportional to the square of the test zone radius r_0 for $r_0 \gg 1/k$ and the value of n_1 .

It is noted that the general rules for the required number of probes presented in (5) are for the 3D case, where the probes are distributed over a sphere and both the elevation and azimuthal distribution of the incoming waves are considered. However, in the case of such 2D channels like SCM or SCME, where the test zone fields are coming from the direction of $\theta_0 = 90^\circ$, we need to consider only the

azimuthal distribution of the incoming field. Hence, we need to consider only the azimuthal dependency of the spherical wave function in (2), and the expansion can be presented by

$$\begin{aligned} \bar{E}_\theta e^{i\bar{k}_0(\theta_0=90^\circ) \cdot \bar{r}} &= \sum_{m=-N}^N \bar{C}_m^\theta(r, \theta = 90^\circ) e^{im\varphi}, \\ \bar{E}_\varphi e^{i\bar{k}_0(\theta_0=90^\circ) \cdot \bar{r}} &= \sum_{m=-N}^N \bar{C}_m^\varphi(r, \theta = 90^\circ) e^{im\varphi}, \end{aligned} \quad (6)$$

where \bar{E}_θ and \bar{E}_φ are the vertical and horizontal polarizations of the test zone field. The \bar{C}_m^θ and \bar{C}_m^φ are the azimuthal mode coefficients of the test zone field derivable from (2). In this way, instead of having a triple summation as in (2), we have, for the two polarizations, a single summation over all m azimuthal modes with $2N + 1$ terms. Hence, by including the two polarizations, the number of required modes J_1 for the field characterization becomes

$$J_1 = 2(2N + 1) = 4([kr_0 + n_1]) + 2, \quad (7)$$

which directly indicates the minimum number of probes, K_{MIN} for 2D case. Hence, the general rules for required number of probes in 2D case becomes

$$K_{\text{MIN}}^{2\text{D}} = 4([kr_0 + n_1]) + 2. \quad (8)$$

Here the superscript 2D refers to the 2D case. Now $K_{\text{MIN}}^{2\text{D}}$ is proportional to the test zone radius r_0 for $r_0 \gg 1/k$ and the value of n_1 .

4. Accurate Rules for the Number of Required Probes in the 2D Case

In (5) and (8) of Section 3, we presented the well-known general rules for the minimum number of probes as a function of the radius of the test zone in wavelengths through the spherical wave theory. The equations contain the unknown number n_1 related to the accuracy of the field synthesis. Although for practical applications the range in which n_1 can vary is relatively small, from approximately 0 to 10 [16, 23], the choice of n_1 significantly affects the K_{MIN} . The purpose of this section is to find accurate values for n_1 for certain selected uncertainty levels of the field synthesis for, in particular 2D case. This we do by reviewing the work done in [17] and by making use of the findings in [24].

In [17] the influence of the number of probes on the test zone size and the quietness of the test zone field in terms of the equivalent reflectivity level have been analyzed for the 2D multiple cluster case. In that study the equivalent reflectivity level refers to the maximum relative error (ε) between the synthesized (E_{syn}) and the target (E_{tar}) plane wave fields as

$$\varepsilon = \max \left(\frac{|E_{\text{syn}} - E_{\text{tar}}|}{\max(|E_{\text{tar}}|)} \right). \quad (9)$$

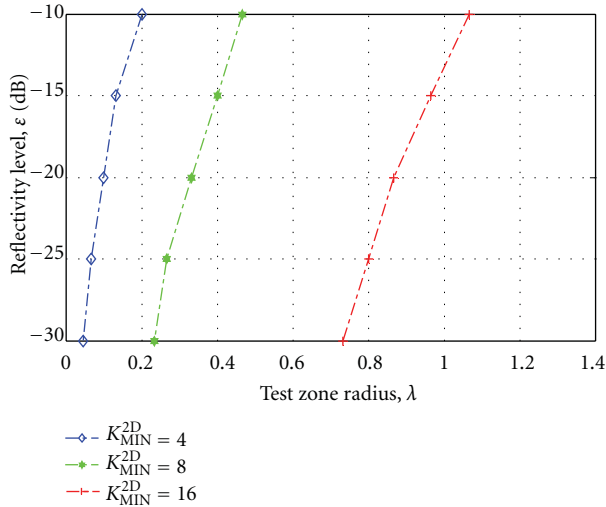


FIGURE 4: The equivalent reflectivity level as a function of the test zone radius for different number of probes for a single-polarized probes in 2D case.

The synthesis was performed by a simple 2-norm matching of the fields of the probes with the incoming plane wave fields arriving to the test zone. The z-polarized (vertically polarized) electrical Hertzian dipoles were considered as probes, and they were placed in the horizontal plane ($\theta = 90^\circ$) on the entire 360° angular region with constant φ intervals and the synthesis of the z-polarized plane wave field arriving from ($\theta = 90^\circ$) was investigated. For the considered single-polarized case, the required number of probes is $K_{\text{MIN}}^{2\text{D}} = 2[kr_0 + n_1] + 1$ instead of the form of (8) for the dual-polarized case. A summary of the results of this investigation is presented in Figure 4.

The results presented in Figure 4 clearly show that the number of probes, $K_{\text{MIN}}^{2\text{D}}$, increases as a function of the test zone radius for any selected equivalent reflectivity level. Now, our goal is to find the values for n_1 in (8) so that this equation would be in line with the results shown in Figure 4, of course by taking into account the fact that (8) is for the dual-polarized case and the results in Figure 4 for the single-polarized case. We make use of the same assumptions for calculating the values for n_1 as presented in [24], where it has been proposed that n_1 would depend on kr_0 as

$$n_1 = o\left(\sqrt[3]{kr_0}\right). \quad (10)$$

As a result of this, appropriate values for n_1 are found, and they are tabulated in Table 1 for the different uncertainty levels of the field synthesis.

The values of n_1 in Table 1 constitute the important contribution of this paper. Applying these values of n_1 in (8) directly provides the minimum number of required probes (dual-polarized) as a function of the radius of the test zone in wavelengths ($k = 2\pi/\lambda$) for the chosen uncertainty level of the field synthesis for the 2D case.

It is important to note that the values of n_1 in Table 1 have been established with the values of kr_0 in the range

TABLE 1: The values of n_1 for different uncertainty levels for the 2D case.

Equivalent reflectivity level, ε	n_1
-10 dB	$0.37 \times \sqrt[3]{kr_0}$
-15 dB	$0.74 \times \sqrt[3]{kr_0}$
-20 dB	$1.08 \times \sqrt[3]{kr_0}$
-25 dB	$1.45 \times \sqrt[3]{kr_0}$
-30 dB	$1.85 \times \sqrt[3]{kr_0}$

from approximately 0.2 to 6.1 from the basis of the results reported in [17]. It has been intentionally chosen that the square bracket round the number inside the bracket to the nearest integer larger than the number, because in that case, for small values of kr_0 , (8) together with the values of n_1 indicates that the required number of probes would be 6 for the dual-polarized case and 3 for the single-polarized case. This is as it should be, because even if the DUT is electrically very small, it may still radiate the 3 azimuthal dipole modes [16] in single polarization. Having said this, it can be claimed that the values of n_1 may be considered to be well applicable also for values of kr_0 less than 0.2. It is further noted that, by comparison of the result of this paper with those presented in [25], we may conclude the values of n_1 are practically applicable for large values of kr_0 , too. Although the application in [25] is the modeling of the radiation of DUTs and the application of this paper is the field synthesis, both rely on the spherical wave theory and the cut-off property of the spherical vector wave functions, and hence, these two things may be considered comparable.

Here we have derived the accurate rules for the required number of probes for the 2D case only. Similar accurate rules could as well be derived for the 3D case, and instead of using (8), (5) would provide the required number of probes for that case. The values that we have provided for n_1 in Table 1 are for the 2D case. However, it is evident from [25] that the values of n_1 for the 2D case serve as a good approximation of those for the 3D case.

5. Conclusions

Anechoic chamber- and fading emulator-based multiprobe method is a very promising method for MIMO performance testing. A crucial aspect largely dictating the cost of the test system, the required number of probes for synthesizing the desired fields inside the multiprobe system, has been examined in this paper. First, through the review of the well-known spherical wave theory, the general rules for the number of probes required for synthesizing the radio propagation channel inside the multiprobe system as a function of the size of the DUT in wavelengths have been presented for both 2D and 3D cases. Based on the results presented in existing literature, accurate rules for the minimum number of required probes for the 2D case have been established that take into account also the uncertainty level of the field synthesis.

Acknowledgments

The research was conducted in the framework of a research project, abbreviated MIMOTA, funded by the Finnish Funding Agency for Technology and Innovation (Tekes) and the companies Nokia, Elektrobit, Pulse Engineering, and ETS-Lindgren and also in the SMARAD centre of excellence funded mainly by the Academy of Finland. Furthermore, T. Laitinen thanks the Academy of Finland (decision notification no. 129055) for the financial support of this work.

References

- [1] S. Sesia, I. Toufik, and M. Baker, *LTE-The UMTS Long Term Evolution*, John Wiley & Sons, Chichester, UK, 2nd edition, 2011.
- [2] <http://www.3gpp.org/>.
- [3] <http://www.ctia.org/>.
- [4] 3GPP TS 34.114, "User equipment (UE) / mobile station (MS) over the air (OTA) antenna performance; conformance testing (release 7)," September 2009.
- [5] CTIA Certification, *Test Plan for Mobile Station Over the Air Performance, Method of Measurement for Radiated RF Power and Receiver Performance, Revision Number 2.2.2*, December 2008.
- [6] Elektrobit, "Updated concept—MIMO OTA testing," 3GPP TSG-RAN4 R4-092435.
- [7] Vodafone, Panasonic, and Tokyo Institute of Technology, "MIMO OTA testing using RF controlled spatial fading emulator," in *R4-091390, 3GPP TSG RAN4 Meeting*, Seoul, South Korea, March 2009.
- [8] Y. Okano, K. Kitao, and T. Imai, "Impact of number of probe antennas for MIMO OTA spatial channel emulator," in *Proceedings of the 4th European Conference on Antennas and Propagation (EuCAP '10)*, April 2010.
- [9] A. Yamamoto, T. Sakata, H. Iwai et al., "BER measurements on a handset adaptive antenna array in the presence of Co-channel interference generated using a spatial fading emulator," in *Proceedings of the IEEE Antennas and Propagation Society International Symposium*, pp. 26–29, Washington, DC, USA, July 2005.
- [10] P. S. Kildal and K. Rosengren, "Correlation and capacity of MIMO systems and mutual coupling, radiation efficiency, and diversity gain of their antennas: simulations and measurements in a reverberation chamber," *IEEE Communications Magazine*, vol. 42, no. 12, pp. 104–112, 2004.
- [11] D. Kurita, Y. Okano, S. Nakamatsu, and T. Okada, "Over-The-Air performance testing system for MIMO antennas employing reverberation chamber," IEICE Technical Report A·P2009-34, 2009.
- [12] C. Wright and S. Basuki, "Utilizing a channel emulator with a reverberation chamber to create the optimal MIMO OTA test methodology," in *Proceedings of the Global Mobile Congress (GMC '10)*, October 2010.
- [13] J. F. Valenzuela-Valdés, A. M. Martínez-González, and D. A. Sánchez-Hernández, "Emulation of MIMO nonisotropic fading environments with reverberation chambers," *IEEE Antennas and Wireless Propagation Letters*, vol. 7, pp. 325–328, 2008.
- [14] Y. Jing, Z. Wen, H. Kong, S. Duffy, and M. Rumney, "Two-stage over the air (OTA) test method for MIMO device performance evaluation," in *Proceedings of the IEEE International Symposium on Antennas and Propagation (APSURSI '11)*, pp. 71–74, July 2011.
- [15] Measurement of radiated performance for MIMO and multi antenna reception for HSPA and LTE terminals (Release 10) 3GPP TR 37.976 V1.1.0 (2010-05), R4-102357.
- [16] J. E. Hansen, *Spherical Near-Field Antenna Measurements*, Peter Peregrinus, London, UK, 1988.
- [17] T. Laitinen, J. Toivanen, P. Kyösti, J. Nuutinen, and P. Vainikainen, "On a MIMO-OTA testing based on multi-probe technology," in *Proceedings of the 20th URSI International Symposium on Electromagnetic Theory (EMTS '10)*, pp. 227–230, August 2010.
- [18] P. Kyösti, J. Nuutinen, and T. Jämsä, "Simulated correlation accuracy of MIMO OTA spatial fading emulator," in *COST-2100, 11th MCM, TD(10)11061*, Alborg, Denmark, June 2010, <http://www.cost2100.org/>.
- [19] T. Imai, Y. Okano, K. Koshiro, K. Saito, and S. Miura, "Theoretical analysis of adequate number of probe antennas in spatial channel emulator for mimo performance evaluation of mobile terminals," in *Proceedings of the 4th European Conference on Antennas and Propagation (EuCAP '10)*, April 2010.
- [20] Panasonic and Tokyo Institute of Technology, "Procedure of the determining the dimension of a spatial fading emulator," in *R4-094317, 3GPP TSG RAN4 Meeting*, Jeju, South Korea, November 2009.
- [21] T. Laitinen, P. Kyösti, T. Jämsä, and P. Vainikainen, "Generation of a field with a laplacian-distributed power azimuth spectrum scattered by a single cluster in a MIMO-OTA test system based on multiple probe antennas," in *Proceedings of the Asia-Pacific Microwave Conference (APMC '10)*, pp. 2127–2130, December 2010.
- [22] T. Laitinen, P. Kyösti, J. P. Nuutinen, and P. Vainikainen, "On the number of OTA antenna elements for planewave synthesis in a MIMO-OTA test system involving a circular antenna array," in *Proceedings of the 4th European Conference on Antennas and Propagation (EuCAP '10)*, April 2010.
- [23] T. Laitinen, *Advanced Spherical Antenna Measurements*, Thesis for the degree of the Doctor of Science in Technology, Helsinki University of Technology, Espoo, Finland, December 2005.
- [24] V. I. Turchin and N. M. Tseytlin, "Antenna testing based on near-field measurements," *Radio Engineering & Electronic Physics*, vol. 24, no. 12, pp. 1–26, 1979.
- [25] F. Jensen and A. Frandsen, "On the number of modes in spherical wave expansions," in *Proceedings of the 26th Annual Meeting & Symposium of the Antenna Measurement Techniques Association (AMTA '04)*, Atlanta, GA, USA, October 2004.

Research Article

MIMO Channel Capacity in 2D and 3D Isotropic Environments

Ryan J. Pirkl and Kate A. Remley

Electromagnetics Division, National Institute of Standards and Technology, RF Fields Group, 325 Broadway Street, MS 818.02, Boulder, CO 80305, USA

Correspondence should be addressed to Ryan J. Pirkl, ryan.pirkl@nist.gov

Received 5 January 2012; Accepted 19 March 2012

Academic Editor: Markus Landmann

Copyright © 2012 R. J. Pirkl and K. A. Remley. This is an open access article distributed under the Creative Commons Attribution License, which permits unrestricted use, distribution, and reproduction in any medium, provided the original work is properly cited.

We analyze theoretical distributions of MIMO channel capacity for different antennas in 2D and 3D statistically isotropic environments, which may be generated by multiprobe anechoic and reverberation chambers, respectively. We observe that the two environments yield comparable capacity distributions provided that (1) the 2D statistically isotropic environment's capacity data are taken at many different antenna orientations and (2) the radiation elements have a low directivity. When these conditions are met, we find that the relative error between the 2D statistically isotropic environment's orientation-combined capacity distribution and the 3D statistically isotropic environment's capacity distribution is typically less than 10% for signal-to-noise ratios greater than 5 dB.

1. Introduction

Multiprobe anechoic chambers and reverberation chambers are capable of generating 2D and 3D statistically isotropic environments, respectively, suitable for over-the-air (OTA) testing of multiple-input multiple-output (MIMO) wireless terminals [1–3]. In CTIA, 3GPP's RAN4, and COST 2100 both multiprobe anechoic and reverberation chambers are being considered for adoption into certification test procedures for MIMO handsets [1, 4–6]. It is possible that test procedures based on both chambers may be adopted, but it is unclear to what extent their test results are comparable. Here, we compare the statistically isotropic environments generated by multiprobe anechoic and reverberation chambers in terms of their capacity distributions for different MIMO antennas-under-test (AUTs).

Capacity determines the maximum obtainable throughput for a wireless device. The relationship between capacity and throughput implies that 2D and 3D statistically isotropic environments will only provide comparable *device* performance test results if their capacity statistics are comparable for any given AUT. Prior work has used channel simulations to compare the mean capacity of 2D and 3D statistically isotropic environments [2]. For a single orientation of the

AUT, large differences in the channel's mean capacity were observed for the 2D and 3D statistically isotropic environments. In contrast, by changing the orientation (and position) of the AUT between simulation trials, the mean capacities of the antennas converged to the same value in both environments.

We expand on the results presented in [2] by comparing the two environments' *theoretical distributions* of MIMO channel capacity for several AUTs. Our procedure extends the analysis presented in [7] to the problem of comparing capacity distributions for MIMO OTA test environments. We observe that for a single orientation of the AUT, the capacity distributions obtained from the two environments are unlikely to be comparable due to the orientation dependence of the 2D isotropic environment's capacity statistics. This is due to the well-known environment dependence of each AUT's complex correlation coefficient and mean effective gains (cf., [7–9]). We also observe that differences in the 2D and 3D environments' capacity distributions may be reduced substantially by comparing the 3D environment's *orientation-independent* capacity distribution to the 2D environment's *orientation-combined* capacity distribution, which is the distribution formed when capacity realizations are combined from different orientations of the AUT. However, we find

that the difference between these two capacity distributions is small (e.g., within 10%) only if the AUTs use low-directivity elements; for high-directivity elements, the difference between the capacity distributions may exceed 20%. This suggests that discrepancies between device performance tests in statistically isotropic environments generated by multiprobe anechoic and reverberation chambers will be small provided that (1) the DUT's performance in the multiprobe anechoic chamber is evaluated at many different orientations, and (2) the DUT's dimensions are on the order of a wavelength or less such that the directivities of the antenna elements are low.

We begin in Section 2 by reviewing the covariance between the signals received by the elements of an AUT when it is placed in a random electromagnetic field. In Section 3, we define the power-angle spectra for 2D and 3D statistically isotropic environments, as well as the set of antenna configurations used in our numerical study of MIMO channel capacity. Capacity distributions for the AUTs in each test environment are presented and analyzed in Section 4. Section 5 explores why certain antenna configurations are more sensitive to orientation in 2D statistically isotropic environments than others. Section 6 summarizes the paper.

2. Antennas in Random Electromagnetic Fields

Let us consider a two-element antenna in a time-harmonic electromagnetic field. Assuming the antenna is in the far-field, whereby the electromagnetic field is composed entirely of homogeneous plane waves, we may express the signal x_i received by the i th antenna element as [8]

$$x_i = \int d\Omega \mathbf{A}_i(\Omega) \cdot \mathbf{F}(\Omega), \quad (1)$$

where $i \in \{1, 2\}$, \cdot denotes the vector dot product, $\mathbf{A}_i(\Omega)$ is the i th element's complex vector radiation pattern defined as

$$\mathbf{A}_i(\Omega) = A_{ih}(\Omega)\hat{\mathbf{h}} + A_{iv}(\Omega)\hat{\mathbf{v}}, \quad (2)$$

and $\mathbf{F}(\Omega)$ is the field's complex vector plane-wave spectrum defined as

$$\mathbf{F}(\Omega) = F_h(\Omega)\hat{\mathbf{h}} + F_v(\Omega)\hat{\mathbf{v}}. \quad (3)$$

In (2) and (3), $\hat{\mathbf{h}}$ and $\hat{\mathbf{v}}$ are the two orthogonal unit vectors defining the horizontal and vertical polarizations, respectively, and Ω denotes a point on the unit sphere with $\int d\Omega$ corresponding to an integration over the unit sphere.

To constrain the scope of our capacity analysis, we consider power-normalized radiation patterns for which

$$\int d\Omega \|\mathbf{A}_i(\Omega)\|^2 = 4\pi. \quad (4)$$

That is, $\|\mathbf{A}_i(\Omega)\|^2$ is equal to the directivity of the i th antenna element, where we neglect impedance mismatches and ohmic loss [8]. We recognize that mismatches and loss do affect the capacity of the MIMO wireless channel by way of a reduction in the signal-to-noise ratio (SNR) and, potentially,

a gain imbalance at the receiver [10]. However, because impedance mismatches and ohmic losses are solely antenna-related quantities that are independent of the environment's power-angle spectrum, their effect on capacity does not provide insight into the differences between MIMO device tests in 2D and 3D statistically isotropic environments.

To describe a random electromagnetic field, we may specify the components, $F_h(\Omega)$ and $F_v(\Omega)$, of the plane-wave spectrum to be random variables characterized by the following covariances [11–13]:

$$\begin{aligned} \mathcal{E}\{F_h(\Omega)F_h^*(\Omega')\} &= P_h(\Omega)\delta(\Omega - \Omega'), \\ \mathcal{E}\{F_v(\Omega)F_v^*(\Omega')\} &= P_v(\Omega)\delta(\Omega - \Omega'), \\ \mathcal{E}\{F_h(\Omega)F_v^*(\Omega')\} &= \mathcal{E}\{F_v(\Omega)F_h^*(\Omega')\} = 0, \end{aligned} \quad (5)$$

where $\mathcal{E}\{\cdot\}$ denotes the expectation operator, $\delta(\cdot)$ is the Dirac delta function, and $P_h(\Omega)$ and $P_v(\Omega)$ are real quantities that describe the power density versus angle-of-arrival for horizontally and vertically polarized incident plane waves, respectively. The electromagnetic field's vector power-angle spectrum is given by

$$\mathbf{P}(\Omega) = P_h(\Omega)\hat{\mathbf{h}} + P_v(\Omega)\hat{\mathbf{v}}. \quad (6)$$

Denoting P_0 as the total power *available* to an AUT, we define the vector power-angle spectrum such that

$$\int d\Omega [\mathbf{P}(\Omega) \cdot \hat{\mathbf{h}} + \mathbf{P}(\Omega) \cdot \hat{\mathbf{v}}] = P_0. \quad (7)$$

The covariance between the signals received by the i th and j th antenna elements is defined as [13]

$$\mathcal{E}\{x_i x_j^*\} = \rho_{ij} \sigma_i \sigma_j, \quad (8)$$

where σ_i and σ_j are the standard deviations of the signals received by i th and j th antenna elements, respectively, and ρ_{ij} is the complex correlation coefficient of the two signals. Combining (1)–(8), the covariance may be written as

$$\begin{aligned} &\rho_{ij} \sigma_i \sigma_j \\ &= \int d\Omega [A_{ih}(\Omega)A_{jh}^*(\Omega)P_h(\Omega) + A_{iv}(\Omega)A_{jv}^*(\Omega)P_v(\Omega)]. \end{aligned} \quad (9)$$

Interpreting σ_i^2 (the variance of x_i) as the power received by the i th antenna element, we may define the element's mean effective gain (MEG) \bar{g}_i as the ratio of received power to available power: [8, 14]

$$\bar{g}_i = \frac{\sigma_i^2}{P_0}. \quad (10)$$

An element's MEG accounts for the interplay between the element's radiation pattern and the distribution of incident power versus angle-of-arrival. For an angle-invariant radiation pattern or power-angle spectrum, $\bar{g}_i = 1/2$, indicating that one-half of the *available* power is received by the antenna

TABLE 1: Specified antenna configurations.

Class	Configuration	2D			3D			$\max(\ \mathbf{A}_i(\Omega)\ ^2)$
		$ \rho_{12} $	\bar{g}_1	\bar{g}_2	$ \rho_{12} $	\bar{g}_1	\bar{g}_2	
Closely spaced dipoles [18]	$d = \lambda$	0.02	0.80	0.80	0.12	0.50	0.50	1.85
	$d = \lambda/2$	0.17	0.73	0.73	0.01	0.50	0.50	2.20
	$d = \lambda/4$	0.18	0.74	0.74	0.00	0.50	0.50	3.14
CTIA reference antennas [19]	“Good”	0.34	0.42	0.42	0.04	0.50	0.50	2.96
	“Nominal”	0.73	0.48	0.48	0.58	0.50	0.50	1.57
	“Bad”	0.90	0.54	0.54	0.90	0.50	0.50	1.77
Cross-polarized dipoles [20]	Free space	0.00	0.38	0.38	0.00	0.50	0.50	1.50
	PEC	0.00	0.00	0.00	0.00	0.50	0.50	5.21

[8]. By use of (8) and (9) with $i = j$ corresponding to the variance of x_i (note that $\rho_{ii} = 1$), we may express \bar{g}_i in terms of the i th antenna’s vector radiation pattern and power-angle spectrum:

$$\bar{g}_i = \frac{1}{P_0} \int d\Omega [|A_{iv}(\Omega)|^2 P_v(\Omega) + |A_{ih}(\Omega)|^2 P_h(\Omega)]. \quad (11)$$

Finally, by combining (9)–(11), the environment-dependent correlation coefficient ρ_{ij} may be expressed as

$$\rho_{ij} = \frac{1}{P_0 \sqrt{\bar{g}_1 \bar{g}_2}} \times \int d\Omega [A_{iv}(\Omega) A_{jv}^*(\Omega) P_v(\Omega) + A_{ih}(\Omega) A_{jh}^*(\Omega) P_h(\Omega)]. \quad (12)$$

3. Simulation Setup

In the following sections, we define the vector power-angle spectra and antenna configurations used in our numerical study of capacity in 2D and 3D statistically isotropic environments.

3.1. Power-Angle Spectra. For statistically isotropic environments, we expect that

$$P_h(\Omega) = P_v(\Omega), \quad (13)$$

whereby the power density versus angle-of-arrival is independent of the polarization of incident waves. For the 2D isotropic environment, the vector power-angle spectrum is only nonzero along the unit sphere’s equator and is given by

$$\mathbf{P}_{2D}(\Omega) = \frac{P_0}{2\pi} \delta(\theta - \pi/2) \frac{1}{2} (\hat{\mathbf{h}} + \hat{\mathbf{v}}), \quad (14)$$

where θ denotes the zenith angle. In contrast, the 3D isotropic environment’s vector power-angle spectrum is constant across the entire unit sphere and is given by

$$\mathbf{P}_{3D}(\Omega) = \frac{P_0}{4\pi} \frac{1}{2} (\hat{\mathbf{h}} + \hat{\mathbf{v}}). \quad (15)$$

Equations (14) and (15) are idealizations of the statistically isotropic environments that may be generated in multiprobe anechoic and reverberation chambers, respectively. Thus, we neglect non-idealities due to, for example, using a finite number of probes in the multiple-probe anechoic chamber [4–6] and unstirred energy in the reverberation chamber [15–17].

3.2. Antennas under Test. In the following sections, we will compare the capacity distributions for three classes of two-element antennas.

- (i) Two closely-spaced and vertically polarized Hertzian dipoles separated by a distance d [18].
- (ii) The recently developed CTIA MIMO reference antennas (so-called “Good”, “Nominal”, and “Bad”) [19].
- (iii) Two colocated and cross-polarized Hertzian dipoles aligned parallel to the x - y plane and located (a) in free space and (b) at a height $h = \lambda/4$ above a perfectly electrically conducting (PEC) surface with surface normal $\hat{\mathbf{z}}$ [20].

The different antenna classes and configurations are intended to span the spectrum of antennas typically used by physically small handheld or mobile devices such as phones or laptops. Where applicable, our antenna descriptions include the effects of mutual coupling between elements.

Table 1 summarizes the different antenna configurations and compares the antennas’ correlation coefficient magnitudes and MEGs for the 2D and 3D statistically isotropic environments as calculated by use of (11)–(15). Due to (4)’s power normalization, $\bar{g}_i = 0.5$ for all antennas in the 3D statistically isotropic environment. For the cross-polarized dipoles above a PEC surface, $\bar{g}_i = 0$ for the 2D statistically isotropic environment, because the gain patterns of the antenna’s elements are zero for angles at and below the horizon [20]. The last column in Table 1 presents the maximum directivity of each antenna’s elements. We will use these values later in Section 5.

4. Capacity

We consider a 2-by-2 MIMO channel with uncorrelated transmit antennas and potentially correlated receive antennas. For the case of an uninformed transmitter and a receiver with perfect channel state information, the cumulative distribution function (CDF) of MIMO capacity is given by [21]

$$F_C(c) = \sum_{i=1}^2 \sum_{j=1, j \neq i}^2 \frac{1}{\gamma_i \gamma_j (\gamma_i - \gamma_j)} \times \left\{ e^{1/\gamma_i + 1/\gamma_j} \frac{\gamma_j - \gamma_i}{\gamma_i} \left(\int_1^{2^c} dv v e^{-v/\gamma_i - 2^c/v\gamma_j} \right) + [\gamma_i + (\gamma_i - \gamma_j)(\gamma_i + 2^c)] e^{(1-2^c)/\gamma_i} \right\}, \quad (16)$$

where γ_i are the eigenvalues of the 2-by-2 matrix $\mathbf{\Gamma}$ defined as

$$\mathbf{\Gamma} = \frac{1}{N_0 n_t} \mathbf{\Sigma}_r. \quad (17)$$

In (17), $n_t = 2$ is the number of transmit antenna elements, N_0 is the noise power density at the receiver, and $\mathbf{\Sigma}_r$ is the receiver's covariance matrix given by

$$\mathbf{\Sigma}_r = \begin{bmatrix} \mathcal{E}\{|x_1|^2\} & \mathcal{E}\{x_1 x_2^*\} \\ \mathcal{E}\{x_2 x_1^*\} & \mathcal{E}\{|x_2|^2\} \end{bmatrix}. \quad (18)$$

Using (8)–(12), $\mathbf{\Sigma}_r$ may be expressed as

$$\mathbf{\Sigma}_r = P_0 \begin{bmatrix} \bar{g}_1 & \rho \sqrt{\bar{g}_1 \bar{g}_2} \\ \rho^* \sqrt{\bar{g}_1 \bar{g}_2} & \bar{g}_2 \end{bmatrix}, \quad (19)$$

where the eigenvalues of $\mathbf{\Gamma}$ are

$$\gamma_2^1 = \frac{P_0}{N_0 n_t} \left[\frac{\bar{g}_1 + \bar{g}_2 \pm \sqrt{\bar{g}_1^2 + \bar{g}_2^2 + 2\bar{g}_1 \bar{g}_2 (2|\rho|^2 - 1)}}{2} \right], \quad (20)$$

and $(P_0/2)/N_0$ defines the SNR of the corresponding single-input single-output link for an isotropic antenna.

4.1. Single Orientation. Figures 1(a) and 1(b) compare the analytic 2-by-2 MIMO capacity CDFs for the different AUTs in the 2D and 3D statistically isotropic environments, respectively. The CDFs were calculated from (16)–(20) with the correlation coefficients and MEGs reported in Table 1. We observe that the different test environments may yield considerably different capacity CDFs for identical AUTs. The cross-polarized dipoles above a PEC surface are particularly problematic, because the MEGs of the antenna elements are zero (see Table 1) for the 2D environment. This implies an SNR of zero and results in a capacity CDF given by a unit step function with a transition at zero bps/Hz.

Figure 1(c) illustrates the shift in the capacity CDFs for the 2D statistically isotropic environment with respect to the

3D statistically isotropic environment. We quantify this shift in terms of a relative error of the 2D environment's capacity curves with respect to the 3D environment's capacity CDFs. We note that the relative error for the cross-polarized dipoles above a PEC surface is 100% due to its step-function capacity CDF in the 2D isotropic environment; this error is outside of the range of relative errors considered in Figure 1(c). Depending on the antenna configuration, the relative error in the 2D environment's capacity CDF may exceed 20%. This suggests that capacity statistics for a given AUT in a 2D and 3D statistically isotropic environment may not be comparable for a single orientation of the AUT. This is in agreement with the conclusions presented in [2] for ergodic capacity based on a single orientation of the AUT.

4.2. Multiple Orientations. As suggested in [2], a possible solution for obtaining comparable capacity statistics is to combine capacity data from different orientations of the AUT in the 2D statistically isotropic environment. Assuming N orientations of the AUT are sampled equally (i.e., an equal number of independent capacity realizations are taken at N unique orientations), the CDF of the combined set of capacity realizations is equal to the mean of the N orientation-dependent capacity CDFs: [22]

$$F_{\hat{C}}(c) = \frac{1}{N} \sum_{n=1}^N F_C^{(n)}(c), \quad (21)$$

where $F_C^{(n)}(c)$ denotes the capacity CDF associated with the n th orientation of the AUT, and $F_{\hat{C}}(c)$ describes the orientation-combined CDF of the resulting (mixture) distribution.

As Figure 2 illustrates, there are three degrees-of-freedom in a 3D rotation of an object to a new orientation [23–25]. In the rotation sequence illustrated in Figure 2, an object is rotated by $\alpha \in [0, \pi]$ in a direction $\beta \in [0, 2\pi)$ such that object's original z -axis is aligned to an axis z' defined by (α, β) . Then, the object is rotated by an angle $\chi \in [0, 2\pi)$ about the z' -axis. To obtain a uniform sampling of the AUT's 3D orientation space, we apply the successive orthogonal images technique [24]. We specify a set of L angle pairs (α, β) corresponding to L points uniformly distributed on the unit sphere. For each angle pair, $\chi = 2\pi(m/M)$ for $m = 0, 1, \dots, M-1$, where M is an integer number of χ rotations per (α, β) pair as given by

$$M = \text{round}(\sqrt{\pi L}), \quad (22)$$

and the total number of orientations is $N = ML$. In (22), $\text{round}(\cdot)$ rounds to the nearest integer. Equation (22) provides the appropriate weighting between M and L to ensure that the N orientations are a uniform sampling of the rotation space (cf., [24, Equation (3.1)]).

A set of $L = 162$ uniformly distributed angle pairs (α, β) were generated by iterative triangularization of an icosahedron. By use of (22), we have $M = 23$ whereby a set of $N = ML = 3726$ uniformly distributed orientations were considered. (Similar results were observed for larger

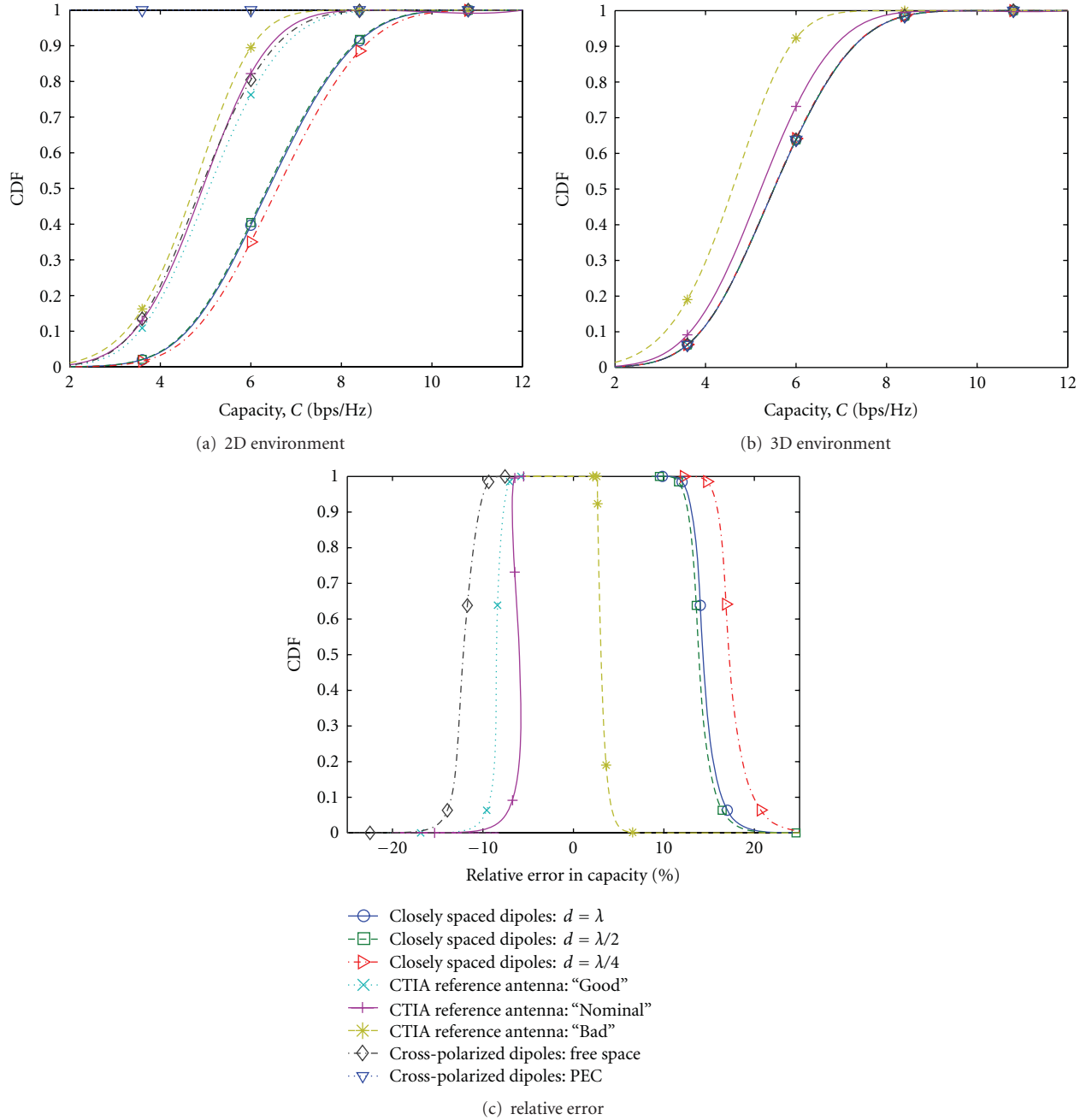


FIGURE 1: Comparison of the capacity CDFs for the different AUTs in statistically isotropic environments at a single orientation: (a) capacity CDFs for the 2D environment, (b) capacity CDFs for the 3D environment, (c) relative error in the 2D environment’s capacity CDFs with respect to the 3D environment’s capacity CDFs. The center plot’s legend applies to all three plots.

choices of N .) The AUT was rotated to each of the N orientations, and (11), (12), and (16) were used to calculate the resulting N capacity CDFs. For each of the AUTs, Figure 3 compares the N orientation-dependent capacity CDFs obtained from the 2D statistically isotropic environment (solid lines), the resulting orientation-combined CDF from the 2D statistically isotropic environment (solid line), and the orientation-independent capacity CDF obtained from the 3D statistically isotropic environment (dashed line). We

observe large variations in the 2D environment’s orientation-dependent capacity CDFs for the closely spaced dipoles (Figures 3(a)–3(c)), as well as the cross-polarized dipoles above a PEC surface (Figure 3(h)).

Figures 4(a) and 4(b) compare the 2D environment’s orientation-combined capacity CDFs to those from the 3D environment’s orientation-independent capacity CDFs; Figure 4(c) examines the relative error in the 2D statistically isotropic environment’s orientation-combined capacity

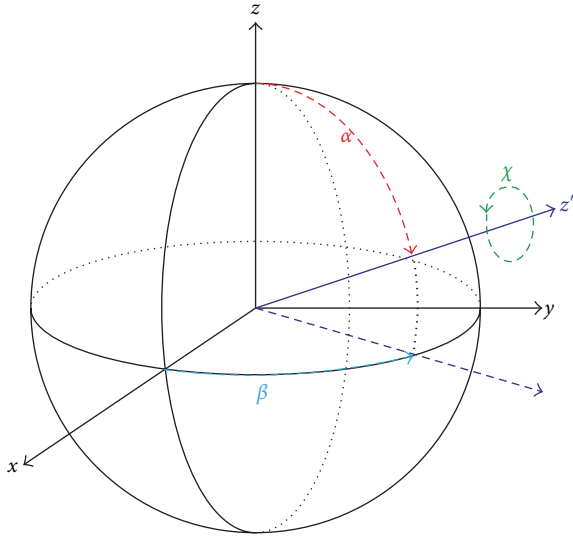


FIGURE 2: There are three degrees of freedom in the specification of a rotation to an arbitrary orientation. The diagram defines a rotation of an object in 3D via Euler angles. The object is rotated by an angle α in the direction β and subsequently rotated by an angle χ about the axis z' defined by (α, β) .

CDFs with respect to the 3D statistically isotropic environment's orientation-independent capacity CDFs. We observe that for the CTIA reference antennas and cross-polarized dipoles in free space, this "error" is quite small, with typical magnitudes below 2%. In comparison, the relative error of the cross-polarized dipoles above the PEC surface and, to an extent, the closely-spaced dipoles, is much larger, with magnitudes exceeding 5–20%. Note that these are the same antenna configurations which showed the greatest variation in the 2D environment's orientation-dependent capacity CDFs (see Figure 3). Thus, Figures 3 and 4(c) suggest that for a given AUT, the 2D environment's orientation-combined capacity statistics will be comparable to the 3D environment's orientation-independent capacity statistics provided that the variations in the 2D environment's orientation-dependent capacity CDFs are small. Repeat studies at SNRs of 5 dB to 20 dB yielded similar errors, albeit with a slight increase in relative error for decreasing SNR. The typical range of error magnitudes remained below 10%.

5. Sensitivity of Capacity to AUT Orientation in 2D Statistically Isotropic Environments

From Figures 3 and 4(c), we observed that for a given AUT, large orientation-dependent variations in the 2D environment's capacity CDF led to a large relative error between the 2D environment's orientation-combined capacity CDF and the 3D environment's orientation-independent capacity CDF. Here, we investigate the source of these large orientation-dependent variations in capacity and determine why some antennas are more sensitive to orientation in the 2D isotropic environment than others. This provides insight

into the range of antenna configurations for which we may expect the 2D environment's orientation-combined capacity CDF to be comparable to the 3D environment's orientation-independent capacity CDF. We base our analysis on the orientation-dependence of each AUT's correlation coefficient and MEGs in the 2D statistically isotropic environment. Note that for the 3D environment, these quantities are orientation invariant and are tabulated in Table 1.

Figure 5 presents scatter plots of each AUT's MEGs and correlation coefficient for different orientations in the 2D statistically isotropic environment. The location of each circle corresponds to the MEG of the AUT's elements; the circle's size/shade corresponds to the magnitude of the correlation coefficient. We observe that the antennas exhibiting the largest variations in the 2D environment's orientation-dependent capacity CDFs, namely, the cross-polarized dipoles above a PEC surface and the closely-spaced dipoles tend to have similar antenna element MEGs at each orientation (i.e., $\bar{g}_1 \approx \bar{g}_2$). This indicates that the average power received by each of the antenna elements is identical, whereby a low (or high) average received power at one element implies an equally low (or high) average received power at the other element. This allows for large variations in the cumulative power received by the two antenna elements. In contrast, the AUTs exhibiting the smallest variations in the orientation-dependent capacity CDFs tend to have MEGs that follow $\bar{g}_1 + \bar{g}_2 \approx 1$. This indicates that the cumulative power received by both antenna elements is approximately constant at different orientations, whereby a low average received power at one element is compensated by a high average received power at the other element.

Based on Figure 5, the 2D environment's orientation-dependent capacity CDFs appear to be more sensitive to joint orientation-dependent variations in the MEGs of an AUT's elements than orientation-dependent variations in its correlation coefficient magnitude (e.g., compare Figures 5(g), 5(h), 3(g) and 3(h)). To confirm this, Figure 6 presents *environment-independent* contour plots of the median capacity for different correlation coefficient magnitudes and MEGs. For the calculations, we specify a nominal single-input single-output SNR of 10 dB (i.e., $(P_0/2)/N_0 = 10$). Figure 6(a) corresponds to the case of equal antenna element MEGs; Figure 6(b) corresponds to the case of constant cumulative received power. As indicated by the range of median capacities for the two cases, the equal MEG case ($\bar{g}_1 = \bar{g}_2$) allows for larger variations in the median capacity than the constant cumulative received power case ($\bar{g}_1 + \bar{g}_2 = 1$). We also observe for both cases that the effect on capacity of large variations in the magnitude of the correlation coefficient is considerably weaker than large variations in MEG. This is indicated by the smaller gradient for changes in \bar{g}_1 as compared to changes in $|\rho_{12}|$.

Based on Figures 3–6 and the maximum directivities listed in Table 1, we expect that the 2D environment's orientation-combined capacity statistics should be comparable to the 3D environment's orientation-independent capacity statistics provided that the maximum directivities of the AUT's elements are small (e.g., $\max(\|\mathbf{A}_i(\Omega)\|^2) \leq 2$). This criterion should lead to smaller orientation-dependent

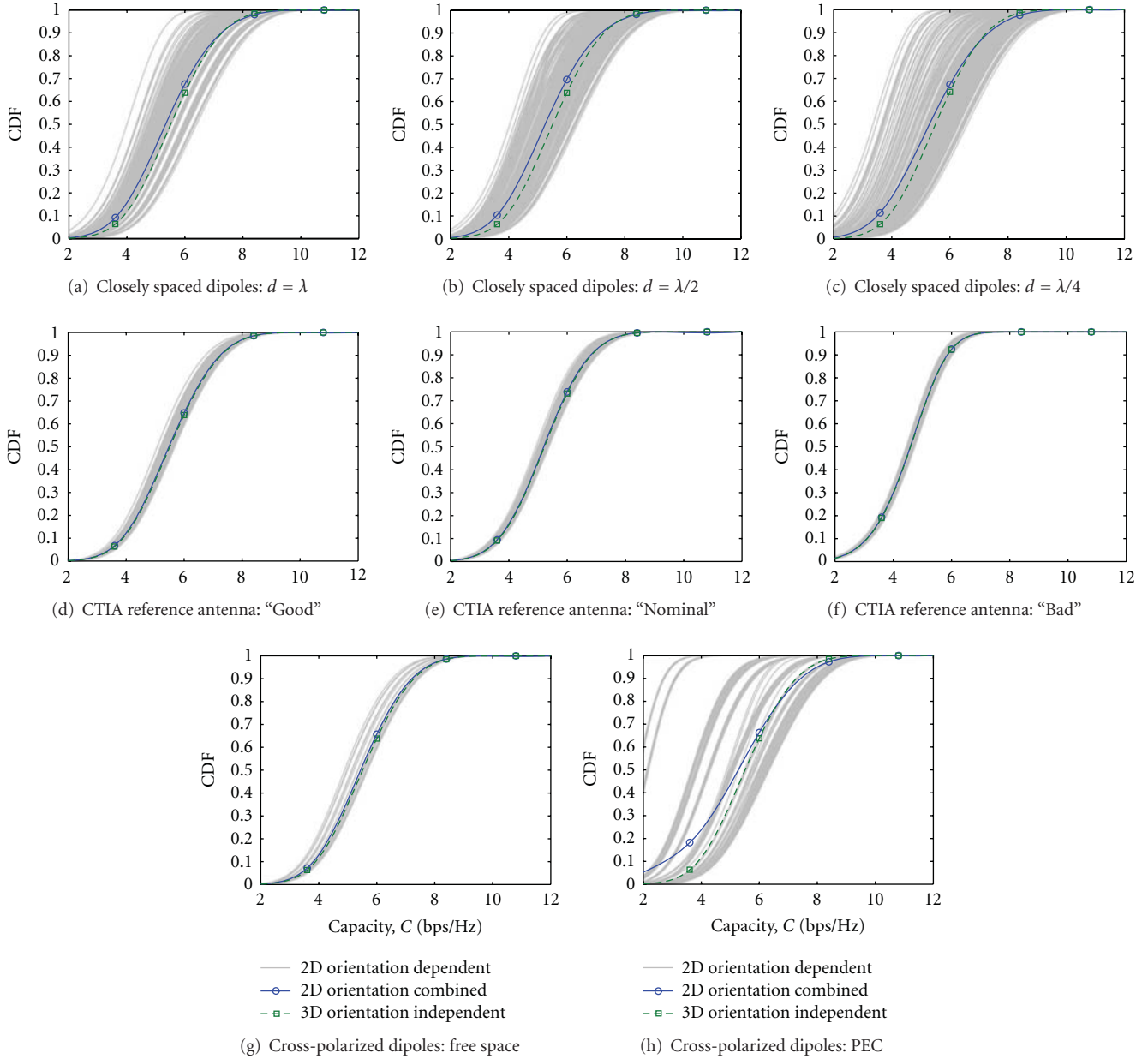


FIGURE 3: Comparison of the capacity CDFs for multiple orientations of the two-element antennas in statistically isotropic environments. Each plot compares the 2D environment’s orientation-dependent capacity CDFs, the 2D environment’s orientation-combined capacity CDFs, and the 3D environment’s orientation-independent capacity CDFs.

fluctuations in the AUT’s MEGs and, thereby, cumulative received power. In [7, 14], we note that similar conclusions were reached concerning the greater variability of MEG for different orientations of antennas with large directivities. Here, we have demonstrated that the variability in capacity is dominated by this variability in MEG. Antennas with markedly different element directivities may also yield comparable capacity CDFs, because it is less likely that $\bar{g}_1 \approx \bar{g}_2$. However, based on the antenna configurations considered here, we expect that low directivity is the more important criteria.

6. Conclusions

Channel capacity determines the maximum theoretical throughput for a given wireless link. By designing test procedures such that the capacity distributions obtained for a given AUT in a 2D and 3D statistically isotropic environment are comparable, we expect that throughput statistics for a corresponding DUT in these two environments will likewise be comparable. More so, we expect that discrepancies between observed throughput statistics for different devices in different test environments will be largely

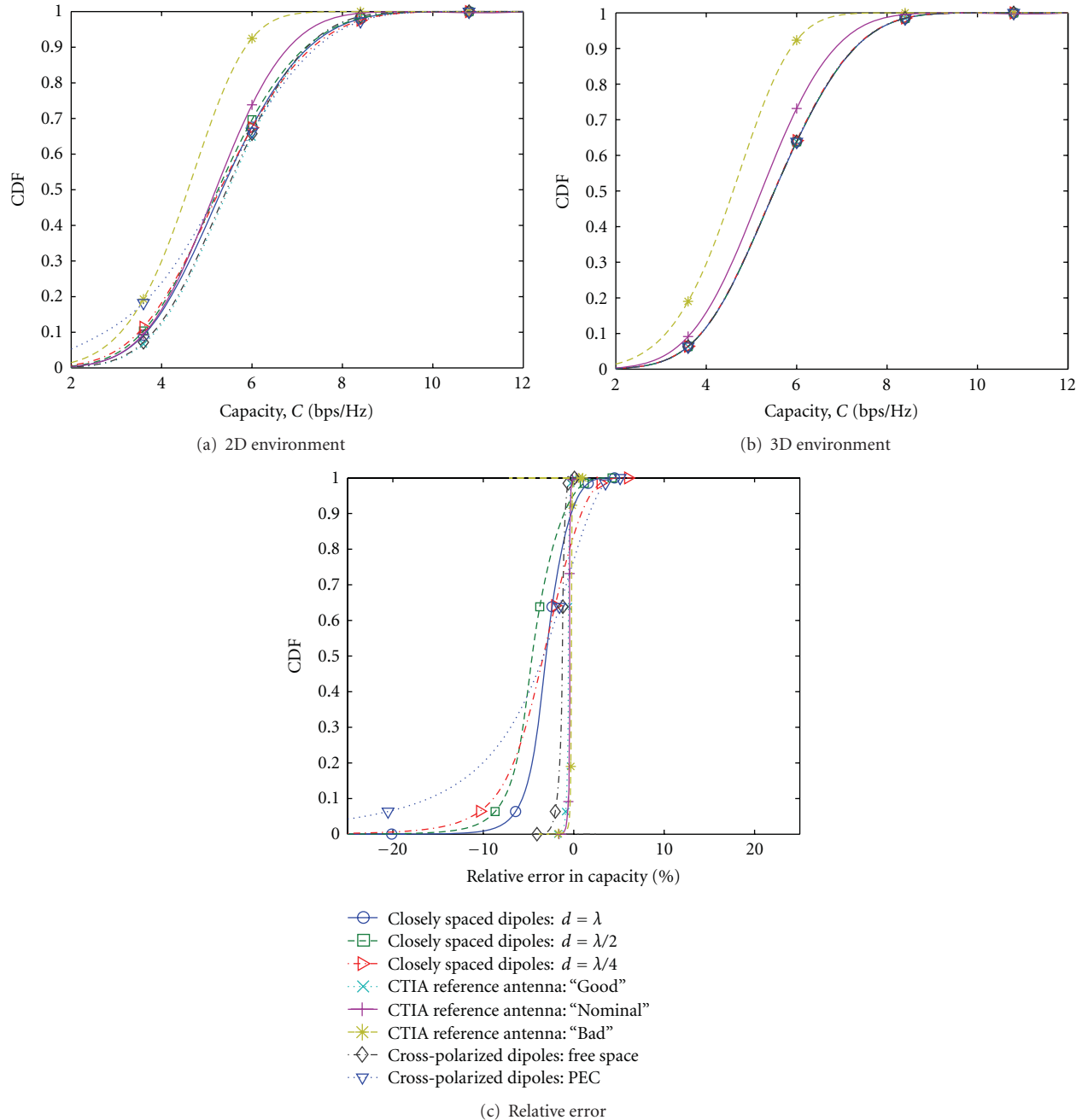


FIGURE 4: Comparison of the capacity CDFs for the different AUTs in statistically isotropic environments at multiple orientations: (a) orientation-combined capacity CDFs for the 2D environment, (b) orientation-independent capacity CDFs for the 3D environment, (c) relative error in the 2D environment's orientation-combined capacity CDFs with respect to the 3D environment's orientation-independent capacity CDFs. The center plot's legend applies to all three plots.

due to fundamental differences in the devices (e.g., antenna loss and mismatch, receiver sensitivity, and algorithm implementation) and *not* fundamental differences in the capacity statistics of the test environments, assuming a sufficient number of AUT orientations in the 2D environment.

Based on the analysis presented here, provided that (1) the DUT is rotated to different orientations in the 2D statistically isotropic environment, and (2) the dimensions

of the DUT are on the order of a wavelength or less such that the element directivities will be low, we expect that throughput statistics for a DUT in 2D and 3D statistically isotropic environments will be within 10% of each other, as suggested by Figures 3 and 4(c). This suggests that with properly designed test procedures, over-the-air tests of multiantenna wireless terminals in multiprobe anechoic and reverberation chambers should be comparable for a

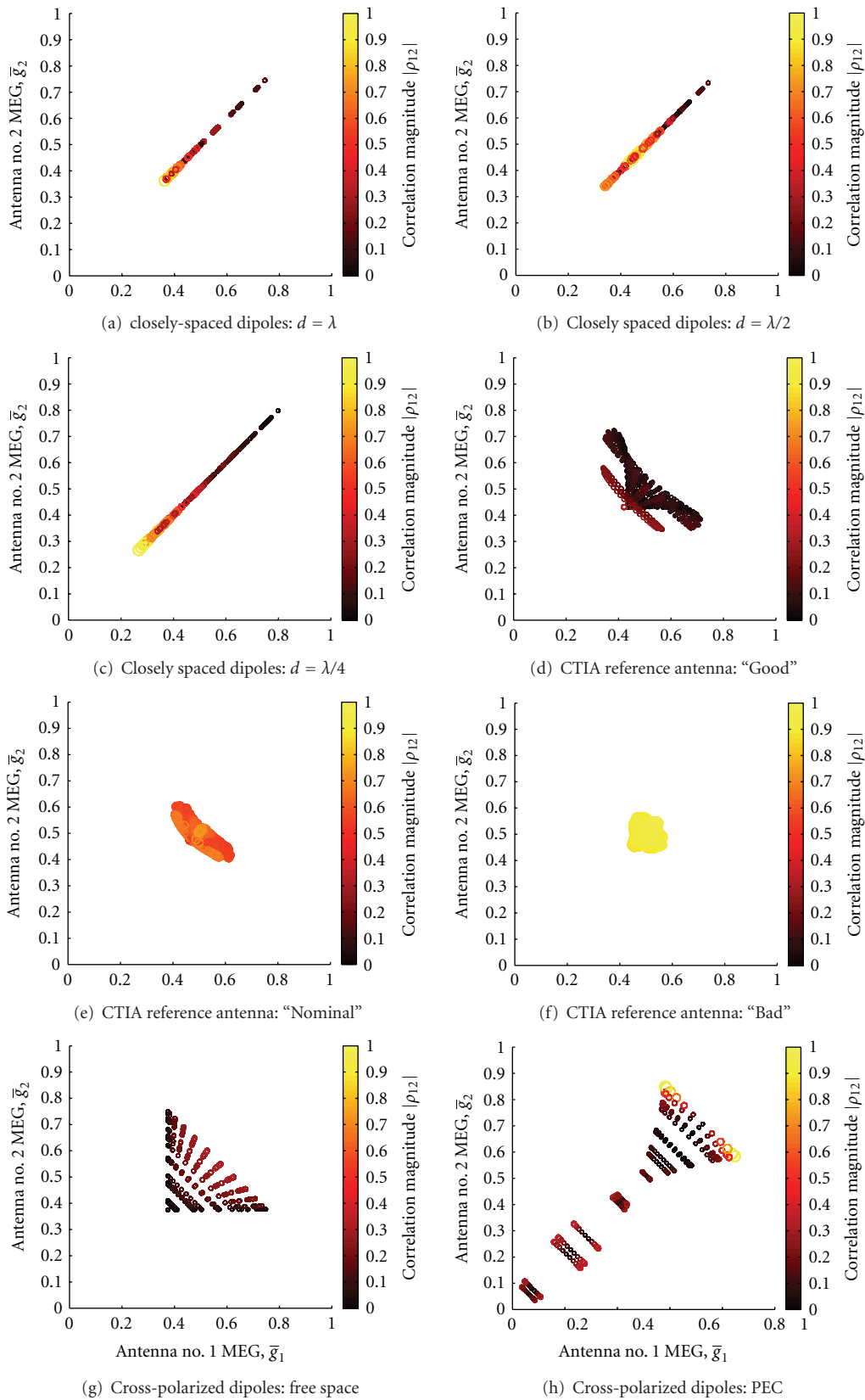


FIGURE 5: Scatter plots of mean effective gain (MEG) and correlation coefficient magnitudes for each AUT in the 2D statistically isotropic environment for N uniformly distributed orientations of the AUT. The position of each circle indicates the MEGs of the two antenna elements; the size/shade of each circle indicates the magnitude of the correlation coefficient.

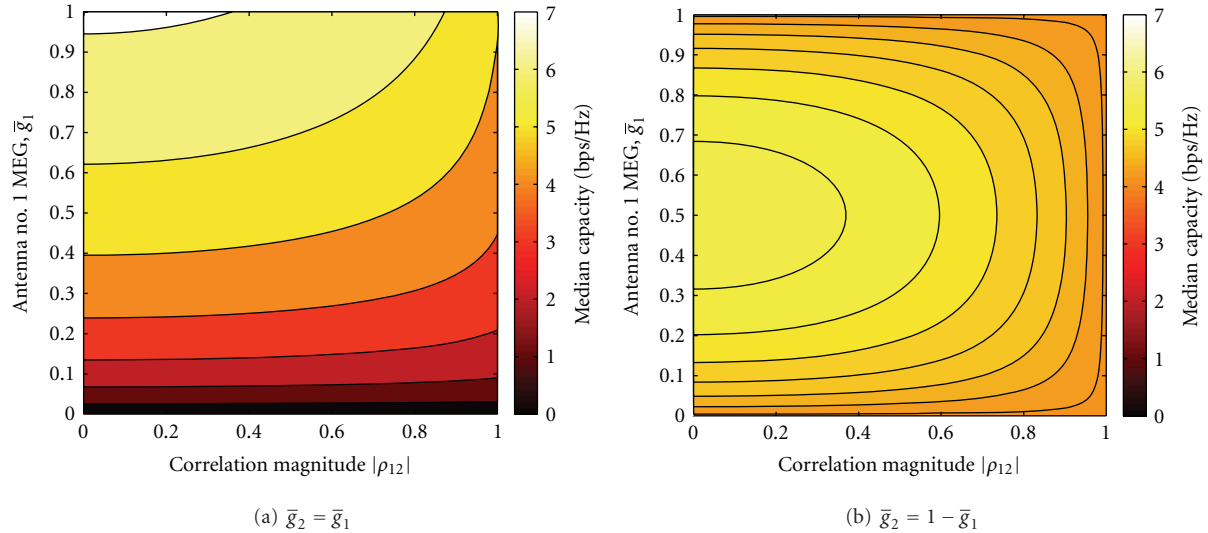


FIGURE 6: Median capacity for ranges of correlation coefficient magnitudes $|\rho_{12}|$ and MEGs, \bar{g}_1 and \bar{g}_2 .

wide range of devices. Finally, it is worth emphasizing that our conclusions are based solely on the distribution of capacity. That is, our conclusions are independent of the actual number of realizations used to calculate a capacity (or throughput) statistic and apply even for the case where a *single* capacity (or throughput) measurement is made at each orientation.

Acknowledgments

The authors acknowledge the cochair of CTIA's MIMO OTA Subgroup (MOSG), Scott Prather of AT&T Wireless, and the lead designer of the the CTIA MIMO reference antennas, Istvan Szini of Motorola Mobility, for providing the complex radiation pattern data for the CTIA MIMO reference antennas. This work was supported by a National Research Council Postdoctoral Research Associateship.

References

- [1] *3rd Generation Partnership Project; Technical Specification Group Radio Access Networks; Measurement of radiated performance for MIMO and multi-antenna reception for HSPA and LTE terminals (Release 10)*, 3GPP Std. TR 37.976, Rev. 1.4.0, 2009.
- [2] U. Carlberg, J. Carlsson, A. Hussain, and P.-S. Kildal, "Ray based multipath simulation tool for studying convergence and estimating ergodic capacity and diversity gain for antennas with given far-field functions," in *Proceedings of the International Conference on Applied Electromagnetics and Communications (ICECom '10)*, pp. 1–4, Dubrovnik, Croatia, September 2010.
- [3] J. Carlsson, U. Carlberg, A. Hussain, and P.-S. Kildal, "About measurements in reverberation chamber and isotropic reference environment," in *Proceedings of the International Conference on Applied Electromagnetics and Communications (ICECom '10)*, pp. 1–4, Dubrovnik, Croatia, September 2010.
- [4] J. P. Nuutinen, P. Kyösti, Y. Gao, and M. D. Foegelle, "On the MIMO OTA test system," in *Proceedings of the 5th International ICST Conference on Communications and Networking in China (ChinaCom '10)*, pp. 1–5, Beijing, China, August 2010.
- [5] T. Laitinen, P. Kyösti, J.-P. Nuutinen, and P. Vainikainen, "On the number of OTA antenna elements for plane-wave synthesis in a MIMOOTA test system involving a circular antenna array," in *Proceedings of the European Conference on Antennas and Propagation*, pp. 1–5, Barcelona, Spain, April 2010.
- [6] T. Laitinen, J. Toivanen, P. Kyösti, J.-P. Nuutinen, and P. Vainikainen, "On a MIMO-OTA testing based on multi-probe technology," in *Proceedings of the URSI International Symposium on Electromagnetic Theory*, pp. 227–230, Berlin, Germany, August 2010.
- [7] B. Yanakiev, J. Ø. Nielsen, M. Christensen, and G. F. Pedersen, "Antennas in real environments," in *Proceedings of the 5th European Conference on Antennas and Propagation (EUCAP '11)*, pp. 2766–2770, Rome, Italy, April 2011.
- [8] R. Vaughan and J. B. Andersen, *Channels, Propagation and Antennas for Mobile Communications*, The Institution of Electrical Engineers, London, UK, 2003.
- [9] B. Yanakiev, J. Nielsen, M. Christensen, and G. F. Pedersen, "On small terminal antenna correlation and impact on MIMO channel capacity," *IEEE Transactions on Antennas and Propagation*, vol. 60, no. 2, pp. 689–699, 2010.
- [10] K. Ogawa, S. Amari, H. Iwai, and A. Yamamoto, "Effects of received power imbalance on the channel capacity of a handset MIMO," in *Proceedings of the IEEE International Symposium on Personal, Indoor and Mobile Radio Communications (PIMRC '07)*, pp. 1–5, Athens, Greece, September 2007.
- [11] D. A. Hill, "Plane wave integral representation for fields in reverberation chambers," *IEEE Transactions on Electromagnetic Compatibility*, vol. 40, no. 3, pp. 209–217, 1998.
- [12] D. A. Hill and J. M. Ladbury, "Spatial-correlation functions of fields and energy density in a reverberation chamber," *IEEE Transactions on Electromagnetic Compatibility*, vol. 44, no. 1, pp. 95–101, 2002.
- [13] P. De Doncker and R. Meys, "Statistical response of antennas under uncorrelated plane wave spectrum illumination," *Electromagnetics*, vol. 24, no. 6, pp. 409–423, 2004.
- [14] A. Alayón Glazunov, A. F. Molisch, and F. Tufvesson, "Mean effective gain of antennas in a wireless channel," *IET*

- Microwaves, Antennas and Propagation*, vol. 3, no. 2, pp. 214–227, 2009.
- [15] P. Corona, G. Ferrara, and M. Migliaccio, “Reverberating chamber electromagnetic field in presence of an unstirred component,” *IEEE Transactions on Electromagnetic Compatibility*, vol. 42, no. 2, pp. 111–115, 2000.
- [16] O. Lundén and M. Bäckström, “How to avoid unstirred high frequency components in mode stirred reverberation chambers,” in *Proceedings of the IEEE International Symposium on Electromagnetic Compatibility (EMC '07)*, pp. 1–4, Honolulu, Hawaii, USA, July 2007.
- [17] R. J. Pirkl, J. M. Ladbury, and K. A. Remley, “The reverberation chamber’s unstirred field: a validation of the image theory interpretation,” in *Proceedings of the International Symposium on Electromagnetic Compatibility (ISEMC '11)*, pp. 670–675, Long Beach, Calif, USA, August 2011.
- [18] B. Clerckx, C. Craeye, D. Vanhoenacker-Janvier, and C. Oestges, “Impact of antenna coupling on 2×2 MIMO communications,” *IEEE Transactions on Vehicular Technology*, vol. 56, no. 3, pp. 1009–1018, 2007.
- [19] I. Szini, *CTIA MIMO 2x2 reference antenna*, CTIA Std. MOSG110 904, 2011.
- [20] C. A. Balanis, *Antenna Theory: Analysis and Design*, John Wiley & Sons, New York, NY, USA, 2nd edition, 1996.
- [21] P. J. Smith, L. M. Garth, and S. Loyka, “Exact capacity distribution for MIMO systems with small numbers of antennas,” *IEEE Communications Letters*, vol. 7, no. 10, pp. 481–483, 2003.
- [22] C. Fobes, M. Evans, N. Hastings, and B. Peacock, *Statistical Distributions*, John Wiley & Sons, 4th edition, 2011.
- [23] R. E. Miles, “On random rotations in R^3 ,” *Biometrika*, vol. 52, no. 3, pp. 636–639, 1965.
- [24] J. C. Mitchell, “Sampling rotation groups by successive orthogonal images,” *SIAM Journal on Scientific Computing*, vol. 30, no. 1, pp. 525–547, 2007.
- [25] A. Yershova, S. Jain, S. M. Lavalley, and J. C. Mitchell, “Generating uniform incremental grids on $SO(3)$ using the hopf fibration,” *International Journal of Robotics Research*, vol. 29, no. 7, pp. 801–812, 2010.

Research Article

3GPP Channel Model Emulation with Analysis of MIMO-LTE Performances in Reverberation Chamber

Nabil Arsalane, Moctar Mouhamadou, Cyril Decroze, David Carsenat, Miguel Angel Garcia-Fernandez, and Thierry Monedière

XLim Laboratory, OSA Department, UMR CNRS 6172, University of Limoges, 123 Avenue Albert Thomas, 87060 Limoges Cedex, France

Correspondence should be addressed to Nabil Arsalane, nabil.arsalane@xlim.fr

Received 2 December 2011; Accepted 24 January 2012

Academic Editor: David A. Sanchez-Hernandez

Copyright © 2012 Nabil Arsalane et al. This is an open access article distributed under the Creative Commons Attribution License, which permits unrestricted use, distribution, and reproduction in any medium, provided the original work is properly cited.

Emulation methodology of multiple clusters channels for evaluating wireless communication devices over-the-air (OTA) performance is investigated. This methodology has been used along with the implementation of the SIMO LTE standard. It consists of evaluating effective diversity gain (EDG) level of SIMO LTE-OFDM system for different channel models according to the received power by establishing an active link between the transmitter and the receiver. The measurement process is set up in a Reverberation Chamber (RC). The obtained results are compared to the reference case of single input-single output (SISO) in order to evaluate the real improvement attained by the implemented system.

1. Introduction

In recent research works, reverberation chamber (RC) is considered as a useful tool to emulate rich multipath environments [1, 2]. In this contribution, this tool is employed for emulating multiclusters channel models. Indeed, RC represents a useful candidate for performance evaluation of wireless communication systems, and they are being considered as a standard for multiple-input multiple-output (MIMO) over-the-air (OTA) measurements in 3GPP and CTIA standardization committees.

Active measurement methods are often based on the use of a channel emulator associated with a real-time transmission system, to test the operational terminals. In this paper, the aim is to suggest an experimental platform using a small size reverberation chamber (reverberant cell) to study the feasibility of emulating multipath channel while maintaining a Rayleigh fading (in order to be able to compare different receivers in reference environments with the same distribution). On this platform, a multicluster emulation method which complies with channels defined by 3GPP models is implemented, using only one vector signal generator. This emulation must be accompanied by a strict control of delay spread, to generate realistic channels [2–4].

This methodology, along with the presented model, emulates a Spatial-Channel-Model-Extended (SCME) for MIMO OTA active measurements. The delay spread control can be achieved through modifying the RC quality factor by loading it with absorbing materials.

The presented approach aims to develop a flexible OTA methodology for quantification and implementation of digital multiantenna transmission systems inside a small size reverberant cell. On this test bed, the measurements are not carried out in real time and are not dedicated to performance evaluation in terms of throughput. However, it allows (through the use of an RF digitizer and baseband processing in MATLAB) to study in detail the influence of several transmission chain parameters, as antenna aspects (in MIMO context: coupling, correlation coefficient ρ), and test of signal shaping and reception algorithms (synchronization, equalization, MIMO coding).

In this paper, this method is applied to test the 3GPP LTE standard, by implementing an LTE-OFDM frame and using diversity at the receiver side. The frame is generated based on the 3GPP standard [5, 6], which specifies a downlink (DL) transmission system using an orthogonal frequency division multiplexing access (OFDMA) [7, 8].

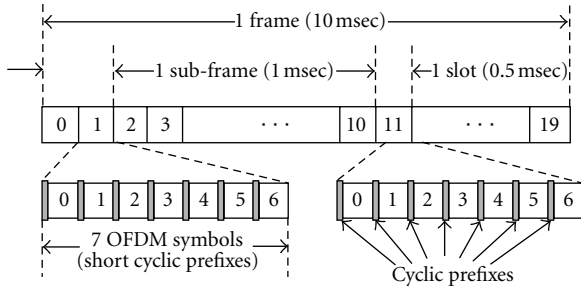


FIGURE 1: LTE Frame [5].

LTE also uses adaptive modulation and coding to get better data throughput. The modulation schemes supported for payload in the uplink and downlink are QPSK, 16QAM, and 64QAM [9].

As shown in Figure 1, the duration of the LTE frames is 10 ms; these frames are divided into 10 subframes, with every subframe being 1 ms long. Each subframe contains two slots of 0.5 ms of duration, which are composed of 6 or 7 OFDM symbols, depending on the employment of the normal or the extended cyclic prefix [10]. The LTE specifications define parameters for system bandwidths from 1.4 MHz to 20 MHz.

After having introduced the LTE requirements, it is necessary to focus on parameters for evaluating the performance of a system under test. In this paper, a SIMO configuration is considered, with two synchronized receivers.

The fundamental parameters usually used to estimate the diversity performance are the correlation coefficient [9, 11], the diversity gain (DG) [12, 13] and the effective diversity gain (EDG) [14], or the mean effective gain (MEG) [11, 15]. They all depend on the signals which are detected on each branch. The definition of the diversity gain and the effective diversity gain and how to measure them in RC are presented in [14]. Generally, these parameters are aimed to SIMO passive measurements at one frequency, which will be applied to the case of LTE active measurements.

The different parts discussed in this paper are as follows. Section 2 gives a description concerning the implementation of test bed. Section 3 shows the method which allows generating clusters and then creating several channel models. Section 4 presents the micro-macro-cell LTE performances for SIMO configuration versus SISO. And finally, Section 5 concludes this paper.

2. Measurement Test Bed

The LTE signal described previously is implemented on the measurement test bed in Figure 2.

The measurement test bed is based on the Aeroflex PXI 3000 series architecture, with two PXI chassis integrating a control PC for generating frames on transmission and for processing received data. The transmit part includes one RF wideband signal generator (76 MHz–6 GHz), which can provide a level of RF power from -120 dBm to $+5$ dBm over a modulation bandwidth of 33 MHz. The receiver integrates two digitizers, which provide conversion of RF signal to

TABLE 1: Parameters of the urban microcell and urban macrocell scenarios.

Scenario	Urban Macro		Urban micro	
	Relative power (dB)	Delay (μ s)	Relative power (dB)	Delay (μ s)
Taps Model	0	0	0	0
	-2.22	0.36	-1.27	0.28
	-1.72	0.25	-2.72	0.20
	-5.72	1.04	-4.30	0.66
	-9.05	2.7	-6.01	0.81
	-12.50	4.59	-8.43	0.92

baseband digital IQ symbols [16]. Data processing is done with MATLAB.

At the transmitter side, a frame based on LTE specifications is generated. The duplex mode used is TDD, and a bandwidth of 5 MHz has been chosen, with 64QAM modulation scheme, over a carrier frequency of 2.35 GHz.

3. Channel Emulation

The characteristics of the LTE-OFDM frame and measurement system to be used has been explained previously. This section will focus on establishing a method for the emulation of 3GPP channel models with a specific delay spread, which requires a control of the delay spread inside the RC.

3.1. 3GPP Channel Model. The 3GPP urban microcell and urban macrocell channel models in [5, 6] are defined to be used for multiantenna OTA comparison measurements. The taps delay in urban micro-cell and urban macro-cell channel models are depicted in Figure 3.

It can be seen that the urban macrocell channel presents a high delay spread compared to the urban microcell.

The taps delay and the power magnitude are listed in details in Table 1.

Some special consideration should be taken into account when implementing channel models in an RC. Indeed these models introduce intracluster delay spread. Then, for each tap an RMS delay spread (τ_{rms}) of 90 ± 5 ns has to be considered.

3.2. Channel Model Emulation

3.2.1. Controlling the RMS Delay Spread. In order to obtain the desired τ_{rms} , we first face up to the question related to chamber loading.

The RC used in this work is the SMART 1000 Mini Reverb-cell [17], which is a rectangular metallic enclosure with dimensions of $110 \text{ cm} \times 70 \text{ cm} \times 60 \text{ cm}$, as shown in Figure 4. The stirring operation is performed by vertical and horizontal stirrers and illuminated by two horn antennas connected to the transmitter.

The delay spread τ_{rms} can be modified by loading the chamber with an appropriate amount of absorbing material [3, 4].

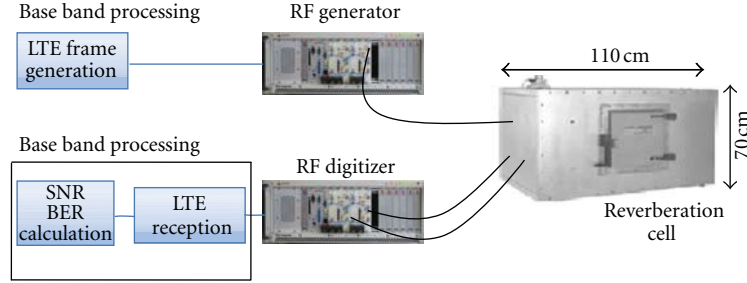


FIGURE 2: Measurement test bed.

TABLE 2: Diversity system under test characteristics.

Frequency (GHz)	Return losses S11 (dB)	Coupling coefficient S21 (dB)	Correlation coefficient (in isotropic environment)	Total efficiency (%)
2.35	-12	-17	<0.05	92.7

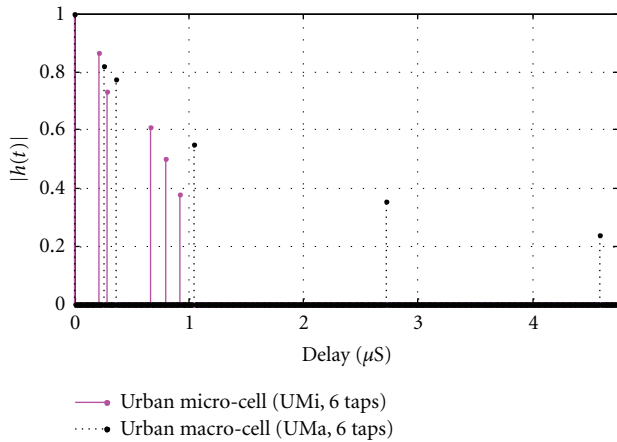


FIGURE 3: Urban micro- and macrocell channel model taps.

The measurements shown in Figure 5 illustrate the dependence of the delay spread on absorbing material located inside the RC.

For the unloaded chamber case, the measured RMS delay spread is equal to 256.4 ns. When the chamber is loaded with a piece of material, which is solid, pyramidal shaped, and carbon loaded (urethane foam absorber [18]) with dimensions of 16 cm × 9 cm × 4 cm, placed in a corner of the RC, the RMS delay spread is around 93 ns. The use of absorbing materials decreases considerably the value of the delay spread and allows achieving the desired result which should be within 90 ± 5 ns.

In order to check the fading distribution, a power measurement is made at the central frequency to plot the normalized CDF. Figure 6 shows that the fading is still Rayleigh even after the addition of losses. The difference concerning the measured mean powers before and after adding absorbing materials is around 3 dB.

In this part, the control of the τ_{rms} has been achieved by the use of absorbing material, and maintaining a Rayleigh

fading distribution. The goal now is to emulate a multi-cluster channel with the same delay spread for each cluster.

3.2.2. Clusters Emulation. The method to emulate the channel model consists of convolving the base band signal to be transmitted with the urban macro-cell or urban micro-cell channel model tap delay line generated using a MATLAB program (see Figure 7).

In order to verify the proper functioning of this method, a channel sounding based on a sliding correlation [19] is performed, with a sampling frequency F_s of 64 MHz at carrier frequency f_0 of 2.35 GHz. The sampling frequency is chosen initially higher, to obtain a good time resolution and verify that the channel is well emulated.

Figures 8(a) and 8(b) present the power delay profile curves measured in RC urban micro- and urban macro-cell channel models, respectively.

The different results presented in this section highlight the possibility of controlling delay spread for each cluster, and emulating 3GPP urban micro- and macro-cell channel models. This is obtained by combining a digital preprocessing and a RC to manage the τ_{rms} value.

4. LTE Active Measurement in Reverberation Chamber

In order to realize these measurements, two boards representing a compact terminal are used: one reference board with one triband antenna, and diversity board with two triband antennas (see Figure 9). These antennas have been studied previously in [20, 21]. The obtained characteristics are listed in Table 2.

4.1. SISO Measurement. By using the LTE system implemented in Section 2, the SISO configuration measurement will be performed. In order to simplify the analysis, the stirrers of the RC used for this study were rotated stepwisely for 1600 positions, so the Doppler spread of the channel is negligible.

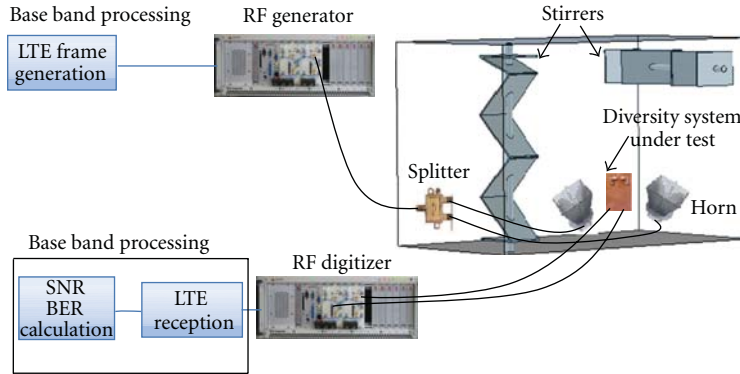


FIGURE 4: Reverberation chamber overview.

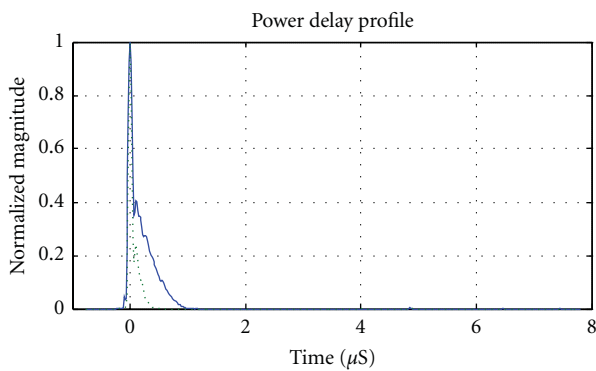


FIGURE 5: Measured PDPs for unloaded and loaded RC.

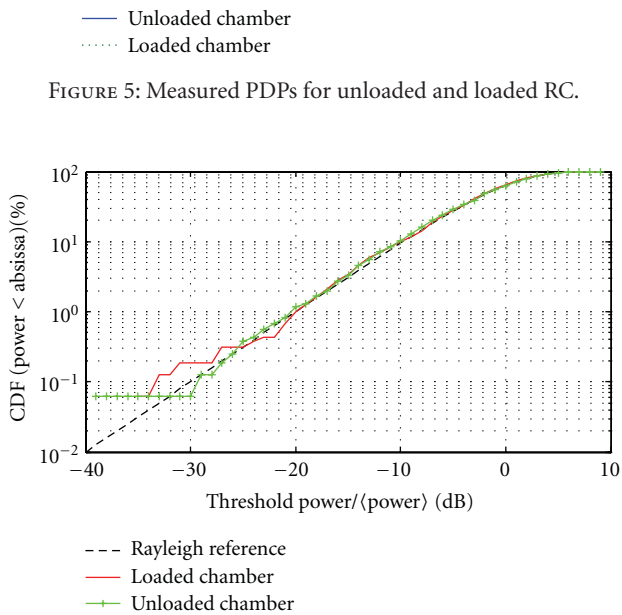


FIGURE 6: Cumulative distribution function measured in the loaded and unloaded RC.

The CDF curves plotted in Figure 10 present two types of results:

- (i) cumulative distribution calculated from the measured power at one frequency in the signal bandwidth,

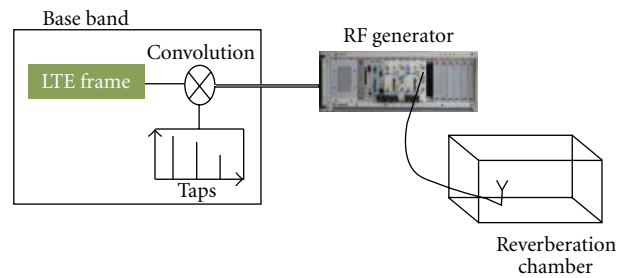
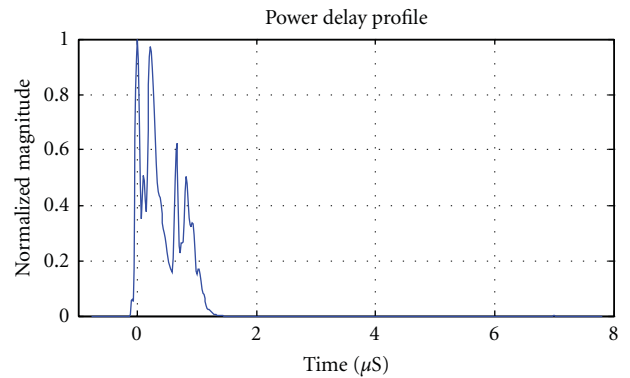
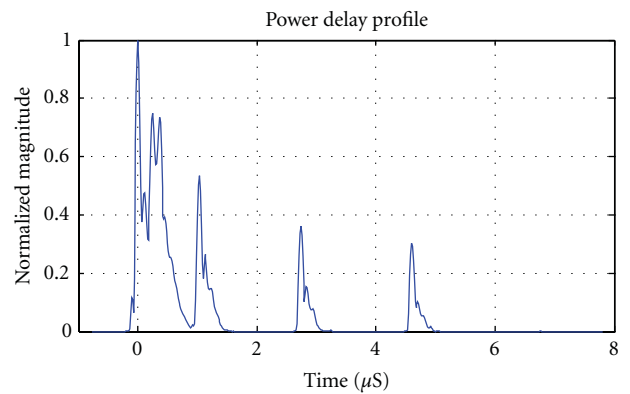


FIGURE 7: Channel emulation overview.



(a)



(b)

FIGURE 8: Power delay profiles measured in RC for urban micro-cell (a) and urban macro-cell (b) channel models.

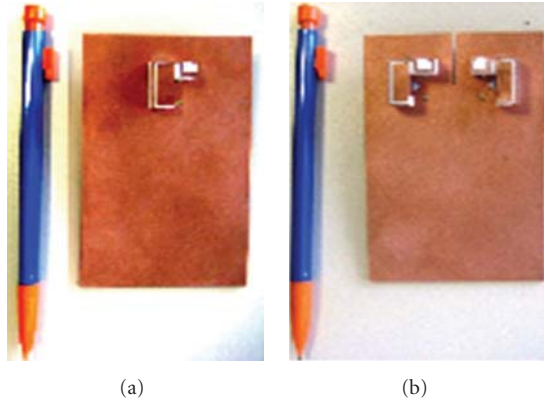


FIGURE 9: Reference antenna (a) and diversity antennas (b) [20, 21].

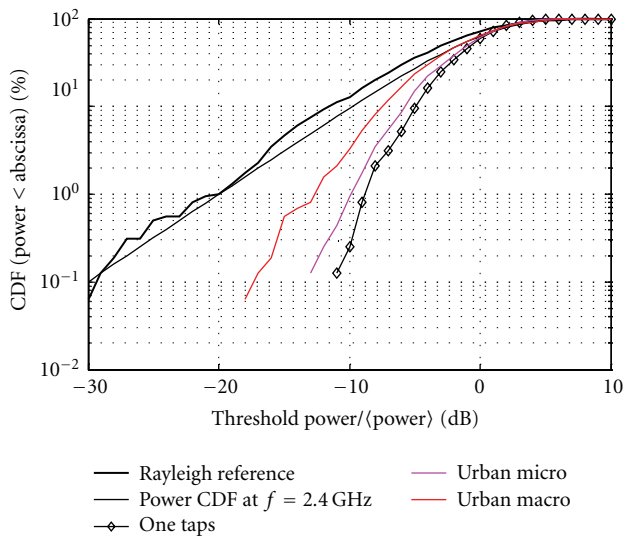


FIGURE 10: SISO cumulative distribution function measured in an RC for one cluster, urban micro-, and macrocell channel model cases.

- (ii) the CDFs from the averaged power of received signal, demodulated after equalization.

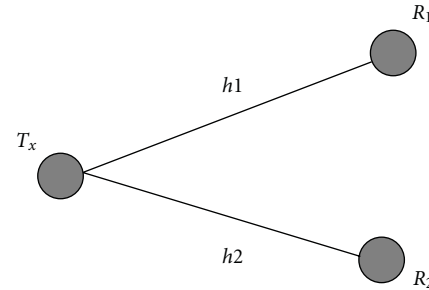
For this comparison, each measured power of these results is normalized to its own average power.

As it is known OFDM signal gives better performance than using mono-carrier signal. It is an efficient way to deal against intersymbol interference, because such interference affects only a small percentage of the subcarriers. These interferences cause a frequency selectivity that can be well observed in Figure 10. Indeed it can be clearly seen that the cumulative power distributions are influenced by the delay spread of the channel model. The performance in urban micro- and urban macrocell channel models is worse compared to the monocluster case. Nevertheless, the received powers of the LTE signals are higher than those in the mono-carrier case (which fit with the Rayleigh reference distribution).

These results can be confirmed by the signal-to-Noise ratio measurement, presented below. The estimation of the

TABLE 3: Measured mean SNR value for SISO configuration for a 64-QAM modulation scheme.

	Monocluster	Urban microcell	Urban macrocell
Mean SNR (dB)	25.7	7.9	6.4


 FIGURE 11: 1×2 Multiple antenna configuration.

measured mean SNR presented in Table 3 is done through the Error Vector Magnitude (EVM) [22]:

$$\text{EVM} = \left[\frac{(1/N) \sum_{i=1}^N |S_{\text{ideal},i} - S_{\text{meas},i}|^2}{(1/N) \sum_{i=1}^N |S_{\text{ideal},i}|^2} \right]^{1/2}, \quad (1)$$

where N is the number of symbols, $S_{\text{ideal},i}$ denotes the ideal constellation point for the i th symbol, and $S_{\text{meas},i}$ is the measured i th symbol.

The SNR is the inverse of the EVM taken in dB, which is given by

$$\text{SNR} = 20 \times \log_{10} \left(\frac{1}{\text{EVM}} \right). \quad (2)$$

The SISO measurement method allows assessing the capacity of a complete LTE transmission chain. This method makes it possible to know the performance as function of the receiver antenna, or base band processing (equalization, synchronization, etc.).

4.2. SIMO Measurement. In this section, the tests of the diversity systems performance are under interest. Diversity combining techniques such as Maximum Ratio Combining (MRC) have been implemented.

Multiple antennas are expressed as a $T \times R$ combination, where T is the number of transmitting antennas, and R is the number of the receiving antennas.

The example shown in Figure 11 presents a total of 2 links between transmit and receive antenna elements. These links are indicated by $h1$ and $h2$. These expressions are associated jointly to form an H matrix (obtained by channel sounding measurements):

$$H_{\text{meas}} = \begin{bmatrix} h1 \\ h2 \end{bmatrix}. \quad (3)$$

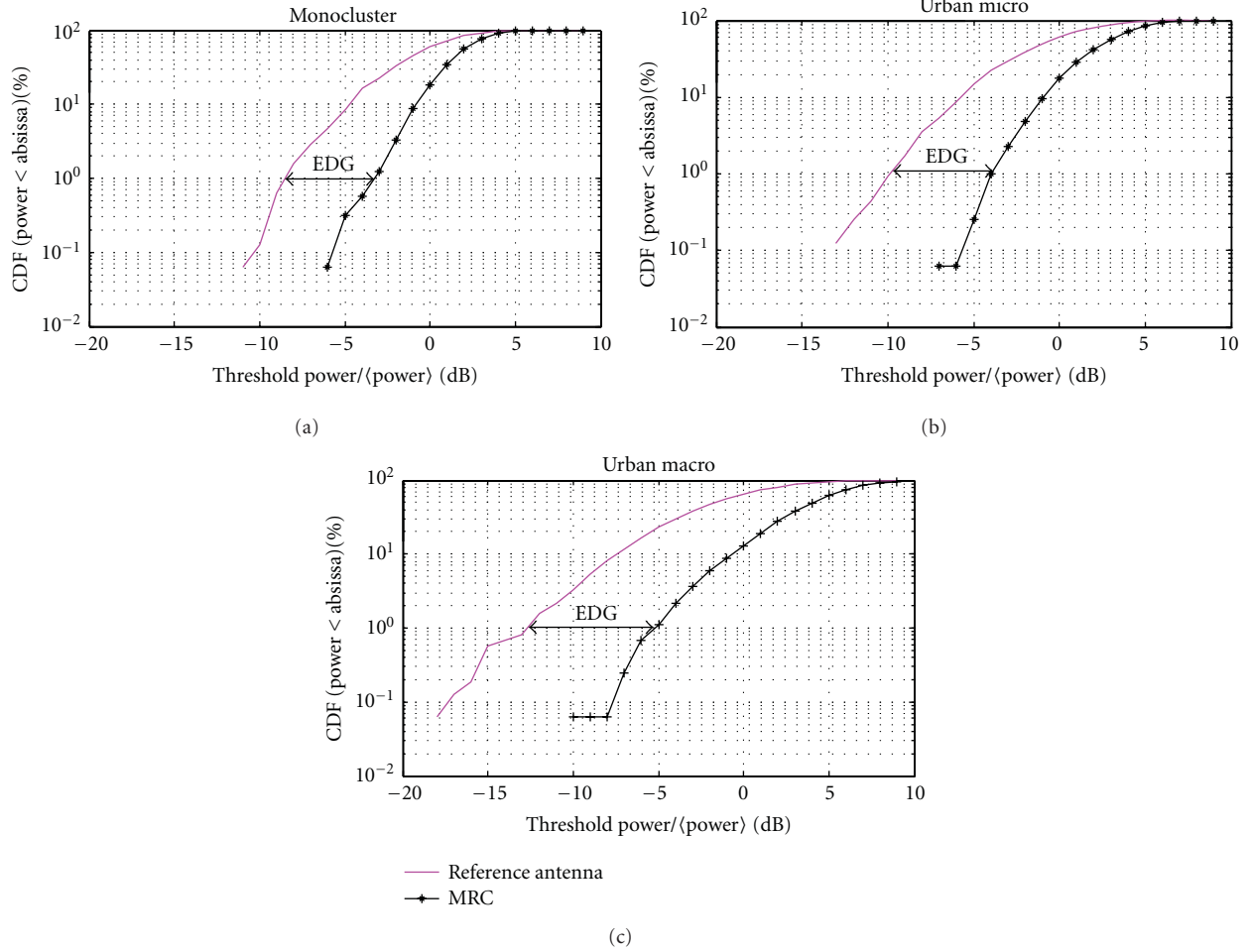


FIGURE 12: SIMO cumulative distribution function measured in an RC for one cluster (a), urban microcell (b), and urban macrocell (c) channel model cases.

The channel impulse responses taking in consideration multipath propagation phenomenon are presented by h_1 and h_2 . The envelope correlation coefficient is as follows:

$$\rho = \frac{R(1,2)}{\sqrt{R(1,1)R(2,2)}}, \quad (4)$$

$$R = E\{(H_{\text{meas}} - E[H_{\text{meas}}])(H_{\text{meas}} - E[H_{\text{meas}}])^H\},$$

where R is the covariance matrix.

The calculation of the fading correlation coefficient for the different channel models generated in the RC is presented in Table 4.

It can be observed that for each channel model, the fading correlation remains low, which will lead to optimal diversity results.

Regarding the effective diversity gain (EDG), it is typically calculated for a particular frequency (passive measurements). EDG is the figure-of-merit (FOM) typically used to evaluate the efficiency of the diversity antenna system [14]. In our case, the evaluation of the EDG is made through the mean power of the received LTE signal in baseband.

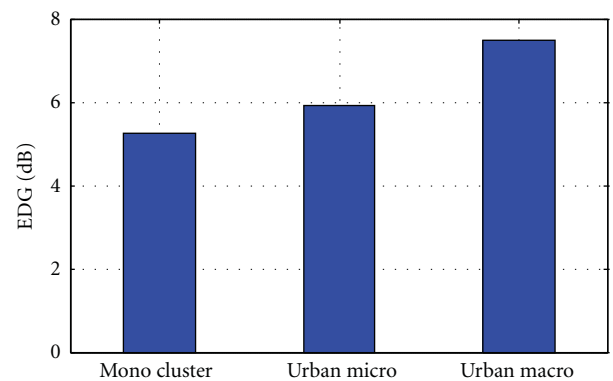


FIGURE 13: EDG for MRC technique at (1%) for one cluster and urban micro- and macrocell channel model cases.

The CDFs of the received power (for the diversity and reference systems) are depicted in Figure 12. These results are normalized by the mean power received by the reference system in order to calculate the EDG at 1% probability (Figure 13).

TABLE 4: Correlation coefficient.

	Scenario		
	One cluster	Urban micro	Urban macro
Fading correlation coefficient	0.15	0.21	0.32

In conclusion, as we can observe in Figure 13 that the more significant improvement in terms of diversity gain is achieved for the macrourban channel case (7.5 dB). The Diversity Gain obtained for the monocenter case is less important, and it reaches 5.2 dB. This limitation is due to the fact that the SNR of the SISO system in this case was already high when compared to the SNR in multiplexed channels.

5. Conclusions

In this paper, we achieve to emulate the 3GPP channel models in a small reverberation cell. The performance of an LTE SISO/SIMO-OFDM system has been studied through active measurements for different channel models with Rayleigh fading distribution. The work developed in this paper permits to evaluate capacity of a wireless system in controlled environments and gives the opportunity to test different transmission chain parameters (base band processing, modulation scheme, antennas, etc.) in the same environment and compare their performance. This approach could be of particular interest for OTA characterization of multiantenna terminals in reverberation chambers, because it helps to understand the influence of the channel characteristics under which measurements have been performed.

Future works will consist in making experiments with specific MIMO schemes, based on LTE specifications. Regarding the control of the delay spread, an analytical method will be developed to estimate it in function of the amount of absorbing material inside the RC. This method will lead to avoid channel sounding measurements, currently needed to achieve the desired delay spread.

References

- [1] J. F. Valenzuela-Valdès, A. M. Martínez-Gonzalez, and D. A. Sánchez-Hernandez, "Diversity gain and MIMO capacity for non isotropic environments using a reverberation chamber," *Antennas and Wireless Propagation Letters, IEEE*, vol. 8, pp. 112–115, 2009.
- [2] D. A. Hill, M. T. Ma, A. R. Ondrejka, B. F. Riddle, M. L. Crawford, and R. T. Johnk, "Aperture excitation of electrically large, lossy cavities," *IEEE Transactions on Electromagnetic Compatibility*, vol. 36, no. 3, pp. 169–178, 1994.
- [3] J. D. Sánchez-Heredia, J. F. Valenzuela-Valdès, A. M. Martínez-Gonzalez, and D. A. Sánchez-Hernandez, "Emulation of MIMO rician fading environments with mode-stirred reverberation chambers," *IEEE Transactions on Antennas and Propagation*, vol. 59, no. 2, pp. 654–660, 2011.
- [4] X. Chen, P. S. Kildal, C. Orlenius, and J. Carlsson, "Channel sounding of loaded reverberation chamber for over-the-air testing of wireless devices: coherence bandwidth versus average mode bandwidth and delay spread," *IEEE Antennas and Wireless Propagation Letters*, vol. 8, Article ID 5072260, pp. 678–681, 2009.
- [5] 3GPP TS 36.101, Evolved Universal Terrestrial Radio Access (E-UTRA); User Equipment (UE) radio transmission and reception (Release 9), version 9.3.0, March 2010.
- [6] 3GPP TR 37.976, Measurement of radiated performance for MIMO and multi-antenna reception for HSPA and LTE terminals (Release 10), version 1.1.0, May 2010.
- [7] A. Diallo, C. Luxey, P. L. Thuc, R. Straj, and G. Kossiavas, "Diversity performance of multiantenna systems for UMTS cellular phones in different propagation environments," *International Journal of Antennas and Propagation*, vol. 2008, Article ID 836050, 10 pages, 2008.
- [8] A. Pascual-Iserte, L. M. Ventura, and X. Nieto, "Residual carrier frequency offset estimation and correction in OFDM MIMO systems," in *Proceedings of the 18th Annual IEEE International Symposium on Personal, Indoor and Mobile Radio Communications (PIMRC'07)*, pp. 1–5, Athens, Greece, September 2007.
- [9] S. Blanch, J. Romeu, and I. Corbella, "Exact representation of antenna system diversity performance from input parameter description," *Electronics Letters*, vol. 39, no. 9, pp. 705–707, 2003.
- [10] LTE forum technology, <http://www.3gpp.org/>.
- [11] M. B. Knudsen and G. F. Pedersen, "Spherical outdoor to indoor power spectrum model at the mobile terminal," *IEEE Journal on Selected Areas in Communications*, vol. 20, no. 6, pp. 1156–1169, 2002.
- [12] T. Bolin, A. Derneryd, G. Kristensson, V. Plicanic, and Z. Ying, "Two-antenna receive diversity performance in indoor environment," *Electronics Letters*, vol. 41, no. 22, pp. 1205–1206, 2005.
- [13] R. G. Vaughan and J. B. Andersen, "Antenna diversity in mobile communication," *IEEE Transactions on Vehicular Technology*, vol. 36, no. 4, pp. 149–172, 1987.
- [14] P. S. Kildal, K. Rosengren, J. Byun, and J. Lee, "Definition of effective diversity gain and how to measure it in a reverberation chamber," *Microwave and Optical Technology Letters*, vol. 34, no. 1, pp. 56–59, 2002.
- [15] T. Taga, "Analysis for mean effective gain of mobile antennas in land mobile radio environments," *IEEE Transactions on Vehicular Technology*, vol. 39, no. 2, pp. 117–131, 1990.
- [16] A. Belhouji, C. Decroze, D. Carsenat, M. Mouhamadou, and T. Monediere, "Active measurements of a MIMO WiMAX-OFDM based system in reverberation chambers," *Microwave and Optical Technology Letters*, vol. 52, no. 10, pp. 2347–2352, 2010.
- [17] ETS-Lindgren's, "SMART 1000 Mini-Reverb Cell," <http://www.ets-lindgren.com/pdf/smart1000.pdf>.
- [18] <http://www.ecanechoicchambers.com/>.
- [19] J. C. Lin and C. Y. Lin, "Noncoherent sequential PN code acquisition using sliding correlation in DS/SS," in *Proceedings of the IEEE International Conference on Communications (ICC'00)*, vol. 1, pp. 341–345, New Orleans, La, USA, June 2000.
- [20] M. Mouhamadou, M. Koubeissi, C. Tounou et al., "Multi-band diversity antenna performances evaluation for multi-standard compact wireless terminal," in *Proceedings of the 3rd European Conference on Antennas and Propagation (EuCAP '09)*, Berlin, Germany, March 2009.

- [21] M. Mouhamadou, M. Koubeissi, C. Tounou et al., "Multi-band diversity antenna performances evaluation for multi-standard compact wireless terminal," in *Proceedings of the 3rd European Conference on Antennas and Propagation (EuCAP '09)*, Berlin, Germany, March 2009.
- [22] R. A. Shafi, S. Rahman, and A. H. M. Razibul, "On the extended relationships among EVM, BER and SNR as performance metrics," in *Proceedings of the International Conference on Electrical and computer Engineering (ICECE '06)*, Dhaka, Bangladesh, December 2006.

Research Article

MIMO Throughput Effectiveness for Basic MIMO OTA Compliance Testing

Adoración Marín-Soler, Guillermo Ypiña-García, Álvaro Belda-Sanchiz, and Antonio M. Martínez-González

EMITE Ingeniería SLNE, Edificio CEDIT, Parque Tecnológico de Fuente Álamo, Ctra. Estrecho-Lobosillo km 2.5, Campus Espinardo, Espinardo, 30320 Fuente Álamo, Murcia, Spain

Correspondence should be addressed to Adoración Marín-Soler, adoracion.marin@emite-ingenieria.es

Received 1 December 2011; Accepted 4 January 2012

Academic Editor: David A. Sanchez-Hernandez

Copyright © 2012 Adoración Marín-Soler et al. This is an open access article distributed under the Creative Commons Attribution License, which permits unrestricted use, distribution, and reproduction in any medium, provided the original work is properly cited.

During the March 2011 meeting of the CTIA MIMO OTA Subgroup (MOSG), the members agreed that the subgroup should first determine “what” aspects of a MIMO-capable device require evaluation; then the group should determine “how” to go about making these measurements. In subsequent meetings of MOSG, new yet-unnamed figures of merit were asked for in order to provide a solution to the carriers’ requirements for LTE MIMO OTA evaluation. Furthermore, the December 2011 3GPP RAN4 status report on LTE MIMO OTA listed the evaluation of the use of statistical performance analysis in order to minimize test time and help ensure accurate performance assessment as an open issue. This contribution addresses these petitions by providing four new figures of merit, which could serve the purpose of evaluating the operators’ top priorities for MIMO OTA compliance testing. The new figures of merit are MIMO Throughput Effectiveness (MTE), MIMO Device Throughput Effectiveness (MDTE), MIMO Throughput Gain (MTG), and MIMO Device Throughput Gain (MDTG). In this paper, MTE is evaluated using the recently available LTE MIMO OTA RR data from 3GPP.

1. Introduction

Two levels of Multiple Input Multiple Output (MIMO) testing have been established: Basic (verification of MIMO Over-The-Air [OTA] performance in an isotropic environment) and Advanced (Evaluation of MIMO OTA performance in a spatial test environment). In March, 2010, the MACSG (anechoic chamber subgroup) and RCSG (reverberation chamber subgroup) chairs held a conference call with several United States (US) operators to review Third Generation Partnership project (3GPP) Radio Access Network 4 (RAN4)’s OTA proposals at a high level and request independent input concerning each operator’s MIMO test priorities. Operators were asked to rank their MIMO OTA test priorities in descending order, with a limit of six priorities. For all intents and purposes, the top priority of all carriers was to determine whether or not a MIMO Device Under Test (DUT) actually provides gain over a comparable Single Input Single Output (SISO) device. In second place operators wanted to look for

information concerning the device’s transmitting radiated performance, particularly at strong signal level compared to SISO.

The task of identifying new Figures of Merit (FoM) was then open as some of the traditional definitions of Single Input Multiple Output (SIMO) FoMs have been reported to be not suitable for characterizing the mobile terminal’s MIMO antenna radiation performance. In a recent communication [1], CTIA (The Wireless Association of US-based Industries MIMO OTA subgroup (MOSG)) proposed to search for a yet-unnamed metric that provides a ratio between the DUT’s radiated and conducted throughput performance in each test condition. This metric requires that the test solution provider has to provide a ratio and show traceability between the DUT’s radiated SIMO and radiated MIMO throughput performance tests. Similarly, the December 2011 3GPP RAN4 status report on Long-Term Evolution (LTE) MIMO OTA listed the evaluation of the use

of statistical performance analysis in order to minimize test time and help ensure accurate performance assessment as an open issue.

In this contribution, the authors introduce novel figures of merit with potential for determining these aspects above in a simple and cost-effective way within the Basic MIMO Testing level using the commonly agreed throughput figure of merit and some statistical analyses. As preliminary examples of the implementation of these FoMs, one of the new FoMs (MIMO Throughput Effectiveness or MTE) is evaluated using the recently available LTE MIMO OTA RR data from 3GPP.

Results show that the new figure serves its purpose to clearly distinguished good from bad MIMO device in a simple and cost-effective way. For Reverberation Chamber-(RC-) based and Anechoic Chamber-(AC-) based methods, the new metric results also show a very low standard deviation between labs (below 0.1). Results for 2-stage methodology were not fully available for this study and will be studied in future contributions if provided. In addition, results also show that intermediate MTE values ($MTE(P_n)$) can provide a clear indication of the ability (or disability) of the MIMO device to maintain throughput when under a variety of situations (under stress) and therefore also serve the different goals of such complex MIMO OTA performance assessment. Finally, results demonstrate that the reverberation chamber technique is a solid methodology for LTE MIMO OTA Basic evaluation, and that standard deviations between labs when using the new evaluated FoM (MTE) fall below 0.08. RC-based methods are very fast in comparison to other existing alternatives. Since test time has been proposed to be added as a metric for LTE MIMO OTA compliance testing [2], RC-based methods represent a promising test methodology for LTE MIMO OTA compliance testing.

2. Proposal

The CTIA MIMO OTA test prerequisites outlined in MOSG110707R2 are assumed. MIMO radiated performance can be assessed in terms of

- (A) measured throughput relative to the theoretical MIMO maximum throughput for a given reference channel with no radio channel impairments,
- (B) measured throughput relative to the DUT-measured MIMO maximum throughput for a given reference channel with no radio channel impairments,
- (C) measured throughput relative to the theoretical SIMO maximum throughput for a given reference channel with no radio channel impairments,
- (D) measured throughput relative to the DUT-measured SIMO maximum throughput for a given reference channel with no radio channel impairments.

Options (A) and (C) allow for inter-DUT analyses, while options (B) and (D) serve intra-DUT performance evaluation. For example, according to 3GPP TS 36.101,

Annex A.3.3.2.1-1, the maximum theoretical throughput for Reference Measurement Channel (RMC) R.11 (10 MHz Frequency Division Duplex [FDD], 16 Quadrature Amplitude Modulation [QAM]) is 11,664 kbps per stream, for a total throughput of 23,328 kbps. This throughput is based on a nonfading channel with no multipath and a receiver correlation coefficient of zero. Measurement of the DUT under ideal conducted conditions allows the CTIA-Authorized Test Lab (CATL) to ensure that the DUT and the test equipment are performing as expected prior to beginning actual OTA testing.

Based on the prerequisites above, we propose that the following steps be followed to determine the new metrics, which could be integrated within the Basic MIMO OTA performance evaluation process.

- (1) Select at least 4 different RMCs (i.e., different reference measurement channels) based on the Channel Quality Indicator (CQI), Rank Indicator (RI), and Precoding Matrix Indicator (PMI) reported by the User equipment (UE). The RMC used shall be the RMC for sustained downlink data rate per section A.3.9 of 3GPP TS 36.521-1 and based on the UE's device category.
- (2) Measure the DUT's maximum MIMO Downlink (DL) throughput using a base station simulator connected directly to the DUT with no radio channel impairments, at a downlink power level (RS_EPRE) of -80 dBm/15 kHz using 2-layer, closed-loop spatial multiplexing for the selected RMCs in step 2. The measured MIMO throughputs at this downlink power level shall be considered the MIMO maximum throughputs for this DUT and eNodeB simulator under unimpaired radio conditions for each selected RMC and shall be $>97\%$ of the theoretical throughput specified by 3GPP TS 36.521-1, A.3.9.
- (3) Measure the DUT's maximum SIMO DL throughput using a base station simulator connected directly to the DUT with no radio channel impairments, at a downlink power level RS_EPRE of -80 dBm/15 kHz (using single-layer transmit diversity). The measured SIMO throughput at this downlink power level shall be considered the SIMO maximum for this DUT and eNodeB simulator under unimpaired radio conditions.
- (4) Place the DUT into a test chamber capable of emulating an isotropic Rayleigh-fading environment (NIST channel model). It is generally agreed that the isotropic environment does give kind of a "global view" on the device's performance, and it is therefore the best *a priori* selection for the Basic MIMO OTA tests. For Single Antenna transmission mode, measure the MIMO DL throughput using a base station simulator connected to the test chamber while emulating the National Institute of Standards and Technology (NIST) channel model and an RMC appropriate to the DUT's capabilities. The average downlink power applied to the DUT has to be

set from -85 dBm/15 kHz (RS_EPRE) down to -120 dBm/15 kHz in 1 dBm/KHz steps. The nature of the noise profile (e.g., Additive White Gaussian Noise [AWGN] or other) is a topic For Future Study [FFS].

- (5) Evaluate the channel-model averaged MIMO Throughput Effectiveness (MTE), MIMO Device Throughput Effectiveness (MDTE), MIMO Throughput Gain (MTG), and MIMO Device Throughput Gain (MDTG) for each averaged channel power step value by

$$\begin{aligned} \text{MTE}(P_n)^{\text{ChM}_m} &= \frac{\sum_{i=1}^C \text{TPUT}(P_n)_{\text{RMC}_i}^{\text{ChM}_m}}{C * \text{TPUT}_{\text{MIMOtheor. max}}(P_n)_{\text{RMC}_i}^{\text{ChM}_m}}, \\ \text{MDTE}(P_n)^{\text{ChM}_m} &= \frac{\sum_{i=1}^C \text{TPUT}(P_n)_{\text{RMC}_i}^{\text{ChM}_m}}{C * \text{TPUT}_{\text{MIMO meas. max}}(P_n)_{\text{RMC}_i}^{\text{ChM}_m}}, \\ \text{MTG}(P_n)^{\text{ChM}_m} &= \frac{\sum_{i=1}^C \text{TPUT}(P_n)_{\text{RMC}_i}^{\text{ChM}_m}}{C * \text{TPUT}_{\text{SIMOtheor. max}}(P_n)_{\text{RMC}_i}^{\text{ChM}_m}}, \\ \text{MDTG}(P_n)^{\text{ChM}_m} &= \frac{\sum_{i=1}^C \text{TPUT}(P_n)_{\text{RMC}_i}^{\text{ChM}_m}}{C * \text{TPUT}_{\text{SIMO meas. max}}(P_n)_{\text{RMC}_i}^{\text{ChM}_m}}, \end{aligned} \quad (1)$$

where C indicates the number of selected RMCs, P_n indicates a dependence on channel power, ChM_m indicates the m th selected channel model for performance evaluation, RMC_i indicates the i th selected Reference Measured Channel, $\text{TPUT}_{\text{MIMOtheor. max}}$ indicates the MIMO maximum theoretical throughput, $\text{TPUT}_{\text{MIMO meas. max}}$ indicates the MIMO maximum DUT-measured throughput for this DUT and eNodeB simulator under unimpaired radio conditions as defined in step 2, $\text{TPUT}_{\text{SIMOtheor. max}}$ indicates the SIMO maximum theoretical throughput, $\text{TPUT}_{\text{SIMO meas. max}}$ indicates the SIMO maximum DUT-measured throughput for this DUT and eNodeB simulator under unimpaired radio conditions as defined in step 3, and C indicates the number of selected Reference Measured Channels for MTE/MDTE/MTG/MDTG performance evaluation.

- (6) Repeat the DL throughput measurements in steps 4 to 5 using the channel models (i.e., the delay and power profiles only) below:
- (a) Spatial Channel Model (SCM) Urban Micro (UMi) channel model,
 - (b) SCM Urban Macro (UMa) channel model.
- (7) Repeat the DL throughput measurements in steps 4 to 6 using the total of transmission modes below:
- (a) open-loop Spatial Multiplexing (SM),
 - (b) closed-loop SM,
 - (c) closed-loop SM with single layer. This makes a total number of tested transmission modes $T = 4$. Other modes can of course be tested and added to the proposal in the future.

- (8) Evaluate the transmission mode-averaged MTE/MDTE/MTG/MDTG for each averaged channel power step value by

$$\begin{aligned} \text{MTE}(P_n)_{T_{x_i}} &= \frac{\sum_{m=1}^C \text{MTE}(P_n)^{\text{ChM}_m}}{C}, \\ \text{MDTE}(P_n)_{T_{x_i}} &= \frac{\sum_{m=1}^C \text{MDTE}(P_n)^{\text{ChM}_m}}{C}, \\ \text{MTG}(P_n)_{T_{x_i}} &= \frac{\sum_{m=1}^C \text{MTG}(P_n)^{\text{ChM}_m}}{C}, \\ \text{MDTG}(P_n)_{T_{x_i}} &= \frac{\sum_{m=1}^C \text{MDTG}(P_n)^{\text{ChM}_m}}{C}. \end{aligned} \quad (2)$$

The obtained $\text{MTE}(P_n)_{T_{x_i}}$ figure can be compared between DUTs, where an $\text{MTE}(P_n)_{T_{x_i}} = 1$ would indicate radiated performance identical to MIMO maximum theoretical throughput performance. In this way, an intermediate metric for evaluation of performance and comparison between DUTs due to transmission mode with respect to a comparable MIMO is obtained.

The obtained $\text{MDTE}(P_n)_{T_{x_i}}$ figure can be used to compare the relative device's behavior for different transmission modes with respect to its optimum MIMO performance, where an $\text{MDTE}(P_n)_{T_{x_i}} = 1$ would indicate radiated performance identical to the device's maximum MIMO throughput performance.

The obtained $\text{MTG}(P_n)_{T_{x_i}}$ figure can be compared between DUTs, where an $\text{MTG}(P_n)_{T_{x_i}} = 1$ would indicate radiated performance identical to SIMO maximum theoretical throughput performance. In this way an intermediate metric for evaluation of performance and comparison between DUTs due to transmission mode with respect to a comparable SIMO is obtained.

The obtained $\text{MDTG}(P_n)_{T_{x_i}}$ figure can be used to compare the relative device's behavior for different transmission modes respect to its optimum SIMO performance, where an $\text{MDTG}(P_n)_{T_{x_i}} = 1$ would indicate radiated performance identical to the device's maximum SIMO throughput performance.

Intermediate values of MTE/MDTE/MTG/MDTG at high signal level ($P_1 = -85$ dBm/15 kHz) can be calculated by

$$\begin{aligned} \text{MTE}(P_1) &= \sum_{i=1}^T \text{MTE}(P_1)_{T_{x_i}}, \\ \text{MDTE}(P_1) &= \sum_{i=1}^T \text{MDTE}(P_1)_{T_{x_i}}, \\ \text{MTG}(P_1) &= \sum_{i=1}^T \text{MTG}(P_1)_{T_{x_i}}, \\ \text{MDTG}(P_1) &= \sum_{i=1}^T \text{MDTG}(P_1)_{T_{x_i}}. \end{aligned} \quad (3)$$

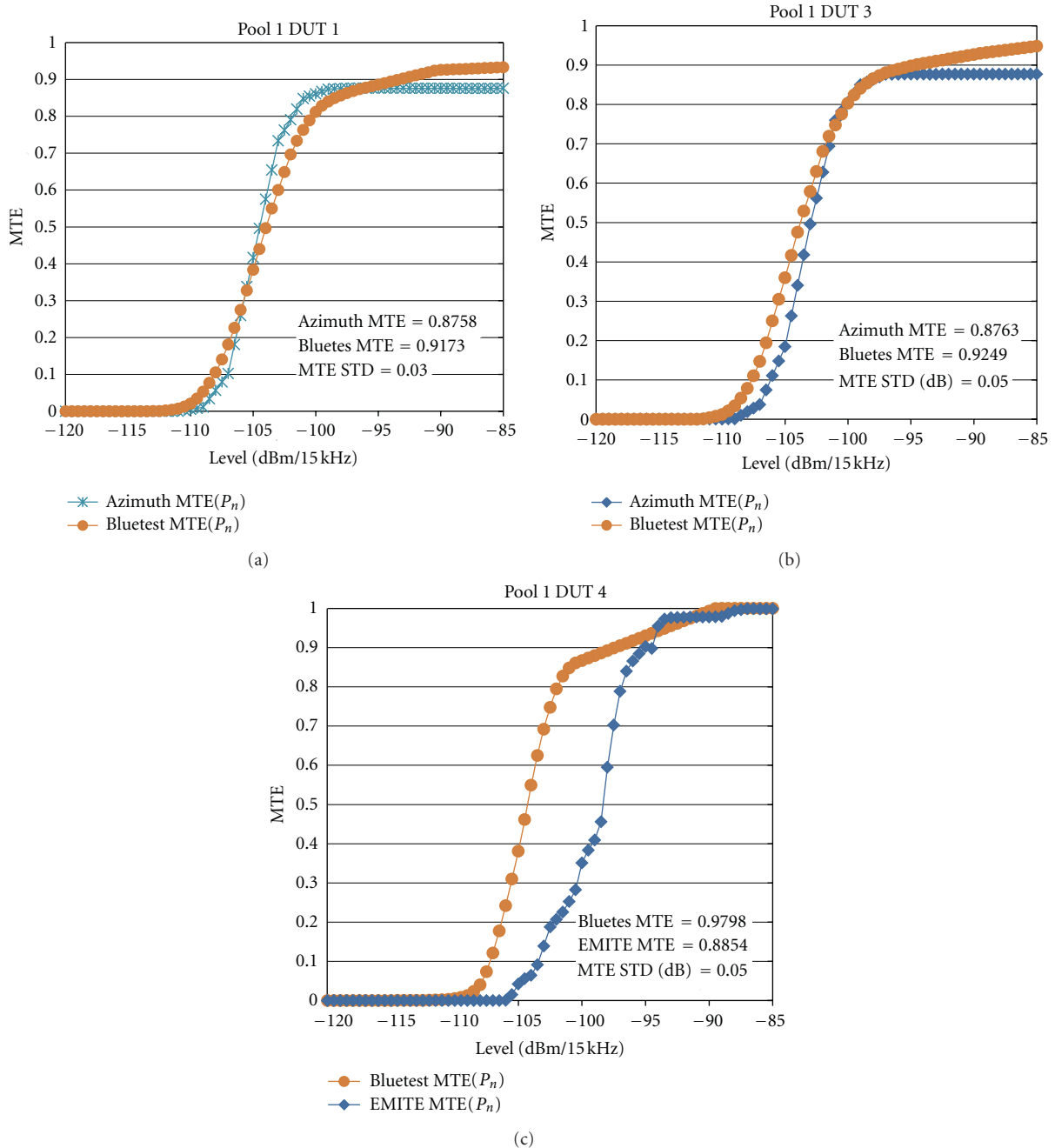


FIGURE 1: MTE for Pool 1 with the RC methodology.

The obtained MTE at -85 dBm/15 kHz figure can be compared between DUTs, where an MTE (-85 dBm/15 kHz) = 1 would indicate radiated performance identical to MIMO maximum theoretical throughput performance. In this way, an intermediate metric for evaluation of performance and comparison between DUTs in strong signal level with respect to a comparable MIMO is obtained.

The obtained MDTE at -85 dBm/15 kHz figure can be used to compare the relative device's behavior for different transmission modes respect to its MIMO performance at high signal level, where an MDTE (-85 dBm/15 kHz) = 1

would indicate radiated performance identical to the device's maximum MIMO throughput performance.

The obtained MTG at -85 dBm/15 kHz figure can be compared between DUTs, where an MTG (-85 dBm/15 kHz) = 1 would indicate radiated performance identical to SIMO maximum throughput performance. In this way, an intermediate metric for evaluation of performance and comparison between DUTs in strong signal level with respect to a comparable SIMO is obtained.

The obtained MDTG at -85 dBm/15 kHz figure can be used to compare the relative device's behavior for different

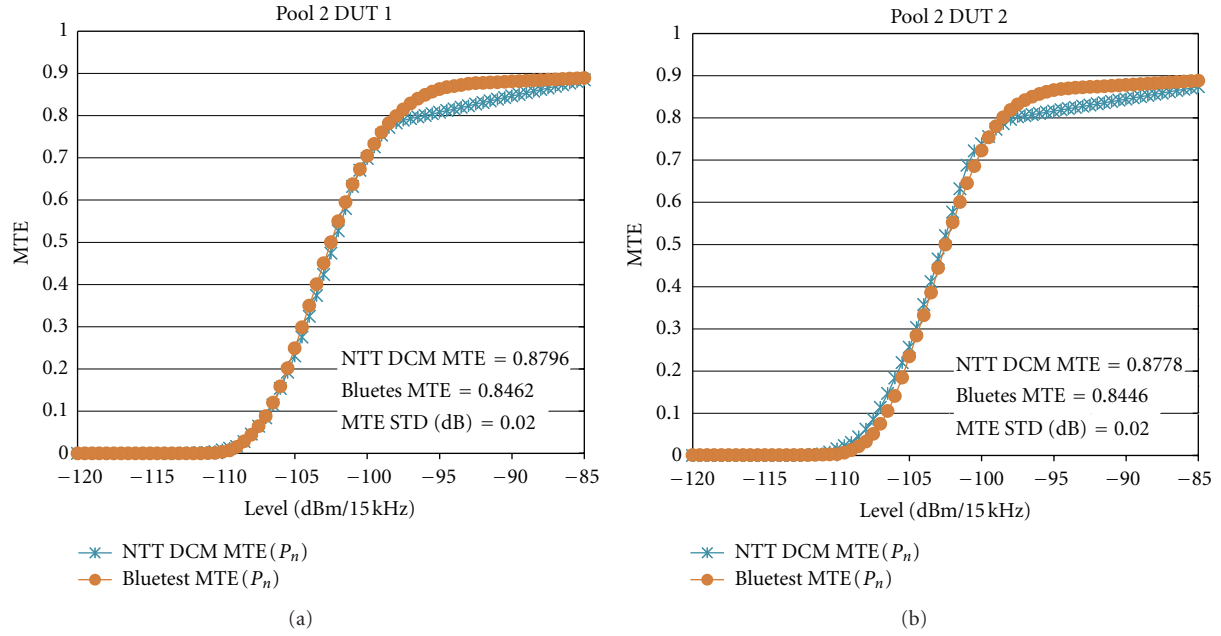


FIGURE 2: MTE for Pool 2 with the RC methodology.

transmission modes with respect to its SIMO performance at high signal level, where an MTG (-85 dBm/15 kHz) = 1 would indicate radiated performance identical to the device's maximum SIMO throughput performance.

- (9) Evaluate MTE/MDTE/MTG/MDTG values for the DUT by

$$\begin{aligned}
 \text{MTE} &= \sum_{n=1}^{36} \frac{\sum_{i=1}^T \text{MTE}(P_n)_{Tx_i}}{36 * T}, \\
 \text{MDTE} &= \sum_{n=1}^{36} \frac{\sum_{i=1}^T \text{MDTE}(P_n)_{Tx_i}}{36 * T}, \\
 \text{MTG} &= \sum_{n=1}^{36} \frac{\sum_{i=1}^T \text{MTG}(P_n)_{Tx_i}}{36 * T}, \\
 \text{MDTG} &= \sum_{n=1}^{36} \frac{\sum_{i=1}^T \text{MDTG}(P_n)_{Tx_i}}{36 * T},
 \end{aligned} \tag{4}$$

where T indicates the number of selected transmission modes.

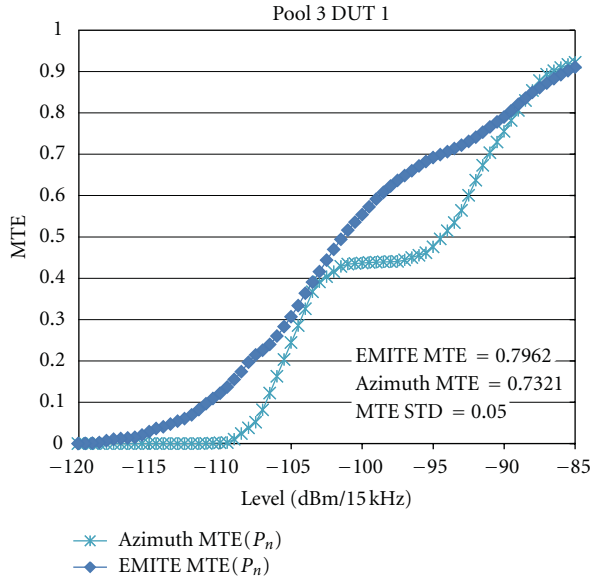
MTE, MDTE, MTG, and MDTG range from 0 to 1. All MTE/MDTE/MTG/MDTG figures and final values can be referred to as the DUTs MIMO Isotropic Performance (MIP). There is no minimum performance value for the MIP parameter at this time.

3. MTE Examples with 3GPP LTE MIMO OTA Round Robin Data

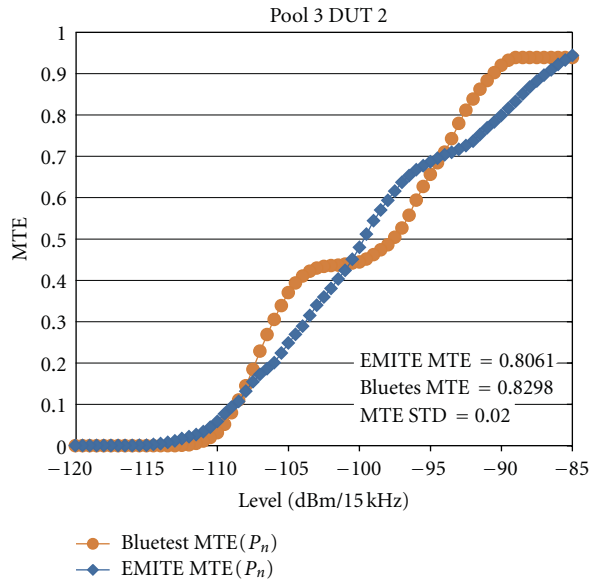
A large number of measured data has become readily available by 3GPP LTE MIMO OTA round robin (RR) campaign.

The data has been divided into three main methodologies: reverberation chamber, anechoic chamber, and two-stage methods. The analyses of the measured data revealed some difficulties for performing in-depth studies and obtaining conclusions. First, not all labs were able to test all available DUTs. Similarly, not all labs tested the DUTs in the diverse Pools for all the channel models. Some labs did not reach 100% throughput values, while others did for the same DUTs and channel models. Different relative throughput values (%) have been specified for the same base station emulator (BSE) settings by different test labs. The measured RS_EPRES range varied a lot between labs for the same devices. Some labs identified different 100% throughput reference for R.11 and R.xxx specified in the test plan [3], which could be attributable to BSE but also to specific subframe settings in the BSE. The fact that the test plan has been dynamically changed throughout the campaign has not helped solving these issues. As a conclusion, the lack of a clearly defined test environment and test equipment aspects has made the resulting data have large uncertainties for a good comparison.

Yet, the large amount of data allows for some statistical studies, and this is the first time it can be performed for LTE MIMO OTA. The statistical analyses performed by EMITE in this document are limited to MTE using 16QAM and open-loop transmission mode as these were the test parameters specified in the 3GPP LTE MIMO OTA test plan. While some labs have performed 64QAM and close-loop transmission mode tests, these do not share other settings and are, therefore, not suitable for comparison. Similarly, previous preliminary analyses [4] have outlined the need to compare tests with identical settings, and the statistical tests by EMITE have been performed over those data sets where similar DUT configurations and settings of the eNodeB



(a)



(b)

FIGURE 3: MTE for Pool 3 with the RC methodology.

have been identified. Finally, as averaged received channel power (RS EPRE) ranging varied slightly between labs, some interpolation has been used to have all test data ranging from -85 to -120 dBm. In the obtained results for MTE analyses, final throughput values higher than the maximum theoretical values/negative were not allowed and set to the maximum theoretical values/0.

3.1. RC-Based Tests. For the RC methodology, tests from EMITE, Bluetest, Azimuth, NTT DCM, and Ericsson have been performed. All these labs have employed three different mode-stirred reverberation chamber types: the E-Series by EMITE, the RTS-Series by Bluetest, and the MIC model

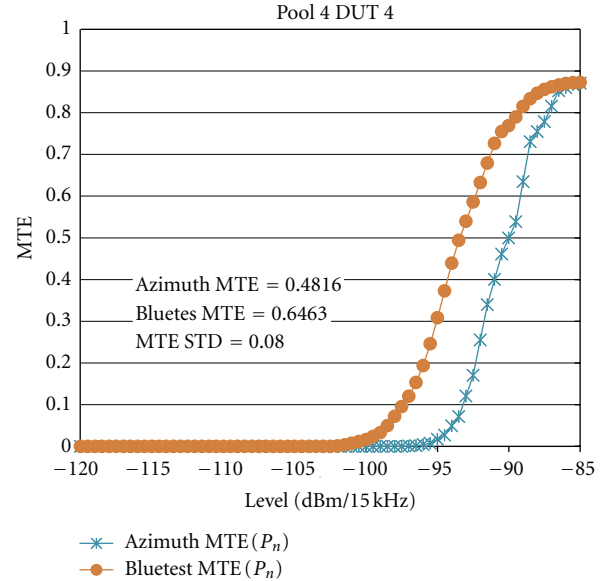


FIGURE 4: MTE for Pool 4 with the RC methodology.

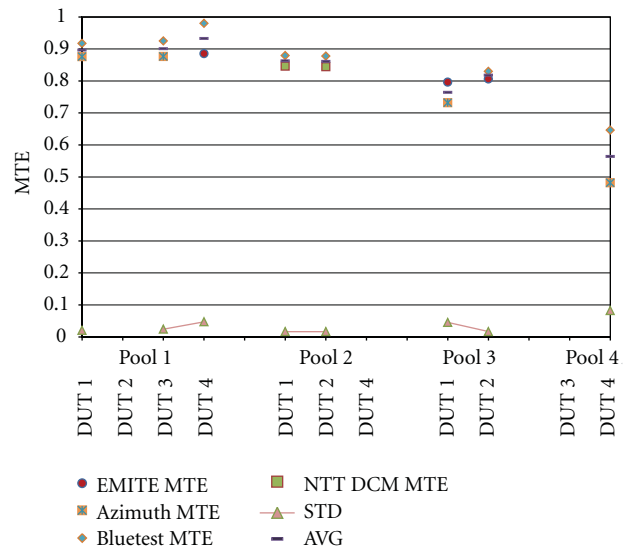


FIGURE 5: MTE for the RC methodology.

by Azimuth. In [4], the coordinator for the mode-stirred reverberation chamber method analyses selected the figures, which showed at least two different labs with identical settings. In consequence, we have studied MTE for these figures. $MTE(P_n)$ for Pools 1 to 4 is depicted in Figures 1, 2, 3, and 4.

Figures 5 and 6 illustrate MTE and the deviations of labs from averaged values. The figures are not complete as there are some DUTs for which there were no available data for comparison (at least two labs with identical settings).

The maximum MTE standard deviation (MTE STD) from group average for the RC-methodology falls below 0.08. It is interesting to observe that the deviations are very small for Pool 3, where three different mode-stirred reverberation chamber types are compared. Pool 3 was tested at

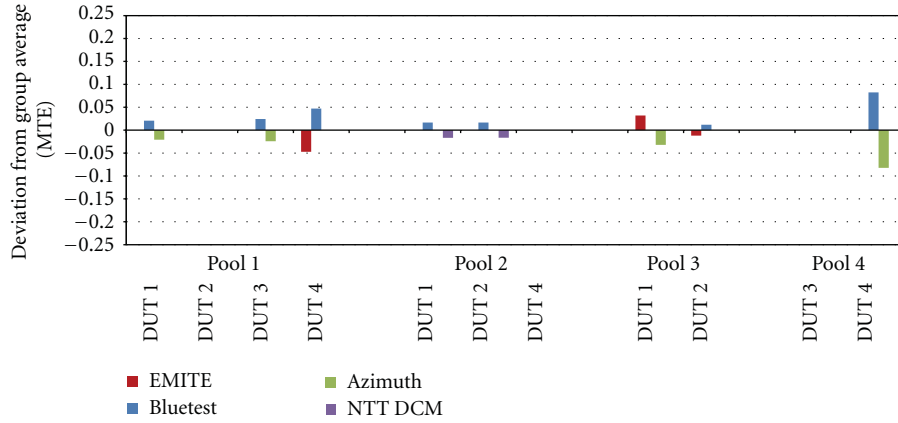


FIGURE 6: Deviation from group average (MTE STD) for the RC methodology.

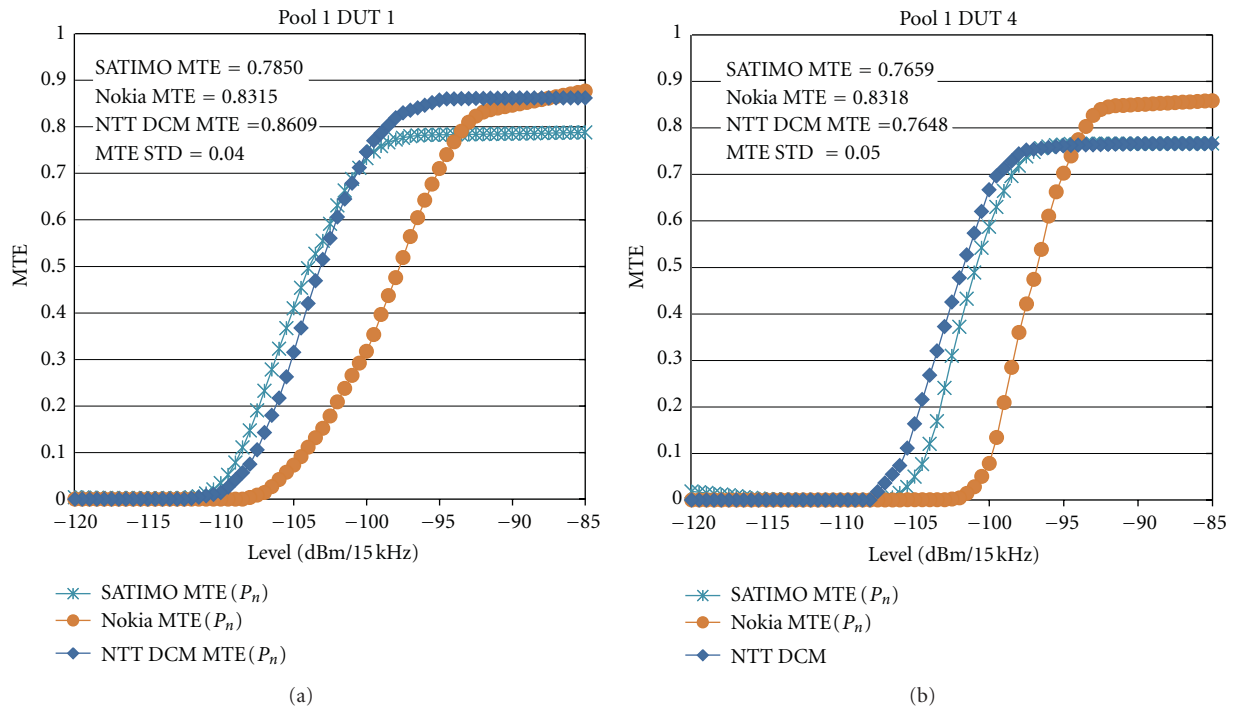


FIGURE 7: MTE for Pool 1 with the AC methodology.

the end of the campaign, and at that time many initial issues and settings doubts were solved and the test plan was updated accordingly. The small STD indicates that the RC methodology is a powerful and stable methodology for LTE Basic MIMO OTA device performance evaluation.

Averaged MTE deviations from group average for all Pools and those labs with more than one tested case compared have also been obtained by

- EMITE: -0.01,
- NTT DCM: -0.02,
- Blue test: 0.03,
- Azimuth: -0.04.

If we consider that an $MTE \geq 0.7$ represents a good MIMO device, from the RC-method MTE results it can be concluded that Pool1 and Pool 2 devices could be considered

good MIMO devices, although Pool 2 devices generally performed slightly worse than Pool1 devices. Pool 3 devices could also be considered good MIMO devices, but they are much closer to the $MTE = 0.7$ threshold outlined before than any device in Pool 1 or Pool 2. Pool 4 devices could be considered bad MIMO devices ($MTE < 0.7$). The largest deviation between labs is obtained for the bad MIMO devices.

3.2. AC-Based Tests. For the AC methodology, tests from SATIMO, Nokia, NTT DCM, and ETS-Spirent have been performed. MTE for Pools 1 to 4 is depicted in Figures 7, 8, 9, and 10.

Figures 11 and 12 illustrate MTE and the deviations of labs from averaged values. The figures are not complete as

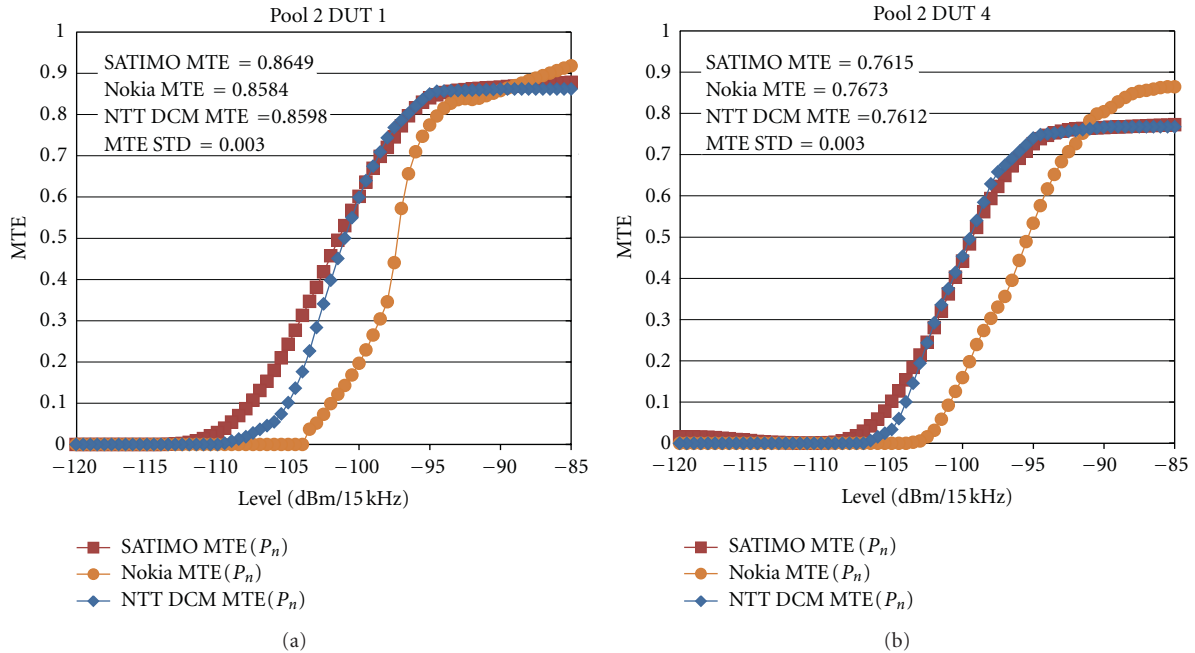


FIGURE 8: MTE for Pool 2 with the AC methodology.

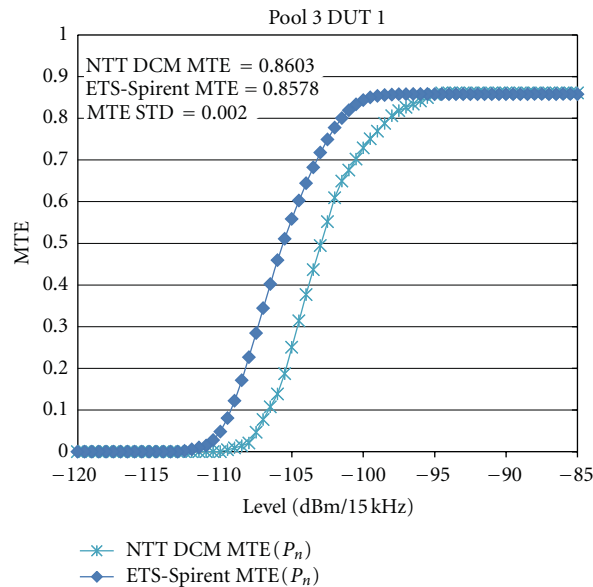


FIGURE 9: MTE for Pool 3 with the AC methodology.

there are some DUTs for which there were no available data for comparison (at least two labs with identical settings).

The maximum MTE standard deviation (MTE STD) from group average for the AC-methodology falls below 0.06. Averaged MTE deviations from group average for all Pools and those labs with more than one tested case compared have also been obtained by

Nokia: 0.01,
 NTT DCM: 0.01,
 SATIMO: -0.02.

From the AC-method MTE results, it can be concluded that Pool 1 and Pool 2 devices are found to be good MIMO devices. The AC-method also ranks Pool 3 DUT 1 as a good MIMO device. Pool 4 devices can be considered bad MIMO devices. The largest deviation between labs is obtained for the bad MIMO devices.

3.3. 2-Stage-Based Tests. The data from 2-stage tests (2S) was not entirely available for comparison. While data from Agilent was supplied in excel format, the data from Nokia

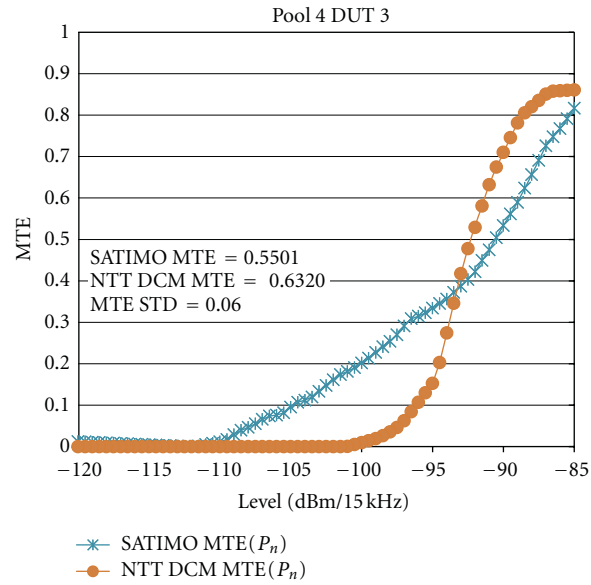


FIGURE 10: MTE for Pool 4 with the AC methodology.

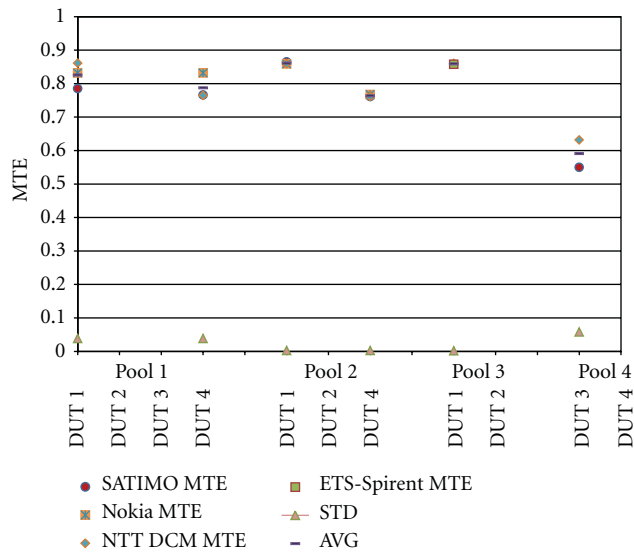


FIGURE 11: MTE for the AC methodology.

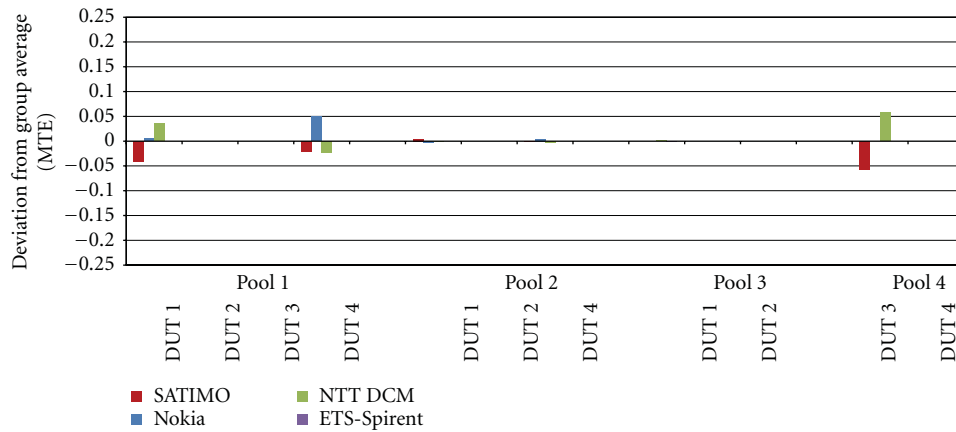


FIGURE 12: Deviation from group average (MTE STD) for the AC methodology.

was not supplied to the 3GPP reflector. Only some comments in [5] could be used (and reproduced here) to predict some conclusions, which would obviously need to be confirmed by MTE analyses. In particular, the ability to more precisely differentiate Pool 3 devices from Pool 1 or Pool 2 and the ability to identify Pool 4 device as bad MIMO devices using the 2S method should be clarified. The following sentences could be further studied.

R4-116104: For Pool3Dev1 and Pool3Dev2, the test results difference is quite large between the two-stage results and the reverberation chamber results. What makes it hard to understand is why the reverberation-chamber-based method has much higher throughput as compared with the test results of the two-stage method.

This statement above in [5] could mean that Pool 3 devices tested with the 2S method would lead to smaller MTE (smaller throughputs for the same RS EPRE), confirming the worse behavior of Pool 3 devices in comparison to Pool 1 and Pool 2 devices outlined by RC-based tests.

R4-116104: For Pool 4 devices, the test results difference is larger and the reverberation-chamber-based method has much worse performance as compared with two-stage method. However, the test results between the multiple-probe-antenna-based method and the two-stage method under this case have much less difference (2-3 dB) as compared to the difference between the two-stage method results and the reverberation-chamber-based method, which is a little bit less than 10 dB.

This statement above at [5] could mean that Pool4 devices may not be identified as bad MIMO devices by the 2S method, but rather as good MIMO devices, unlike what happened for both AC and RC methods.

When the analysis of MTE for 2-stage-based test data sets is finished, the above comments and some other issues could be further clarified.

4. Conclusions

Novel throughput-based figures of merit have been presented to respond to CTIA MOSG query for a global evaluation metric. 3GPP/CTIA LTE MIMO OTA Round Robin data has been used for validation of MIMO Throughput Effectiveness (MTE). MTE has demonstrated a great potential for solving the operators' top priorities regarding MIMO OTA compliance testing and performance evaluation. RC-based and AC-based methods have also shown to be able to differentiate good from bad MIMO devices using MTE. Given the short testing times of RC-based methods in comparison to other methods, the mode-stirred reverberation chamber methodology has proven to be a strong candidate for LTE MIMO OTA Basic evaluation with very low MTE deviation from group average between labs. Future studies include MTE for 2S test data sets and obtaining MDTE, MTG, and MDTG figures.

Acknowledgment

Only this work was supported by EMITE Ing.

References

- [1] S. Prather and A. Youtz, "OTA performance criteria for MIMO devices," CTIA Document MOSG110707R2, October 2011.
- [2] L. Anaya, "Status report TSG on SI: measurement of radiated performance for MIMO and multi-antenna reception for HSPA and LTE terminals," 3GPP RAN4 document RP-111150, December, 2011.
- [3] 3rd Generation Partnership Project (3GPP), "Measurement of radiated performance for MIMO and multi-antenna reception for HSPA and LTE terminals (Release 10)," Tech. Rep. 37.976 V1.5.0, Technical Specification Group Radio Access Networks, 2011.
- [4] Bluetest, EMITE, NTT DoCoMo, Ericsson, and Azimuth Systems, "Summary of the round robin data obtained with the reverberation chamber methodology," 3GPP RAN4 document R4-116164, November, 2011.
- [5] Agilent Technologies, "Summary of two-stage measurement results," 3GPP RAN4 document R4-116104, November, 2011.

Research Article

Mode-Stirred Chamber Sample Selection Technique Applied to Antenna Correlation Coefficient

Paul Hallbjörner,¹ Juan D. Sánchez-Heredia,² and Antonio M. Martínez-González²

¹ Electronics Department, SP Technical Research Institute of Sweden, Box 857, 501 15 Borås, Sweden

² Departamento de Tecnologías de la Información y Comunicaciones, Universidad Politécnica de Cartagena, 30202 Cartagena, Spain

Correspondence should be addressed to Paul Hallbjörner, paul.hallbjorner@sp.se

Received 29 November 2011; Accepted 9 January 2012

Academic Editor: David A. Sanchez-Hernandez

Copyright © 2012 Paul Hallbjörner et al. This is an open access article distributed under the Creative Commons Attribution License, which permits unrestricted use, distribution, and reproduction in any medium, provided the original work is properly cited.

Mode-stirred chambers provide an excellent tool for antenna characterization. Recent research has focused on making the mode-stirred chamber technique more versatile. One result of these efforts is the sample selection technique, by which a subset of data with specific properties is extracted from a measured set of raw data. This paper presents how to apply the sample selection technique to measurements of the correlation coefficient in dual antenna measurements, for example, for diversity or MIMO applications. Theoretical background and useful mathematical relations are presented. The application is verified through measurements.

1. Introduction

Mode-stirred chambers (MSCs) have since about a decade come to widespread use for antenna characterization and tests of wireless terminals [1–5]. Lately, much research has focused on how to make MSCs more flexible and versatile. One example is the sample selection technique [6–8]. It has been demonstrated in previous work to be applicable to the amplitude distribution of a measured signal. This paper presents an extension of the sample selection technique, in which it is applied to the correlation coefficient between the received signals from two antennas. The fundamental principle of the sample selection technique is the same as in previous work; it is merely applied to another parameter. Applying it to the correlation coefficient improves the usefulness of the sample selection technique in tests of diversity and/or MIMO antennas, where the correlation coefficient is critical. The aim of the presented work is to study the efficiency and accuracy of the proposed technique and demonstrate its practical usefulness.

2. Sample Selection Applied to Correlation Coefficient

In an MSC measurement, a sequence of samples is recorded. The sample set has a certain statistical distribution, described by a probability density function (PDF). The correlation coefficient is calculated from dual channel measurements of the signals from a pair of antennas. Dual channel data can be described by a bivariate (2D) PDF, according to [9, 10]

$$f(x_1, x_2) = \frac{x_1 x_2}{(1 - \rho^2) s_1^2 s_2^2} \exp\left(-\frac{1}{2(1 - \rho^2)} \cdot \left(\frac{x_1^2}{s_1^2} + \frac{x_2^2}{s_2^2}\right)\right) \cdot I_0\left(\frac{\rho x_1 x_2}{(1 - \rho^2) s_1 s_2}\right), \quad (1)$$

where I_0 is the modified Bessel function of the first kind and of order zero. The parameters s_1 and s_2 in (1) define the amplitudes on the two channels, respectively, and ρ is

the complex correlation coefficient between the data on the two channels, that is, $\rho = |\rho_c|$. There can be an imbalance in the initial data, which can be accounted for in the PDF by letting $s_1 \neq s_2$.

Sample selection is here applied for the purpose of achieving a different correlation coefficient than the one at hand for the whole sequence. This means that for one and the same antenna pair, different scenarios can be extracted in subsets of the initial data, something which can be useful in various performance analyses and tests. The sample selection technique can also be used to change the channel imbalance, but this is also possible by simply weighting the data on one of the channels. In this paper, it is assumed that any imbalance in the initial data should be maintained after sample selection.

For illustration, two examples of PDFs according to (1) are plotted in Figure 1. In each plot, the channels are balanced ($s_1 = s_2$), and different values of ρ are applied.

2.1. Accuracy in the Result. The accuracy with which the target correlation coefficient can be achieved is investigated through numerical simulations using Matlab. The initial data consists of N_i samples distributed according to the PDF $f_i(x)$. From these, N_t samples are selected which have a specific target PDF denoted by $f_t(x)$. The individual branch distributions are first verified, by generating two Rayleigh distributed sequences of initial data with $N_i = 50000$, $s_{1i} = 1$, $s_{2i} = 2$, and $\rho_i = 0.7$. The selection process is carried out with maintained branch amplitudes in the target data, that is, $s_{1t} = 1$ and $s_{2t} = 2$, and with target correlation $\rho_t = 0.2$. Figures 2(a) and 2(b) show the histogram PDF of the simulated data after sample selection, together with a solid curve marking the theoretical Rayleigh PDF.

Following this, the accuracy of the achieved correlation coefficient is investigated by performing sample selection on 500 realizations and plotting the histogram PDF of the achieved correlation coefficients. This is done for two values of ρ_i (0 and 0.7) and four values of ρ_t (0.3, 0.5, 0.7, and 0.9), thus in total eight cases. Each case uses $N_i = 10000$, $s_{1i} = 1$, and $s_{2i} = 2$. For comparison, in each case, sequences of length N_t and with target correlation coefficient ρ_t are also generated directly, that is, without any sample selection process. Due to the finite length of the sequences, these will also show some spread in the correlation coefficient. Figures 3(a) and 3(b) show PDFs of the achieved correlation coefficients, with histograms for the sample selection results, and solid lines for the directly generated data. The numbers next to the peaks are the N_t values. Apparently, the accuracy depends on ρ_i and ρ_t . Comparing the sample selection results with the directly generated data shows that the selection process itself does not increase the uncertainty by any significant amount, even though a small shift in the distribution is seen in Figure 3(a) for $\rho_t = 0.3$ and $\rho_t = 0.9$. The small shift, as well as some irregularities in the histograms, can be attributed to fluctuations due to the limited number of samples.

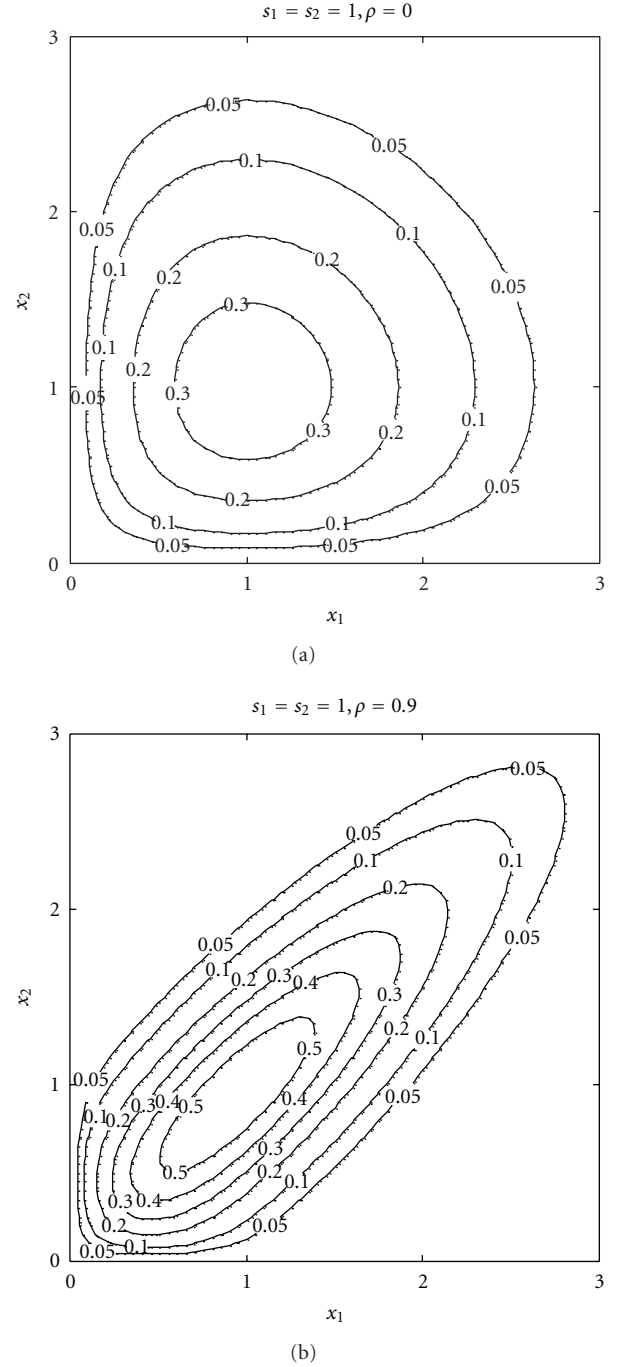


FIGURE 1: PDF for 2D Rayleigh distributed data, $\rho = 0$ (a) and $\rho = 0.9$ (b).

Varying N_t shows that the spread of the achieved correlation coefficient follows the relation

$$\sigma_\rho \propto \frac{1}{\sqrt{N_t}}. \quad (2)$$

This means that the proportion of remaining samples is critical for the accuracy.

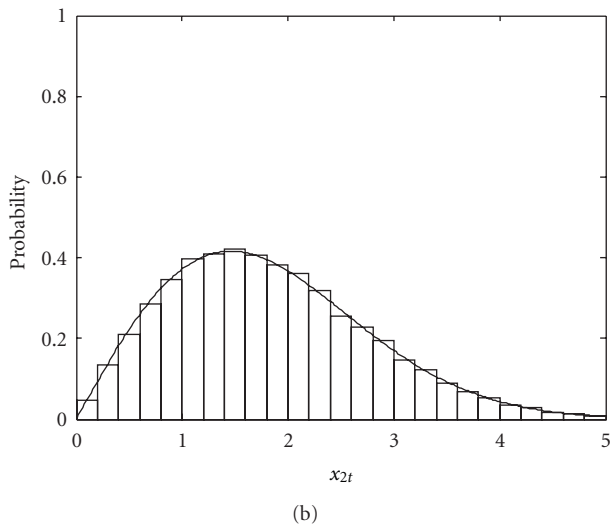
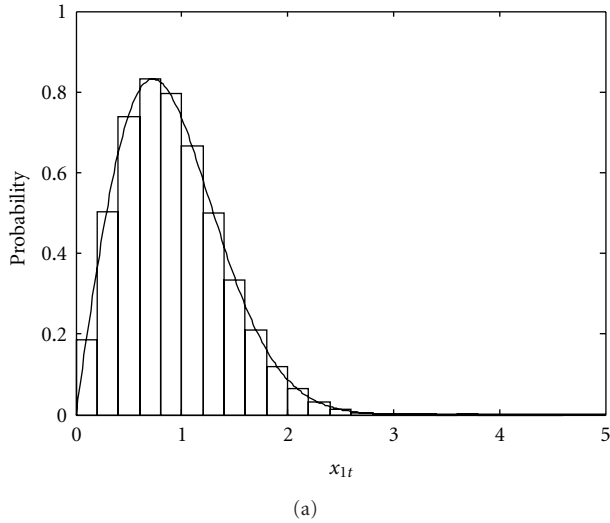


FIGURE 2: (a) PDF of the amplitudes on branch 1 of simulated sequence after sample selection, together with theoretical Rayleigh curve for $s = 1$. (b) PDF of the amplitudes on branch 2 of simulated sequence after sample selection, together with theoretical Rayleigh curve for $s = 2$.

2.2. Proportion of Remaining Samples. The proportion of remaining samples (N_t/N_i) in the proposed technique is limited by a theoretical relation [11], which for the general case is

$$q = \min\left(\frac{f_i(x)}{f_t(x)}\right). \quad (3)$$

Substituting (1) in (3), it is found after some manipulations that q is a function of ρ_i and ρ_t , and the expression depends on whether the correlation coefficient is reduced or increased in the sample selection process. For a reduction in correlation coefficient, it is

$$q_- = \frac{1 - \rho_i^2}{1 - \rho_t^2}, \quad (4)$$

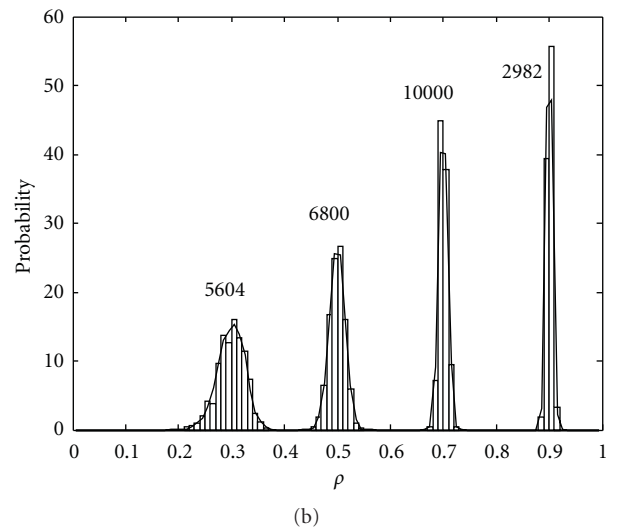
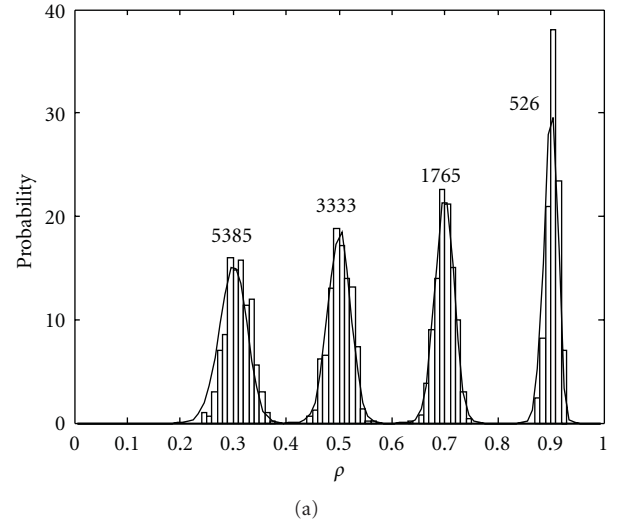


FIGURE 3: (a) PDFs for $\rho_i = 0$ and $\rho_t = 0.3, 0.5, 0.7,$ and 0.9 . $N_i = 10000$ in all cases. Numbers next to the peaks are N_t values. Histograms are the results of simulations with 500 realizations. Solid lines show spreads due to finite sequence length for the N_t values at hand. (b) PDFs for $\rho_i = 0.7$ and $\rho_t = 0.3, 0.5, 0.7,$ and 0.9 . $N_i = 10000$ in all cases. Numbers next to the peaks are N_t values. Histograms are the results of simulations with 500 realizations. Solid lines show spreads due to finite sequence length for the N_t values at hand.

whereas for an increase in correlation coefficient, it is

$$q_+ = \frac{(1 + \rho_i)(1 - \rho_t)}{(1 - \rho_i)(1 + \rho_t)}. \quad (5)$$

Equations (4) and (5) are illustrated in Figure 4, as functions of ρ_t for three different values of ρ_i .

3. Measurement Example

Measurements are performed in a mode-stirred chamber, on a pair of mobile terminal antennas. The measurement frequency is 2600 MHz. The data is recorded with a network

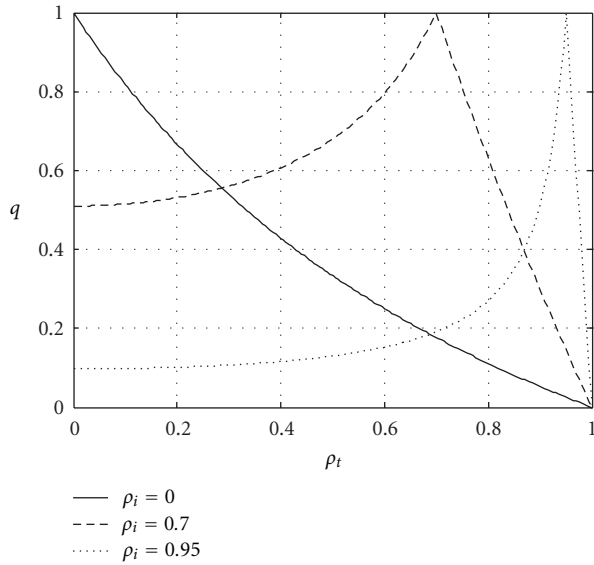


FIGURE 4: Proportion of remaining samples as a function of target correlation coefficient ρ_t , for three different values of initial correlation coefficient ρ_i .

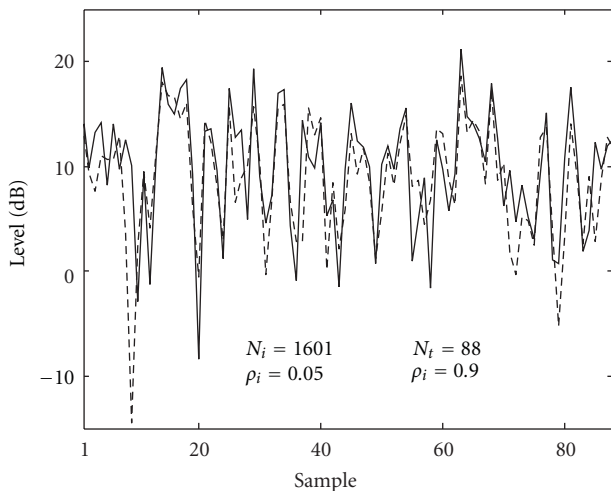


FIGURE 5: Remaining sequences after selection, with $\rho_t = 0.9$. Solid line is channel 1 and broken line is channel 2.

analyzer, as two simultaneous sequences of transmission coefficients, each of 1601 samples in length. These sequences constitute the initial data. A small imbalance of 1 dB (amplitude ratio 1.13) and a correlation coefficient of 0.05 are found in the initial data.

The sample selection technique is then applied for the purpose of increasing the correlation coefficient to 0.9, while maintaining the same imbalance. According to (5), $q = 0.058$, which means that it should be possible to have 93 samples in the output sequences. In practice, for relatively short sequences such as these, different realizations will give slightly different values of N_t due to statistical fluctuations. Results of two realizations are presented in Figures 5 and 6. Figure 5 shows the resulting sequences on the two channels,

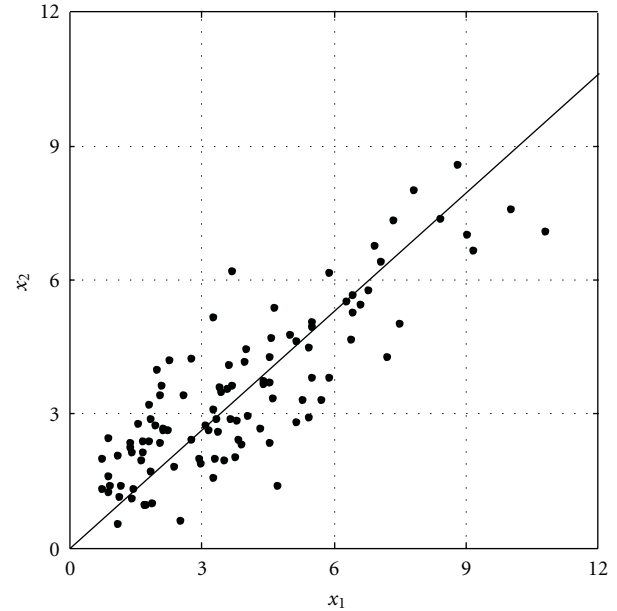


FIGURE 6: Remaining samples after selection, with $\rho_t = 0.9$.

with $N_t = 88$ and $\rho_t = 0.9$ achieved. Figure 6 shows the sample vectors, that is, (x_1, x_2) pairs, of a resulting sequence. These figures show that the vectors are correlated and that the imbalance, marked with a solid line in Figure 6, is maintained after sample selection.

4. Conclusion

It is demonstrated how the sample selection technique can be applied to the correlation coefficient between the signals from a pair of antennas. The initial sequences can have any correlation coefficient in the interval $(0, 1)$, as well as any mean power imbalance. The sample selection technique can achieve any correlation coefficient within the interval $(0, 1)$ in the result. Simulations show that using sample selection does not reduce the accuracy in the result, compared to data generated directly with the desired correlation coefficient. Expressions for the maximum proportion of remaining samples are presented. The proposed technique is demonstrated on measured dual channel data from a mode-stirred chamber.

Acknowledgments

This work was supported in part by the Spanish National R & D Programme through TEC 2008-05811 and by Fundación Séneca, the R & D coordinating agency for the Region of Murcia (Spain) under the 11783/PI/09 and 11610/IV2/09 Projects.

References

- [1] H. A. Mendes, "A new approach to electromagnetic field-strength measurements in shielded enclosures," Wescon, Los Angeles, Calif, USA, August 1968.

- [2] P. Corona, G. Latmiral, E. Paolini, and L. Piccioli, "Use of a reverberating enclosure for measurements of radiated power in the microwave range," *IEEE Transactions on Electromagnetic Compatibility*, vol. 18, no. 2, pp. 54–59, 1976.
- [3] J. Krogerus, *Comparison of methods for measuring total radiated power and radiation efficiency of handset antennas*, M.S. thesis, Master of Science Thesis at Helsinki University of Technology, Department of Electrical and Communications Engineering, 1999.
- [4] K. Madsén and P. Hallbjörner, "Reverberation chamber for mobile phone antenna tests," in *Proceedings of the Reverberation Chamber, Anechoic Chamber and OATS Users Meeting*, Seattle, Wash, USA, June 2001.
- [5] J. F. Valenzuela-Valdés, A. M. Martínez-González, and D. A. Sánchez-Hernández, "Emulation of MIMO nonisotropic fading environments with reverberation chambers," *IEEE Antennas and Wireless Propagation Letters*, vol. 7, Article ID 928488, pp. 325–328, 2008.
- [6] EMITE Ing. Document R4-101436, "Standardized fading channel emulation for MIMO OTA using a mode-stirred chamber with sample selection method," in *Proceedings of the 3GPP TSG RAN WG4 Adhoc#2 Meeting*, Dublin, Ireland, April 2010.
- [7] J. D. Sánchez-Heredia, M. Grudén, J. F. Valenzuela-Valdés, and D. A. Sanchez-Hernandez, "Sample-selection method for arbitrary fading emulation using mode-stirred chambers," *IEEE Antennas and Wireless Propagation Letters*, vol. 9, Article ID 5460965, pp. 409–412, 2010.
- [8] J. D. Sánchez Heredia, M. A. Garcia Fernandez, M. Grudén et al., "Arbitrary fading emulation using mode-stirred reverberation chambers with stochastic sample handling," in *Proceedings of the 5th European Conference on Antennas and Propagation (EuCAP '11)*, pp. 152–154, Rome, Italy, April 2011.
- [9] M. Nakagami, "The m-distribution—a general formula of intensity distribution of rapid fading," in *Statistical Methods in Radio Wave Propagation*, W.C. Hoffman, Pergamon, 1960.
- [10] C. Tellambura and A. D. S. Jayalath, "Generation of bivariate rayleigh and nakagami-m fading envelopes," *IEEE Communications Letters*, vol. 4, no. 5, pp. 170–172, 2000.
- [11] P. Hallbjörner, J. D. Sánchez-Heredia, E. de los Reyes, and D. A. Sánchez-Hernández, "Limit for the proportion of remaining samples in the mode-stirred chamber sample selection technique," *Microwave and Optical Technology Letters*, vol. 53, no. 11, pp. 2608–2610, 2011.

Research Article

On the Relationship between Field Amplitude Distribution, Its Maxima Distribution, and Field Uniformity inside a Mode-Stirred Reverberation Chamber

M. A. García-Fernández, C. Decroze, D. Carsenat, N. Arsalane, and G. Andrieu

OSA Department, XLim Laboratory, UMR CNRS 6172, University of Limoges, 123 avenue Albert Thomas, 87060 Limoges Cedex, France

Correspondence should be addressed to M. A. García-Fernández, garciafernandez.ma@upct.es

Received 2 December 2011; Accepted 24 January 2012

Academic Editor: David A. Sanchez-Hernandez

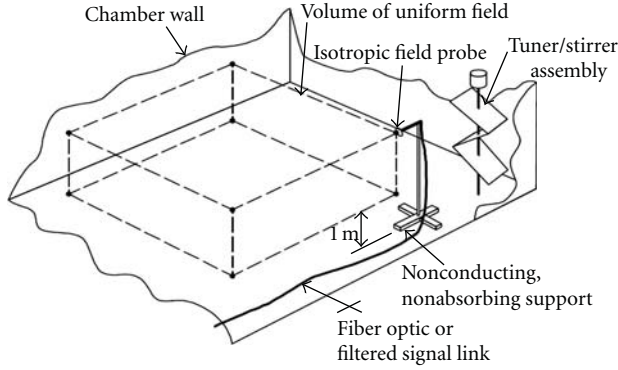
Copyright © 2012 M. A. García-Fernández et al. This is an open access article distributed under the Creative Commons Attribution License, which permits unrestricted use, distribution, and reproduction in any medium, provided the original work is properly cited.

A mode-stirred reverberation chamber (RC) is nowadays a commonly accepted performing tool for over-the-air (OTA) communication system evaluation, and their standardization is underway. Before performing active measurements of wireless communication systems using an RC, field uniformity inside the RC working volume has to be measured following the calibration method described in IEC standards 61000-4-21 and 61000-4-3, which requires 24 calibration measurements of field amplitude. In this contribution, we present the statistical laws that describe electromagnetic field maxima distribution, and based on them, a novel expression that could be useful to obtain a lower limit for the number of stirrer positions required at least to obtain a specific value for the normalized dispersion used to evaluate field uniformity with the IEC calibration method, being therefore of particular interest for OTA measurements.

1. Introduction

A mode-stirred reverberation chamber (RC) is an electrically large, highly conductive enclosed cavity commonly accepted as performing tool for electromagnetic (EM) measurements (both emissions and immunity) on electronic equipment and for over-the-air (OTA) communication system evaluation. It is typically equipped with mechanical stirrers that modify its electromagnetic field boundary conditions, and when it is well stirred, that is, when a sufficient number of modes are excited, the resulting environment is essentially statistically uniform and statistically isotropic (i.e., the energy having arrived from all aspect angles and at all polarizations) with independence of location [1], achieving the field uniformity requirements, except for those observation points in close proximity to walls [2] and nearby objects. The field uniformity property of an ideal reverberation chamber is such that the mean-square value of the electric field and its rectangular components is considered independent of

position [1]; likewise, the real and imaginary parts of each rectangular component of the electric and magnetic field throughout the chamber are Gaussian distributed, independent with identical variances; thus, the electric or magnetic field inside an ideal RC follows a single-cluster Rayleigh probability density function in amplitude and uniform distribution of phase, whereas the power fits an exponential one [3], which resembles the multipath fading in indoor scenarios of wireless communications systems. This RC behavior concerns high frequencies and can be qualified of “asymptotic” or “overmoded.” On another hand, the “undermoded” case corresponds to the lower part of the spectrum that is close to the lowest usable frequency (LUF) [4, 5]. Standard guidelines for RC operation usually involve estimating the LUF from the field uniformity of a given working volume. Field uniformity also permits to assess the behavior goodness of the RC, and its definition is based on the calibration procedure [4, 5]. The field is determined at eight points located at the working volume corners, as depicted in Figure 1, and



- Probe location for calibration

FIGURE 1: Chamber working volume [4].

normalized (to the square root of the input power). For each of the 8×3 normalized rectangular components, E_R , the maximum value among N^* stirrer positions, $E_{R\text{Max}}$, is evaluated. From these $E_{R\text{Max}}$ maxima values, the mean value $\langle E_{R\text{Max}} \rangle$ and empiric standard deviation $\sigma_{E_{R\text{Max}}}$ are calculated. Then, field uniformity is evaluated by calculating a normalized dispersion, S (dB), expressing the standard deviation $\sigma_{E_{R\text{Max}}}$ in terms of dB relative to the mean $\langle E_{R\text{Max}} \rangle$, that is,

$$S \text{ (dB)} = 20 \log_{10} \left(1 + \frac{\sigma_{E_{R\text{Max}}}}{\langle E_{R\text{Max}} \rangle} \right). \quad (1)$$

This is typically the figure of merit used to assess the performance of the RC, since the field within it is considered to be uniform if S (dB) is within 3 dB above 400 MHz, 4 dB at 100 MHz decreasing linearly to 3 dB at 400 MHz, and within 4 dB below 100 MHz [4]. Thus, field uniformity is a requirement for an RC to become a site for electromagnetic compatibility tests, in both radiated emission and susceptibility, and to provide measure reproducibility. Once field uniformity is attained in the working volume defined inside an RC, if a specific lower value of S (dB) is desired in order to obtain more accuracy for certain measurements, a higher number N^* of stirrer positions are required, and if it is determined only through trial and error, calibration costs will increase, owing to the fact that calibration according to IEC standards [4, 6] is a long process, as explained before. Thus, in this contribution, we present the statistical laws that describe electromagnetic field maxima distribution, and based on them, we develop a novel methodology which relates the normalized dispersion S (dB) and the number N of independent samples among the ones given by N^* stirrer positions (whose relationship is estimated in [7]) when uniformity of the field amplitude distribution of the 3 rectangular components at the 8 points of the working volume defined inside an RC is accomplished. This methodology does not replace the IEC calibration method [4, 6], since the only way to ensure the required uniformity is to perform the corresponding 24 measurements for N^* stirrer positions, and check that the collected samples are identically distributed, fitting a certain asymptotic law whose cumulative distribution function (CDF) is known. But once

this is accomplished, the presented methodology can help to search for the number N^* of stirrer positions necessary to obtain a desired lower S (dB) value quicker than only through trial and error, and thus decreasing calibration costs. This methodology has been validated through both simulations (by a Monte Carlo simulation, following the work presented in [5]) and measurements inside an RC. This contribution is of special interest for OTA measurements, whose standardization is underway [8], since it gives insights on the relationship between field amplitude distribution, its maxima distribution, and under the previously mentioned conditions, field uniformity inside an RC.

2. Statistical Derivation of Field Amplitude, Maxima Distribution, and Its Relationship with Field Uniformity

As in [9], where extreme value theory is used to deal with asymptotic distributions of extreme values, such as maxima, let X_1, X_2, \dots, X_N be independent and identically distributed (i.i.d.) random variables with a parent distribution function $F(x)$ and maxima $Y_N = \max_{1 \leq i \leq N} \{X_i\}$. If there exist constants $a_N \in \mathbb{R}, b_N > 0$, and some nondegenerate distribution function G such that the distribution of $(Y_N - a_N)/b_N$ converges to G , then G belongs to one of the three standard extreme value distributions: Frechet, Weibull, and Gumbel distributions. The following lemma indicates a sufficient condition for a parent distribution function $F(x)$ belonging to the domain of attraction of the Gumbel distribution.

Lemma 1. *Let X_1, X_2, \dots, X_N be i.i.d. random variables with a parent distribution function $F(x)$. Define $\omega(F) = \sup\{x : F(x) < 1\}$. Assume that there is a real number x_1 such that, for all $x_1 \leq x < \omega(F)$, $f(x) = F'(x)$ and $F''(x)$ exist and $f(x) \neq 0$. If*

$$\lim_{x \rightarrow \omega(F)} \frac{d}{dx} \left[\frac{1 - F(x)}{f(x)} \right] = 0, \quad (2)$$

then there exist constants a_N and $b_N > 0$ such that $(Y_N - a_N)/b_N$ uniformly converges in distribution to a normalized Gumbel random variable as $N \rightarrow \infty$. The normalizing constants a_N and b_N are determined by

$$\begin{aligned} a_N &= F^{-1} \left(1 - \frac{1}{N} \right), \\ b_N &= F^{-1} \left(1 - \frac{1}{Ne} \right) - F^{-1} \left(1 - \frac{1}{N} \right), \end{aligned} \quad (3)$$

where $F^{-1}(x) = \inf\{y : F(y) \geq x\}$ [9–11]. Therefore, if the amplitude of an electric field rectangular component inside the RC working volume, E_R , follows a parent distribution function $F(x)$, then the maxima values among N independent samples obtained through the stirring process, $E_{R\text{Max}}$, will follow a

Gumbel distribution, whose probability density function (PDF) is

$$g(y; a_N, b_N) = \frac{1}{b_N} \cdot \exp\left[-\frac{y - a_N}{b_N}\right] \cdot \exp\left[-\exp\left[-\frac{y - a_N}{b_N}\right]\right] \quad (4)$$

[12], where its location and scale parameters, a_N and b_N , respectively, can be straightforwardly derived from (3). For example, if the amplitude of an electric field rectangular component inside an RC is Rayleigh distributed, that is, $E_R \sim \text{Rayleigh}(\sigma)$, since the assumption in (2) is accomplished for $F(x) = \text{Rayleigh}(\sigma)$, the maximum value among N^* stirrer positions will be asymptotically Gumbel distributed, that is, $E_{R\text{Max}} \sim \text{Gumbel}(a_N, b_N)$, with $a_N = \sqrt{2\sigma^2 \ln(N)}$ and $b_N = \sqrt{2\sigma^2}(\sqrt{1 + \ln(N)} - \sqrt{\ln(N)})$, where N is the number of independent samples among the ones given by the N^* stirrer positions (whose relationship is estimated in [7], as mentioned in the introduction). Moreover, according to IEC 61000-4-21 standard [4], if the field amplitudes are normalized to the square root of the input power, $\sqrt{2\sigma^2}$ will be equal to 1, and so the expressions for a_N and b_N are even more simplified, that is, $a_N = \sqrt{\ln(N)}$ and $b_N = \sqrt{1 + \ln(N)} - \sqrt{\ln(N)}$. Furthermore, after knowing that the distribution of maxima values uniformly converges to a Gumbel one, in order to calculate its moments, moment convergence has to be ensured. Even though convergence in distribution is not equivalent to moment convergence in general, following the relation between convergence in distribution and moment convergence [9, 13], convergence in distribution for the maximum of nonnegative random variables, as field amplitude inside an RC, results in moment convergence. Thus, the mean value $\langle E_{R\text{Max}} \rangle$ and empiric standard deviation $\sigma_{E_{R\text{Max}}}$ of maxima values $E_{R\text{Max}}$ which follow a Gumbel distribution can be straightforwardly derived from their mathematical definition, using the Gumbel PDF described in (4), resulting in

$$\begin{aligned} \langle E_{R\text{Max}} \rangle &= a_N + \gamma b_N, \\ \sigma_{E_{R\text{Max}}} &= \frac{\pi}{\sqrt{6}} b_N, \end{aligned} \quad (5)$$

where $\gamma = 0.5772\dots$ is the Euler constant [11], and a_N and b_N were already presented in (3).

Likewise, in the particular case of attaining field uniformity inside an RC, evaluated through the IEC calibration method [4, 6], and when the collected samples of field amplitude are identically distributed for the 3 rectangular components at the 8 points of its working volume, field uniformity could also be evaluated by the following normalized dispersion:

$$\tilde{S} \text{ (dB)} = 20 \log_{10} \left(1 + \frac{\pi}{\sqrt{6}} \frac{1}{\gamma + (a_N/b_N)} \right). \quad (6)$$

It is obtained by substituting $\langle E_{R\text{Max}} \rangle$ and $\sigma_{E_{R\text{Max}}}$ in (1) for the values obtained from (5). However, \tilde{S} (dB) is not necessarily equal to S (dB), and the previously described distribution uniformity needs to be evaluated by the IEC

calibration method [4, 6] and attained in order to be comparable. The advantage that (6) provides is that once the described distribution uniformity is accomplished, in order to achieve a lower dispersion S (dB), the higher number N^* of stirrer positions which would be required at least can be calculated faster using it if we consider that the ratio between N and N^* should not be increased when N^* is increased if the stirring method is not altered. It is worthy to note that field uniformity evaluated by means of (6) only depends on its coefficients a_N and b_N , which are described in (3), and thus on the distribution of the field amplitude inside the RC working volume, $F(x)$, and the number of independent samples, N , among the ones given by the N^* stirrer positions. Following the previous example, if the field amplitude distribution results to be Rayleigh (σ) for the 3 rectangular components at the 8 points of the working volume defined inside an RC, (6) becomes

$$\tilde{S} \text{ (dB)} = 20 \log_{10} \left(1 + \frac{\pi}{\sqrt{6}} \frac{1}{\gamma + 1/(\sqrt{1 + (1/\ln(N))} - 1)} \right), \quad (7)$$

which depends only on the number N of independent collected samples. Thus, (6) and (7) can also be useful to calculate the number N of independent samples among the ones given by the N^* stirrer positions from the S (dB) value calculated according to IEC standards [4, 6] when the previously described distribution uniformity is accomplished.

3. Validation through Monte Carlo Simulations

Following the works presented in [5, 14], we use a Monte Carlo simulation in order to validate the expression presented in (5), and also the one in (6) for the case of having the previously described distribution uniformity, by confirming that the maxima values among N independent samples which follow a given parent distribution $F(x)$ follow a distribution that converges asymptotically to a Gumbel one, comparing the maxima mean value and standard deviation to the ones given by (5), and also comparing the field uniformity dispersion S (dB) to the \tilde{S} (dB) given by (6).

Thus, using a MATLAB script, 24 signals of a determined length N (modeling the 3 rectangular components of the electric field at the 8 working volume corners along the same number of independent stirrer positions) are randomly generated following one specific distribution function, $F(x)$. Then, the maximum value of each signal is calculated, and the mean value and standard deviation of these 24 maxima are computed. The procedure is iterated 1000 times, and the averaged results are depicted in Figures 2 and 3, in solid lines. They are compared with the ones predicted by (5), in dotted lines. Different numbers N of independent samples (or alternatively, independent stirrer positions), and a Rice distribution as parent distribution, with different K -factors (including $K = 0$ in order to study the results for a Rayleigh distribution) have been used. As we can see, since maxima distribution only converges asymptotically to a Gumbel one (but does not fit exactly for a finite number N of independent

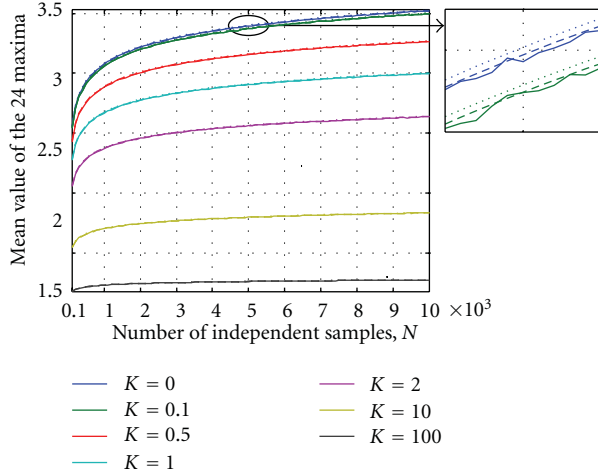


FIGURE 2: Mean value of the 24 maxima, averaged along 1000 runs of a Monte Carlo simulation, and the comparison to the values predicted by (5), for a Rice distribution as parent distribution with different K -factors.

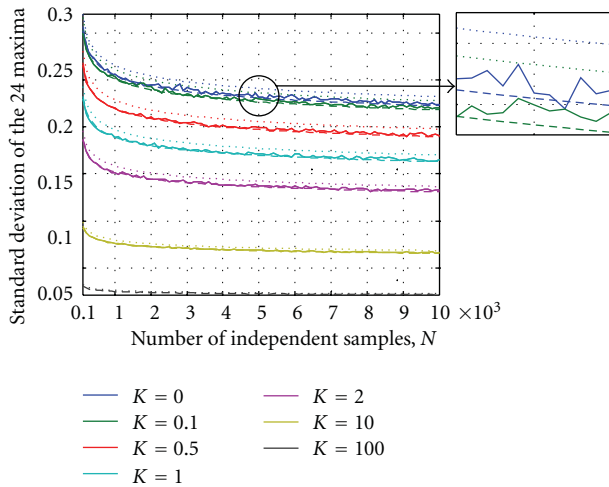


FIGURE 3: Standard deviation of the 24 maxima, averaged along 1000 runs of a Monte Carlo simulation, and the comparison to the values predicted by (5), for a Rice distribution as parent distribution with different K -factors.

samples), there is a small bias from the simulated results to the predicted ones. However, this bias has also been corrected by multiplying b_N , obtained following (3), by a factor of $23/24 = 0.9583\dots$ (related to the $M = 24$ maxima, as $(M - 1)/M$), and recalculating the statistics by means of (5), as shown in dashed lines.

Afterwards, field uniformity is evaluated by calculating the normalized dispersion S (dB) according to IEC standards [4, 6] from the simulated samples (using the statistics of the 24 maxima), and the obtained values are averaged over the 1000 Monte Carlo runs and depicted (in green) in Figures 4–6, for different K -factors. Moreover, S (dB) extrema [S (dB)_{min} S (dB)_{max}] have been also computed, as in [5] (and depicted in blue and red, resp.). These results are

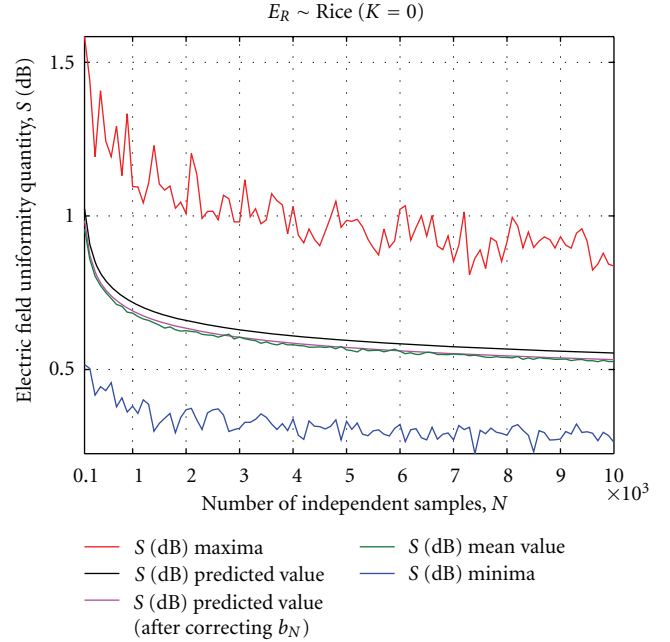


FIGURE 4: S (dB) mean value, averaged along 1000 runs of a Monte Carlo simulation, and the comparison to the values predicted by (6), for a Rayleigh distribution as parent distribution (Rice distribution with $K = 0$).

compared with the ones predicted by (6), \tilde{S} (dB) (depicted in black). Since a small bias appears for the same reason already explained for the statistics (mean value and standard deviation) case, b_N is multiplied by the same correcting factor of $23/24$, and the resulting \tilde{S} (dB) is also presented (in magenta).

As we can see, the mean value of the calculated S (dB), averaged along the 1000 runs of the Monte Carlo simulation, asymptotically converges to the \tilde{S} (dB) given by (6), with b_N calculated following (3). Moreover, after multiplying b_N by the correction factor of $23/24$, the mean value of the calculated S (dB) fits \tilde{S} (dB). Similar results are obtained for other parent distributions, $F(x)$, as Weibull or Nakagami, and they are therefore not presented here for brevity. It is also worthy to note that field uniformity is improved when the K -factor of the Rice distribution (followed by the amplitude of the electric field rectangular components) increases. This is obvious since when the dominant direct coupling component of the field is increased, the Rice K -factor is also increased, and in this case, the coefficient of variation of amplitude of the electric field rectangular components is reduced, thus decreasing the normalized dispersion used to evaluate the field uniformity. Likewise, we can observe from the results that the absolute deviation between both extrema of S (dB) along the 1000 Monte Carlo simulations (which are performed considering distribution uniformity) is up to 1 dB (when each rectangular component is modeled by $N = 100$ independent samples following a Rayleigh distribution), and this should be taken in consideration when an RC calibration is performed according to the IEC standards [4, 6] in order

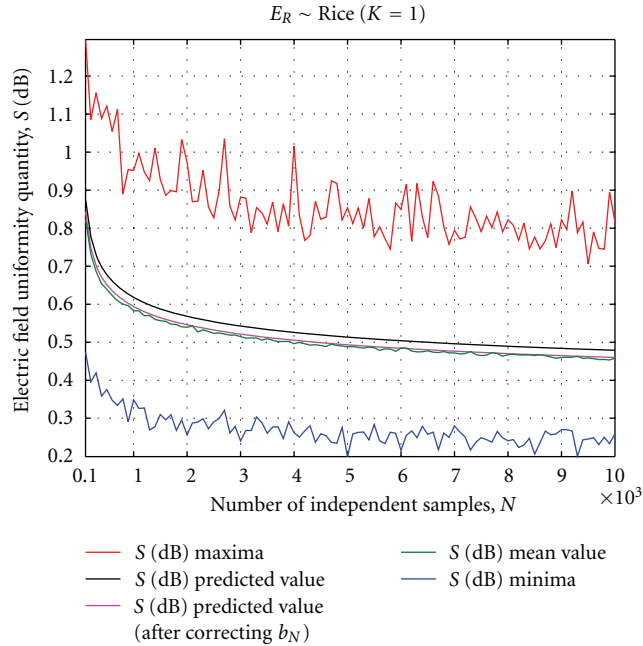


FIGURE 5: S (dB) mean value, averaged along 1000 runs of a Monte Carlo simulation, and the comparison to the values predicted by (6), for a Rice distribution with $K = 1$ as parent distribution.

to consider the field within the RC as uniform or not, specially when the value of S (dB) resulted too close to the corresponding limit of 3 dB or 4 dB [4] (depending on the frequency, as mentioned in the introduction).

4. Validation through Measurements in Reverberation Chambers

In order to ensure the validity of (5), and also the one of (6) when the previously described distribution uniformity is accomplished, several measurements have been carried out in one of the RCs of the OSA Department at XLim Laboratory, whose inner view is shown in Figure 7.

Following the IEC calibration method [4, 6], the amplitude of the x -, y -, and z -rectangular components of the electric field has been measured using a triaxial probe located at the 8 corners of a delimited working volume, at a frequency of 2 GHz. At this frequency, the RC is considered to work under the “overmoded” regime inside its factory-delimited working volume, and this requirement is necessary in order to compare the results obtained from the measurements to the ones provided by the equations presented before. The associated empirical CDFs are shown in Figure 8, considering two different working volumes: one slightly inside the factory-delimited working volume and the factory-delimited working volume itself. As we can see, they asymptotically converge to a Rayleigh distribution (the differences will be attributed to a lack of independent samples, since the measurement counts only with $N^* = 100$ stirrer positions). Then, the maxima values for each one of the normalized rectangular components are evaluated,

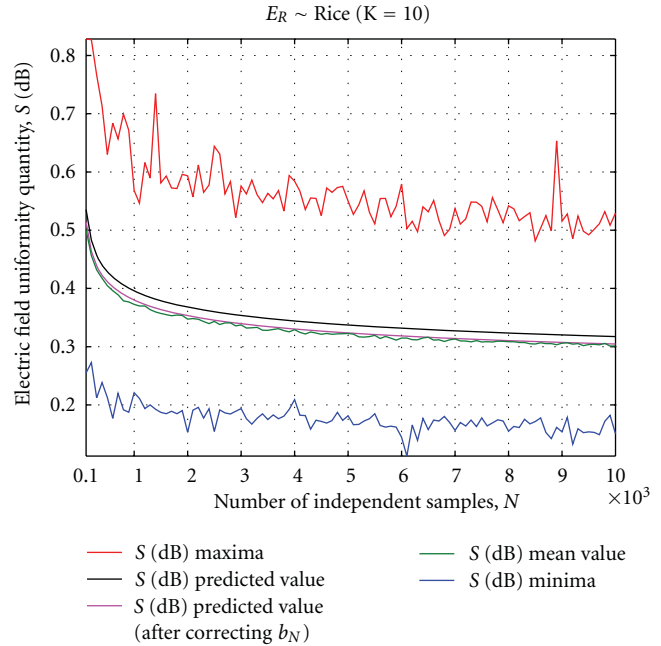


FIGURE 6: S (dB) mean value, averaged along 1000 runs of a Monte Carlo simulation, and the comparison to the values predicted by (6), for a Rice distribution with $K = 10$ as parent distribution.



FIGURE 7: Inner view of the RC used in this study.

TABLE 1: Measured results.

Measurement	$\langle E_{RMax} \rangle$	$\sigma_{E_{RMax}}$	S (dB)
I	2.2625	0.3284	1.1771
II	2.2249	0.2830	1.0399

and from these maxima, E_{RMax} , the mean value $\langle E_{RMax} \rangle$ and empiric standard deviation $\sigma_{E_{RMax}}$ are calculated and compared to the values given by (5). Finally, field uniformity is evaluated by calculating the normalized dispersion S (dB) according to IEC standards [4, 6], and the obtained value is compared to the one given (6). The results obtained from the measurements performed for the two different working volumes, following the IEC calibration method [4, 6], are shown in Table 1.

Likewise, when the amplitude of the rectangular components is considered to be Rayleigh, (5) gives $\langle E_{RMax} \rangle = 2.2739$ and $\sigma_{E_{RMax}} = 0.2842$, for $N = 100$ independent

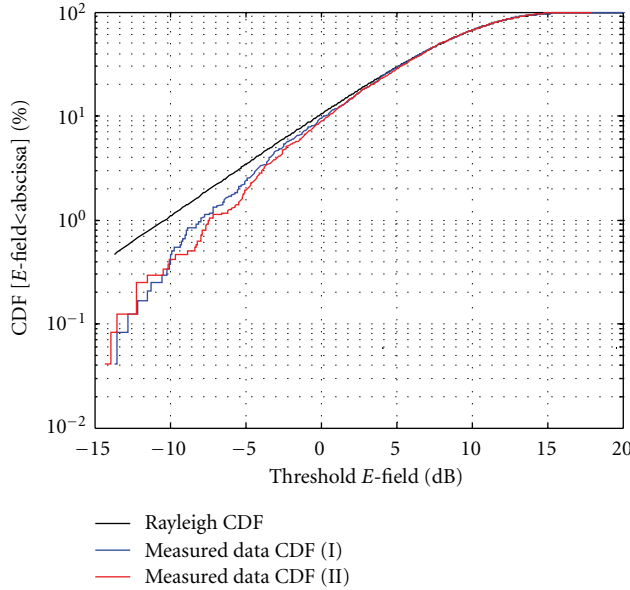


FIGURE 8: CDFs of the electric field (x -, y -, and z -rectangular components) at a frequency of 2 GHz.

samples. In addition, (6), or (7) since the considered distribution is a Rayleigh one, gives a value of \tilde{S} (dB) = 1.0228..., also for $N = 100$ independent samples. As we can see, the measured values are very close to the one given by the equations presented in this contribution, since the assumption of having the same distribution for the amplitudes of all the rectangular components is accomplished for both measurements, as depicted in Figure 8. Moreover, the measured values of S (dB) resulted to be also situated between the minimum and maximum values, [S (dB) $_{\min} = 0.5161, S$ (dB) $_{\max} = 1.5841$] calculated by the Monte Carlo simulation for $N = 100$ independent samples, as previously depicted in Figure 4.

Furthermore, after performing the calibration according to the IEC standards [4, 6], and confirming that the distribution of the amplitude of the rectangular components of the electric field has resulted to be Rayleigh, if a lower S (dB) value was desired, in order to obtain a higher accuracy, the number N^* of stirrer positions that would be required at least can be calculated using (7). For example, if S (dB) was desired to be lower than 0.5 dB, substituting \tilde{S} (dB) by 0.5 dB in (7), we obtain that the number N of independent samples that are required *at least* for that purpose would be 29429, and performing a calibration according to IEC standards [4, 6] with a number N^* of stirrer positions lower than this higher number N would be useless, since increasing the number N^* of stirrer positions cannot decrease the distribution uniformity and cannot also increase the ratio between N and N^* if the stirring method is not altered. This is specially important after seeing that the S (dB) value obtained for $N^* = 100$ stirrer positions is around 1 dB, and that the absolute deviation from one calibration realization to another in the same conditions has resulted to be up to 1 dB, as confirmed by the Monte Carlo simulations

previously depicted in Figure 4, and thus, the value of S (dB) = 0.5 dB desired in this example could be obtained by chance using a lower number N^* of stirrer positions but only because of a deviation, and not because the field is really as uniform as desired and as S (dB) = 0.5 dB indicates. Therefore, (7), and in general, (6), becomes useful for calculating a lower limit for the number N^* of stirrer positions to be selected in order to obtain a specific value for S (dB) dispersion when performing a calibration according to the IEC standards [4, 6], specially once distribution uniformity is attained in a previous calibration with a lower number N^* of stirrer positions. In this way, the search for the desired value of S (dB) would be faster if compared to searching for it only through trial and error, and consequently, the associated calibration time and costs would be reduced.

5. Discussion and Conclusions

In this paper, the statistical laws that describe electromagnetic field maxima distribution as a Gumbel one with parameters given by (3) have been presented, thus permitting to calculate the statistics mean value and standard deviation of the maxima values distributed so using (5). Based on that, we present in (6) a novel expression which relates the normalized dispersion S (dB) used to evaluate field uniformity to the number N of independent samples collected among the N^* stirrer positions used to calibrate an RC according to the IEC standards [4, 6] for the special case of having distribution uniformity, that is, when the field amplitude of the 3 rectangular components measured at the 8 points of the working volume defined inside the RC follows the same distribution. This study has been successfully validated both through Monte Carlo simulations and measurements in an RC.

Moreover, as it has been shown in Figures 4–6, field uniformity measured through the IEC calibration method [4, 6] can vary more than 1 dB between two calibration realizations even when the amplitude of the electric field rectangular components is independent and identically distributed at the eight points located at the working volume corners. Thus, since repeating the calibration process enough times to calculate an estimation of the mean value of the normalized dispersion S (dB) is usually unaffordable due to time requirements, it is essential to know a lower limit for the number N^* of stirrer positions to be selected in order to obtain a specific value for S (dB). This lower limit can be easily obtained from (6) by substituting \tilde{S} (dB) by the desired S (dB) value, taking into account that the more distribution uniformity we have and the more independent the samples between two consecutive stirrer positions are, the more this lower limit approaches the real number N^* of stirrer positions required for this purpose.

Therefore, this contribution is of special interest for OTA measurements, whose standardization is underway [8], since it not only gives insights on the relationship between field amplitude distribution and its maxima distribution, but also it could help to accelerate the achievement of a specific value of S (dB) when performing a calibration according to IEC

standards [4, 6] compared to doing it only through trial and error and consequently could help to reduce calibration time and costs.

Acknowledgment

This research has been partially funded by a fellowship grant by Fundación Séneca, the Regional R&D Coordinating Unit of the Region of Murcia (Spain).

References

- [1] D. A. Hill, "Electromagnetic Theory of Reverberation Chambers," (US) Technical Note 1506, National Institute of Standards and Technology, 1998.
- [2] L. R. Arnaut and P. D. West, "Electromagnetic reverberation near a perfectly conducting boundary," *IEEE Transactions on Electromagnetic Compatibility*, vol. 48, no. 2, pp. 359–371, 2006.
- [3] D. A. Hill, "Plane wave integral representation for fields in reverberation chambers," *IEEE Transactions on Electromagnetic Compatibility*, vol. 40, no. 3, pp. 209–217, 1998.
- [4] Electromagnetic Compatibility (EMC)—Part 4-21, "Testing and measurement techniques—reverberation chamber test methods," IEC 61000-4-21, 2003.
- [5] G. Orjubin, E. Richalot, S. Mengué, and O. Picon, "Statistical model of an undermoded reverberation chamber," *IEEE Transactions on Electromagnetic Compatibility*, vol. 48, no. 1, pp. 248–251, 2006.
- [6] Electromagnetic Compatibility (EMC)—Part 4-3, "Testing and measurement techniques—radiated, radio-frequency, electromagnetic field immunity test," IEC 61000-4-3, 2006.
- [7] C. Lemoine, P. Besnier, and M. Drissi, "Estimating the effective sample size to select independent measurements in a reverberation chamber," *IEEE Transactions on Electromagnetic Compatibility*, vol. 50, no. 2, pp. 227–236, 2008.
- [8] M. A. García-Fernández, J. D. Sánchez-Heredia, A. M. Martínez-González, D. A. Sánchez-Hernández, and J. F. Valenzuela-Valdés, "Advances in mode-stirred reverberation chambers for wireless communication performance evaluation," *IEEE Communications Magazine*, vol. 49, no. 7, pp. 140–147, 2011.
- [9] G. Song and Y. Li, "Asymptotic throughput analysis for channel-aware scheduling," *IEEE Transactions on Communications*, vol. 54, no. 10, pp. 1827–1834, 2006.
- [10] H. A. David, *Order Statistics*, Wiley, New York, NY, USA, 1970.
- [11] J. Galambos, *The Asymptotic Theory of Extreme Order Statistics*, Wiley, New York, NY, USA, 1978.
- [12] E. J. Gumbel, "Statistical theory of extreme values and some practical applications," in *A Series of Lectures, National Bureau of Standards*, Applied Mathematics Series, 33, pp. 8–51, US Government Printing Office, Washington, DC, USA, 1954.
- [13] J. Pickands III, "Moment convergence of sample extremes," *The Annals of Mathematical Statistics*, vol. 39, no. 3, pp. 881–889, 1968.
- [14] J. M. Ladbury, "Monte Carlo Simulation of Reverberation Chambers," Internal Note, National Institute of Standards and Technology (NIST), Boulder, Colo, USA, 1999.